ADVANCED CARBON CHEMISTRY FOR RECHARGEABLE BATTERIES

EDITED BY: Hongshuai Hou, Weijie Li, Tang Wei and Weihua Chen
PUBLISHED IN: Frontiers in Chemistry

frontiers Research Topics

ISSN 1664-8714
ISBN 978-2-88966-127-5
DOI 10.3389/978-2-88966-127-5

About Frontiers

Frontiers is more than just an open-access publisher of scholarly articles: it is a pioneering approach to the world of academia, radically improving the way scholarly research is managed. The grand vision of Frontiers is a world where all people have an equal opportunity to seek, share and generate knowledge. Frontiers provides immediate and permanent online open access to all its publications, but this alone is not enough to realize our grand goals.

Frontiers Journal Series

The Frontiers Journal Series is a multi-tier and interdisciplinary set of open-access, online journals, promising a paradigm shift from the current review, selection and dissemination processes in academic publishing. All Frontiers journals are driven by researchers for researchers; therefore, they constitute a service to the scholarly community. At the same time, the Frontiers Journal Series operates on a revolutionary invention, the tiered publishing system, initially addressing specific communities of scholars, and gradually climbing up to broader public understanding, thus serving the interests of the lay society, too.

Dedication to Quality

Each Frontiers article is a landmark of the highest quality, thanks to genuinely collaborative interactions between authors and review editors, who include some of the world's best academicians. Research must be certified by peers before entering a stream of knowledge that may eventually reach the public - and shape society; therefore, Frontiers only applies the most rigorous and unbiased reviews.
Frontiers revolutionizes research publishing by freely delivering the most outstanding research, evaluated with no bias from both the academic and social point of view. By applying the most advanced information technologies, Frontiers is catapulting scholarly publishing into a new generation.

What are Frontiers Research Topics?

Frontiers Research Topics are very popular trademarks of the Frontiers Journals Series: they are collections of at least ten articles, all centered on a particular subject. With their unique mix of varied contributions from Original Research to Review Articles, Frontiers Research Topics unify the most influential researchers, the latest key findings and historical advances in a hot research area! Find out more on how to host your own Frontiers Research Topic or contribute to one as an author by contacting the Frontiers Editorial Office: researchtopics@frontiersin.org

ADVANCED CARBON CHEMISTRY FOR RECHARGEABLE BATTERIES

Topic Editors:
Hongshuai Hou, Central South University, China
Weijie Li, University of Wollongong, Australia
Tang Wei, Xi'an Jiaotong University, China
Weihua Chen, Zhengzhou University, China

Citation: Hou, H., Li, W., Wei, T., Chen, W., eds. (2020). Advanced Carbon Chemistry for Rechargeable Batteries. Lausanne: Frontiers Media SA.
doi: 10.3389/978-2-88966-127-5

Table of Contents

frontiers in Chemistry

EDITORIAL
published: 08 September 2020
doi: 10.3389/fchem.2020.00667

Editorial: Advanced Carbon Chemistry for Rechargeable Batteries

Hongshuai Hou[1]*, *Weijie Li*[2], *Weihua Chen*[3] and *Wei Tang*[4]

[1] Central South University, Changsha, China, [2] University of Wollongong, Wollongong, NSW, Australia, [3] Zhengzhou University, Zhengzhou, China, [4] Xi'an Jiaotong University, Xi'an, China

Keywords: carbon materials, batteries, electrochemistry, energy storage, energy chemistry

Editorial on the Research Topic

Advanced Carbon Chemistry for Rechargeable Batteries

The growing demand for green, alternative, and sustainable energy technology greatly expedites the development of energy storage/conversion devices like rechargeable batteries and supercapacitors. Carbon-based materials, which serve as a prevalent candidate in rechargeable batteries, have been widely explored due to their abundance, non-toxicity, stability, and durability. Furthermore, in other types of anode materials (including alloys, metal oxides, and metal sulfide), the introduction of carbon heterophase nanocomposite has been considered a prevalent strategy in enhancing the cycling performance due to an integrated structure stability during the charging/discharging process.

Amorphous carbon literally represents carbon with a low graphitization degree. The long-term disordered and short-term ordered structure is a typical feature for amorphous carbon in terms of micro texture. Specifically, amorphous carbon comprised of *sp*2 hybridized carbon which is rich in suspending bonds and other structural defects. Compared with graphite materials, amorphous carbon anodes exhibit a larger specific surface area, an abundance of porous structures and more active sites, which could bring about improved electrochemical properties.

When applied in rechargeable batteries, the microstructure and morphology, the graphitization degree, the specific surface area, the surface functionality, and porosity of carbon materials work synergistically to affect electrochemical performances. The unmodified bulk carbon used in anode material suffers from poor electrochemical performances due to the limited electron transport, sluggish ion migration, and undeveloped active sites. Consequently, in order to enhance the reversible capacity and electrochemical performance of carbon-based anode materials, the rational design and modification for advanced carbon-based materials has been proposed.

Heteroatom doping (B, N, P, S) has been regarded as a promising method to enhance the electrochemical properties of the carbon electrode. Heteroatom doping of large radius atoms (P, S) increases the interlayer spacing and induces structural distortion, providing more active sites for Li^+, Na^+, and K^+ storage. Heteroatom doping for small diameter atoms (B, N) may adjust the electron cloud density to facilitate the charge transfer and enhance the electrode-electrolyte interactions, and prove the wettability of the surface. In this topic collection, P/N-co-doped carbon nanosheets, N-doped graphene, and S-doped hard carbon@rGO composites for rechargeable batteries are reported, the chemical mechanism and process are discussed systematically. In addition, defects, pore structure, and micromorphology

OPEN ACCESS

Edited and reviewed by:
Nosang Vincent Myung,
University of California, Riverside,
United States

***Correspondence:**
Hongshuai Hou
hs-hou@csu.edu.cn

Specialty section:
This article was submitted to Electrochemistry, a section of the journal Frontiers in Chemistry

Received: *01 June 2020*
Accepted: *29 June 2020*
Published: *08 September 2020*

Citation:
Hou H, Li W, Chen W and Tang W (2020) Editorial: Advanced Carbon Chemistry for Rechargeable Batteries. Front. Chem. 8:667. doi: 10.3389/fchem.2020.00667

of carbon materials on the electrochemical performances are discussed as well.

Carbon materials are often utilized as "additives" to improve the electrochemical performances of other electrode materials, such as metal oxides/sulfides/phosphides. The introduction of carbon materials can not only enhance the conductivity but also accommodate the volume change of electrode materials, which leads to the improved cycle stability and rate capability. In this topic collection, silicon, FeOOH, $CuCo_2S_4$, and Cu_3P modified by functional carbon materials are reported.

We hope it will be helpful for readers to further understand the advanced carbon chemistry for rechargeable batteries.

AUTHOR CONTRIBUTIONS

HH, WL, WC, and WT co-edit this Research Topic. All authors contributed to the article and approved the submitted version.

Conflict of Interest: The authors declare that the research was conducted in the absence of any commercial or financial relationships that could be construed as a potential conflict of interest.

frontiers in Chemistry

ORIGINAL RESEARCH
published: 31 October 2019
doi: 10.3389/fchem.2019.00733

Hierarchical Nitrogen-Doped Porous Carbon Microspheres as Anode for High Performance Sodium Ion Batteries

*Kaiqi Xu[1], Qicang Pan[2], Fenghua Zheng[2], Guobin Zhong[1], Chao Wang[1], Shijia Wu[1] and Chenghao Yang[2]**

[1] Electric Power Research Institute of Guangdong Power Grid Co., Ltd., Guangzhou, China, [2] Guangzhou Key Laboratory for Surface Chemistry of Energy Materials, New Energy Research Institute, School of Environment and Energy, South China University of Technology, Guangzhou, China

Sodium ion batteries (SIBs) have been considered as a promising alternative to lithium ion batteries (LIBs) for large scale energy storage in the future. However, the commercial graphite anode is not suitable for SIBs because of its low Na^+ ions storage capability and poor cycling stability. Recently, another alternative as anode for SIBs, amorphous carbon materials, have attracted tremendous attention because of their abundant resource, nontoxicity, and most importantly, stability. Here, N-doped hierarchical porous carbon microspheres (NHPCS) derived from Ni-MOF have been prepared and used as anode for SIBs. Benefiting from the open porous structure and expanded interlayer distance, the diffusion of Na^+ is greatly facilitated and the Na^+ storage capacity is significantly enhanced concurrently. The NHPCS exhibit high reversible capacity (291 mA h g^{-1} at current of 200 mA g^{-1}), excellent rate performance (256 mA h g^{-1} at high current of 1,000 mA g^{-1}), and outstanding cycling stability (204 mA h g^{-1} after 200 cycles).

Keywords: Ni-MOF, hierarchical porosity, carbon microspheres, anode material, sodium ion batteries

OPEN ACCESS

Edited by:
Hongshuai Hou,
Central South University, China

Reviewed by:
Zhian Zhang,
Central South University, China
Yunhua Xu,
Tianjin University, China

***Correspondence:**
Chenghao Yang
esyangc@scut.edu.cn

Specialty section:
This article was submitted to Electrochemistry, a section of the journal Frontiers in Chemistry

Received: *06 September 2019*
Accepted: *14 October 2019*
Published: *31 October 2019*

Citation:
Xu K, Pan Q, Zheng F, Zhong G, Wang C, Wu S and Yang C (2019) Hierarchical Nitrogen-Doped Porous Carbon Microspheres as Anode for High Performance Sodium Ion Batteries. Front. Chem. 7:733. doi: 10.3389/fchem.2019.00733

INTRODUCTION

Lithium ion batteries (LIBs) have been widely used as the power sources for portable electric devices, electric vehicles (EV), and hybrid electric vehicles (HEVs), because of their high energy density, high operate voltage and long services life (Zheng et al., 2015; Huang et al., 2016; Wang et al., 2017; Pan et al., 2018a). While, the applications LIBs in large-scale electrochemical energy system (EES) is restricted by the limited lithium resources in the earth's crust (Liu Y. Z. et al., 2018). Alternatively, sodium ion batteries (SIBs) working with the similar intercalation chemistry have attracted much attention, for the abundance of Na on the earth (Larcher and Tarascon, 2015; Li W. et al., 2015; Li et al., 2018). Nevertheless, the commercial graphite anode is not suitable for the fabrication of high performance SIBs, because of the poor diffusion kinetics of the much larger Na^+ ions compared to Li^+ ions (Luo et al., 2016; Hwang et al., 2017). Therefore, it is urgent to find an appropriate anode material for SIBs.

Recently, metallic alloy, metal sulfide and metal oxide have been explored as anode materials for SIBs (Liu et al., 2015; Ning et al., 2015; Pan et al., 2018b). Although exhibiting high capacity, these materials are subject to large volume change during the sodiation/desodiation process, and as a result, they are reported to suffer fast capacity loss and poor rate capability (Yabuuchi et al., 2014).

Carbonaceous materials, for example, expanded graphite, graphene, carbon nanotubes, and other amorphous carbon, were also studied as alternatives (Wen et al., 2014; Luo et al., 2015; Xu et al., 2015; Li et al., 2016a). These materials have attracted many attentions because of their abundant resource, stability, and low cost (Hou et al., 2017a).Among them, amorphous carbon, e.g., hard carbon and soft carbon, show high Na^+ accommodation capacity (Li et al., 2016b; Jian et al., 2017), but low initial coulombic efficiency, low capacity, and fast capacity degradation (Qian et al., 2018).

Heteroatom-doping with B, N, S, or P is an effective strategy to enhance the electrical conductivity and increase the specific surface area carbonaceous materials, hence enhance electron transport and provide more Na^+ storage active sites (Li D. et al., 2015; Yang et al., 2015). P-doped carbon nanosheets, S-doped hard carbon, N-doped carbon, and S, N-codoped carbon nanosheets have been demonstrated to effectively improve the electrochemical performance (Wang et al., 2016; Hou et al., 2017b; Yang et al., 2017; Hong et al., 2018). Hollow porous structures have promise to improve the cycling and rate performance of carbonaceous materials for SIBs, as this unique porous structure (1) can offer more Na^+ storage active sites, and therefore has the potential to give rise to higher capacity; (2) offer faster Na^+ transportation channels, which contributes to excellent rate capability; and (3) buffer the volume expansion during the repeated sodiation/desodiation process, leading to improved cycling performance (Li Z. et al., 2015; Zhang et al., 2015).

Herein, we developed a synergetic strategy to combine the above-mentioned merits of the heteroatom-doping and porous structures into one material by preparing Ni-MOF derived N-doped hierarchical porous carbon microspheres (NHPCS). This hierarchical porous structure are shown to offer more active sites for Na^+ storage, provide fast Na^+ diffusion channels, and alleviate the volume expansion during the sodiation/desodiation process. Meanwhile, the incorporation of N expanded interlayer distance and increased the surface area of the carbon microspheres, which enhances the cycling and rate performance. Benefiting from this unique design, NHPCS combines the advantages of both heteroatom-doping and porous structures, and are shown to exhibit high reversible capacity, outstanding rate performance and good cycling stability.

EXPERIMENTAL SECTION

0.864 g nickel nitrate hexahydrate, 0.3 g 1, 3, 5-benzenetricarboxylic acid (H3BTC), and 3.0 g polyvinylpyrrolidone (PVP) were dissolved in a mixed solution (20 ml DMF, 20 ml absolute ethanol, and 20 ml deionized water, stirring for 30 min). The as-obtained mixture was transferred into 100 mL Teflon-lined autoclave and heated at 150°C for 10 h. Afterwards, the formed participate was centrifuged with ethanol three times and dried at 80°C overnight. Subsequently, the obtained Ni-MOF was annealed with melamine (with a weight ratio of 1:1) at 800°C for 1 h under Ar atmosphere. Finally, the obtained product was wash with 2 M HCl to remove Ni nanoparticles and the N-doped hierarchical porous carbon microspheres (NHPCS) were obtained. Hierarchical porous carbon microspheres (HPCS) were synthesized with the same procedure except that annealing process was conducted without melamine.

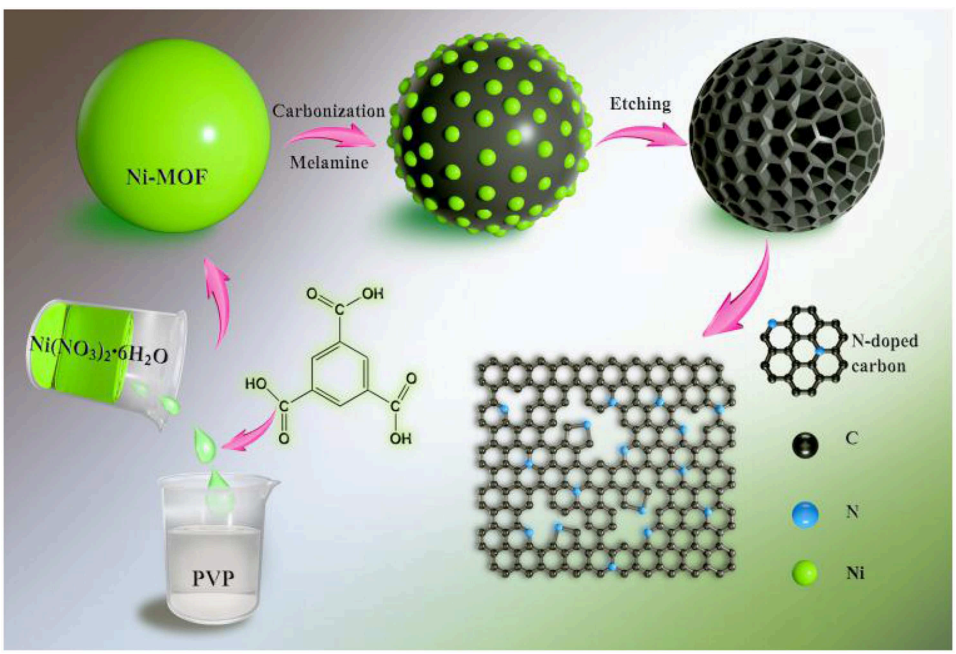

FIGURE 1 | Schematic illustration for the fabrication of N-doped hierarchical porous carbon microspheres (NHPCS).

MATERIAL CHARACTERIZATION

The crystalline phases of samples were characterized by XRD (Rigaku D/max 2500). The morphology of NHPCS/HPCS were observed by SEM (Hitachi, SU8010) and TEM (JEOL JEM-2100F). The XPS tests were carried out to determine the chemical composition and chemical state of elements of the sample.

To determine the specific area, the nitrogen absorption/desorption isotherm measurements were performed using ASAP2020 Surface Area and Porosity Analyzer. Raman measurements were performed using a laser Raman spectrometer (Jobin Yvon, Model T6400).

ELECTROCHEMICAL MEASUREMENTS

To prepare electrode, the NHPCS/HPCS active material was mixed with PVDF and acetylene black with a mass ratio of 8:1:1. N-methyl-2-pyrrolidene (NMP) was added to the mixture and a uniform slurry was obtained after grinding. The slurry was then coated onto the Cu foil, and dried at 80°C for 12 h. Subsequently, 2,032 coin cells were assembled using sodium metal foil as counter electrode, glass fiber as separator. The electrolyte was 1 M $NaCF_3SO_3$ in DEGDME. The cycling and rate performance of NHPCS and HPCS was tested at Land BT2013A systems using CR2032 coin cell.

RESULTS AND DISCUSSIONS

Figure 1 shows the overall schematic illustration for the fabrication of N-doped hierarchical porous carbon microspheres (NHPCS). Firstly, Ni-MOF precursors were obtained *via* a simple hydrothermal method (see Experimental Section for detail). PVP plays an important role to form the Ni-MOF spheres during the hydrothermal process. The shape inducing effects of PVP could be attributed to the groups of hydrophobic vinyl and hydrophilic carbonyl that lead to the formation of polarized micelles. Subsequently, the obtained Ni-MOF precursors were calcinated with melamine under Ar atmosphere. This annealing process converts MOF to N-C microspheres while maintains the framework of Ni-MOF template, with the Ni nanoparticles uniformly distributing in the carbon microspheres. Finally, the NHPCS was obtained after removing the Ni nanoparticles by etching with HCl aqueous solution.

The morphology of the Ni-MOF, Ni/C, Ni/N-C microspheres was investigated by SEM (**Supporting Information**). The

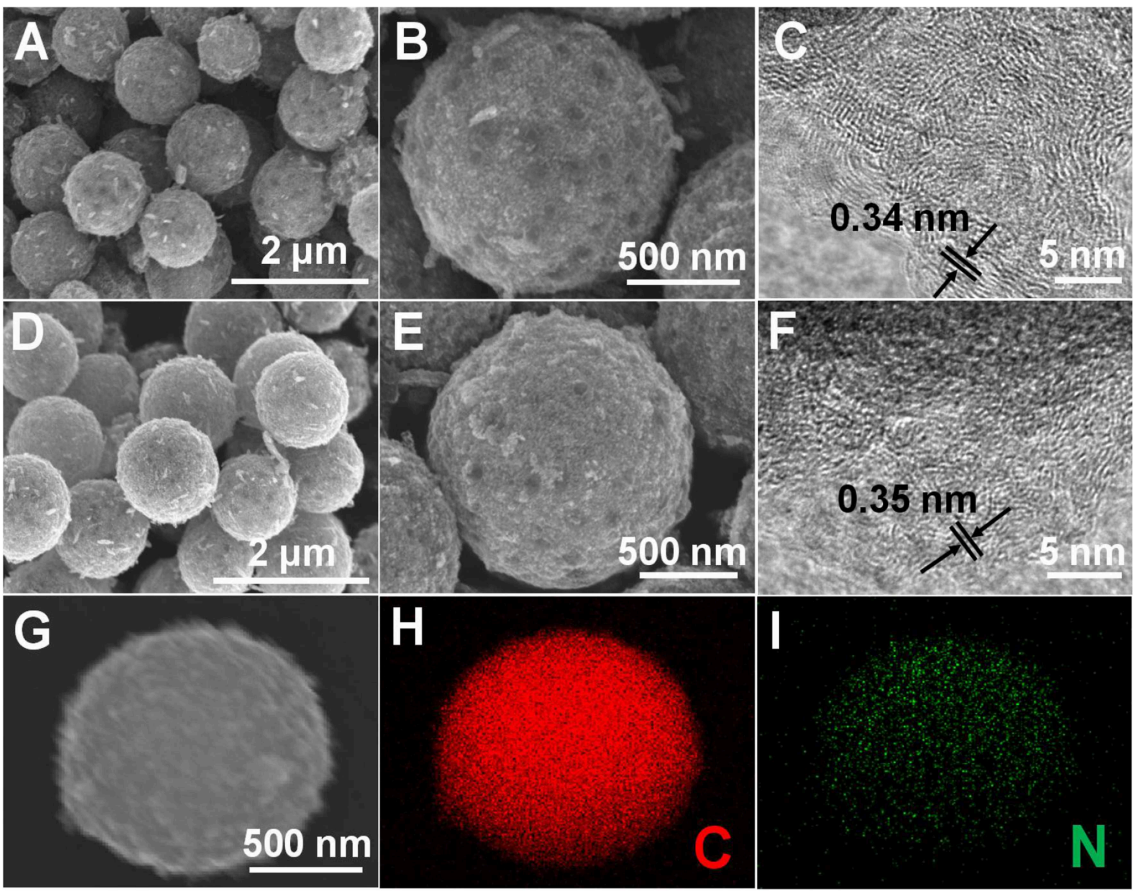

FIGURE 2 | SEM and TEM images of HPCS **(A–C)** and NHPCS **(D–F)**, EDS elemental mapping of NHPCS **(G–I)**.

SEM images in **Figures S1A,B** show that of Ni-MOF precursor exhibits a very uniform sphere structure with a diameter of around 1.5 μm. This uniform sphere structure was successfully retained after the annealing process, as confirmed from the morphology of the as-formed Ni/C microspheres (**Figure S1C**) The existence of nickel metal was confirmed by XRD (**Figure S2A**; Lou et al., 2017). Ni/N-C microspheres was synthesized by annealing the Ni-MOF precursor with melamine. Notably, the uniform sphere structure was well maintained after the N-doping process, as shown in **Figure S1D**. XRD patterns were collected for HPCS and NHPCS (**Figure S2A**). A broad peak located at around 24.6° was observed for both samples, which attributed to the (002) diffraction of the disordered carbon structure (Xu et al., 2016; Niu et al., 2017). In the final product, the existence of small amount of Ni nanoparticles might greatly enhance its electronic conductivity.

The structural features of HPCS and NHPCS were examined by SEM and TEM. The SEM results strongly support that the morphology of HPCS and NHPCS are well consistent with the Ni-MOF precursor (**Figures 2A,B,D,E**), which confirms that the morphology of Ni-MOF precursor can be well maintained during the annealing process. TEM images of HPCS and NHPCS were displayed in **Figure S3**. There are abundant micropore interconnected with each other in HPCS and NHPCS. On the other hand, minor amount of Ni nanoparticles were retained in the obtained HPCS and NHPCS, which is in good accordance with the XRD results. The HRTEM images exhibit that the interlayer distance of HPCS and NHPCS are 0.34 and 0.35 nm, respectively (**Figures 2C,F**). This indicates that nitrogen doping can increase the interlayer spacing between the carbon layers (Yan et al., 2016). Moreover, the EDS elemental mapping of NHPCS shows that the N atoms are uniformly dispersed in the carbon microspheres, suggesting that the nitrogen is successfully doped into carbon spheres (**Figures 2H,I**).

Figure 3A displays the Raman spectra of HPCS and NHPCS. Two peaks are exhibited at around 1,338 and 1,582 cm^{-1}, which can be ascribed to the D band and G band corresponding to defect-induced band and crystalline graphite band, respectively (Liu Y. et al., 2018). Therefore, the relative amount of disorder or defects in the carbon structure can be obtained according to the relative intensity ration of the D peak to the G peak (I_D/I_G). The I_D/I_G values of HPCS and NHPCS are 1.0 and 1.02, respectively, implying that nitrogen doping improves the disorder degree of carbon materials (Li et al., 2016c).

The XPS measurement was carried out to investigate the surface chemical composition of NHPCS. The survey spectra

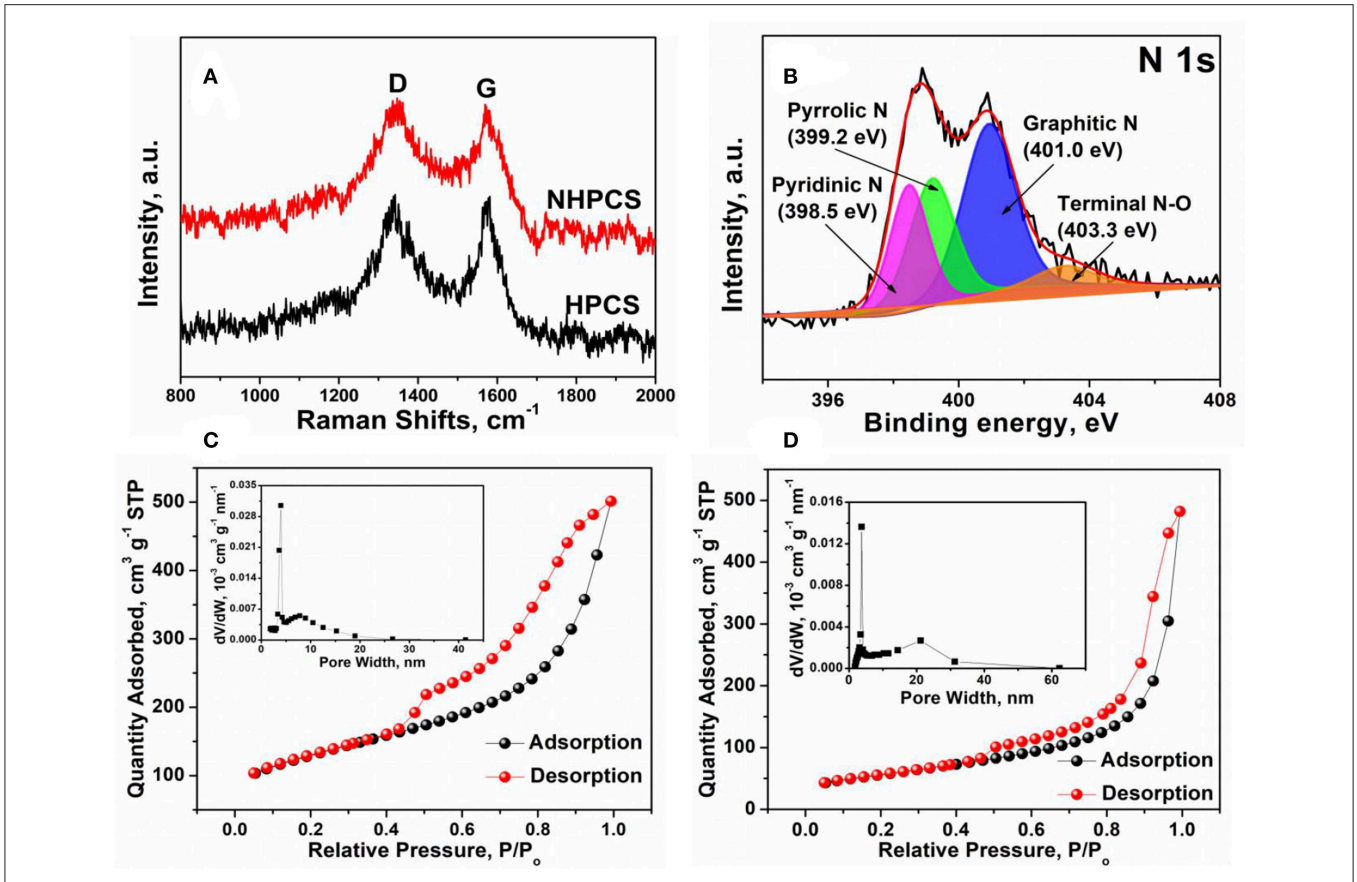

FIGURE 3 | (A) Raman spectra of HPCS and NHPCS; **(B)** XPS N 1 s spectra of NHPCS; **(C,D)** N_2 adsorption isotherm and corresponding pore width distribution for HPCS and NHPCS.

indicate that C, O, Ni, and N elements exist in NHPCS, which can be further confirmed that the existence of small amount of Ni nanoparticles etching with HCl aqueous solution (**Figure S2B**). And the high-resolution N 1 s spectra as shown in **Figure 3B**, four peaks at 398.5, 399.2, 401.0, and 403.3 eV can be ascribed to the typical pyridinic, pyrrolic, graphitic, and quaternary nitrogen, respectively (Liu et al., 2016). The XPS results further confirm that the N-doped carbon was successfully obtained. Furthermore, nitrogen adsorption-desorption isotherms were performed to characterize the surface area and pore structure of HPCS and NHPCS. **Figures 3C,D** displays the nitrogen adsorption-desorption isotherms for HPCS and NHPCS (inset of C and D are the corresponding pore size distribution curves), respectively. The two curves exhibit similar typical IV isortherm with H_2-type hysteresis loops at the relative pressure (P/P_0) range of 0.5–1.0, suggesting the mesoporous features of the structures, and the specific surface area for HPCS and NHPCS are 200.21 and 223.25 m^2 g^{-1}, respectively. The pores of HPCS are mainly distributed at 3.97 and 7.81 nm, while the pores of NHPCS are mainly distributed at 3.72 and 21.15 nm according to the pore size distribution curves, which further suggesting the mesoporous features of the structures in the HPCS and NHPCS.

The electrochemical performance of HPCS and NHPCS were evaluated using 2,032 coin cells and 1 M $NaCF_3SO_3$ in DEGDME used as the electrolyte. **Figure 4A** shows the CV curves of NHPCS electrode during the initial four cycles. In the first discharge process, two peaks at around 1.0 and 0.6 V can be observed, which are disappeared in next three cycles, corresponding to

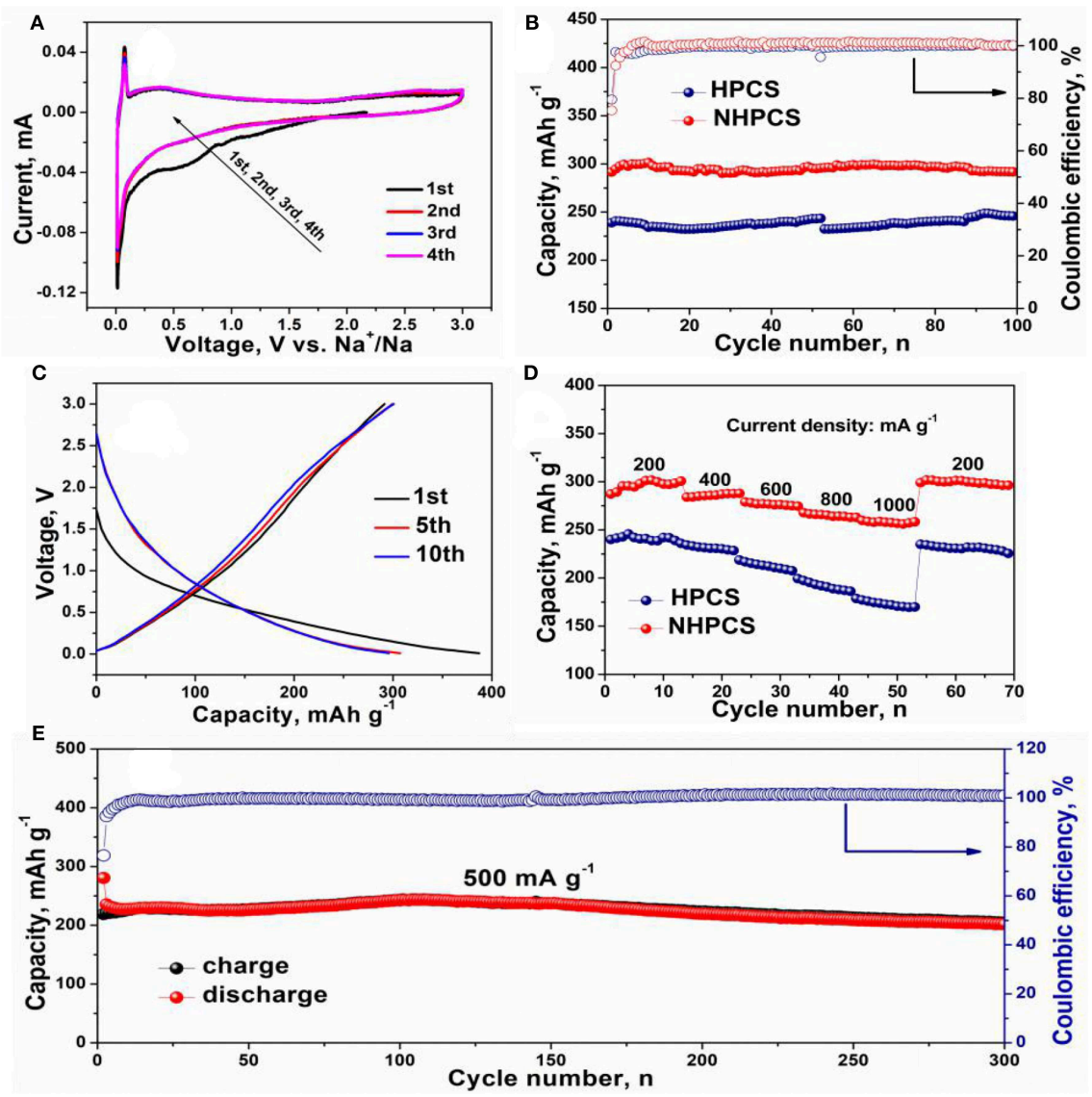

FIGURE 4 | CV curves of NHPCS **(A)**, cycle performance of HPCS and NHPCS at 200 mA g^{-1} **(B)**, charge and discharge profiles of NHPCS **(C)**, rate performance of HPCS and NHPCS **(D)**, long-term cycling performance of NHPCS at 500 mA g^{-1} **(E)**.

the formation of SEI film and side reactions (Hong et al., 2014; Zhu et al., 2018). Subsequently, a strong redox peak at around 0.03 V can be observed, which can be ascribed to Na^+ insertion/extraction from NHPCS. And the CV curves are highly overlapped with each other after the first cycle, which indicating an outstanding reversible cycling stability.

Figure 4B displays the cycling performance of HPCS and NHPCS at 200 mA g^{-1}, a high reversible capacity of 291.8 mA h g^{-1} can be obtained after 100 cycles for NHPCS. And NHPCS also exhibits outstanding cycling stability during the charge/discharge process at 200 mA g^{-1}. But for HPCS, lower reversible capacity of 245.9 mA h g^{-1} was obtained after 100 cycles at the same current density. Furthermore, the coulombic efficiency of NHPCS approaches 100% during the cycling process, which is higher than HPCS. Subsequently, the charge and discharge profiles of NHPCS are provided in **Figure 4C**, a long slope below 1.0 V in the first sodiation process can be observed. For the charge process, the curve became steeper. The initial discharge and charge capacities of NHPCS are 387 and 291 mA h g^{-1}, corresponding to an initial coulombic efficiency of 75.2%. And the charge and discharge profiles of HPCS are provided in **Figure S4A**, which show similar shapes to NHPCS. Furthermore, the initial discharge and charge capacities of HPCS are 297.2 and 239.3 mA h g^{-1}, corresponding to an initial coulombic efficiency of 80.2 %. Power density is very important for SIBs in practical application for electric vehicles. Therefore, the rate performances of NHPCS and HPCS at different current density range from 200 to 1,000 mA g^{-1} have been tested (**Figure 4D**). A high reversible capacity of 298, 285, 276, 265, and 256 mA h g^{-1} at current density of 200, 400, 600, 800, and 1,000 mA g^{-1}, respectively. And for HPCS, lower reversible capacity of 240, 231, 214, 192, and 172 mA h g^{-1} at current density of 200, 400, 600, 800, and 1,000 mA g^{-1} were obtained, respectively. These results indicate that high reversible capacity and cycling stability can be attributed to, which can facilitate Na^+ transport, offer more active sites for Na^+, and improve the adsorption capacity of Na^+. Furthermore, long-term cycling performance of NHPCS was further tested at 500 mA g^{-1}, and the result is display in **Figure 4E**. NHPCS exhibits excellent cycling stability and high reversible capacity. 204 mA h g^{-1} can be remained after 300 cycles.

To further analyze the reasons for the improved cycling and rate performance of NHPCS, the EIS measurements of NHPCS and HPCS were tested, and the corresponding Nyquist plots are shown in **Figure 5**. The two Nyquist plots exhibit similar shapes and consist of a semicircle in high-frequency region and a sloping line in low-frequency region (Pan et al., 2017; Zheng et al., 2018). Subsequently, charge transfer resistances of NHPCS and HPCS can be obtained according to the EIS curves and equivalent electric circuit (**Figure 5**). The Rct of NHPCS and HPCS are 3.98 and 5.37Ω, respectively (as shown in **Table S1**). The lower charge transfer resistance of NHPCS was attributed to the nitrogen doped which can enhance electronic conductivity and facilitate the transport of Na^+ ions (Wang et al., 2013; Fu et al., 2014). Furthermore, the morphology change after cycling were also investigated to further analyze

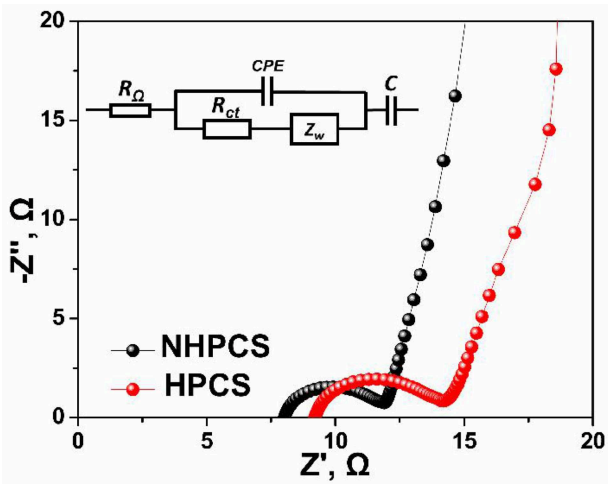

FIGURE 5 | Nyquist plots of NHPCS and HPCS before cycling. Inserted is the equivalent circuit, R_Ω is the electrolyte resistance, R_{ct} is the charge-transfer resistance, and Z_w is the Warburg impedance.

the outstanding cycling stability of NHPCS. The SEM images of NC after 100 cycles as shown in **Figure S6**. The sphere structure was maintained well after 100 cycles, indicating that the NHPCS with a good structural stability during the cycling process.

NHPCS exhibits remarkable cycling performance and rate capability when tested as anode for SIBs, which can be owing to the unique hierarchical porous structure and N doping. The detailed reasons can be summarized as follows: (1) The unique hierarchical porous structure can offer more Na^+ storage active sites and buffer the volume change during the sodiation/desodiation process. (2) The hierarchical porous structure can facilitate Na^+ transport and provide a short diffusion distance for Na^+. (3) The nitrogen doping can enhance electronic conductivity to facilitate the transport of Na^+ and the electrons.

CONCLUSIONS

In summary, N-doped hierarchical porous carbon microspheres (NHPCS) have been successfully fabricated from Ni-MOF with annealed exist of melamine. Benefiting from the nitrogen doped and hierarchical porous structure, NHPCS can offer more Na^+ storage active sites and provide fast Na^+ ions transfer channels. As a result, when evaluated as anode for SIBs. NHPCS can exhibit high reversible capacity of 291 mA h g^{-1} at 200 mA g^{-1}. When the current density increase to 1,000 mA g^{-1}, high reversible capacity of 256 mA h g^{-1} was also can be obtained. Moreover, NHPCS possess a high reversible capacity of 204 mA h g^{-1} after 300 cycles at 500 mA g^{-1}. Therefore, NHPCS should be considered as promising anode materials for SIBs because of its outstanding rate capability and excellent cycling performance.

DATA AVAILABILITY STATEMENT

All datasets generated and analyzed for this study are included in the article/**Supplementary Material**.

AUTHOR CONTRIBUTIONS

KX conducted the experiments. CY is the supervisor of this research work. KX and QP helped with writing. KX, QP, FZ, GZ, CW, and SW performed the characterization and data analysis. All authors involved the analysis of experimental data and manuscript preparation.

ACKNOWLEDGMENTS

We gratefully acknowledge the financial support from the Guangdong Power Grid Co., Ltd. (Grant No. GDKJXM20161890).

SUPPLEMENTARY MATERIAL

The Supplementary Material for this article can be found online at: https://www.frontiersin.org/articles/10.3389/fchem.2019.00733/full#supplementary-material

REFERENCES

Fu, L. J., Tang, K., Song, K. P., van Aken, P. A., Yu, Y., and Maier, J. (2014). Nitrogen doped porous carbon fibres as anode materials for sodium ion batteries with excellent rate performance. *Nanoscale* 6, 1384–1389. doi: 10.1039/c3nr05374a

Hong, K. L., Qie, L., Zeng, R., Yi, Z. Q., Zhang, W., Wang, D., et al. (2014). Biomass derived hard carbon used as a high performance anode material for sodium ion batteries. *J. Mater. Chem. A* 2, 12733–12738. doi: 10.1039/c4ta02068e

Hong, Z., Zhen, Y., Ruan, Y., Kang, M., Zhou, K., Zhang, J.-M., et al. (2018). Rational design and general synthesis of S-doped hard carbon with tunable doping sites toward excellent Na-ion storage performance. *Adv. Mater.* 30:1802035. doi: 10.1002/adma.201802035

Hou, H., Qiu, X., Wei, W., Zhang, Y., and Ji, X. (2017a). Carbon anode materials for advanced sodium-ion batteries. *Adv. Energy Mater.* 7:1602898. doi: 10.1002/aenm.201602898

Hou, H., Shao, L., Zhang, Y., Zou, G., Chen, J., and Ji, X. (2017b). Large-area carbon nanosheets doped with phosphorus: a high-performance anode material for sodium-ion batteries. *Adv. Sci.* 4:1600243. doi: 10.1002/advs.201600243

Huang, Y. G., Pan, Q. C., Wang, H. Q., Ji, C., Wu, X. M., He, Z. Q., et al. (2016). Preparation of a $Sn@SnO_2@c@MoS_2$ composite as a high-performance anode material for lithium-ion batteries. *J. Mater. Chem. A* 4, 7185–7189. doi: 10.1039/c6ta02080a

Hwang, J. Y., Myung, S. T., and Sun, Y. K. (2017). Sodium-ion batteries: present and future. *Chem. Soc. Rev.* 46, 3529–3614. doi: 10.1039/c6cs00776g

Jian, Z., Bommier, C., Luo, L., Li, Z., Wang, W., Wang, C., et al. (2017). Insights on the mechanism of Na-ion storage in soft carbon anode. *Chem. Mater.* 29, 2314–2320. doi: 10.1021/acs.chemmater.6b05474

Larcher, D., and Tarascon, J. M. (2015). Towards greener and more sustainable batteries for electrical energy storage. *Nat. Chem.* 7, 19–29. doi: 10.1038/nchem.2085

Li, B., Dai, F., Xiao, Q. F., Yang, L., Shen, J. M., Zhang, C. M., et al. (2016c). Nitrogen-doped activated carbon for a high energy hybrid supercapacitor. *Energy Environ. Sci.* 9, 102–106. doi: 10.1039/c5ee03149d

Li, D., Chen, H., Liu, G., Wei, M., Ding, L.-X., Wang, S., et al. (2015). Porous nitrogen doped carbon sphere as high performance anode of sodium-ion battery. *Carbon* 94, 888–894. doi: 10.1016/j.carbon.2015.07.067

Li, L., Zheng, Y., Zhang, S. L., Yang, J. P., Shao, Z. P., and Guo, Z. P. (2018). Recent progress on sodium ion batteries: potential high-performance anodes. *Energy Environ. Sci.* 11, 2310–2340. doi: 10.1039/c8ee01023d

Li, W., Zhou, M., Li, H., Wang, K., Cheng, S., and Jiang, K. (2015). A high performance sulfur-doped disordered carbon anode for sodium ion batteries. *Energy Environ. Sci.* 8, 2916–2921. doi: 10.1039/c5ee01985k

Li, Y., Hu, Y.-S., Li, H., Chen, L., and Huang, X. (2016a). A superior low-cost amorphous carbon anode made from pitch and lignin for sodium-ion batteries. *J. Mater. Chem. A* 4, 96–104. doi: 10.1039/C5TA08601A

Li, Y., Hu, Y. S., Titirici, M. M., Chen, L., and Huang, X. (2016b). Hard carbon microtubes made from renewable cotton as high-performance anode material for sodium-ion batteries. *Adv. Energy Mater.* 6:1600659. doi: 10.1002/aenm.201600659

Li, Z., Ding, J., and Mitlin, D. (2015). Tin and Tin compounds for sodium ion battery anodes: phase transformations and performance. *Acc. Chem. Res.* 48, 1657–1665. doi: 10.1021/acs.accounts.5b00114

Liu, H., Jia, M., Cao, B., Chen, R., Lv, X., Tang, R., et al. (2016). Nitrogen-doped carbon/graphene hybrid anode material for sodium-ion batteries with excellent rate capability. *J. Power Sources* 319, 195–201. doi: 10.1016/j.jpowsour.2016.04.040

Liu, Y., Yang, C., Pan, Q., Li, Y., Wang, G., Ou, X., et al. (2018). Nitrogen-doped bamboo-like carbon nanotubes as anode material for high performance potassium ion batteries. *J. Mater. Chem. A* 6, 15162–15169. doi: 10.1039/C8TA04694H

Liu, Y. C., Zhang, N., Jiao, L. F., and Chen, J. (2015). Tin nanodots encapsulated in porous nitrogen-doped carbon nanofibers as a free-standing anode for advanced sodium-ion batteries. *Adv. Mater.* 27, 6702–6707. doi: 10.1002/adma.201503015

Liu, Y. Z., Zhong, W. T., Yang, C. H., Pan, Q. C., Li, Y. P., Wang, G., et al. (2018). Direct synthesis of FeS/N-doped carbon composite for high-performance sodium-ion batteries. *J. Mater. Chem. A* 6, 24702–24708. doi: 10.1039/c8ta08562e

Lou, P., Cui, Z., Jia, Z., Sun, J., Tan, Y., and Guo, X. (2017). Monodispersed carbon-coated cubic NiP_2 nanoparticles anchored on carbon nanotubes as ultra-long-life anodes for reversible lithium storage. *ACS Nano* 11, 3705–3715. doi: 10.1021/acsnano.6b08223

Luo, W., Shen, F., Bommier, C., Zhu, H. L., Ji, X. L., and Hu, L. B. (2016). Na-ion battery anodes: materials and electrochemistry. *Acc. Chem. Res.* 49, 231–240. doi: 10.1021/acs.accounts.5b00482

Luo, X.-F., Yang, C.-H., Peng, Y.-Y., Pu, N.-W., Ger, M.-D., Hsieh, C.-T., et al. (2015). Graphene nanosheets, carbon nanotubes, graphite, and activated carbon as anode materials for sodium-ion batteries. *J. Mater. Chem. A* 3, 10320–10326. doi: 10.1039/C5TA00727E

Ning, Z., Han, X., Liu, Y., Hu, X., Zhao, Q., and Chen, J. (2015). 3D porous γ-Fe_2O_3@C nanocomposite as high-performance anode material of Na-ion batteries. *Adv. Energy Mater.* 5:1401123. doi: 10.1002/aenm.201401123

Niu, J., Liang, J., Shao, R., Liu, M., Dou, M., Li, Z., et al. (2017). Tremella-like N, O-codoped hierarchically porous carbon nanosheets as high-performance anode materials for high energy and ultrafast Na-ion capacitors. *Nano Energy* 41, 285–292. doi: 10.1016/j.nanoen.2017.09.041

Pan, Q. C., Zhang, Q. B., Zheng, F. H., Liu, Y. Z., Li, Y. P., Ou, X., et al. (2018b). Construction of MoS_2/C hierarchical tubular heterostructures for high-performance sodium ion batteries. *ACS Nano* 12, 12578–12586. doi: 10.1021/acsnano.8b07172

Pan, Q. C., Zheng, F. H., Ou, X., Yang, C. H., Xiong, X. H., and Liu, M. L. (2017). MoS_2 encapsulated SnO_2-SnS/C nanosheets as a high performance anode material for lithium ion batteries. *Chem. Eng. J.* 316, 393–400. doi: 10.1016/j.cej.2017.01.111

Pan, Q. C., Zheng, F. H., Wu, Y. N., Ou, X., Yang, C. H., Xiong, X. H., et al. (2018a). MoS_2-covered SnS nanosheets as anode material for lithium-ion batteries with high capacity and long cycle life. *J. Mater. Chem. A* 6, 592–598. doi: 10.1039/c7ta08346g

Qian, J., Wu, F., Ye, Y., Zhang, M., Huang, Y., Xing, Y., et al. (2018). Boosting fast sodium storage of a large-scalable carbon anode with an ultralong cycle life. *Adv. Energy Mater.* 8:1703159. doi: 10.1002/aenm.201703159

Wang, H. Q., Pan, Q. C., Wu, Q., Zhang, X. H., Huang, Y. G., Lushington, A., et al. (2017). Ultrasmall MoS_2 embedded in carbon nanosheets-coated Sn/SnO_x as anode material for high-rate and long life Li-ion batteries. *J. Mater. Chem. A* 5, 4576–4582. doi: 10.1039/c6ta10932b

Wang, S., Xia, L., Yu, L., Zhang, L., Wang, H., and Lou, X. W. (2016). Free-standing nitrogen-doped carbon nanofiber films: integrated electrodes for sodium-ion batteries with ultralong cycle life and superior rate capability. *Adv. Energy Mater.* 6:1502217. doi: 10.1002/aenm.201502217

Wang, Z. H., Qie, L., Yuan, L. X., Zhang, W. X., Hu, X. L., and Huang, Y. H. (2013). Functionalized N-doped interconnected carbon nanofibers as an anode material for sodium-ion storage with excellent performance. *Carbon* 55, 328–334. doi: 10.1016/j.carbon.2012.12.072

Wen, Y., He, K., Zhu, Y. J., Han, F. D., Xu, Y. H., Matsuda, I., et al. (2014). Expanded graphite as superior anode for sodium-ion batteries. *Nat. Commun.* 5:4033. doi: 10.1038/ncomms5033

Xu, D., Chen, C., Xie, J., Zhang, B., Miao, L., Cai, J., et al. (2016). A hierarchical N/S-codoped carbon anode fabricated facilely from cellulose/polyaniline microspheres for high-performance sodium-ion batteries. *Adv. Energy Mater.* 6:1501929. doi: 10.1002/aenm.201501929

Xu, J., Wang, M., Wickramaratne, N. P., Jaroniec, M., Dou, S., and Dai, L. (2015). High-performance sodium ion batteries based on a 3D anode from nitrogen-doped graphene foams. *Adv. Mater.* 27, 2042–2048. doi: 10.1002/adma.201405370

Yabuuchi, N., Kubota, K., Dahbi, M., and Komaba, S. (2014). Research development on sodium-ion batteries. *Chem. Rev.* 114, 11636–11682. doi: 10.1021/cr500192f

Yan, D., Yu, C., Zhang, X., Qin, W., Lu, T., Hu, B., et al. (2016). Nitrogen-doped carbon microspheres derived from oatmeal as high capacity and superior long life anode material for sodium ion battery. *Electrochim. Acta* 191, 385–391. doi: 10.1016/j.electacta.2016.01.105

Yang, F., Zhang, Z., Du, K., Zhao, X., Chen, W., Lai, Y., et al. (2015). Dopamine derived nitrogen-doped carbon sheets as anode materials for high-performance sodium ion batteries. *Carbon* 91, 88–95. doi: 10.1016/j.carbon.2015.04.049

Yang, J., Zhou, X., Wu, D., Zhao, X., and Zhou, Z. (2017). S-doped N-rich carbon nanosheets with expanded interlayer distance as anode materials for sodium-ion batteries. *Adv. Mater.* 29:1604108. doi: 10.1002/adma.201604108

Zhang, K., Li, X., Liang, J., Zhu, Y., Hu, L., Cheng, Q., et al. (2015). Nitrogen-doped porous interconnected double-shelled hollow carbon spheres with high capacity for lithium ion batteries and sodium ion batteries. *Electrochim. Acta* 155, 174–182. doi: 10.1016/j.electacta.2014.12.108

Zheng, F. H., Ou, X., Pan, Q. C., Xiong, X. H., Yang, C. H., Fu, Z. Y., et al. (2018). Nanoscale gadolinium doped ceria (GDC) surface modification of Li-rich layered oxide as a high performance cathode material for lithium ion batteries. *Chem. Eng. J.* 334, 497–507. doi: 10.1016/j.cej.2017.10.050

Zheng, F. H., Yang, C. H., Xiong, X. H., Xiong, J. W., Hu, R. Z., Chen, Y., et al. (2015). Nanoscale surface modification of lithium-rich layered-oxide composite cathodes for suppressing voltage fade. *Angew. Chem. Int. Ed.* 54, 13058–13062. doi: 10.1002/anie.201506408

Zhu, Z. Y., Liang, F., Zhou, Z. R., Zeng, X. Y., Wang, D., Dong, P., et al. (2018). Expanded biomass-derived hard carbon with ultrastable performance in sodium-ion batteries. *J. Mater. Chem. A* 6, 1513–1522. doi: 10.1039/c7ta07951f

Conflict of Interest: KX, GZ, CW, and SW are now employed by the company Electric Power Research Institute of Guangdong Power Grid Co., Ltd. The authors declare that this study received funding from Electric Power Research Institute of Guangdong Power Grid Co., Ltd. The funder had the following involvement with the study: KX, GZ, and CW were involved in the study design and data analysis. KX and SW were involved in the preparation of the manuscript and decision to publish.

The remaining authors declare that the research was conducted in the absence of any commercial or financial relationships that could be construed as a potential conflict of interest.

frontiers in Chemistry

ORIGINAL RESEARCH
published: 17 January 2020
doi: 10.3389/fchem.2019.00867

Optimal Quantity of Nano-Silicon for Electrospun Silicon/Carbon Fibers as High Capacity Anodes

Renheng Wang[1], Yiling Sun[1], Keyu Xiong[1], Junchao Zheng[2], Zhengfang Qian[1]* and Zhenjiang He[2,3]**

[1] College of Physics and Optoelectronic Engineering, Shenzhen University, Shenzhen, China, [2] School of Metallurgy and Environment, Central South University, Changsha, China, [3] College of Environmental Science and Engineering, Donghua University, Shanghai, China

In this study, silicon/carbon composite nanofibers (Si@CNFs) were prepared as electrode materials for lithium-ion batteries via a simple electrospinning method and then subjected to heat treatment. The morphology and structure of these materials were characterized by X-ray diffraction (XRD), scanning electron microscopy (SEM), and transmission electron microscopy (TEM). The results show that the structure provides good electrical conductivity and affords sufficient space to accommodate volume expansion during charging/discharging. Furtherly, electrochemical performance tests show that the optimized Si@CNFs have an initial reversible capacity of 1,820 mAh g^{-1} at a current density of 400 mA g^{-1} and capacity retention of 80.7% after 100 cycles at a current density of 800 mA g^{-1}. Interestingly, the optimized Si@CNFs have a superior capacity of 1,000 mAh g^{-1} (400 mA g^{-1}) than others, which is attributed to the carbon substrate nanofiber being able to accommodate the volume expansion of Si. The SEI resistance generated by the Si@CNFs samples is smaller than that of the Si nanoparticles, which confirms that SEI film generated from the Si@CNFs is much thinner than that from the Si nanoparticles. In addition, the connected carbon substrate nanofiber can form a fiber network to enhance the electronic conductivity.

Keywords: composite anode, high capacity, silicon, electrospun, nanofiber

OPEN ACCESS

Edited by:
Weihua Chen,
Zhengzhou University, China

Reviewed by:
Chao Lai,
Jiangsu Normal University, China
Zhisheng Lv,
Nanyang Technological University, Singapore

****Correspondence:***
Renheng Wang
wangrh@szu.edu.cn
Zhengfang Qian
zq001@szu.edu.cn
Zhenjiang He
hzjcsu@csu.edu.cn

Specialty section:
This article was submitted to Electrochemistry, a section of the journal Frontiers in Chemistry

Received: *25 September 2019*
Accepted: *02 December 2019*
Published: *17 January 2020*

Citation:
Wang R, Sun Y, Xiong K, Zheng J, Qian Z and He Z (2020) Optimal Quantity of Nano-Silicon for Electrospun Silicon/Carbon Fibers as High Capacity Anodes. Front. Chem. 7:867. doi: 10.3389/fchem.2019.00867

INTRODUCTION

Lithium-ion batteries (LIBs) are recognized as the green energy of the new century due to their high specific energy, high operating voltage, long cycle life, environmental friendliness, and lack of a memory effect. They have been widely used in the energy storage systems of smartphones, portable audio-visual equipment, small aircraft, electric bicycles, and various small power tools. However, conventional graphite anodes and lithium metal oxide cathodes show relatively low specific energies (~400 Wh kg^{-1} theoretically and ~200 Wh kg^{-1} practically), which cannot meet the growing demand for large-capacity electrochemical energy storage.

The development of new materials with excellent performance and low cost is of great significance for improving battery performance and reducing battery cost. Therefore, research on LIBs should mainly focus on the three aspects of battery cost, battery capacity, and new electrode materials (Lv et al., 2018a,b, 2019; An et al., 2019; Li R. et al., 2019; Li Y. et al., 2019; Wu et al., 2019; Yuan et al., 2019). With the development of anode materials for LIBs, the defects and advantages

of various new materials are highlighted. Among all anode materials, silicon (Si) is particularly promising due to its extremely high theoretical capacity (∼4,200 mAh g^{-1}), low discharge voltage, and natural abundance (Wen et al., 2013; Pan et al., 2015; Tang et al., 2015; Xie et al., 2015; Casimir et al., 2016; Wang and Yang, 2017; Yamaguchi et al., 2017; Zuo et al., 2017; Fang et al., 2019). However, Si as an anode material undergoes significant volume expansion during the Li^+ ion lithiation/delithiation process, leading to particle fracture and loss of capacity (Datta et al., 2011; Zhong et al., 2014; Huang et al., 2016; Jeong et al., 2016; Lin et al., 2016; Yang et al., 2016; Kim et al., 2017).

One generally accepted strategy to overcome this volume expansion is to synthesize nanoscale Si particles. Kim devised a simple, reproducible and cost-effective method for fabricating nanoporous Si flakes that demonstrate high electrochemical performance (Kim et al., 2017). Chen et al. reported an effective method for synthesizing Si nanotubes that exhibit significantly improved electrochemical properties (Wen et al., 2013). However, the above method of nanocrystallization only partially alleviates this problem and meanwhile improves the cycle performance to only a limited extent. Nowadays, silicon/carbon (Si/C) is being widely synthesized for use as an anode in LIBs because it combines the advantages of both carbon and Si and has been proposed to a very promising material to replace the commercially available graphite. Nathalie et al. have developed a two-stage LCVP to synthesized core-shell Si/C nanoparticles (Sourice et al., 2016). Sun reported a 3D Si/CNCS nanocomposite consisting of a CNC three-dimensional interconnected conductive network and a unique Si/CNC hollow sphere structure. The Si/CNCS nanocomposite can effectively alleviate volume expansion and improve electronic conductivity (Yue et al., 2016). Additionally, Si/C composite nanofibers (Si@CNFs) can be prepared for use as anodes in LIBs through a simple and low-cost method combining electrospinning and subsequent thermal treatment (Ji and Zhang, 2009; Hwang et al., 2012; Wu et al., 2014, 2016).

In this work, Si@CNFs materials were fabricated via a facile electrospinning technique. The Si@CNFs display an initial reversible capacity of 1,820 mAh g^{-1} at a current density of 400 mA g^{-1} and capacity retention of 80.7% after 100 cycles at a current density of 800 mA g^{-1} and exhibit a superior capacity of 1,000 mAh g^{-1} at a current density of 400 mA g^{-1}. The SEI resistance generated by the Si@CNFs samples is smaller than that of the Si nanoparticles, which confirms that SEI film generated from the Si@CNFs is much thinner than that from the Si nanoparticles. In addition, the connected carbon substrate nanofiber can form a fiber network that enhances the electronic conductivity. The crystal structure was measured by X-ray diffractometer (PAnalytical X'Pert ProMRD, Holland). The surface morphology was analyzed by field emission scanning electron microscopy (SEM, JEOL, JSM-5612LV). The microstructure was observed by transmission electron microscopy (TEM, JEOL-JEM-2100F). The cycling performances of Si nanoparticles and Si@CNFs are evaluated. The charge transfer resistances of Si nanoparticles and Si@CNFs anodes are analyzed by electrochemical impedance spectroscopy (EIS).

EXPERIMENTAL METHODS

The preparation of Si@CNFs was carried out through the facile electrospinning method shown in **Figure 1a**. Specifically, first, 1 g polyacrylonitrile (0.15 M), purchased from Sigma Aldrich, was dissolved in 10 mL N, N-Dimethylformamide (DMF). Meanwhile, 0.10, 0.20, or 0.30 g of Si nanoparticles was mixed well with the above solution, followed by stirring and keeping the mixed solution under sonication for 10 min. This solution was added to the nanofibers for electrospinning using an electrospinning device. The operating parameters were as follows: an applied voltage of direct current (DC) 25 kV (Dongwen, P503-1ACDF), working distance of 15 cm between the collector (aluminum foil) and solution syringe needle, and pumping rate of 2 mL h^{-1}. The prepared composite nanofibers were annealed in air at 260°C for 2 h and in an argon atmosphere at 600°C for 6 h to obtain Si@CNFs. The Si nanoparticles were labeled as S1. The Si@CNFs prepared using 0.10, 0.20, and 0.30 g Si nanoparticles correspond to the names S2, S3, and S4 in this article, respectively.

The electrochemical performances of all samples were tested using 2025-type coin half-cells. Celgard 2400 microporous polypropylene membrane was used as the separator, and the lithium metal sheet was used as the negative electrode. One mol L^{-1} $LiPF_6$/EC+EMC+DMC (by weight ratio, 1:1:1) was used as the electrolyte. Si nanoparticles, polyvinylidene fluoride (PVDF), and acetylene black were weighed according to the mass ratio of 8:1:1 and thoroughly mixed and ground, an appropriate amount of N-methylpyrrolidinone (NMP) was added to prepare an electrode slurry, and the slurry was uniformly coated on the copper foil with an applicator. After drying in a vacuum oven at 120°C for 15 h, it was punched into a pellet with a mass of 2.0 mg. The Si@CNFs were used directly as an electrode film. The CR2025 button cell was assembled in a glove box filled with argon at a relative humidity of less than 5% and an oxygen pressure of less than 1.0 ppm. After 12 h of activation, the electrochemical performance tests were performed in a voltage range of 0.01–2.0 V from 400 to 4,000 mA g^{-1}.

RESULTS AND DISCUSSION

Figure 1b shows the typical XRD patterns of all samples. The pure carbon fiber shows a diffraction peak at 2θ =25.0°, belonging to the (002) plane (Li et al., 2014). However, the peak of the nanofiber is weak and broad, resulting from disordered carbon. The diffraction peaks of Si@CNFs are at 2θ values of 28.5°, 47.4°, 56.3°, 69.2°, 76.8°, and 88.3°, respectively, corresponding to the (111), (220), (311), (400), (331), and (422) peaks of Si crystals in the nanofibers (Chen et al., 2011; Xie et al., 2014). It is obvious that the fluctuations in the XRD patterns of S2, S3, and S4 at 2θ of 5°-40° are caused by the action of carbon nanofibers. In addition, under these synthesis conditions, the synthesis procedures have no impact on the crystal structure of silicon.

Figures 1c–f illustrates SEM images of Si nanoparticles and electrospun Si@CNFs. The size of Si nanoparticles is about 30–60 nm, as shown in **Figure 1c**, as they easily form agglomerated

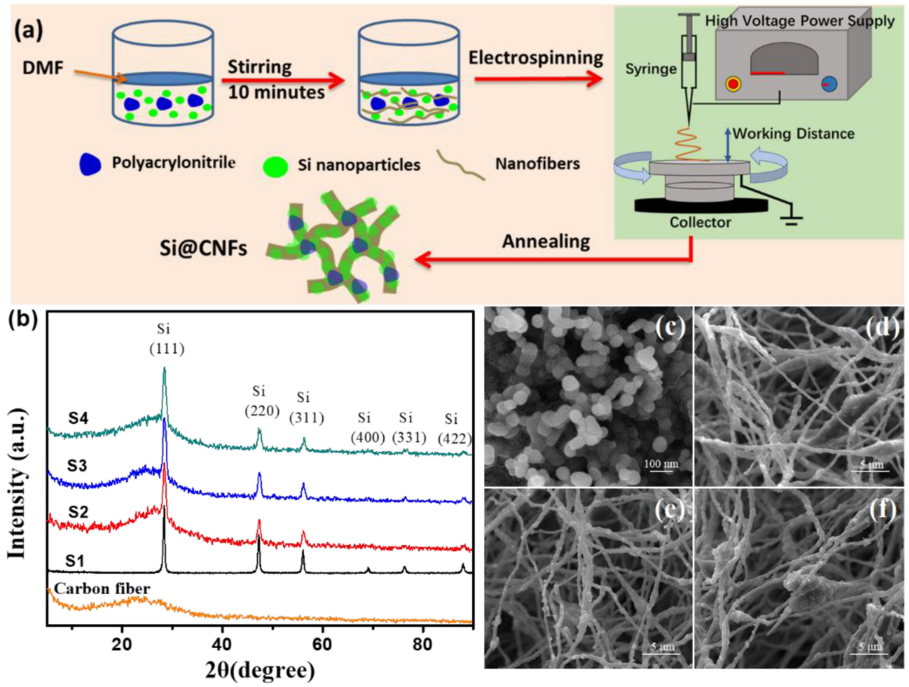

FIGURE 1 | (a) Schematic illustration of Si@CNF preparation. **(b)** XRD patterns of carbon nanofibers, Si nanoparticles (S1), and Si@CNFs (S2, S3, and S4); SEM images of **(c)** S1, **(d)** S2, **(e)** S3, and **(f)** S4 samples.

particles. However, the independent fiber skeleton of Si@CNFs has diameters of 300–500 nm, as displayed in **Figures 1d–f**. The net structure of the interconnected carbon network can be beneficial in improving the electrode surface and providing fast ion-conducting channels. The structure is expected to provide good electrical conductivity and afford sufficient space to accommodate volume expansion during charging/discharging. Besides, a compact fiber can avoid the formation of an unstable solid electrolyte interphase (SEI) layer on the surface of Si nanoparticles (Wu et al., 2016). The distributions and elemental mappings of Si in Si@CNFs were measured by energy dispersive spectrometer (EDS), as shown in **Figure 2**. The Si component is uniformly distributed in the three matrixes along both the radial and axial directions.

Figure 3 displays the microstructures of Si nanoparticles (S1) and Si@CNFs (S3). The clear crystal grain edge and the complete crystallinity of the 0.3123 nm lattice spacing are clearly seen in **Figures 3a,b**. The lattice spacing is derived from Si (111), with different lattice stripes extending to the particle boundaries. As seen in **Figures 3c,d**, the structure of the carbon nanofibers looks like a fishnet. The Si in S3 is well wrapped up by carbon nanofibers, providing enough space to accommodate huge volume changes during charging and discharging (Zhou et al., 2016; Wang et al., 2017a,b). It can be concluded that electrospinning is an effective technique for synthesizing S3.

Figure 4 and **Table 1** show the electrochemical performances of Si nanoparticle and Si@CNF half-cells at different current

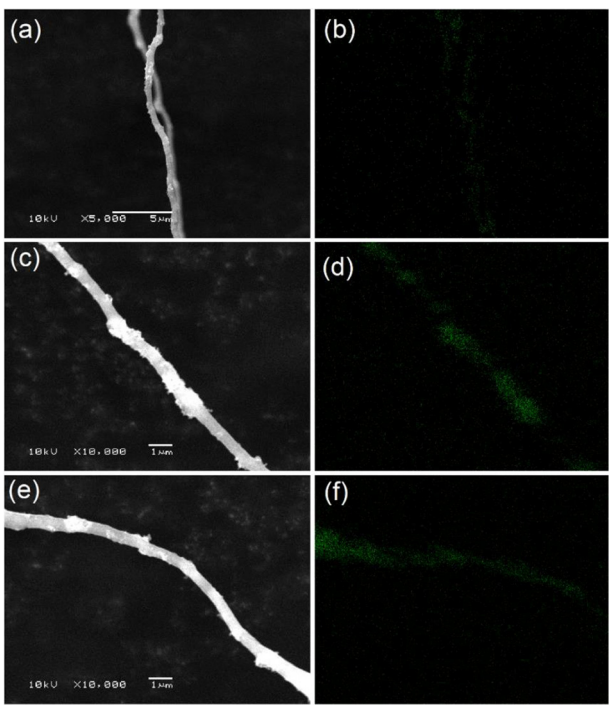

FIGURE 2 | EDS images of sample S2 **(a,b)**, sample S3 **(c,d)**, and sample S4 **(e,f)**.

densities. **Figures 4A–D** display the initial charge and discharge of four samples. It can be seen that the initial charge-discharge capacities of Si@CNF samples are higher than that of the Si nanoparticle sample at all current densities. When the current density is 400 mA g^{-1}, the capacity of the Si nanoparticles is 3,555 mAh g^{-1}, but the capacity declines sharply to 966 mAh g^{-1} when the current density increases to 4,000 mA g^{-1}, only 27.2% of the initial capacity. However, Si@CNFs (take sample S3 as an example) have better rate performances. The initial capacities are 1,820, 1,166, 1,050, and 1,000 mAh g^{-1} at 400, 800, 2,000, and 4,000 mA g^{-1}, respectively. It is clear from **Figure 4E** that Si nanoparticles still delivered the worst cycle performance at 800 mA g^{-1}, only 5.8% of the initial capacity after 50 cycled charging/discharging processes. However, Si@CNFs remarkably improved the cycle stability vs. Si nanoparticles. After 100 cycles, the discharge capacities of sample S2, S3, and S4 represent 89.3, 80.7, and 50.8% of the initial capacity, respectively. Obviously, a reduction in the capacity of Si@CNFs will occur with a decrease in the silicon content, which is due to the higher specific capacity of silicon nanoparticles than of carbon nanofibers. However, the cycle stability of Si@CNFs dropped with an increase in silicon content. Therefore, ensuring that there is an appropriate amount of silicon nanoparticles wrapped in carbon nanofibers is a key point for improving the rate capacity and

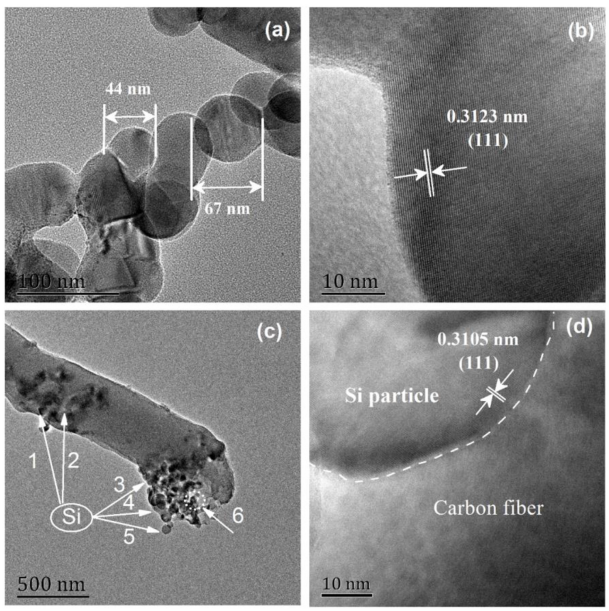

FIGURE 3 | HRTEM images of Si nanoparticles (S1) **(a,b)**, Si@CNFs (S3) **(c,d)**.

TABLE 1 | Rate performances of silicon nanoparticles and Si@CNFs.

Sample	Discharge capacity at 400 mA g^{-1}/ (mAh g^{-1})	Discharge capacity at 800 mA g^{-1}/ (mAh g^{-1})	Discharge capacity at 2,000 mA g^{-1}/ (mAh g^{-1})	Discharge capacity at 4,000 mA g^{-1}/ (mAh g^{-1})
S1	3,555	1,531	1,096	966
S2	1,306	956	852	802
S3	1,820	1,166	1,050	1,000
S4	2,413	1,479	1,289	1,112

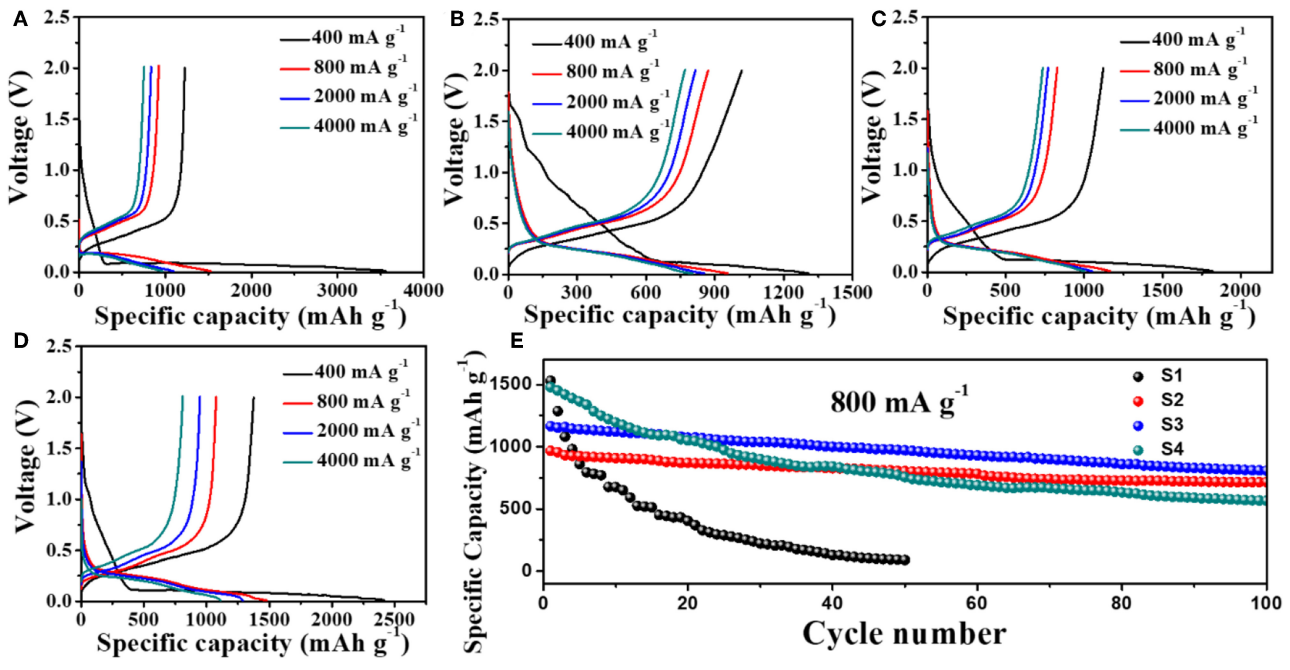

FIGURE 4 | Initial charge/discharge curves of **(A)** Si nanoparticles (S1) and Si@CNFs **(B)** S2, **(C)** S3, **(D)** S4, and **(E)** cycling performances of Si nanoparticles (S1) and Si@CNFs (S2, S3, S4) between 0.01 and 2.0 V at 25°C.

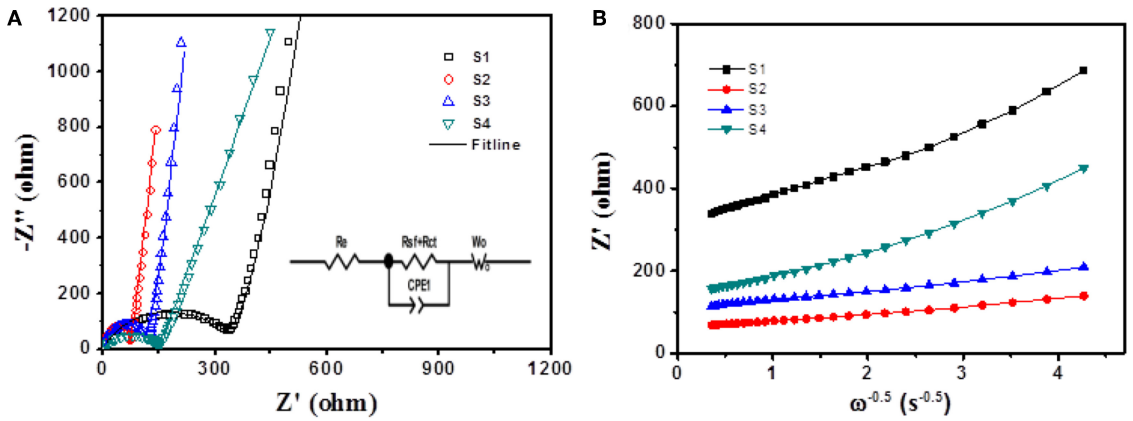

FIGURE 5 | (A) Electrochemical impedance spectra of Si nanoparticles (S1) and Si@CNFs (S2, S3, S4); the inset illustration is the equivalent circuit diagram as fitted by ZView software. **(B)** Plots of Z′ vs. $\omega^{-0.5}$ for Si nanoparticles and Si@CNFs.

cycling performance at the same time. Here, sample S3 displays the best comprehensive performance.

In order to achieve an in-depth understanding of the superior electrochemical performance of Si@CNFs, EIS measurements were used to evaluate the electrode kinetics factors of Si nanoparticles and Si@CNFs, as shown in **Figure 5**. The inset illustration is the equivalent circuit diagram fitted by ZView software (Wang et al., 2017a,b). From **Figure 5A**, it can be found that the EIS plots were composed of three parts: a semicircular arc at high frequency corresponding to SEI resistance (R_{sf}), a semicircle at intermediate frequency related to charge-transfer resistance (R_{ct}), and a straight line at low frequency connected to the Warburg diffusion process of lithium ions into the electrode material (W_O). R_e represents solution resistance, and *CPE* is attributed to the double-layer capacitance and the passivation film capacitance. The corresponding resistance values are displayed in **Table 2**. The R_e values of all samples are very similar and small. The R_{sf} and R_{ct} values of the Si@CNFs samples are smaller than those of the Si nanoparticles, which confirms that the SEI film generated from the Si@CNFs was much thinner than that from the Si nanoparticles. This may prove that the Si@CNFs can effectively reduce the diffusion resistance and charge transfer resistance, thus making it easier for Li^+ to migrate/embed in the lattice. It is noted that R_{ct} increases from 68.0 (S2) to 332.8 Ω (S1) when the Si content is increased. The decrease in R_{ct} may result from the enhanced electron and ionic conductivity of carbon nanofibers. In detail, the existence of carbon nanofibers can reduce R_{ct}, but the influence becomes weak when the silicon content reaches a certain value. Furthermore, the specific capacity of Si@CNFs decreased sharply when the silicon content was reduced. In addition, the exchange current densities (i^0) were calculated by the formula ($i^0 = RT/nFR_{ct}$), and the results are shown in **Table 2**. The S2 sample has the highest exchange current density (3.78×10^{-4} mA cm^{-2}) in all samples, and S3 also has a higher exchange current density (2.49×10^{-4} mA cm^{-2}) than S1 (7.72×10^{-5} mA cm^{-2}) and S4 (1.78×10^{-4} mA cm^{-2}). Thus, the EIS results indicate that the Si@CNFs possesses good charge transfer kinetics within the electrode.

TABLE 2 | Impedance parameters of Si nanoparticles and Si@CNFs.

Sample	R_{Sf} (Ω)	R_{ct} (Ω)	i^0 (mA cm^{-2})
S1	4.22	332.8	7.72×10^{-5}
S2	3.51	68.0	3.78×10^{-4}
S3	3.29	103.1	2.49×10^{-4}
S4	3.86	144.5	1.78×10^{-4}

Figure 5B shows the relationship between the real axis and the square root of the lower angular frequency (Xie et al., 2014; Wang et al., 2017b). The slopes of the straight lines indicate the values of the Warburg impedance coefficient (σ_w). It is noted that the lithium-ion diffusion process resistance of sample S2 is lower than those of the other samples, indicating that its net structure has the shortest diffusion length.

CONCLUSION

Si@CNFs materials have been synthesized by electrospinning technology, and the crystal structures of Si@CNFs are similar to those of Si nanoparticles. The Si nanoparticles in Si@CNFs are well wrapped up by carbon nanofibers. This network structure may provide good electrical conductivity, afford sufficient space to accommodate volume expansion during charging/discharging, enhance Li^+ diffusion, and reduce charge-discharge resistance. It is interesting that the optimized Si@CNFs hold a superior capacity of 1,000 mAh g^{-1} (400 mA g^{-1}), which is attributed to the carbon substrate nanofiber being able to accommodate the volume expansion of Si. The SEI resistance generated by Si@CNFs is lower than that of others. However, too much carbon content will decrease the specific capacity of Si@CNFs. Sample S3 displays the best comprehensive performance and delivers a reversible capacity of 1,820 mAh g^{-1} between 0.01 and 2.0 V at 400 mA g^{-1}, corresponding to 80.7% of the 100-cycle initial discharge capacity at 800 mA g^{-1}. We believe that Si@CNFs are a promising anode material for LIBs.

DATA AVAILABILITY STATEMENT

All datasets generated for this study are included in the article/supplementary material.

AUTHOR CONTRIBUTIONS

RW and ZH designed and engineered the samples and performed the experiments. RW, ZH, and ZQ performed the data analysis. ZH, YS, ZQ, and RW wrote the paper. All authors contributed to the theoretical analysis and the general discussion.

FUNDING

The work was supported by the National Science Foundation for Young Scientists of China (Grant No. 51804199), the Science and Technology Innovation Commission of Shenzhen (Grant No. 20180123), the Natural Science Foundation of Guangdong Province (2019A1515012111), the Shenzhen Science and Technology Program (KQTD20180412181422399), the National Science Foundation of China (Grant No. 51604081), and the Chenguang Program supported by the Shanghai Education Development Foundation and Shanghai Municipal Education Commission (Grant No. 16CG40).

ACKNOWLEDGMENTS

The authors also acknowledge the assistance on SEM and TEM observations received from the Electron Microscope Center and Instrumental Analysis Center of Shenzhen University (Xili Campus).

REFERENCES

An, C., Yuan, Y., Zhang, B., Tang, L., Xiao, B., He, Z., et al. (2019). Graphene wrapped $FeSe_2$ nano-microspheres with high pseudocapacitive contribution for enhanced Na-ion storage. *Adv. Energy Mater.* 9:1900356. doi: 10.1002/aenm.201900356

Casimir, A., Zhang, H., Ogoke, O., Amine, J. C., Lu, J., and Wu, G. J. (2016). Silicon-based anodes for lithium-ion batteries: effectiveness of materials synthesis and electrode preparation. *Nano Energy* 27, 359–376. doi: 10.1016/j.nanoen.2016.07.023

Chen, H., Xiao, Y., Wang, L., and Yang, Y. (2011). Silicon nanowires coated with copper layer as anode materials for lithium-ion batteries. *J. Power Sources* 196, 6657–6662. doi: 10.1016/j.jpowsour.2010.12.075

Datta, M. K., Maranchi, J., Chung, S. J., Epur, R., Kadakia, K., Jampani, P., et al. (2011). Amorphous silicon–carbon based nano-scale thin film anode materials for lithium ion batteries. *Electrochim. Acta* 56, 4717–4723. doi: 10.1016/j.electacta.2011.01.124

Fang, R., Xiao, W., Miao, C., Mei, P., Zhang, Y., Yan, X., et al. (2019). Enhanced lithium storage performance of core-shell structural Si@TiO_2/NC composite anode via facile sol-gel and *in situ* N-doped carbon coating processes. *Electrochim. Acta* 317, 575–582. doi: 10.1016/j.electacta.2019.06.028

Huang, X., Zhang, P., Wu, J., Lin, Y., and Guo, R. (2016). Nickel/silicon core/shell nanosheet arrays as electrode materials for lithium ion batteries. *Mater. Res. Bull.* 80, 30–35. doi: 10.1016/j.materresbull.2016.03.021

Hwang, T. H., Lee, Y. M., Kong, B.-S., Seo, J.-S., and Choi, J. W. (2012). Electrospun core–shell fibers for robust silicon nanoparticle-based lithium ion battery anodes. *Nano Lett.* 12, 802–807. doi: 10.1021/nl203817r

Jeong, M.-G., Islam, M., Du, H. L., Lee, Y.-S., Sun, H.-H., Choi, W., et al. (2016). Nitrogen-doped carbon coated porous silicon as high performance anode material for lithium-ion batteries. *Electrochim. Acta* 209, 299–307. doi: 10.1016/j.electacta.2016.05.080

Ji, L., and Zhang, X. (2009). Electrospun carbon nanofibers containing silicon particles as an energy-storage medium. *Carbon* 47, 3219–3226. doi: 10.1016/j.carbon.2009.07.039

Kim, Y.-Y., Lee, J.-H., and Kim, H.-J. (2017). Nanoporous silicon flakes as anode active material for lithium-ion batteries. *Phys. E Low Dimens. Syst. Nanostruct.* 85, 223–226. doi: 10.1016/j.physe.2016.09.007

Li, N., Jin, S., Liao, Q., Cui, H., and Wang, C. (2014). Encapsulated within graphene shell silicon nanoparticles anchored on vertically aligned graphene trees as lithium ion battery anodes. *Nano Energy* 5, 105–115. doi: 10.1016/j.nanoen.2014.02.011

Li, R., Xiao, W., Miao, C., Fang, R., Wang, Z., and Zhang, M. (2019). Sphere-like SnO_2/TiO_2 composites as high-performance anodes for lithium ion batteries. *Ceram. Int.* 45, 923–928. doi: 10.1016/j.ceramint.2019.04.059

Li, Y., Zhang, H., Xiao, Z., and Wang, R. (2019). Flexible $Li[Li_{0.2}Ni_{0.13}Co_{0.13}Mn_{0.54}]O_2$/carbon nanotubes/nanofibrillated celluloses composite electrode for high-performance lithium-ion battery. *Front. Chem.* 7:555. doi: 10.3389/fchem.2019.00555

Lin, J., He, J., Chen, Y., Li, Q., Yu, B., Xu, C., et al. (2016). Pomegranate-like silicon/nitrogen-doped graphene microspheres as superior-capacity anode for lithium-ion batteries. *Electrochim. Acta* 215, 667–673. doi: 10.1016/j.electacta.2016.08.147

Lv, Z., Li, W., Yang, L., Loh, X. J., and Chen, X. (2019). Custom-made electrochemical energy storage devices. *ACS Energy Lett.* 4, 606–614. doi: 10.1021/acsenergylett.8b02408

Lv, Z., Luo, Y., Tang, Y., Wei, J., Zhu, Z., Zhou, X., et al. (2018b). Editable supercapacitors with customizable stretchability based on mechanically strengthened ultralong MnO_2 nanowire composite. *Adv. Mater.* 30:1704531. doi: 10.1002/adma.201704531

Lv, Z., Tang, Y., Zhu, Z., Wei, J., Li, W., Xia, H., et al. (2018a). Honeycomb-lantern-inspired 3D stretchable supercapacitors with enhanced Specifc Areal Capacitance. *Adv. Mater.* 30:1805468. doi: 10.1002/adma.201805468

Pan, J., Zhang, Q., Li, J., Beck, M. J., Xiao, X., and Cheng, Y.-T. (2015). Effects of stress on lithium transport in amorphous silicon electrodes for lithium-ion batteries. *Nano Energy* 13, 192–199. doi: 10.1016/j.nanoen.2015.02.020

Sourice, J., Bordes, A., Boulineau, A., Alper, J. P., Franger, S., Quinsac, A., et al. (2016). Core-shell amorphous silicon-carbon nanoparticles for high performance anodes in lithium ion batteries. *J. Power Sources* 328, 527–535. doi: 10.1016/j.jpowsour.2016.08.057

Tang, F.-L., Lei, J.-F., Cui, Z.-Y., Ouyang, J., Gang, L., and Zhao, L.-Z. (2015). Fabrication, characterization and electrochemical properties of porous coral-structured Si/C composite anode for lithium ion battery. *T. Nonferr. Metal. Soc.* 25, 4046–4053. doi: 10.1016/S1003-6326(15)64054-7

Wang, R., Li, X., Wang, Z., and Zhang, H. (2017a). Electrochemical analysis graphite/electrolyte interface in lithium-ion batteries: p-Toluenesulfonyl isocyanate as electrolyte additive. *Nano Energy* 34, 131–140. doi: 10.1016/j.nanoen.2017.02.037

Wang, R., Wang, Z., Li, X., and Zhang, H. (2017b). Electrochemical analysis the influence of propargyl methanesulfonate as electrolyte additive for spinel LTO interface layer. *Electrochim. Acta* 241, 208–219. doi: 10.1016/j.electacta.2017.04.125

Wang, W., and Yang, S. J. (2017). Enhanced overall electrochemical performance of silicon/carbon anode for lithium-ion batteries using fluoroethylene carbonate as an electrolyte additive. *J. Alloy Compd.* 695, 3249–3255. doi: 10.1016/j.jallcom.2016.11.248

Wen, Z., Lu, G., Mao, S., Kim, H., Cui, S., Yu, K., et al. (2013). Silicon nanotube anode for lithium-ion batteries. *Electrochem. Commun.* 29, 67–70. doi: 10.1016/j.elecom.2013.01.015

Wu, J., Qin, X., Miao, C., He, Y.-B., Liang, G., Zhou, D., et al. (2016). A honeycomb-cobweb inspired hierarchical core–shell structure design for electrospun silicon/carbon fibers as lithium-ion battery anodes. *Carbon* 98, 582–591. doi: 10.1016/j.carbon.2015.11.048

Wu, L., Zheng, J., Wang, L., Xiong, X., Shao, Y., Wang, G., et al. (2019). PPy-encapsulated SnS_2 nanosheets stabilized by defects on a TiO_2 support as a durable anode material for lithium-ion batteries. *Angew. Chem. Int. Ed.* 58, 811–815. doi: 10.1002/anie.201811784

Wu, Q., Tran, T., Lu, W., and Wu, J. (2014). Electrospun silicon/carbon/titanium oxide composite nanofibers for lithium ion batteries. *J. Power Sources* 258, 39–45. doi: 10.1016/j.jpowsour.2014.02.047

Xie, J., Wang, G., Huo, Y., Zhang, S., Cao, G., and Zhao, X. (2014). Nanostructured silicon spheres prepared by a controllable magnesiothermic reduction as anode for lithium ion batteries. *Electrochim. Acta* 135, 94–100. doi: 10.1016/j.electacta.2014.05.012

Xie, Y., Qiu, M., Gao, X., Guan, D., and Yuan, C. (2015). Phase field modeling of silicon nanowire based lithium ion battery composite electrode. *Electrochim. Acta* 186, 542–551. doi: 10.1016/j.electacta.2015.11.022

Yamaguchi, K., Domi, Y., Usui, H., Shimizu, M., Matsumoto, K., Nokami, T., et al. (2017). Influence of the structure of the anion in an ionic liquid electrolyte on the electrochemical performance of a silicon negative electrode for a lithium-ion battery. *J. Power Sources* 338, 103–107. doi: 10.1016/j.jpowsour.2016.10.111

Yang, Y., Wang, Z., Zhou, R., Guo, H., and Li, X. (2016). Effects of lithium fluoride coating on the performance of nano-silicon as anode material for lithium-ion batteries. *Mater. Lett.* 184, 65–68. doi: 10.1016/j.matlet.2016.08.006

Yuan, M., Li, Y., Chen, Q., Chen, C., Liu, X., Zeng, W., et al. (2019). Surfactant-assisted hydrothermal synthesis of V_2O_5 coated $LiNi_{1/3}Co_{1/3}Mn_{1/3}O_2$ with ideal electrochemical performance. *Electrochim. Acta* 323, 134822–134828. doi: 10.1016/j.electacta.2019.134822

Yue, X., Sun, W., Zhang, J., Wang, F., and Sun, K. J. (2016). Facile synthesis of 3D silicon/carbon nanotube capsule composites as anodes for high-performance lithium-ion batteries. *J. Power Sources* 329, 422–427. doi: 10.1016/j.jpowsour.2016.08.104

Zhong, H., Zhan, H., and Zhou, Y.-H. (2014). Synthesis of nanosized mesoporous silicon by magnesium-thermal method used as anode material for lithium ion battery. *J. Power Sources* 262, 10–14. doi: 10.1016/j.jpowsour.2014.03.108

Zhou, X., Wu, L., Yang, J., Tang, J., Xi, L., and Wang, B. (2016). Synthesis of nano-sized silicon from natural halloysite clay and its high performance as anode for lithium-ion batteries. *J. Power Sources* 324, 33–40. doi: 10.1016/j.jpowsour.2016.05.058

Zuo, X., Zhu, J., Müller-Buschbaum, P., and Cheng, Y.-J. (2017). Silicon based lithium-ion battery anodes: a chronicle perspective review. *Nano Energy* 31, 113–143. doi: 10.1016/j.nanoen.2016.11.013

Conflict of Interest: The authors declare that the research was conducted in the absence of any commercial or financial relationships that could be construed as a potential conflict of interest.

frontiers in Chemistry

ORIGINAL RESEARCH
published: 04 February 2020
doi: 10.3389/fchem.2020.00043

Defect Rich Hierarchical Porous Carbon for High Power Supercapacitors

Peng Cai[1], *Kangyu Zou*[1], *Xinglan Deng*[1], *Baowei Wang*[1], *Guoqiang Zou*[1]*, *Hongshuai Hou*[1] *and Xiaobo Ji*[1,2]

[1] College of Chemistry and Chemical Engineering, Central South University, Changsha, China, [2] School of Materials Science and Engineering, Zhengzhou University, Zhengzhou, China

Tuning hierarchical pore structure of carbon materials is an effective way to achieve high energy density under high power density of carbon-based supercapacitors. However, at present, most of methods for regulating pores of carbon materials are too complicated to be achieved. In this work, a durian shell derived porous carbon (DSPC) with abundant porous is prepared through chemical activation as a defect strategy. Hierarchical porous structure can largely enhance the transfer rate of electron/ion. Furthermore, DSPC with multiple porous structure exhibits excellent properties when utilized as electrode materials for electric double layer capacitors (EDLCs), delivering a specific capacitance of 321 F g^{-1} at 0.5 A g^{-1} in aqueous electrolyte. Remarkably, a high energy density of 27.7 Wh kg^{-1} is obtained at 675 W kg^{-1} in an organic two-electrode device. And large capacity can be remained even at high charge/discharge rate. Significantly, hierarchical porous structure allows efficient ion diffusion and charge transfer, resulting in a prominent cycling stability. This work is looking forward to providing a promising strategy to prepare hierarchical porous carbon-based materials for supercapacitors with ultrafast electron/ion transport.

Keywords: high power density, hierarchical porous carbon, supercapacitors, biomass carbon, EDLC

OPEN ACCESS

Edited by:
Cheng Zhong,
Tianjin University, China

Reviewed by:
Jia Ding,
Tianjin University, China
Jin Huile,
Wenzhou University, China

***Correspondence:**
Guoqiang Zou
gq-zou@csu.edu.cn

Specialty section:
This article was submitted to Electrochemistry, a section of the journal Frontiers in Chemistry

Received: *04 December 2019*
Accepted: *14 January 2020*
Published: *04 February 2020*

Citation:
Cai P, Zou K, Deng X, Wang B, Zou G, Hou H and Ji X (2020) Defect Rich Hierarchical Porous Carbon for High Power Supercapacitors. Front. Chem. 8:43. doi: 10.3389/fchem.2020.00043

INTRODUCTION

Supercapacitors (SCs) have been triggered intensive attention in energy storage due to their fast reaction dynamics, ultrahigh power density, and excellent cycling stability (Li et al., 2011; Xie et al., 2012; Hao et al., 2013; Wang and Xia, 2013; Béguin et al., 2014). Among various kinds of electrode materials for SCs, carbon materials are most promising because of their large availability, high conductivity, and cycling stability. Preparing carbon materials economically and efficiently, increasing the energy density, and enhancing the power density of carbon materials are important aspects of developing carbon materials for advanced supercapacitors (Chen X. et al., 2014; Han et al., 2014; Yang and Zhou, 2017). Since the capacity of carbon materials depends on the amounts of electrostatic charges stored at the interfaces of the electrodes and electrolytes, a lot of researches have been done to design the desired carbon materials for ions storage. Tailoring the hierarchical pore structure to match the appropriate electrolyte ions is an effective method to achieve large capacitance, efficient ion diffusion, and charge transfer (Zhu et al., 2011; Fang et al., 2012; Chen et al., 2016, 2017; Yu et al., 2016; Liu et al., 2017; Shi et al., 2017, 2019).

In recent years, some brilliant materials (Li et al., 2015, 2019a; Han et al., 2016; Cao et al., 2017; Lv et al., 2017a,b; Xu B. et al., 2017; Zhou and Hu, 2017; Zhou et al., 2018), including carbon nanotubes, grapheme, and their derivatives, have been widely explored and utilized because of their excellent thermal stability, remarkable tenacity, and high strength (Wen et al., 2016; Zhu et al., 2017; Liu et al., 2018). However, there are some obstacles in applying these materials as electrode materials for supercapacitors. The charge/discharge processes are directly affected by ionic kinetics, obviously under harsh charge/discharge conditions (current density higher than 10 A g^{-1}) (An et al., 2001; Ra et al., 2009; Gao et al., 2012; Hahm et al., 2012; Sun et al., 2013; Zhu et al., 2016a). For instance, a capacitance of 362.2 F g^{-1} is obtained for the treated fullerene/graphite carbon electrodes at the low current density. However, when the current density increases to fifty times, the capacitance drops rapidly to half of the original value (Chen Z. et al., 2014; Zheng et al., 2015; Xu M. et al., 2017; Chen et al., 2018; Li et al., 2019b). It is not hard to note that increasing energy density under high power density of carbon electrodes is a great challenge. To the best of our knowledge, the poor performance in large current condition is associated with the sluggish ion migration in pores (Ye et al., 2019). It is difficult to keep good performances during charge/discharge processes without reasonable pore design. And electronic conductivity and ionic kinetics in electrodes can also be improved through regulating intrinsical structures of carbon materials (Raymundo-Piñero et al., 2011; Mun et al., 2013; Zhu et al., 2016b). In general, internal pores affect ion transport while external pores are related to ion diffusion from electrolyte. Particularly, the reduced electrode potential caused by low access to ion in pores is the main impediments under large current (Presser et al., 2011; Gao et al., 2013; Wang et al., 2015). In order to explain the importance of the pores in carbon electrode theoretically, the transmission line model is employed to imitate the charge reserve characteristic of different pore shapes, showing that porous electrodes are conducive to charge accumulation (Black and Andreas, 2010; Zhang et al., 2017). The results are proposed that electrodes with multiscale pores are beneficial to ion diffusion, which is the key to obtain large capacitance at ultra-high current density. Micropores larger than 0.7 nm are found to be used as electrolyte reservoirs to store ions (Péan et al., 2014). Under the effect of the electric field, due to the shortened length of the ion diffusion, the accumulated ions can diffuse into the nearby micropores in a shorter time than the ions in the electrolyte. And pores larger than 2 nm assist to decrease the ion confinement in the micropores, significantly enhancing the effective self-diffusion coefficient of the ions, which is advantageous for obtaining excellent rate performance (Forse et al., 2017). Therefore, a better understanding of the relationship between pore structure and capacitance performance is essential to fabricate hierarchical porous structure in carbon materials. It will accelerate ion kinetics to obtain carbon electrode materials with high ion transfer rate, which can achieve high energy storage under high current density. In order to obtain high-performance carbon electrode materials with hierarchical pore stricture, the strategy for fast ion transfer leaded by economical and efficient synthesis has been focused as main interests (Chen et al., 2013; Wang et al., 2017).

The main approaches to design hierarchical porous carbon materials are as following: (1) pores or defects generated on the surface or matrix through physical or chemical activation; (2) pores created by multidimensional carbon coupling/self-assembly; (3) adjustment of microstructures by means of templates; (4) pores congregated by the polymerization of nanoscale building blocks (Kang et al., 2015; Ni and Li, 2016; Yin et al., 2018; Kong et al., 2019). In these methods above, the size and shape of the pore array can be well-adjusted by changing the characteristics of template. However, the instability of nanoscale templates under high temperature or solvent treatment limits its extensive application (Fuertes et al., 2005; Lv et al., 2012). The process of multi-dimensional carbon coupling with the guest species and polymerization through building blocks is also tedious. Consequently, a wide range of biomass precursors combined with efficient activation methods are properly employed to prepare high-performance hierarchical porous carbon materials. Hierarchical pores in the surface would be beneficial to the transport of ions between adjacent layers, maximizing the reachable surface area. Due to the resulted multiple porous structure, the advantageous electronegativity also shows that carbon materials possess superior electrochemical performance in energy storage (Gao et al., 2019; Cai et al., 2020). Durian is widely distributed in the Southeast Asia region and around 90,000 metric tons of durian wastes were generated annually. Note that the advantages of durian shells are easy availability, cheap and high economic value. The reason of choosing durian shell as precursor to prepare carbon electrode can be attributed to main two reasons: (1) the hierarchical porous structure of the durian shell shows fast mass transfer channel, carbon material derived from durian shell precursor maintain the inherit structure features, possessing the fast ion/electron transport rate; (2) durian shell contain some heteroatoms, which can introduce defects during carbonization process, increasing the wettability of the surface of the carbon material, and promoting the contact of electrolyte area. In this work, a multi-stage porous carbon material (DSPC) is successfully obtained through the pre-carbonization and activation of the durian shell. By adjusting the activation temperature, the degree of porosity of the DSPC can be well-manipulated. The DSPC exhibits typical hierarchical porosity, reasonable aperture distribution, and high specific surface area. Surprisingly, symmetric supercapacitors based on DSPC electrodes deliver large capacity and fast ion transfer characteristics in aqueous electrolyte and organic electrolyte.

EXPERIMENTAL SECTION

Preparation of DSPCs

Firstly, the durian shell is cleaned several times by distilled water to remove some impurities and put into an oven under 120°C and for 24 h. Secondly, the dried durian shell is directly transferred to a tubular furnace in Ar atmosphere. The carbonized temperature is set to 400°C for 2 h with a heating rate of 3°C min^{-1}. The obtained sample is marked as DSPC. Finally, the DSPC

is manufactured with surface defects to obtain hierarchical channels. DSPC is mixed and grinded with KOH of 4:1 mass ratio. In order to explore the most appropriate the ratio of KOH to C, the corresponding electrochemical results are obtained in **Figure S1**. They are divided into five parts for subsequent activation and immediately transferred to a tubular furnace for generating surface defects. The temperature is 600, 700, 800, 900, and 1,000°C for 1 h. All the samples after being calcined are added 6 M HCl until pH = 7. All samples are then washed to neutral and dried in an oven. The carbon materials activated under different temperature are denoted as DSPC-600, DSPC-700, DSPC-800, DSPC-900, and DSPC-1000, respectively.

Material Characterization

The structure of DSPCs are explored by X-ray diffraction (XRD) with a scan rate of 10°C min^{-1} by using Kα radiation of Cu ($\lambda = 0.1542$ nm). Degree of graphitization is measured through Raman spectroscopy (DXR, Thermo-Fisher Scientific). The morphology of all the samples are investigated by field-emission scanning electron microscopy (FESEM, JSM-7600F, JEOL) and transmission electron microscopy (JEM-2010F at 200 kV, JEOL). The specific surface area is acquired from the N_2 adsorption-desorption isotherms and is obtained by the Brunauere Emmette Teller (BET) equation. The chemical bond of DSPCs are collected from X-ray photoelectron spectrometer (XPS) instrument.

Electrochemical Characterization

All the samples are measured on a three-electrode system using aqueous electrolyte and on two-electrode system using aqueous electrolyte and organic electrolyte for determining their capacitive performance.

For three-electrode aqueous electrolyte system, every carbon samples are grinded with carbon black and polytetrafluoroethylene (PTFE) with a weight ratio of 8:1:1 loaded on nickel foam. The electrode plates are then dried in a vacuum at 80°C for 12 h. Pieces are pressed under 10 MPa for 1 min. The mass load of each electrode plate is 2.2 mg/cm^2. Platinum electrode is selected as the counter electrode, and a saturated calomel electrode is selected as the reference electrode. The electrolyte is 6 M KOH.

For two-electrode aqueous electrolyte system, every carbon samples are grinded with carbon black and polytetrafluoroethylene (PTFE) with a weight ratio of 8:1:1 loaded on nickel foam. The electrode plates are then dried in a vacuum at 80°C for 12 h. Pieces are pressed under 10 MPa for 1 min. The electrolyte is 6 M KOH. CR2016-type coin cells are assembled accordingly. Electrochemical test begins after several hours.

For two-electrode organic electrolyte system, each carbon samples are grinded with carbon black and polyvinylidene fluoride (PVDF) with a weight ratio of 8:1:1 loaded on Al foils. The electrode plates are then dried in a vacuum at 120°C for 12 h. CR2016-type coin cells are assembled inside the Braunglovebox with argon atmosphere (<0.1 ppm of both O_2 and H_2O). Galvanostatic charge/discharge (GCD) tests are carried out between 0 and 2.7 V by an Arbin BT2000 instrument. The cyclic voltammetry (CV) tests are carried out at different scan rates on a Solartron 1470 Multistat system. The electrochemical impedance spectroscopy (EIS) measurements are performed using an electrochemical workstation.

The gravimetric capacitance is calculated from the CV curves and discharge curves, according to the formula:

$$Cs = \frac{I\Delta t}{m\Delta V}$$

where Cs is the specific capacitance and ΔV is the voltage drop. Δt is the discharging time. I/m is referred to the current density.

The power density and energy density of the devices are obtained thorough using the following equations:

$$P = \frac{\Delta V \times I}{2 \times m}$$

$$E = \frac{P * t}{3600}$$

Here, ΔV is referred to the discharge voltage, I is referred to the discharge current, t is referred to the discharge time and m is referred to the total mass of active materials, respectively.

RESULTS AND DISCUSSION

SEM and TEM images of hierarchical porous carbon materials prepared from the durian shell are shown in **Figure 1** and **Figure S2**. It is obvious that the pores are hardly manufactured at 600°C. When the temperature is increased to 700°C, the pore structure in the carbon material is gradually generated, and an uneven structure is produced on the surface. As the temperature is further risen up to 800°C, the pore structure formed in the carbon material are widely ranged and the structure is uniform. When the temperature is raised to 900°C, the defect of the surface is degenerated and destroyed, and the pore structure of the material is broken. As the temperature is kept at 1,000°C, the structure of hierarchical pores is collapsed more severely, and the surface defect structure is difficult to be observed. According to TEM images, an amorphous dominated porous structure and defect architecture are further revealed.

The XRD measurement of all samples are exhibited in **Figure 2A**. The broad peaks located at 23° and inconspicuous peaks centered at 43° are perceived, indicating that all the samples are in amorphous constructions maintained few regions of crystallinity (Hou et al., 2015, 2017; Ge et al., 2018; Zou et al., 2018; Wu et al., 2019). More detailer pore structures of the samples are collected by the nitrogen adsorption/desorption measurements in **Figures 2B,C**. The isotherms of all DSPCs exhibit a combination of I-type and IV-type isotherm characteristics at a relative pressure >0.4, suggesting that both micropores and mesopores exist. Notably, the specific surface area of DSPC-600, DSPC-700, DSPC-800, DSPC-900, and DSPC-1000 are 1006, 1217, 2535, 2602, and 899 $m^2 g^{-1}$, respectively. When the temperature is increased slightly, the surface area of micropores and mesoporous increase. As the increase of temperature, the proportion of micropores decreases while the proportion of mesopores increases according

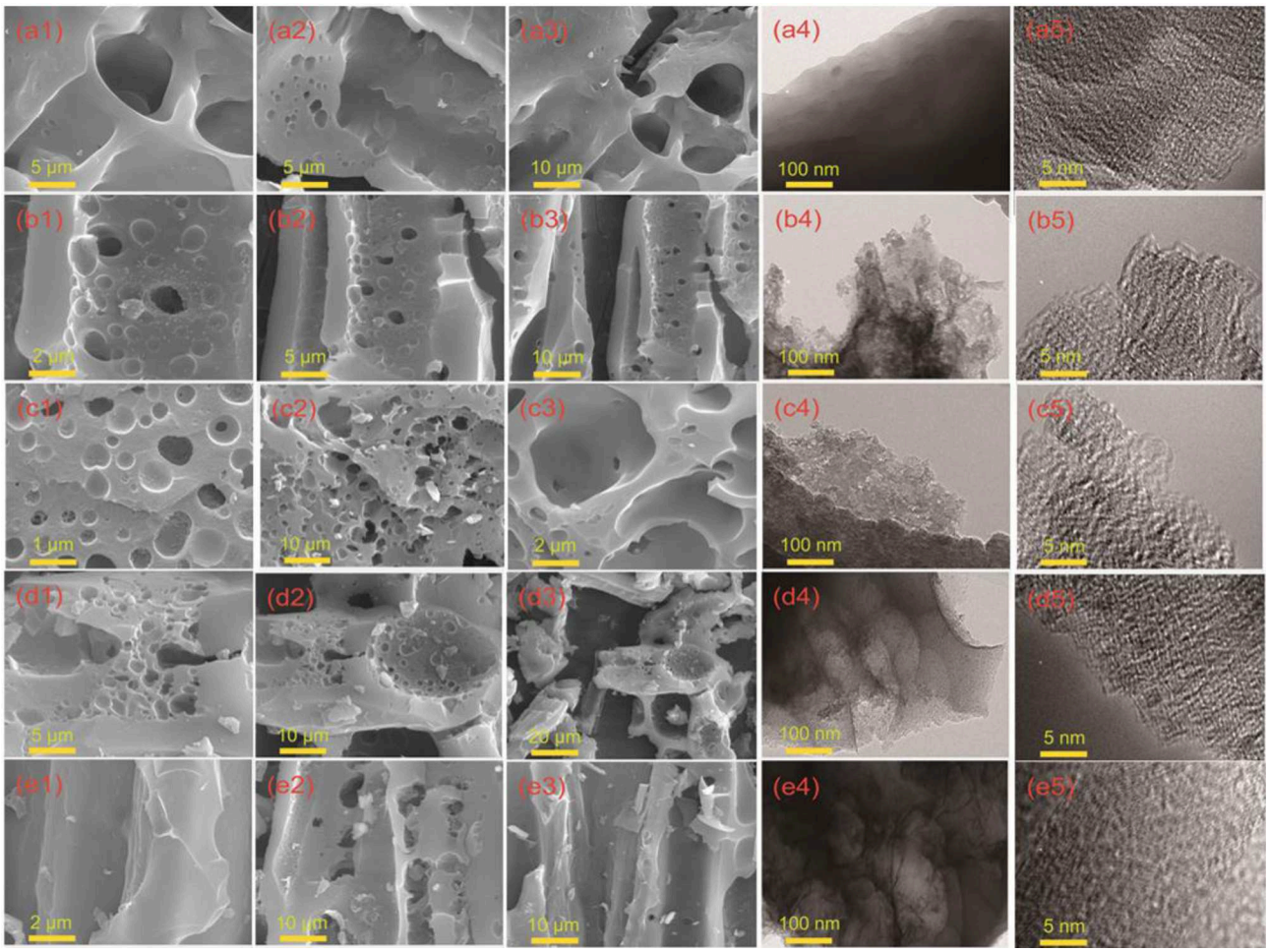

FIGURE 1 | Morphology and structure characterization of DSPCs. **(a1-a3)** SEM image of DSPC-600, **(a4,a5)** TEM and HRTEM image of DSPC-600. **(b1-b3)** SEM image of DSPC-700, **(b4,b5)** TEM and HRTEM image of DSPC-700. **(c1-c3)** SEM image of DSPC-800, **(c4,c5)** TEM and HRTEM image of DSPC-800. **(d1-d3)** SEM image of DSPC-900, **(d4,d5)** TEM and HRTEM image of DSPC-900. **(e1-e3)** SEM image of DSPC-1000, **(e4,e5)** TEM and HRTEM image of DSPC-1000.

to the higher platform and lower starting angles of the low-pressure areas of DSPC-900 in **Figure 2B**. The plots of pore size distributions are revealed the porous structure for all the samples. Furthermore, wide existence of nanopores in plots of pore size distributions illustrates hierarchical porous structure of DSPC-800. Risen from 800°C to 1,000°C, the distribution of micropores gradually decreases and the distribution of mesopores becomes larger. In general, as depicted in **Figure 2C**, the DSPC-800 exhibits a hierarchically aperture and porosity structure. The Raman spectra of the acquired samples are deconvoluted into two peaks including G peak and D peak, and the intensity ratio of G band vs. D band (IG/ID) can be used to describe the degree of graphitization. The G peak is induced by Sp2-hybrid carbon and D peak is related to the disordered graphite structure. As shown in **Figure 2D**, the values of IG/ID of all samples are 1.65, 2.52, 6.6, 2.06, and 1.59, respectively, demonstrating the high graphitization degree of DSPC-800. Note that Sp2 hybridization-dominant carbon is widely employed to improve ion transfer rate and efficient energy storage because of large graphitization, high electrical conductivity, and thermal stability. Benefiting from high value of IG/ID in DSPC-800 superior kinetics performance during chare/discharge process could be delivered. Furthermore, the surface chemical environment of DSPC-800 is determined in details by XPS analysis. Carbon content in the DSPC-800 is 91.02 at%, and the oxygen content of the DSPC-800 is 8.98 at %. As shown in **Figure 2E**, the C1s profiles is divided into four peaks of COOH (290 eV), C = O (286.7 eV), C-O (285–286.eV) and C = C/C-C (284.6 eV). The high-resolution O1s spectra can be deconvoluted into three peaks located at 531.0, 533, and 536 eV, which is corresponding to the C=O, C-O, and carbonyl (**Figure 2F**), respectively (Yang et al., 2019; Zhu et al., 2020).

The capacitive performance of DSPCs are firstly measured in 6.0 M KOH/H_2O electrolyte by using a three-electrode system. The CV curves of all the samples exhibit quasi-rectangular appearance at the scan rate of 5–100 mV s^{-1}, implying an ideal capacitive characteristic in **Figures 3a1–e1**. The DSPC-800 shows the largest area of CV curves among all the samples, suggesting outstanding charge storage feature. In addition, according to the

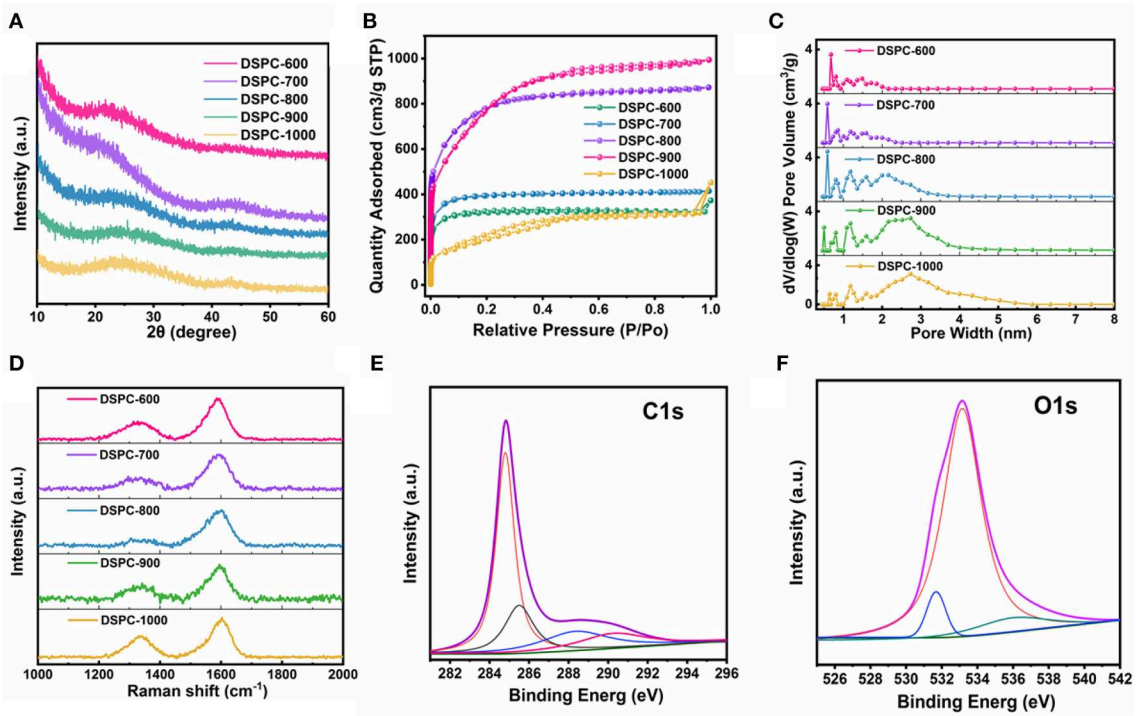

FIGURE 2 | (A) XRD patterns, **(B)** N_2 adsorption-desorption isotherms, **(C)** Pore size distribution, and **(D)** Raman spectrum of DSPCs. **(E,F)** high-resolution XPS C1s and O1s spectra for DSPC-800.

results in **Figure S1**, the ratio of KOH to C should be selected as 4: 1 rather than 3:1 or 5:1. As displayed in **Figure 3c2**, the GCD curve of DSPC-800 presents the longest discharge time among the five samples at the current density of 10 A g^{-1}, suggesting the largest capacitance among all the samples. Based on the results of GCD curves, the specific capacitances of DSPC-600, DSPC-700, DSPC-800, DSPC-900, and DSPC-1000 are 239.5, 336.6, 320.5, 209.6, and 186 F g^{-1} at a current density of 0.5 A g^{-1} (**Figures 3a2,b2,d2,e2**), exhibiting that the specific capacitances of DSPCs are 194.1, 249.1, 253.1, 158.9, and 159 at 5 A g^{-1}, respectively. Impressively, the specific capacitances of DSPCs are 130.4, 93.7, 154.75, 50, and 60 F g^{-1} at a current density of 50 A g^{-1}, separately. The capacitive performances of DSPCs are subsequently evaluated in 6.0 M KOH/H_2O electrolyte using a two-electrode system. The CV curves of the device are listed in **Figure 3c3**, in which the quasi-rectangular appearance of DSPC-800 is kept even at the scan rate of 100 mV s^{-1}, demonstrating an excellent rate performance. This result is further illustrated by the GCD curves at different current densities in **Figures 3a3–e3**. When the current density is 0.5 A g^{-1}, the specific capacitances of DSPCs devices are determined as 56.1, 60.9, 82, 52, and 46.3 F g^{-1}, respectively, corresponding to the specific capacitances of 45.1, 42.7, 63.3, 33, and 32 F g^{-1} at 5 A g^{-1}, respectively. As the current density increases to 20 A g^{-1}, specific capacitances of 30.2, 25.1, 32.1, 9.3, and 12 F g^{-1} are achieved for DSPCs samples. The highest specific capacitance of DSPC-800 is attributed to hierarchical porous structure, which can bring numerous active sites for the charge storage in **Figures 3a4–e4**.

All the samples are further tested in organic electrolyte in two-electrode devices based on DSPCs. The device of DSPC-600 measured in organic electrolyte is shown an obvious polarization, which is attributed to sluggish ion kinetics behavior of the electrode (**Figure 4a1**). The low energy density of the device of DSPC-600 is 0.01 Wh kg^{-1}, which is suggested andante charge transport and ion diffusion in large current density shown in **Figure 4a3**. The low capacity can be attributed to the less surface defects and low conductivity due to the low activation temperature. The other four devices are shown with a quasi-rectangular shape CV curve that can be interpreted as the presence of higher surface defects. The DSPC-800 device shows a highly symmetric shape, suggesting great electrochemical reversibility (**Figures 4b1–e1**). It is important to noted that the device of DSPC-800 exhibits smallest IR drop at 10 A g^{-1}, implying that surface defect structure with relatively high hierarchical aperture and porosity can facilitate transfer rate of the electrolyte ions and decrease the ionic diffusivity resistance. This result is further illustrated by the GCD curves at different current densities (**Figures 4a3–e3**). The energy density of all the devices are 21.5, 24.3, 27.7, 22, and 10.4 Wh kg^{-1} at a power density of 675 W kg^{-1}, respectively. Furthermore, energy densities of 0.6, 20.7, 21.5, 16.4, and 8.4 Wh kg^{-1} can be obtained for related samples at a power density of 6,750 W kg^{-1}. Surprisingly, even at 67,500 W kg^{-1}, the device of DSPC-800 can also deliver an energy density of 4.2 Wh kg^{-1}. The highest energy density of the devices with DSPC-800 as electrode are attributed to multiple pores

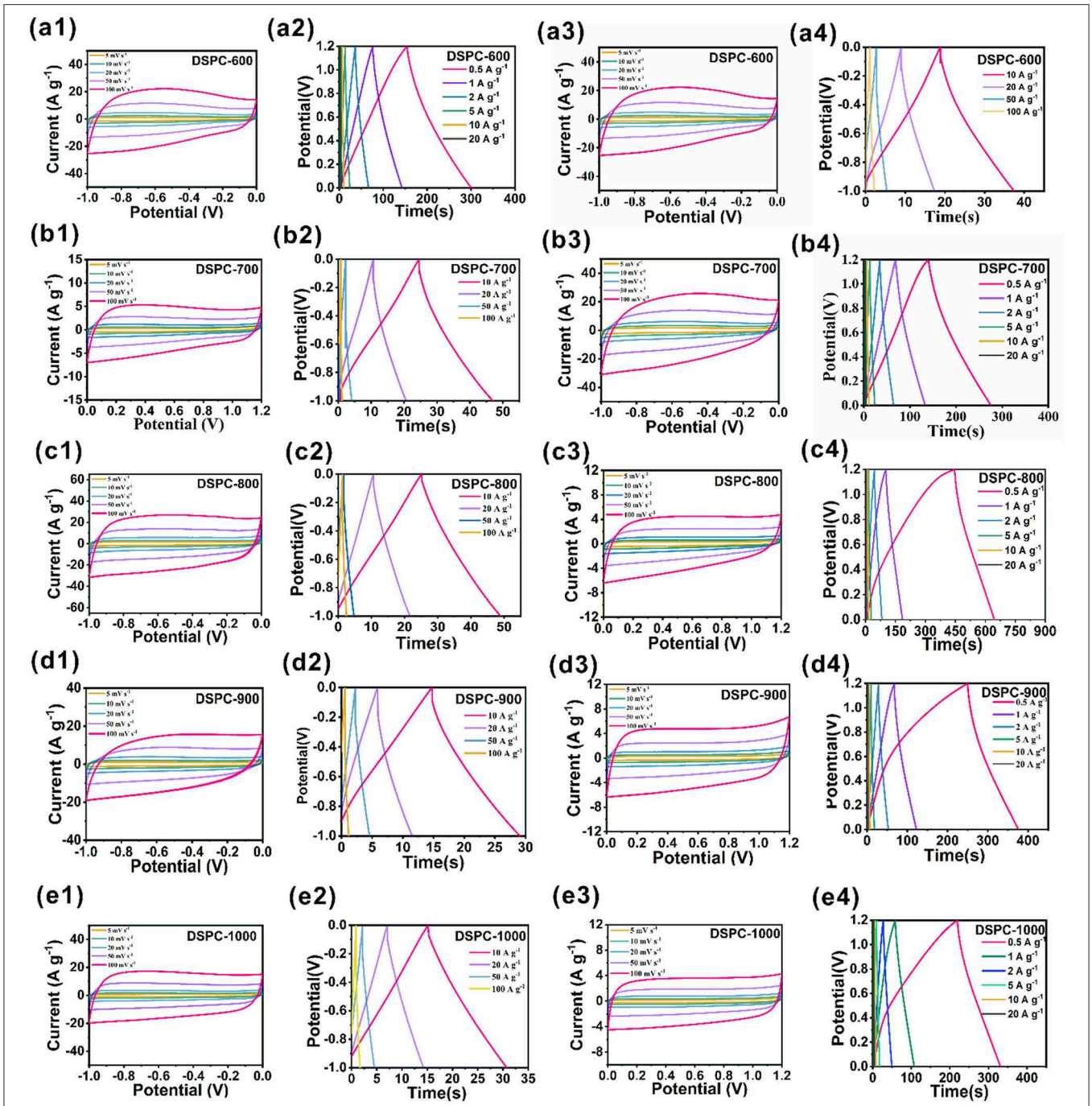

FIGURE 3 | Electrochemical performances of DSPCs. **(a1–e1)** CV curves at three electrode system in 6 M KOH, **(a2–e2)** charge/discharge curves at three electrode system in 6 M KOH, **(a3–e3)** CV curves at two electrode system in 6 M KOH, **(a4–e4)** charge/discharge curves at two electrode system in 6 M KOH.

that can supply numerous active sites for the charge storage in **Figure 4**. It is clear that hierarchical porous structure can effectively improve the electrochemical properties of materials in both aqueous electrolyte and organic electrolyte system, suggesting that the introduction of hierarchical porous structure is significant.

A number of electrochemical measurements including cycling stability and electrochemical impedance spectroscopy (EIS) are carried out to investigate the electrochemical performance of DSPCs. Low resistance and rate capability are determined by the efficiency of charge transport and ion diffusion in aqueous electrolyte system (Xu et al., 2014). The contact resistance between the electrode material and the electrolyte also affects resistance (Rs). Because the ion transfer characteristics of these synthesized materials are different, Rs is generally different (Jin et al., 2018a,b; Nawwar et al., 2019; Wang and Cui, 2019;

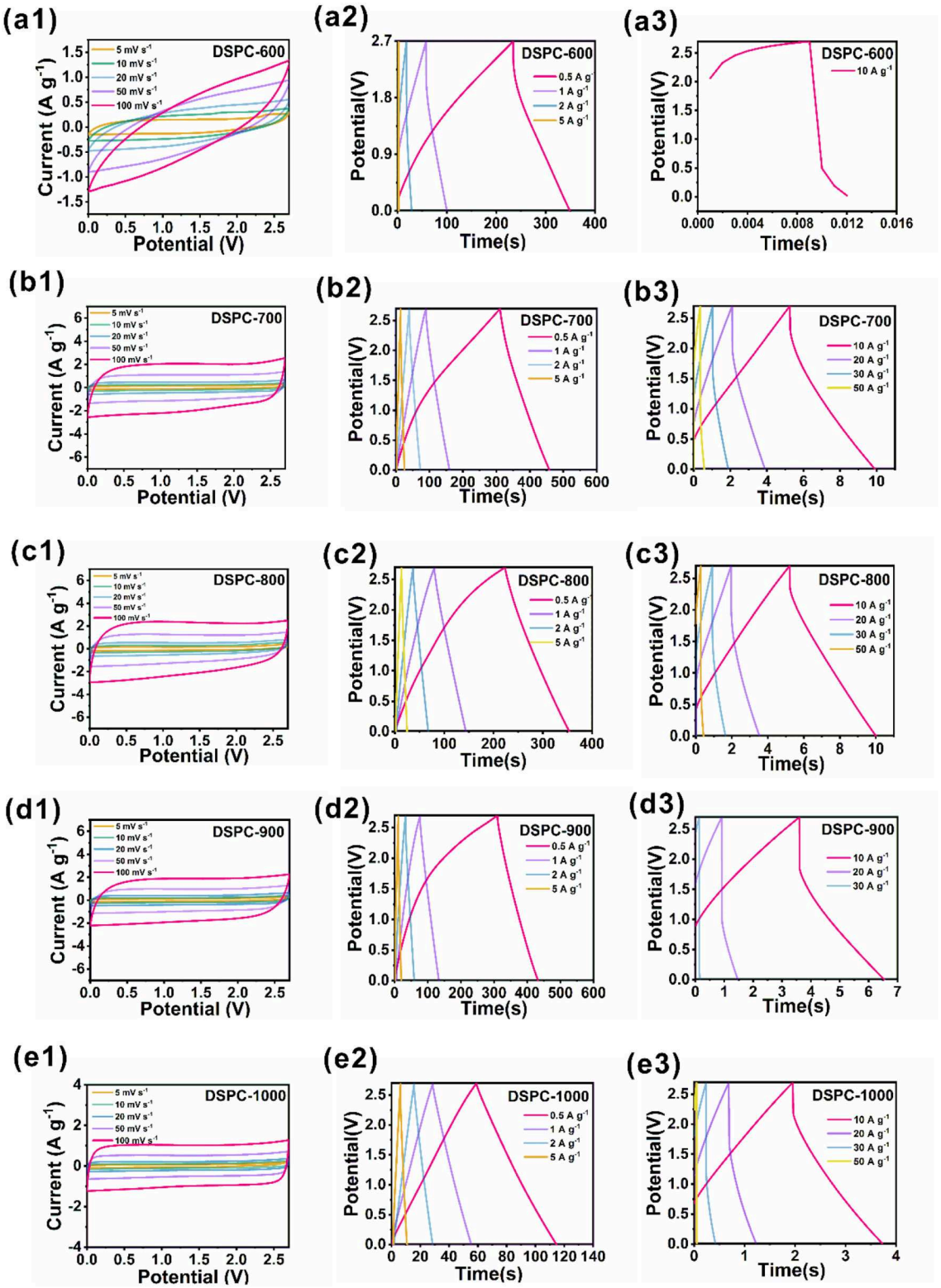

FIGURE 4 | Electrochemical performances of DSPCs. **(a1–e1)** CV curves at two electrode system in organic electrolyte, **(a2–e2)** charge/discharge curves at two electrode system in organic electrolyte, **(a3–e3)** charge/discharge curves at two electrode system tested in large current in organic electrolyte.

Yuan and Lu, 2019). The surface defect of DSPCs is critical for achieving such high specific capacitance. EIS analysis is revealed that DSPC-800 exhibits an ignorable combined series resistance, which is greater than other samples. The steep slope of the Nyquist plot in the low frequency domain indicates fast ion transport in the surface defect electrode. The lack of semicircle of DSPC-800 in the middle frequency domain further suggests that the charge transfer resistance (Rct) at the electrode/electrolyte interface is negligible (**Figure 5A**). In organic electrolyte system, DSPC-800 also exhibits a small resistance, which is similar to the results in aqueous electrolyte system in **Figure 5A**. The large resistance of DSPC-600 is correlated with previous results. Bode phase diagram also discloses some important information in **Figures 5B,E**. Firstly, the 0.1 Hz phase angle is approximately the ideal phase angle, that is -90°, and the ideal phase angle is closed to the ideal capacitive behavior. Secondly, the characteristic frequency (f_0) is corresponded to a -45° phase angle. The characteristic time constant can be expressed as: $\tau_0 = 1/f_0$. The smaller τ_0 represents the faster frequency response and τ_0 is related to the rate characteristics. Bode phase diagram is revealed that surface defect is contributed to ion diffusion (**Figures 5B,E**). A high capacity residue of 88.71% can be acquired for DSPC-800 in aqueous electrolyte system at 20 A g^{-1} after 10,000 cycles. The capacity retentions of other devices are 82.9, 84.75, 57.64, and 72.98% in aqueous electrolyte system at 20 A g^{-1} (**Figure 5C**), respectively. DSPC-800 is also preserved good cycle performance in organic electrolyte system after several thousand times (**Figure 5**). Note that carbon materials with hierarchical porous structure assembled devices can deliver remarkable performance and show practical applications (**Figures 5G–I**).

CONCLUSION

Here, defect strategy is demonstrated as an effective method to construct hierarchical porous structure with fast ion transport property. The hierarchical porous structure provides larger surface area for the infiltration of electrolyte for ions transport into interior multiple pores. Consequently, hierarchical porous structure can optimize ion kinetics by affecting ion transport of internal pores and ion diffusion of external pores from electrolyte, especially at large current density. Due to the hierarchical porous structure tuned high ionic conductivity and optimized ionic kinetics of electrodes, the power performance is impressive, delivering excellent gravimetric capacitance both in aqueous and organic electrolyte. This work provides a bright and effective approach to fabricate the carbon materials with hierarchical porous structure. Surprisingly, it has been successfully applied in energy storage under large current density. Considering the advantages of low cost and abundance, hierarchical porous carbon is extremely promising for the development of advanced electrode materials in super capacitors.

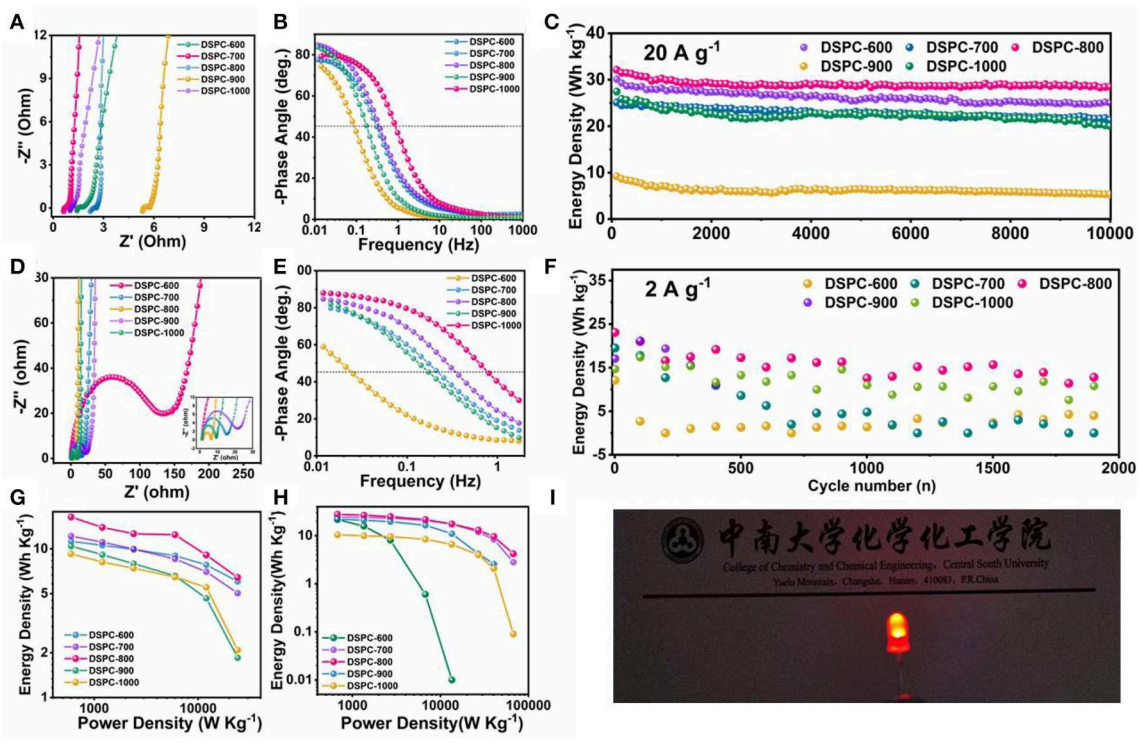

FIGURE 5 | (A) EIS analysis in 6 M KOH, **(B)** Bold plot in 6 M KOH, **(C)** cycle performance in 6 M KOH, **(D)** EIS analysis in organic electrolyte, **(E)** Bold plot in organic electrolyte, **(F)** cycle performance in organic electrolyte, **(G,H)** Ragon plot in 6 M KOH and organic electrolyte, **(I)** optical picture of device of DSPC-800 in organic electrolyte.

DATA AVAILABILITY STATEMENT

The raw data supporting the conclusions of this article will be made available by the authors, without undue reservation, to any qualified researcher.

AUTHOR CONTRIBUTIONS

PC and GZ designed the research, performed the experiments, and made contributions to the acquisition, analysis, and interpretation of data for the work. KZ, XD, and BW carried out the partial experimental characterization. HH and XJ revised this article and approved of the version to be published. All authors incorporated in the discussion of experimental results.

FUNDING

This work was financially supported by the National Key Research and Development Program of China (2018YFC1901605), the National Postdoctoral Program for Innovative Talents (BX201600192), and the Hunan Provincial Science and Technology Plan (2017TP1001), Innovation Mover Program of Central South University (GCX20190893Y).

SUPPLEMENTARY MATERIAL

The Supplementary Material for this article can be found online at: https://www.frontiersin.org/articles/10.3389/fchem.2020.00043/full#supplementary-material

REFERENCES

An, K. H., Kim, W. S., Park, Y. S., Moon, J. M., Bae, D. J., Lim, S. C., et al. (2001). Electrochemical properties of high-power supercapacitors using single-walled carbon nanotube electrodes. *Adv. Funct. Mater.* 11, 387–392. doi: 10.1002/1616-3028(200110)11:5andlt;387::AID-ADFM387andgt;3.0.CO;2-G

Béguin, F., Presser, V., Balducci, A., and Frackowiak, E. (2014). Carbons and electrolytes for advanced supercapacitors. *Adv. Mater. Weinheim.* 26, 2219–2251. doi: 10.1002/adma.201304137

Black, J., Andreas, H. J. (2010) Pore Shape Affects Spontaneous Charge Redistribution in Small Pores. *Phys. Chem. C.* 114, 12030–12038. doi: 10.1021/jp103766q

Cai, P., Zou, Y., Zou, G., Hou, H., and Ji, X. (2020). Quinone/ester-based oxygen functional groups enhanced full carbon Li-ion capacitor. *Nanoscale* doi: 10.1039/C9NR10339B. [Epub ahead of print].

Cao, D., Yin, C., Shi, D., Fu, Z., and Zhang, J. (2017). Cubic perovskite fluoride as open framework cathode for Na-ion batteries. *Adv. Funct. Mater.* 28:1701130. doi: 10.1002/adfm.201701130

Chen, D., Tian, J., Liu, C., and Du, M. (2016). A bracket approach to improve the stability and gas sorption performance of a metal-organic framework via in situ incorporating the size-matching molecular building blocks. *Chem. Commun.* 52, 8413–8416. doi: 10.1039/c6cc02359B

Chen, D., Tian, J., Wang, Z., Liu, C., Chen, M., and Du, M. (2017). An anionic Na (I)–organic framework platform: separation of organic dyes and post-modification for highly sensitive detection of picric acid. *Chem. Commun.* 53, 10668–10671. doi: 10.1039/C7CC06073D

Chen, J., Li, L., Wu, L., Yao, Q., Yang, H., Liu, Z., et al. (2018). Enhanced cycle stability of $Na_{0.9}Ni_{0.45}Mn_{0.55}O_2$ through tailoring O3/P2 hybrid structures for sodium-ion batteries. *J. Power Sour.* 406, 110–117. doi: 10.1016/j.jpowsour.2018.10.058

Chen, X., Lin, H., Chen, P., Guan, G., Deng, J., and Peng, H. (2014). Smart, stretchable supercapacitors. *Adv. Mater. Weinheim.* 26, 4444–4449. doi: 10.1002/adma.201400842

Chen, X., Qiu, L., Ren, J., Guan, G., Lin, H., Zhang, Z., et al. (2013). Novel electric double-layer capacitor with a coaxial fiber structure. *Adv. Mater. Weinheim.* 25, 6436–6461. doi: 10.1002/adma.201301519

Chen, Z., Xu, M., Du, B., Zhu, H., and Xie, T., Wang,W. (2014). Morphology control of lithium iron phosphate nanoparticles by soluble starch-assisted hydrothermal synthesis. *J. Power Sour.* 272, 837–844. doi: 10.1016/j.jpowsour.2014.09.019

Fang, Y., Luo, B., Jia, Y., Li, X., Wang, B., Song, Q., et al. (2012). Renewing functionalized graphene as electrodes for high-performance supercapacitors. *Adv. Mater. Weinheim.* 24, 6348–6355. doi: 10.1002/adma.201202774

Forse, A., Griffin, J., Merlet, C., Carretero-Gonzalez, J., Raji, A., Trease, N., et al. (2017). Direct observation of ion dynamics in supercapacitor electrodes using in situ diffusion NMR spectroscopy. *Nat. Energy* 2:16216. doi: 10.1038/nenergy.2016.216

Fuertes, A., Lota, G., Centeno, T. A., and Frackowiak, E. (2005). Templated mesoporous carbons for supercapacitor application. *Electrochim. Acta* 50, 2799–2805. doi: 10.1016/j.electacta.2004.11.027

Gao, X., Jiang, F., Yang, Y., Zhang, Y., Zou, G., Hou, H., et al. (2019). Chalcopyrite-derived NaxMO2 (M = Cu, Fe, Mn) cathode: tuning impurities for self-doping. *ACS Appl. Mater. Inter.* 12, 2432–2444. doi: 10.1021/acsami.9b17952

Gao, Y., Presser, V., Zhang, L., Niu, J., McDonough, J., Pérez, C., et al. (2012). High power supercapacitor electrodes based on flexible TiC-CDC nano-felts. *J. Power Sources* 201, 368–375. doi: 10.1016/j.jpowsour.2011.10.128

Gao, Y., Zhou, Y., Qian, M., He, X., Redepenning, J., Goodman, P., et al. (2013). Chemical activation of carbon nano-onions for high-rate supercapacitor electrodes *Carbon N. Y.* 51, 52–58. doi: 10.1016/j.carbon.2012.08.009

Ge, P., Hou, H., Cao, X., Li, S., Zhao, G., Guo, T., et al. (2018). Multidimensional evolution of carbon structures underpinned by temperature-induced intermediate of chloride for Sodium-ion batteries. *Adv. Sci.* 5:1800080. doi: 10.1002/advs.201800080

Hahm, M., Reddy, A., Cole, D., Rivera, M., Vento, J., Nam, J., et al. (2012). Carbon nanotube–nanocup hybrid structures for high power supercapacitor applications. *Nano Lett.* 12, 5616–5621. doi: 10.1021/nl3027372

Han, S., Wu, D., Li, S., Zhang, F., and Feng, X. (2014). Porous graphene materials for advanced electrochemical energy storage and conversion devices. *Adv. Mater. Weinheim.* 26, 849–864. doi: 10.1002/adma.201303115

Han, Y., Hu, J., Yin, C., Zhang, Y., and Xie, J. (2016). Iron-based fluorides of tetragonal tungsten bronze structure as potential cathodes for Na-ion batteries. *J. Mater. Chem. A.* 4, 7382–7389. doi: 10.1039/C6TA02061E

Hao, L., Li, X., and Zhi, L. (2013). Carbonaceous electrode materials for supercapacitors. *Adv. Mater. Weinheim.* 25, 3899–3904. doi: 10.1002/adma.201301204

Hou, H., Banks, C. E., Jing, M., Zhang, Y., and Ji, X. (2015). Carbon quantum dots and their derivative 3D porous carbon frameworks for Sodium-ion batteries with ultralong cycle life. *Adv. Mater. Weinheim.* 27, 7861–7866. doi: 10.1002/adma.201503816

Hou, H., Shao, L., Zhang, Y., Zou, G., Chen, J., and Ji, X. (2017), Large-area carbon nanosheets doped with phosphorus: a high-performance anode material for sodium-ion batteries. *Adv. Sci.* 4:1600243. doi: 10.1002/advs.201600243

Jin, H., Feng, X., Li, J., Li, M., Xia, Y., Yuan, Y., et al. (2018a). Heteroatom-doped porous carbon materials with unprecedented high volumetric capacitive performance. *Angew. Chem. Int. Ed.* 58, 2397–2401. doi: 10.1002/anie.201813686

Jin, H., Li, J., Yuan, Y., Wang, J., Lu, J., and Wang, S. (2018b). Recent progress in biomass-derived electrode materials for high volumetric performance supercapacitors. *Adv. Energy Mater.* 8:1801007. doi: 10.1002/aenm.201801007

Kang, D., Liu, Q., Gu, J., Su, Y., Zhang, W., and Zhang, D. (2015). "Egg-Box"-assisted fabrication of porous carbon with small mesopores for high-rate electric double layer capacitors. *ACS Nano.* 9, 11225–11233. doi: 10.1021/acsnano.5b04821

Kong, D., Gao, Y., Xiao, Z., Xu, X., Li, X., and Zhi, L. (2019). Rational design of carbon-rich materials for energy storage and conversion. *Adv. Mater. Weinheim.* 31:1804973. doi: 10.1002/adma.201804973

Li, J., Wei, H., Peng, Y., Geng, L., Zhu, L., Cao, X., et al. (2019a). A multifunctional self-healing G-PyB/KCl hydrogel: smart conductive, rapid room-temperature phase-selective gelation, and ultrasensitive detection of alpha-fetoprotein. *Chem. Commun.* 55, 7922–7925. doi: 10.1039/C9CC02770J

Li, J., Yun, X., Hu, Z., Xi, L., Li, N., Tang, H., et al. (2019b). Three-dimensional nitrogen and phosphorus co-doped carbon quantum dots/reduced graphene oxide composite aerogels with a hierarchical porous structure as superior electrode materials for supercapacitors. *J. Mater. Chem. A.* 7, 26311–26325. doi: 10.1039/C9TA08151H

Li, L., Wu, Z., Sun, H., Chen, D., and Gao, J. (2015). A foldable lithium–sulfur battery. *ACS Nano.* 9, 11342–11350. doi: 10.1021/acsnano.5b05068

Li, W., Zhang, F., Dou, Y., Wu, Z., Liu, H., Qian, X., et al. (2011). A self-template strategy for the synthesis of mesoporous carbon nanofibers as advanced supercapacitor electrodes. *Adv. Energy Mater.* 1, 382–386. doi: 10.1002/aenm.201000096

Liu, C., Zhang, Z., Chen, M., Zhao, H., Duan, F., Chen, D., et al. (2017). Pore modulation of zirconium–organic frameworks for high efficiency detection of trace proteins. *Chem. Commun.* 53, 3941–3944. doi: 10.1039/C7CC00029D

Liu, D., Ni, K., Ye, J., Xie, J., Zhu, Y., and Song, L. (2018). Tailoring the structure of carbon nanomaterials toward high-end energy applications. *Adv. Mater. Weinheim.* 30:1802104. doi: 10.1002/adma.201802104

Lv, J., Liang, T., Yang, M., Ken, S., and Hideo, M. (2017a). Performance comparison of $NiCo_2O_4$ and $NiCo_2S_4$ formed on Ni foam for supercapacitor. *Compos. Part B-Eng.* 123, 28–33. doi: 10.1016/j.compositesb.2017.05.021

Lv, J., Yang, M., Liang, T., and Miura, H. (2017b). Facile synthesis of Co_3O_4@MnO_2 core–shell nanocomposites for high-performance supercapacitor. *Mater. Lett.* 197, 127–130. doi: 10.1016/j.matlet.2017.03.127

Lv, Y., Gan, L., Liu, M., Xiong, W., Xu, Z., Zhu, D., et al. (2012). A self-template synthesis of hierarchical porous carbon foams based on banana peel for supercapacitor electrodes. *J. Power Sour.* 209, 152–157. doi: 10.1016/j.jpowsour.2012.02.089

Mun, Y., Jo, C., Hyeon, T., Lee, J., Ha, K., Jun, K., et al. (2013). Simple synthesis of hierarchically structured partially graphitized carbon by emulsion/block-copolymer co-template method for high power supercapacitors. *Carbon N. Y.* 64, 391–402. doi: 10.1016/j.carbon.2013.07.092

Nawwar, M., Poon, R., Chen, R., Sahu, R. P., Puri, I. K., and Zhitomirsky, I. (2019). High areal capacitance of Fe_3O_4-decorated carbon nanotubes for supercapacitor electrodes. *Carbon Energy* 1, 124–133. doi: 10.1002/cey2.6

Ni, J., and Li, Y. (2016). Carbon nanomaterials in different dimensions for electrochemical energy storage. *Adv. Energy Mater.* 6:1600278. doi: 10.1002/aenm.201600278

Péan, C., Merlet, C., Rotenberg, B., Madden, P., Taberna, P., Daffos, B., et al. (2014). On the dynamics of charging in nanoporous carbon-based supercapacitors. *ACS Nano.* 8, 1576–1583. doi: 10.1021/nn4058243

Presser, V., Zhang, L., Niu, J., McDonough, J., Perez, C., Fong, H., et al. (2011). Flexible nano-felts of carbide-derived carbon with ultra-high power handling capability. *Adv. Energy Mater.* 1, 423–430. doi: 10.1002/aenm.201100047

Ra, E. J., Raymundo-Piñero, E., Lee, Y. H., and Béguin, F. (2009). High power supercapacitors using polyacrylonitrile-based carbon nanofiber paper. *Carbon N. Y.* 47, 2984–2992. doi: 10.1016/j.carbon.2009.06.051

Raymundo-Piñero, E., Cadek, M., Wachtler, M., and Béguin, F. (2011). Carbon nanotubes as nanotexturing agents for high power supercapacitors based on seaweed carbons. *ChemSusChem.* 4, 943–949. doi: 10.1002/cssc.201000376

Shi, D., Zheng, R., Liu, C., Chen, D., Zhao, J., and Du, M. (2019). Dual functionalized mixed keggin- and lindqvist-type Cu_{24}-based POM@MOF for visible-light-driven H_2 and O_2 Evolution. *Inorg. Chem.* 58, 7229–7235. doi: 10.1021/acs.inorgchem.9b00206

Shi, D., Zheng, R., Sun, M., Cao, X., Sun, C., Cui, C., et al. (2017). Semi-conductive copper (I)–organic frameworks for efficient light-driven hydrogen generation without additional photosensitizers and cocatalysts. *Angew. Chem. Int. Ed.* 56, 14637–14641. doi: 10.1002/anie.201709869

Sun, L., Tian, C., Li, M., Meng, X., Wang, L., Wang, R., et al. (2013). From coconut shell to porous graphene-like nanosheets for high-power supercapacitors. *J. Mater. Chem. A.* 1, 6462–6470. doi: 10.1039/c3ta10897j

Wang, F., Wu, X., Yuan, X., Liu, Z., Zhang, Y., Fu, L., et al. (2017). Latest advances in supercapacitors: from new electrode materials to novel device designs. *Chem. Soc. Rev.* 46, 6816–6854. doi: 10.1039/c7cs00205J

Wang, H., and Cui, Y. (2019). Nanodiamonds for energy. *Carbon Energy.* 1, 13–18. doi: 10.1002/cey2.9

Wang, L., Dubin, M., Hwang, J., Shao, Y., Marsh, K., McVerry, B., et al. (2015). Flash converted graphene for ultra-high power supercapacitors *Adv. Energy Mater.* 5:1500786. doi: 10.1002/aenm.201500786

Wang, Y., and Xia, Y. (2013). Recent progress in supercapacitors: From materials design to system construction. *Adv. Mater. Weinheim.* 25, 5336–5342. doi: 10.1002/adma.201301932

Wen, L., Li, F., and Cheng, H. (2016). Carbon nanotubes and graphene for flexible electrochemical energy storage: from materials to devices. *Adv. Mater. Weinheim.* 28, 4306–4337. doi: 10.1002/adma.201504225

Wu, T., Zhang, C., Zou, G., Hu, J., Zhu, L., Cao, X., et al. (2019). The bond evolution mechanism of covalent sulfurized carbon during electrochemical sodium storage process. *Sci. Chi. Mater.* 62, 1127–1138. doi: 10.1007/s40843-019-9418-8

Xie, K., Qin, X., Wang, X., Wang, Y., Tao, H., Wu, Q., et al. (2012). Carbon nanocages as supercapacitor electrode materials. *Adv. Mater. Weinheim.* 24, 347–352. doi: 10.1002/adma.201103872

Xu, B., Duan, H., Liu, H., Wang, C., and Zhong, S. (2017). Stabilization of garnet/liquid electrolyte interface using superbase additives for hybrid Li batteries. *ACS Appl. Mater. Inter.* 9, 21077–21082. doi: 10.1021/acsami.7b05599

Xu, M., Fei, L., Lu, W., Chen, Z., Li, T., Liu, Y., et al. (2017). Engineering hetero-epitaxial nanostructures with aligned Li-ion channels in Li-rich layered oxides for high-performance cathode application. *Nano Energy* 35, 271–280. doi: 10.1016/j.nanoen.2017.03.051

Xu, Y., Lin, Z., Zhong, X., Huang, X., Weiss, N., Huang, Y., et al. (2014). Holey graphene frameworks for highly efficient capacitive energy storage. *Nat. Commun.* 5:4554. doi: 10.1038/ncomms5554

Yang, L., Hong, W., Tian, Y., Zou, G., Hou, H., Sun, W., et al. (2019). Heteroatom-doped carbon inlaid with Sb_2X_3 (X= S, Se) nanodots for high-performance potassium-ion batteries. *Chem. Eng. J.* 385:123838. doi: 10.1016/j.cej.2019.123838

Yang, M., and Zhou, Z. (2017). Recent breakthroughs in supercapacitors boosted by nitrogen-rich porous carbon materials. *Adv. Sci.* 4:1600408. doi: 10.1002/advs.201600408

Ye, J., Simon, P., and Zhu, Y. (2019). Designing ionic channels in novel carbons for electrochemical energy storage. *Nat. Sci. Rev.* 13, 2095–5138. doi: 10.1093/nsr/nwz140

Yin, Y., Yu, Z., Ma, Z., Zhang, T., Lu, Y., Ma, T., et al. (2018). Bio-inspired low-tortuosity carbon host for high-performance lithium-metal anode. *Nat.Sci.Rev.* 6, 247–256. doi: 10.1093/nsr/nwy148

Yu, P., Zhang, Z., Zheng, L., Teng, F., Hu, L., and Fang, X. (2016). A novel sustainable flour derived hierarchical nitrogen-doped porous carbon/polyaniline electrode for advanced asymmetric supercapacitors. *Adv. Energy Mater.* 6:1601111. doi: 10.1002/aenm.201601111

Yuan, Y., and Lu, J. (2019). Demanding energy from carbon. *Carbon Energy.* 1, 8–12. doi: 10.1002/cey2.12

Zhang, F., Liu, T., Li, M., Yu, M., Luo, Y., Tong, Y., et al. (2017). Multiscale pore network boosts capacitance of carbon electrodes for ultrafast charging. *Nano Lett.* 17, 3097–3104. doi: 10.1021/acs.nanolett.7b00533

Zheng, S., Ju, H., and Lu, X. (2015). A high-performance supercapacitor based on KOH activated 1D C_{70} Microstructures. *Adv. Energy Mater.* 5:1500871. doi: 10.1002/aenm.201500871

Zhou, H., Cao, Y., Ma, Z., and Li, S. (2018). Facile synthesis of nickel-doped Co_9S_8 hollow nanoparticles with large surface-controlled pseudocapacitive and fast sodium storage. *Nanotechnology* 29, 195–201. doi: 10.1088/1361-6528/aab120

Zhou, H., and Hu, J. (2017). Facile synthesis of multi-walled carbon nanotubes/Co_9S_8 composites with enhanced performances for sodium-ion battery. *Mater. Lett.* 175, 26–30. doi: 10.1016/j.matlet.2017.02.004

Zhu, H., Wang, X., Yang, F., and Yang, X. (2011). Promising carbons for supercapacitors derived from fungi. *Adv. Mater. Weinheim.* 23, 2745–2748. doi: 10.1002/adma.201100901

Zhu, J., Childress, A., Karakaya, M., Dandeliya, S., Srivastava, A., Lin, Y., et al. (2016a). Defect-engineered graphene for high-energy- and high-power-density supercapacitor devices. *Adv. Mater. Weinheim.* 28, 7185–7192. doi: 10.1002/adma.201602028

Zhu, J., Xu, Y., Zhang, Y., Feng, T., Wang, J., Mao, S., et al. (2016b). Porous and high electronic conductivity nitrogen-doped nano-sheet carbon derived from polypyrrole for high-power supercapacitors. *Carbon N. Y.* 107, 638–645. doi: 10.1016/j.carbon.2016.06.063

Zhu, Y., Ji, H., Cheng, H., and Ruoff, R. (2017). Mass production and industrial applications of graphene materials. *Nat. Sci. Rev.* 5, 90–101. doi: 10.1093/nsr/nwx055

Zhu, Y., Li, J., Yun, X., Zhao, G., Ge, P., Zou, G., et al. (2020). Graphitic carbon quantum dots modified nickel cobalt sulfide as cathode materials for alkaline aqueous batteries. *Nano-Micro Lett.* 12, 1–18. doi: 10.1007/s40820-019-0355-0

Zou, G., Hou, H., Foster, W., Banks, C. E., Guo, T., Jiang, Y., et al. (2018). Advanced hierarchical vesicular carbon Co-doped with S, P, N for high-rate sodium storage. *Adv. Sci.* 5:1800241. doi: 10.1002/advs.201800241

Conflict of Interest: The authors declare that the research was conducted in the absence of any commercial or financial relationships that could be construed as a potential conflict of interest.

frontiers in Chemistry

ORIGINAL RESEARCH
published: 18 February 2020
doi: 10.3389/fchem.2020.00006

Boosting Specific Energy and Power of Carbon-Ionic Liquid Supercapacitors by Engineering Carbon Pore Structures

Dong Zhang[1†], Hongquan Gao[1†], Guomin Hua[1†], Haitao Zhou[1], Jianchun Wu[1], Bowei Zhu[1], Chao Liu[1], Jianhong Yang[1*] and De Chen[1,2*]*

[1] School of Materials Science and Engineering, Jiangsu University, Zhenjiang, China, [2] Department of Chemical Engineering, Norwegian University of Science and Technology, Trondheim, Norway

OPEN ACCESS

Edited by:
Hongshuai Hou,
Central South University, China

Reviewed by:
Xing Ou,
Central South University, China
Yirong Zhu,
Hunan University of Technology, China

***Correspondence:**
Hongquan Gao
hongquangao@ujs.edu.cn
Jianhong Yang
jhyang@ujs.edu.cn
De Chen
de.chen@ntnu.no

[†]These authors have contributed equally to this work

Specialty section:
This article was submitted to Electrochemistry, a section of the journal Frontiers in Chemistry

Received: 06 December 2019
Accepted: 07 January 2020
Published: 18 February 2020

Citation:
Zhang D, Gao H, Hua G, Zhou H, Wu J, Zhu B, Liu C, Yang J and Chen D (2020) Boosting Specific Energy and Power of Carbon-Ionic Liquid Supercapacitors by Engineering Carbon Pore Structures. Front. Chem. 8:6. doi: 10.3389/fchem.2020.00006

Carbon-ionic liquid (C-IL) supercapacitors (SCs) promise to provide high capacitance and high operating voltage, and thus high specific energy. It is still highly demanding to enhance the capacitance in order to achieve high power and energy density. We synthesized a high-pore-volume and specific-surface-area activated carbon material with a slit mesoporous structure by two-step processes of carbonization and the activation from polypyrrole. The novel slit-pore-structured carbon materials provide a specific capacity of 310 F g^{-1} at 0.5 A g^{-1} for C-IL SCs, which is among one of the highest recorded specific capacitances. The slit mesoporous activated carbons have a maximum ion volume utilization of 74%, which effectively enhances ion storage, and a better interaction with ions in ionic liquid electrolyte, thus providing superior capacitance. We believe that this work provides a new strategy of engineering pore structure to enhance specific capacitance and rate performance of C-IL SCs.

Keywords: hierarchical porous carbon, slit-pore structure, ion-packing density, ionic liquid, supercapacitors

INTRODUCTION

As the portable energy storage market grows, such as the grid energy storage of electric vehicles and renewable energy, it becomes urgent to develop energy storage devices possessing high specific power and high specific energy (Armand and Tarascon, 2008; Simon and Gogotsi, 2008; Fang et al., 2018; Yun et al., 2019a; Zou et al., 2019). A supercapacitor (SC), a safe and reliable energy storage device with fast charge–discharge capability and a long cycling life, is a competitive energy storage option to meet the increasing power demands (Winter and Brodd, 2004; Aricò et al., 2005; Miller and Simon, 2008; Miller, 2012; Hou et al., 2015; Li et al., 2019; Yun et al., 2019b). However, compared with various batteries (60–200 Wh kg^{-1}), the wide application of commercial activated carbon–based SCs has been limited due to their low specific energy (<5 Wh kg^{-1}; Aurbach et al., 2000; Burke, 2000; Jang et al., 2011; Zhou et al., 2018). Therefore, without sacrificing the specific power of the SCs itself, increasing its specific energy is the ultimate method to address the problem.

The specific energy density of an SC can be calculated by the equation $E = CV^2/2$ (Miller, 2012). Therefore, the energy density can be increased by developing a high capacitance electrode material or enlarging its voltage window. In particular, it is more remarkable to increase the specific capacitance of SCs. Therefore, the preparation of a carbon-based SC with a high ion-accessible specific surface area (SSA) will improve its capacitance greatly. However, this is not the case

when the SSA of the material is very large (>2,000 m^2 g^{-1}). For instance, the maximum SSA of activated carbon reported in the previous literature was limited at about 4,000 m^2 g^{-1}, but the material showed a relatively low specific capacitance (165 F g^{-1}) in aqueous electrolyte (To et al., 2015). It can be seen that the specific capacitance is also related to the ion-accessible holes. Chmiola et al. (2006) demonstrated that anions and cations in the organic electrolyte can enter the microporous region [pore size ≈ ion size (d_{ion}) of electrolyte] to obtain the highest specific capacitance. Recently, Wei et al. have prepared a specific microporous activated carbon electrode by a chemical activation method, and this kind of activated carbon exhibits an ultra-high specific capacitance of 200–300 F g^{-1} in an organic electrolyte or an ionic liquid (IL) (Wei et al., 2011, 2012). Extremely narrow micropores have been proven to possess optimized high capacitance. However, as with the IL electrolyte with a high voltage window used, the power characteristics of extremely narrow micropores are still limited, especially under the condition of high specific power. With such a limitation mainly due to the large ionic size of IL, the ion transport resistance in the IL electrolyte is high, which causes a rapid decrease in capacitance, thereby affecting the rate performance of the SC (Kondrat et al., 2012; Merlet et al., 2012; Peng et al., 2014; Wen et al., 2016). Chen et al. have found that the pore size region of the favorable capacitors, except for the micropore region, is the mesoporous region (pore size ≈ 2 to 3.5 times ion size of IL; Wang et al., 2016b). Compared with the micropores, the mesopores are also more favorable for rapid ion migration and improving the rate performance of the IL-based SC. Due to the model-confined favorable ion packing, the rich mesopore nanocarbon materials synthesized in this study delivered high capacitance (290 F g^{-1}). Chen and coworkers also proposed a model to describe the confined ion packing in the cylindrical pores and pointed to the importance of the three-dimensional (3D) structure of the pores, instead of only a 2D surface, in determining the capacitance of the carbon-IL SCs. The higher mesopore volume and reasonable mesoporous pore size distribution (PSD) not only increase the specific capacitance of the material but also reduce the resistance during electrolyte ion transport, resulting in superior rate capability. However, the capacitance and pore volume relationship needs experimental validation. In addition, based on the analysis of the 3D pore–IL interaction, not only the PSD and pore volume but also the pore morphology could play a privileged role for capacitance. However, the possible effect of the pore morphology on the capacitance has not been addressed so far.

Herein, we focus on the effect of the pore properties such as pore morphology, pore volume, and PSD on the capacitance and rate capability of carbon-IL SCs. A high-pore-volume and specific-surface-area activated carbon material with a slit-pore structure was synthesized by two-step process of carbonization and activation. A series of spherical porous carbon materials was synthesized, namely, carbon nanospheres (CNSs), by using a polypyrrole (PPy) as the carbon source. The PPy after carbonization was activated by KOH at different temperatures. By changing the activation temperature, the regulation of the PSD of the activated carbon material and the increase of the mesopore volume ratio are realized. Superior performance of CNSs-IL SCs is achieved by slit-pore morphology, large pore volume, and proper PSD.

EXPERIMENT

Synthesis of the CNSs

A solution of 1 M hydrochloric acid (HCl) (37%) solution containing 4.04 g of pyrrole (Aladdin 99%) was mixed at a volume ratio of 1:1 with another solution of 1 M HCl containing 13.74 g of ammonia peroxydisulfate (Aladdin 98%) oxidant. After the mixture was stirred at 500 rad min^{-1} for 2 h, the PPy was filtered and washed with water and ethanol and then dried in a vacuum overnight at 60°C. Then, the synthesized PPy was carbonized at 650°C with a heating rate of 10°C min^{-1} for 2 h in a quartz tube furnace under an argon atmosphere. The carbonized PPy (CPPy) and potassium hydroxide (KOH) pellets (Aladdin 95%) were then ground in ethanol at a mass ratio of 1:4. The mixture was then activated between 800 and 900°C. The heating rate was 5°C min^{-1}, and the maximum temperature was maintained for 1 h. Therefore, the PPys activated (referred to as APPy) at 800, 850, and 900°C were named APPy-800, APPy-850, and APPy-900, respectively. The synthesized APPy samples were washed repeatedly with 1 M HCl solution, distilled water, and ethanol until pH was 7. Finally, the samples were dried overnight at 60°C in air.

Material Characterization

The morphology information and microstructures of the synthesized samples were determined by field-emission scanning electron microscopy (FE-SEM, JSM-7800F) and high-resolution transmission electron microscopy (HR-TEM, Tecnai G2 F30). Brunauer–Emmett–Teller (BET) SSA and PSD of the CNSs were studied by a Micromeritic BEL, BELSORP-MAX instrument. X-ray photoelectron spectroscopy (XPS, Thermo ESCALAB 250XI) was carried out for analysis of the surface chemical composition. X-ray diffraction (XRD) analysis was conducted by a Bruker AXS D8 Discover diffractometer with the Cu K_α radiation ($\lambda = 0.1540598$ nm). In addition, the carbon materials were investigated by Raman spectroscopy (Renishaw inVia) with a laser wavelength of 532 nm.

Electrochemical Characterization

The electrode materials were prepared by mixing 80 wt.% APPy, 10 wt.% acetylene black, and 10 wt.% polytetrafluoroethylene (PTFE) in a small amount of ethanol. The obtained electrode materials of the SCs were coated over a nickel foam disk (Alfa Aesar) and pressed at 6 MPa. The mass of the coated active material was approximately 2 mg cm^{-2}. Then the electrodes were dried at 120°C for 12 h in a vacuum oven. Finally, the two-electrode cells were assembled using CR2025 coin cells in an argon-filled glove box (<1 ppm O_2 and <1 ppm H_2O). The two electrodes in the coin cells were separated by a thin microporous monolayer membrane (Celgard 3501) separator and filled with 15 ml of neat 1-ethyl-3-methylimidazolium tetrafluoroborate ($EMIMBF_4$) (Sigma-Aldrich 99%) electrolyte.

The prepared CR2025 coin cells (SCs) were stably placed overnight at room temperature before electrochemical measurements were taken. Impedance spectra (EIS) of the electrodes recorded in a frequency range from 10 to 100 kHz with a voltage amplitude of 10 mV at the open-circuit potential and cyclic voltammetry (CV) of the electrodes were carried out on a Princeton VersaSTAT potentiostat analyzer. Galvanostatic charge–discharge (GCD) tests and cycling stability tests were performed on an MTI S eight-channel battery analyzer. The specific capacitance, specific energy, and specific power of the cells were calculated from the GCD measurements by using Equations S1–S3 (as seen in the **Supplementary Material**).

RESULTS AND DISCUSSION

We prepared PPy-derived porous carbon by a carbonization–activation process (**Figure 1a**). This preparation of porous carbon by a two-step process has a range of physical properties depending on the carbon source and the corresponding activation process. In the present work, the microstructure and morphology information of the synthesized PPy, CPPy, and APPy-850 was characterized using FE-SEM and HR-TEM. The image shows the agglomerates composed of 3D spherical PPys (**Figure S1A**) with diameters of 100–200 nm. After pyrolysis of the PPy at 650°C for 2 h (**Figure S1B**), the diameters of the sphere remain unchanged. The surface of the sphere becomes rough after activation at 850°C (**Figure 1b**), and uniformly distributed mesopores can be observed on the macroporous framework based on high-magnification SEM (**Figure 1c**) and HR-TEM (**Figure 1d**) observation. The image (**Figure 1e**) clearly shows that CPPy is etched with KOH during the activation process, thus obtaining a distribution of micro- and sub-mesopores. It is also shown that the electron diffraction photograph in the inset of **Figure 1d** confirms the graphitic domain structure (circled area in **Figure 1e**; Xu et al., 2019). The micro- and sub-mesopores are mainly caused by the delamination of the graphitic domain. After activation, these domains are delaminated, and slit-shaped pores are produced. When the degree of delamination is high, cylindrical or conical pores form. A large number of slit-shaped pores formed in APPy-850 are apparent in **Figure S1C** (circled area). Simultaneously, such a hierarchical pore structure allows the IL to be better stored and transferred inside the electrode.

The N_2 adsorption/desorption method was used to measure the pore characteristics of the APPys obtained at different activation temperatures. Although the SSA obtained from the BET method is not rigorous (Rouquerol et al., 2007), herein, the BET method is used to evaluate the relative surface area of different samples. The results indicate that the activation temperature has a significant effect on the SSA, the pore structure, and PSD (**Figures 2A,B**). The SSA of APPy-800, APPy-850, and APPy-900 are 2207.1, 3818.8, and 2620.5 $m^2\ g^{-1}$, respectively.

Regarding the specific pore structure in the APPys, the hysteresis loop shapes have often been identified with specific mesopore structures. The hysteresis loop made by slit pores seems nearly horizontal and parallel over a wide range of p/p_o. And the hysteresis loop made by cylindrical pores is almost vertical and nearly parallel over an appreciable range of gas uptake (Sing, 1985; Thommes et al., 2000, 2002). Illustrated hysteresis loops corresponding to cylindrical pores and slit pores are presented as an insert in **Figure 2A**. As presented in **Figure 2A**, the hysteresis loop between the N_2 adsorption and desorption isotherms indicates that the porous carbon materials mainly contain slit mesopores, rather than cylindrical pores. Furthermore, the mesopore content in the porous carbon materials can be evaluated by the size of the hysteresis loop (Sing, 1982). In general, a larger hysteresis loop indicates a high proportion of mesopores, and a small hysteresis loop implies a low proportion of mesopores. By comparison of the hysteresis loops of three porous carbon materials, APPy-800, APPy-850, APPy-900, it can observed that APPy-850 has the highest content of mesopores.

According to the non-local density functional theory (NL-DFT) based on the slit-pore model, the pore structure parameters of APPys are listed in **Table S1**. It can be observed that the pore volumes of APPy-800, APPy-850, and APPy-900 are 0.987, 2.098, and 1.487 $cm^3\ g^{-1}$, respectively. The PSD of APPys are

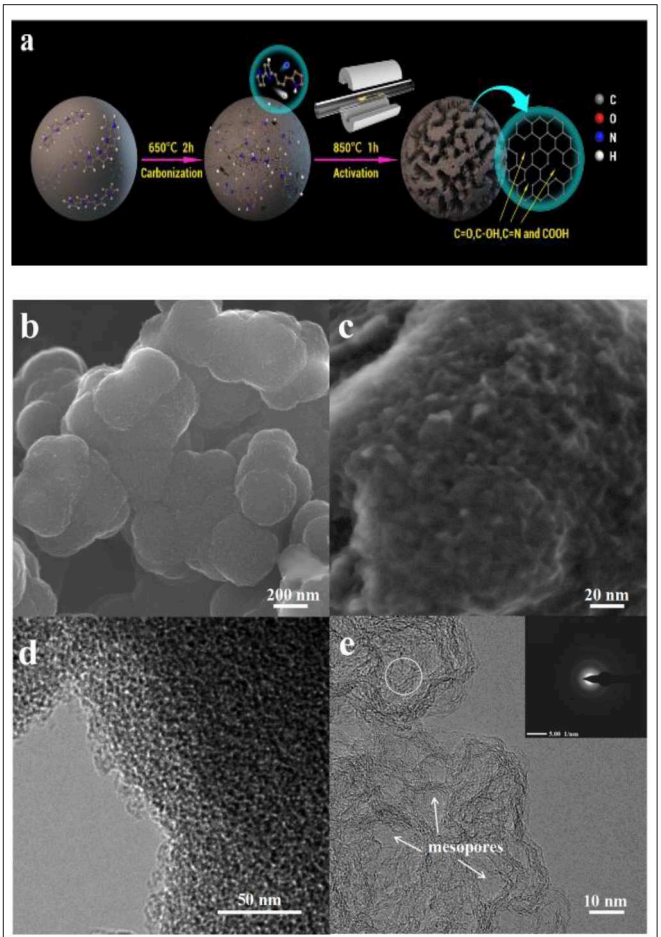

FIGURE 1 | (a) Schematic illustration of the synthesis of polypyrrole (Ppy)-derived porous carbon materials. **(b,c)** Scanning electron microscopy (SEM) image of PPy activated at 850°C (APPy-850). **(d,e)** Transmission electron microscopy (TEM) image of APPy-850.

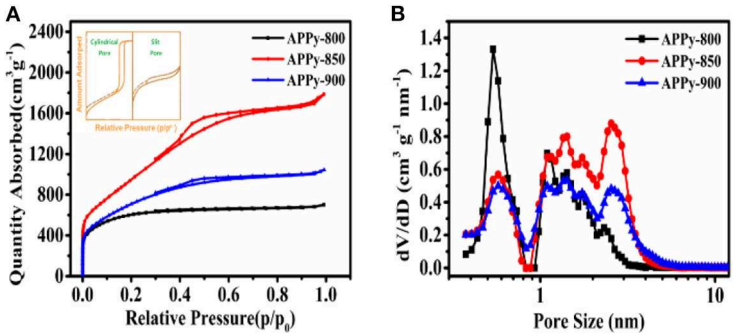

FIGURE 2 | (A) Nitrogen adsorption/desorption isotherm at 77 K. **(B)** Pore size distributions calculated using a slit-pore density functional theory (DFT) model.

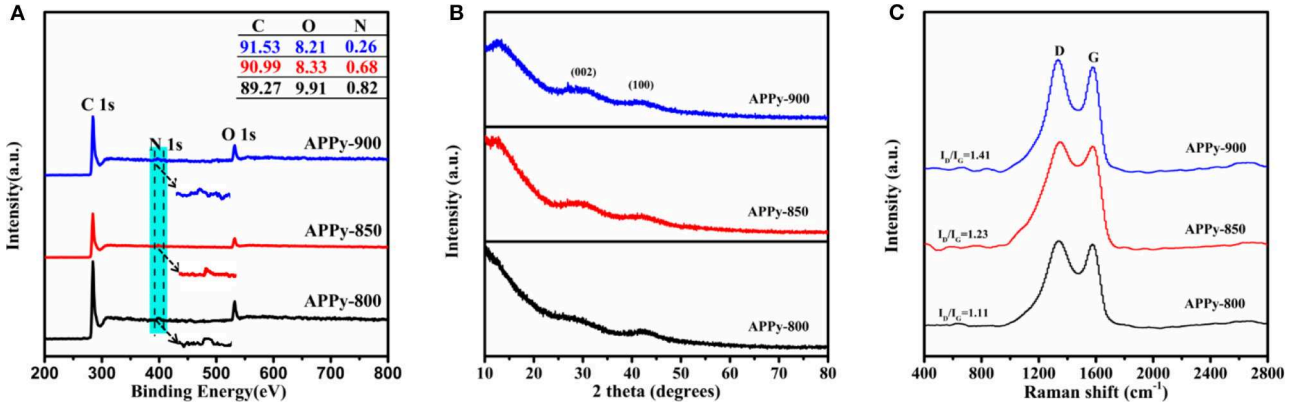

FIGURE 3 | (A) X-ray photoelectron spectroscopy (XPS) spectra, and inset is a table of detailed elements in materials. **(B)** X-ray diffraction (XRD) patterns of the APPy porous carbons. **(C)** Raman spectra of the APPy porous carbons.

presented in **Figure 2B**; it can be seen that pore volumes of APPy-850 and APPy-900 increase in the range of mesopore size and decrease in the range of micropore size in comparison to APPy-800. The narrow small mesopore size ranges from 2 to 5 nm. The ratios of mesopore volume to total pore volume in APPy-850 and APPy-900 samples are 72 and 68%, respectively. In addition, it can be observed that the activation process at high temperature (900°C) decreases SSA and pore volume, which is detrimental to achieving high-performing porous carbon materials. Such degradation may be due to excessive temperature, which makes the ablation of C atoms in the KOH activation process more serious, leading to collapse of the pores (Xu et al., 2014).

The chemical compositions of APPy C1s, O1s, and N1s signals are analyzed by the XPS spectra, and the surface composition of carbons is shown in the XPS survey spectra (**Figure 3A** and **Table S2**). From the XPS survey, the samples of APPy-850 are mainly made up of 90.99 at.% carbon with 8.33 at.% oxygen and 0.68 at.% nitrogen, with no other heteroatoms being observable. The high-resolution C1s spectra of APPy (**Figure S2**) can be deconvoluted by five peaks, representing C-I (284.6 eV), a dominated component for graphitized carbon; C-II (286.0–286.3 eV), carbon in phenolic, alcohol, ether, or C=N groups; C-III (287.3–287.6 eV), carbon in carbonyl or quinine groups; C-IV (288.8–289.1 eV), carbon in carboxyl or ester groups; and C-V (290.5–291.2 eV), carbon in carbonate groups and/or adsorbed CO and CO_2 (Zhou et al., 2007, 2019). The high-resolution O1s core level spectra can be mainly deconvoluted by four peaks, representing O-I (531.4 eV), C=O quinone-type groups, O-II (532.5 eV), C-OH phenol groups and/or C-O-C ether groups, O-III (533.4 eV), non-carbonyl (ether-type) oxygen atoms in esters, and O-IV (534–535 eV), anhydrides groups and COOH carboxylic groups (**Figure S2**; Li et al., 2014). It is widely accepted that the surface redox reaction between oxygen functionalities on carbons and electrolyte ions can contribute to the pseudocapacitance through the quinone/hydroquinone redox pair (about 60% of total oxygen; Liu et al., 2016). It is confirmed that in non-aqueous electrolytes, the reversible oxidation/reduction of hydroquinone/quinone and carbonyl (C=O) groups may cause pseudocapacitance (Gupta and Linschitz, 1997). So a small peak of pseudocapacitance at ~2 V can be observed on the discharge section of the CV curve of APPy-850-SC (**Figures 4B,E**). The nitrogen content in the three APPy samples is relatively low (<0.82 at.%). These traces of N atoms may be doped into carbon materials to enhance the wettability of the interface between the electrode and electrolyte (Li et al., 2007).

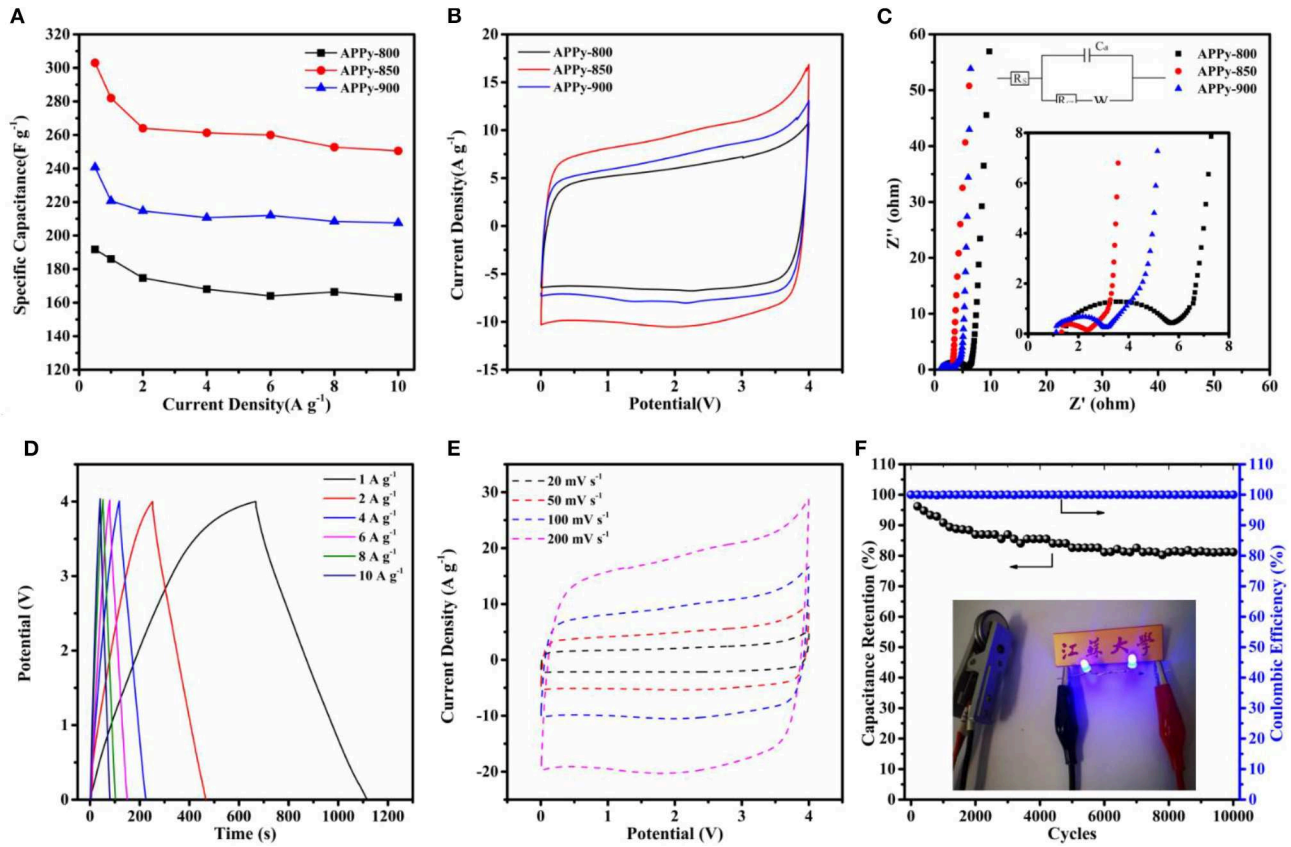

FIGURE 4 | (A) Rate capability: current density vs. specific capacitance. **(B)** Cyclic voltammetry (CV) curve of three samples at 100 mv s^{-1}. **(C)** Nyquist plots of three samples; the inset is a magnification of the high-frequency range data and fitting equivalent circuit. **(D)** Galvanostatic charge–discharge (GCD) curve of APPy-850-SC at current densities of 1, 2, 4, 6, 8, and 10 A g^{-1}. **(E)** CV curve of APPy-850-SC at a scan rate of 20–200 mV s^{-1}. **(F)** Cycling stability and coulombic efficiency of APPy-850-SC at 6 A g^{-1} for 10,000 cycles. The inset shows photographs of two blue LEDs.

The structural features of the porous carbon were further evaluated by using XRD. The XRD pattern (**Figure 3B**) shows two discernible broad peaks at 25–30°, which corresponds to the (002) plane, and 42–44°, corresponding to the (100) plane of graphite, respectively (Jiang et al., 2013). The broad (002) XRD peaks confirm the low degree of order in these carbons, which is understandable since they are both carbonized and activated at low temperatures. A large increase in the low-angle scatter from the porous carbon can be also noted, which is consistent with the presence of a high density of pores. These results are consistent with the observations from HR-TEM (**Figure 1e**), which indicate that APPy porous carbon consists predominantly of curved monoatomic layers of carbon, forming a large number of slit-shaped pores between the interlaced flakes (arrows in **Figure S1C**). The two characteristic G- and D-bands of the Raman spectrum of APPy materials are shown at ∼1,595 and ∼1,350 cm^{-1}, respectively (**Figure 3C**; Tsai et al., 2013). The former corresponds to the graphitic order, while the latter corresponds to the degree of disorder/defectiveness in the structure. As the activation temperature increases, the I_D/I_G ratio is gradually increased from ∼1.11 in APPy-800, ∼1.23 in APPy-850 to ∼1.41 in APPy-900, indicating an increase of the degree of disorder/defectiveness in the structures. According to XRD diffraction and the Raman spectrum, it can be confirmed that the obtained porous carbon materials consist of stacking graphene-like layers. Intriguingly, as the activation temperature increases, the I_D/I_G ratio is gradually increased from ∼1.11 in APPy-800, ∼1.23 in APPy-850 to ∼1.41 in APPy-900, indicating an increase of the disorder degree in the structures. This is a little controversy to the general observation. Such a discrepancy can be attributed to the activation temperature. When the activation temperature is below 900°C, the increase of activation temperature will lead to poor graphitization degree (Yan et al., 2020).

The GCD measurement results are in the range of 0.5–10 A g^{-1}, which confirmed the superior capacitance performance of APPy, as shown in **Figure 4A**. The APPy-850 shows a high gravimetric capacitance of 310 F g^{-1} (0–4 V) at 0.5 A g^{-1} and high capacitance retention of 83% up to 10 A g^{-1}. The excellent performance of this sample is attributed to the large specific surface area and high pore volume, contributed mainly by the rich mesoporous structure. This structure facilitates the rapid transport of ions and thus contributes to high rate performance (Guo et al., 2013). The CV curves of the three APPy samples at the same scan rates (100 mV s^{-1}) are shown in the fully

operated voltage ranging from 0 to 4 V (**Figure 4B**). Among them, the APPy-850 shows a larger CV area, indicating that it possesses a higher specific capacitance. The Nyquist plots to investigate the electrochemical behavior of the three APPy samples are shown in **Figure 4C**, and the inset is an EIS plot at high-frequency region and equivalent circuit. The impedance spectrum mainly consists of a semicircle in the high-frequency region and an approximate straight line in the low-frequency region, where the behavior is mainly capacitive. The 45° segment in the Nyquist plot may be due to the inhomogeneity of the internal pores, indicating that the transport of electrolyte ions during charge and discharge is controlled by the diffusion process (Manohar et al., 2008; He and Mansfeld, 2009). The semicircle reflects the resistance during charge transfer and is related to the porous structure of the electrode (Gamby et al., 2001). From the inset of **Figure 4C**, the amplitude of the semicircle of the APPy-850 is much smaller than that of the others, indicating that the APPy-850 shows the capacitive behavior at lower resistance values than others. That means the impedance of the electrode with the APPy-850 is less dependent on frequency, and thus, the pore ion accessibility of the APPy-850 is higher than that of the others, indicating that the activation temperature of 850°C provides the best porosity structure for IL ion diffusion.

For the optimized APPy-850, the charge/discharge curve (**Figure 4D** and **Figure S3**) still shows a quasi-triangle, indicating excellent electrochemical reversibility and charge/discharge efficiency (Stoller et al., 2008). As shown in **Figure 4E** and **Figure S3**, the CV exhibits an approximately rectangular shape, confirming that the capacitance obtained is mainly due to the electric double layer capacitance contribution. Even at a high scanning rate of 200 mV s^{-1}, its rectangular shape is maintained, indicating excellent current response capability. This good current performance is due to the structure in which the mesopores and the micropores are cross-linked with each other can store a large amount of electrolyte ions and effectively shorten the ion transport time (Chen et al., 2012; Wang et al., 2016a). Apart from high capacitive performance, long-term cyclic performance is another important factor for a superior energy storage device. The cells were investigated by GCD at a current density of 6 A g^{-1} within the voltage range of 1.8–3.6 V (**Figure 4F**). After 10,000 cycles, it still maintains about 81% of the initial capacitance, indicating that APPy-850 porous carbon is a well-stabilized SC electrode material (Zhang et al., 2015). Since there is still sufficient free space between the mesoporous structures of these porous carbons, the volume expansion due to prolonged ion insertion/extraction is effectively buffered. Two devices also were connected to light emitting diodes (LEDs, 3.6 V), and the two blue LEDs were successfully lighted up (the inset of **Figure 4F**) for over 10 min after charging for 15 s.

According to the specific capacitance data measured by GCD in **Table S1**, **Figure 5A** reveals that the increase in the effective slit-pore volume of APPys between the slit-pore diameters of 1 and 10 nm can lead to the increase in the specific capacity. The specific capacitance increases linearly from 193 to 310 F g^{-1}, as the slit-pore volume increases from 0.61 to 1.727 cm^3 g^{-1}. This result shows that the specific capacity is novel linearly proportional to the slit-pore volume. Regarding the relationship between pore volume and specific capacity, a cylindrical pore model has recently been used to interpret such a relationship in terms of Equation 1 and Equation S4 (Wang et al., 2016a)

$$N_{total} = \sum_{D_1}^{D_i} [V(D_i) \cdot f(\phi(D_i/d_{ion}), d_{ion})](i = 1, 2, 3 \ldots n) \quad (1)$$

where N_{total} is the number of adsorbed ions, V is the specific pore volume, f is the ion-packing function, Φ is a function of ion volume utilization fraction (Φ = the volume of the adsorbed ions/the total volume of the pore), d_{ion} is effective ion size (0.97 nm), and D is the pore size. Due to the ion volume utilization fraction, Φ is a function of D/d_{ion} in the cylindrical pore model, so the increase in specific capacity is not a perfect linear dependence on the increase in cylindrical pore volume. However, the novel slit-pore structure carbon

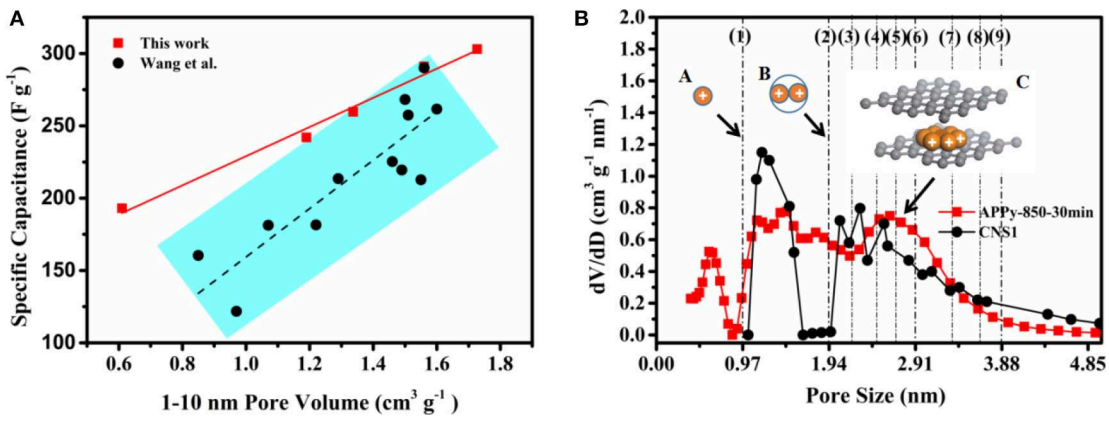

FIGURE 5 | (A) Relationship between pore volume and specific capacitance, **(B)** Pore size distribution curve calculated using different models and charge ion-packing configurations. Note: CNS1 stands for carbon nanosponge (CNS), which carbonized at 650°C, followed by activation at 900°C for 60 min. The data of CNS1 are cited from Wang et al. (2016b).

materials in this work give rise to a linear dependence of specific capacity on slit-pore volume; it implies that the ion volume utilization fraction Φ is a constant rather than a function of D/d_{ion}. Such a difference in the ion volume utilization fraction Φ indicates that the ion-packing configuration in the novel slit-pore structure is different from that in cylindrical pore structure.

In the following, the difference of ion-packing configuration between a cylindrical pore structure and a slit-pore structure will be investigated. **Figure 5B** shows PSD curves of the two materials. The PSD curves of CNS1 are calculated using a cylindrical pore DFT model with the pore volume of 1.5 cm^3 g^{-1} between the pore diameters of 1 and 10 nm. The PSD curves of APPy-850-30 min are calculated using a slit-pore DFT model with the pore volume of 1.56 cm^3 g^{-1} between the pore diameters of 1 and 10 nm. The PSD in the region of 1–5 nm mainly contributing to the pore volume is considered in this work. When the pore size is ($D/d_{ion} < 1$), no ions can access the surface inside the pore. When the pore size can exactly adapt the integer number of ions, the densest-surface ion-packing configurations lead to the highest volume utilization. When the pore size within the range accommodates the two nearest integer number of ions, the volume utilization decreases with the increase of D/d_{ion}, as demonstrated by the cylindrical pore model (Hodak and Girifalco, 2003; Mughal et al., 2011, 2012). An example is illustrated as schemes A to B in **Figure 5B**. In the case of D/d_{ion} equals 1 and 2, the ion volume utilization fractions are 21.2 and 15%, respectively (calculated by ϕ of Equation 1). It is also interesting to note that the volume utilization fractions of other integer number of ions (3, 4, 5, 6, 7, 8, and 9) are not higher than the case where the ion-packing number is 1 in the range of 1–5 nm. The densest-surface ion-packing configuration of each layer in the surface of the slit pore has only a hexagonal close-packed (HCP) mode in scheme C of **Figure 5B**, and the layer of IL ions having an HCP mode will stack up layer by layer as the slit-pore size increases. The HCP structure of ions in the slit pore has the highest volume utilization (74%) (Szczurek et al., 2014). It is evident that a slit-pore structure is superior to the conventional cylindrical pore structure, and it can accommodate more electrolyte ions at an identical pore volume. Therefore, in this work, the slit-pore structures of the APPy materials increase the specific capacitance of the material in the same volume.

To further confirm the superior performance of our SC with an APPy-850–based electrode, the Ragone plot for APPy-850 material is compared with other electrode materials in **Figure 6**. Based on the active mass in the electrode, the APPy-850-SC possessed an excellent specific energy of 171.5 Wh kg^{-1} at the specific power of 664 W kg^{-1}. Even at a much higher specific power of 15 kW kg^{-1}, the APPy-850-SC still maintains a high specific energy of 129.1 Wh kg^{-1}. In **Table S3**, the performance of the current system is compared with other SCs based on the same IL electrolyte. The APPy-850-SC exhibits significantly higher specific capacity and remains quite competitive with other performances.

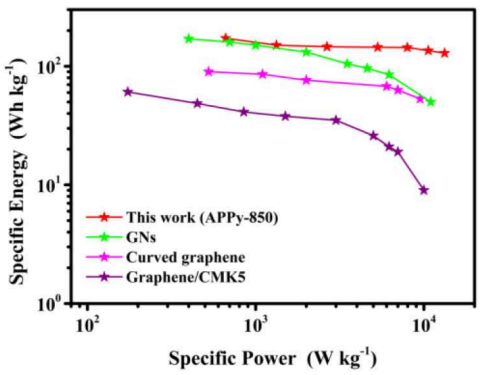

FIGURE 6 | Ragone plots of APPy-850–based electrode compared with those of typical cathode materials based on 1-ethyl-3-methylimidazolium tetrafluoroborate ($EMIMBF_4$) electrolytes (Liu et al., 2010; Lei et al., 2013; Gao et al., 2017).

CONCLUSIONS

Here we have shown a privilege role of the ion-packing density in determining the performance of carbon-IL SCs. We have shown that the specific capacity of the porous material is linearly proportional to the effective pore volume and is also closely related to the pore structure. We report that the 2D slit-pore structure with the HCP configuration of ions has the highest ion-packing density. The slit-pore structure has superior ion-packing density compared to cylinder-like pores. As a result, optimized synthetic APPy-850 hierarchical porous carbon with a high pore volume and a rich slit mesoporous structure achieved a specific capacity of 310 F g^{-1} at 0.5 A g^{-1} for IL SCs, which is one of the highest recorded specific capacitances. At the same time, high specific energy and excellent cycling performance at high specific power are also shown. This work provides a new idea to increase the specific capacity and rate performance of carbon materials by increasing the volume fraction of the slit-type mesopores, which makes it potentially possible to develop SCs with higher specific energy and specific power.

DATA AVAILABILITY STATEMENT

All datasets generated for this study are included in the article/**Supplementary Material**.

AUTHOR CONTRIBUTIONS

All authors listed have made a substantial, direct, and intellectual contribution to the work, and approved it for publication.

FUNDING

We acknowledge funding from the National Natural Science Foundation of China (grants 51774151 and 51702131) and

Natural Science Foundation of Jiangsu Provence, China (grant SBK2017041705). This work was also supported by the Institute of Green Materials and Metallurgy (grant 5501670001) and Jiangsu University Foundation (grant 4111220019).

SUPPLEMENTARY MATERIAL

The Supplementary Material for this article can be found online at: https://www.frontiersin.org/articles/10.3389/fchem.2020.00006/full#supplementary-material

REFERENCES

Aricò, A. S., Bruce, P., Scrosati, B., Tarascon, J. M., and van Schalkwijk, W. (2005). Nanostructured materials for advanced energy conversion and storage devices. *Nat. Mater.* 4, 366–377. doi: 10.1038/nmat1368

Armand, M., and Tarascon, J. M. (2008). Building better batteries. *Nature* 451, 652–657. doi: 10.1038/451652a

Aurbach, D., Lu, Z., Schechter, A., Gofer, Y., Gizbar, H., Turgeman, R., et al. (2000). Prototype systems for rechargeable magnesium batteries. *Nature* 407, 724–727. doi: 10.1038/35037553

Burke, A. (2000). Ultracapacitors: why, how, and where is the technology. *J Power Sources* 91, 37–50. doi: 10.1016/S0378-7753(00)00485-7

Chen, Y., Zhang, X., Zhang, H., Sun, X., Zhang, D., and Ma, Y. (2012). High-performance supercapacitors based on a graphene-activated carbon composite prepared by chemical activation. *RSC Adv.* 2, 7747–7753. doi: 10.1039/c2ra20667f

Chmiola, J., Yushin, G., Gogotsi, Y., Portet, C., Simon, P., and Taberna, P. L. (2006). Anomalous increase in carbon capacitance at pore sizes less than 1 nanometer. *Science* 313,1760–1763. doi: 10.1126/science.1132195

Fang, Z., Peng, J., Ma, N., Liang, L., Gao, H., Zhou, H., et al. (2018). Preparation and optimization of new high-power nanoscale Li4Ti5O12 full-cell system. *J. Nanosci. Nanotechnol.* 18, 8232–8239. doi: 10.1166/jnn.2018.16385

Gamby, J., Taberna, P. L., Simon, P., Fauvarque, J. F., and Chesneau, M. (2001). Studies and characterisations of various activated carbons used for carbon/carbon supercapacitors. *J. Power Sources* 101, 109–116. doi: 10.1016/S0378-7753(01)00707-8

Gao, B., Zhou, H., and Yang, J. (2017). One-step preparation of nitrogen-doped graphene nanosheets for high-performance supercapacitors. *Appl. Surf. Sci.* 409, 350–357. doi: 10.1016/j.apsusc.2017.03.015

Guo, D. C., Mi, J., Hao, G. P., Dong, W., Xiong, G., Li, W. C., et al. (2013). Ionic liquid C16mimBF4 assisted synthesis of poly(benzoxazine-co-resol)-based hierarchically porous carbons with superior performance in supercapacitors. *Energy Environ. Sci.* 6, 652–659. doi: 10.1039/C2EE23127A

Gupta, N., and Linschitz, H. (1997). Hydrogen-bonding and protonation effects in electrochemistry of quinones in aprotic solvents. *J. Am. Chem. Soc.* 119, 6384–6391. doi: 10.1021/ja970028j

He, Z., and Mansfeld, F. (2009). Exploring the use of electrochemical impedance spectroscopy (EIS) in microbial fuel cell studies. *Energy Environ. Sci.* 2, 215–219. doi: 10.1039/B814914C

Hodak, M., and Girifalco, L. A. (2003). Ordered phases of fullerene molecules formed inside carbon nanotubes. *Phys. Rev. B* 67:075419. doi: 10.1103/PhysRevB.67.075419

Hou, H., Craig, E., Banks Jing, M., Zhang, Y., and Ji, X. (2015). Sodium-ion batteries: carbon quantum dots and their derivative 3D porous carbon frameworks for sodium-ion batteries with ultralong cycle life. *Adv. Mater.* 27:7895. doi: 10.1002/adma.201570325

Jang, B. Z., Liu, C., Neff, D., Yu, Z., Wang, M. C., Xiong, W., et al. (2011). Graphene surface-enabled lithium ion-exchanging cells: next-generation high-power energy storage devices. *Nano Lett.* 11, 3785–3791. doi: 10.1021/nl2018492

Jiang, H., Lee, P. S., and Li, C. (2013). 3D carbon based nanostructures for advanced supercapacitors. *Energy Environ. Sci.* 6, 41–53. doi: 10.1039/C2EE23284G

Kondrat, S., Pérez, C. R., Presser, V., Gogotsi, Y., and Kornyshev, A. A. (2012). Effect of pore size and its dispersity on the energy storage in nanoporous supercapacitors. *Energy Environ. Sci.* 5, 6474–6479. doi: 10.1039/c2ee03092f

Lei, Z., Liu, Z., Wang, H., Sun, X., Lu, L., and Zhao, X. S. (2013). A high-energy-density supercapacitor with graphene-CMK-5 as the electrode and ionic liquid as the electrolyte. *J. Mater. Chem. A* 1, 2313–2321. doi: 10.1039/c2ta01040b

Li, J., Yun, X., Hu, Z., Xi, L., Li, N., Tang, H., et al. (2019). Three-dimensional nitrogen and phosphorus co-doped carbon quantum dots/reduced graphene oxide composite aerogels with a hierarchical porous structure as superior electrode materials for supercapacitors. *J. Mater. Chem. A* 7, 26311–26325. doi: 10.1039/C9TA08151H

Li, W., Chen, D., Li, Z., Shi, Y., Wan, Y., Wang, G., et al. (2007). Nitrogen-containing carbon spheres with very large uniform mesopores: the superior electrode materials for EDLC in organic electrolyte. *Carbon* 45, 1757–1763. doi: 10.1016/j.carbon.2007.05.004

Li, Z., Xu, Z., Wang, H., Ding, J., Zahiri, B., Holt, C. M. B., et al. (2014). Colossal pseudocapacitance in a high functionality-high surface area carbon anode doubles the energy of an asymmetric supercapacitor. *Energy Environ. Sci.* 7, 1708–1718. doi: 10.1039/C3EE43979H

Liu, C., Yu, Z., Neff, D., Zhamu, A., and Jang, B. Z. (2010). Graphene-based supercapacitor with an ultrahigh energy density. *Nano Lett.* 10, 4863–4868. doi: 10.1021/nl102661q

Liu, C.-H., Tang, Y.-J., Wang, X.-L., Huang, W., Li, S.-L., Dong, L.-Z., et al. (2016). Highly active Co-Mo-C/NRGO composite as an efficient oxygen electrode for water-oxygen redox cycle. *J. Mater. Chem. A* 4, 18100–18106. doi: 10.1039/C6TA07952K

Manohar, A. K., Bretschger, O., Nealson, K. H., and Mansfeld, F. (2008). The use of electrochemical impedance spectroscopy (EIS) in the evaluation of the electrochemical properties of a microbial fuel cell. *Bioelectrochemistry* 72, 149–154. doi: 10.1016/j.bioelechem.2008.01.004

Merlet, C., Rotenberg, B., Madden, P. A., Taberna, P.-L., Simon, P., Gogotsi, Y., et al. (2012). On the molecular origin of supercapacitance in nanoporous carbon electrodes. *Nat. Mater.* 11, 306–310. doi: 10.1038/nmat3260

Miller, J. R. (2012). Valuing reversible energy storage. *Science* 335, 1312–1313. doi: 10.1126/science.1219134

Miller, J. R., and Simon, P. (2008). Materials science. electrochemical capacitors for energy management. *Science* 321, 651–652. doi: 10.1126/science.1158736

Mughal, A., Chan, H. K., and Weaire, D. (2011). Phyllotactic description of hard sphere packing in cylindrical channels. *Phys. Rev. Lett.* 106:115704. doi: 10.1103/PhysRevLett.106.115704

Mughal, A., Chan, H. K., Weaire, D., and Hutzler, S. (2012). Dense packings of spheres in cylinders: simulations. *Phys. Rev. E* 85:051305. doi: 10.1103/PhysRevE.85.051305

Peng, C., Wen, Z., Qin, Y., Schmidt-Mende, L., Li, C., Yang, S., et al. (2014). Three-dimensional graphitized carbon nanovesicles for high-performance supercapacitors based on ionic liquids. *Chem. Sus. Chem.* 7, 777–784. doi: 10.1002/cssc.201301193

Rouquerol, J., Llewellyn, P., and Rouquerol, F. (2007). Is the bet equation applicable to microporous adsorbents? *Studies Surf. Sci. Catal.* 160, 49–56. doi: 10.1016/S0167-2991(07)80008-5

Simon, P., and Gogotsi, Y. (2008). Materials for electrochemical capacitors. *Nat. Mater.* 7, 845–854. doi: 10.1038/nmat2297

Sing, K. (1982). Reporting physisorption data for gas/solid systems with special reference to the determination of surface area and porosity. *Pure Appl. Chem.* 54, 2201–2218. doi: 10.1351/pac198254112201

Sing, K. S. W. (1985). Reporting physisorption data for gas/solid systems with special reference to the determination of surface area and porosity. *Pure Appl. Chem.* 57, 603–619. doi: 10.1351/pac198557040603

Stoller, M. D., Park, S., Zhu, Y., An, J., and Ruoff, R. S. (2008). Graphene-based ultracapacitors. *Nano Lett.* 8, 3498–3502. doi: 10.1021/nl802558y

Szczurek, A., Fierro, V., Pizzi, A., and Celzard, A. (2014). Emulsion-templated porous carbon monoliths derived from tannins. *Carbon* 74, 352–362. doi: 10.1016/j.carbon.2014.03.047

Thommes, M., Köhn, R., and Fröba, M. (2000). Sorption and pore condensation behavior of nitrogen, argon, and krypton in mesoporous MCM-48 silica materials. *J. Phys. Chem. B* 104, 7932–7943. doi: 10.1021/jp994133m

Thommes, M., Köhn, R., and Fröba, M. (2002). Sorption and pore condensation behavior of pure fluids in mesoporous MCM-48 silica, MCM-41 silica, SBA-15 silica and controlled-pore glass at temperatures above and below the bulk triple point. *Appl. Surf. Sci.* 196, 239–249. doi: 10.1016/S0169-4332(02)00062-4

To, J. W. F., Chen, Z., Yao, H., He, J., Kim, K., Chou, H. H., et al. (2015). Ultrahigh surface area three-dimensional porous graphitic carbon from conjugated polymeric molecular framework. *Acs Cent. Sci.* 1, 68–76. doi: 10.1021/acscentsci.5b00149

Tsai, W.-Y., Lin, R., Murali, S., Li Zhang, L., McDonough, J. K., Ruoff, R. S., et al. (2013). Outstanding performance of activated graphene based supercapacitors in ionic liquid electrolyte from −50 to 80°C. *Nano Energy* 2, 403–411. doi: 10.1016/j.nanoen.2012.11.006

Wang, X., Zhou, H., Lou, F., Li, Y., Buan, M. E. M., Duan, X., et al. (2016a). Boosted supercapacitive energy with high rate capability of a carbon framework with hierarchical pore structure in an ionic liquid. *Chem. Sus. Chem.* 9, 3093–3101. doi: 10.1002/cssc.201600779

Wang, X., Zhou, H., Sheridan, E., Walmsley, J. C., Ren, D., and Chen, D. (2016b). Geometrically confined favourable ion packing for high gravimetric capacitance in carbon-ionic liquid supercapacitors. *Energy Environ. Sci.* 9, 232–239. doi: 10.1039/C5EE02702K

Wei, L., Sevilla, M., Fuertes, A. B., Mokaya, R., and Yushin, G. (2011). Hydrothermal carbonization of abundant renewable natural organic chemicals for high-performance supercapacitor electrodes. *Adv. Energy Mater.* 1, 356–361. doi: 10.1002/aenm.201100019

Wei, L., Sevilla, M., Fuertes, A. B., Mokaya, R., and Yushin, G. (2012). Polypyrrole-derived activated carbons for high-performance electrical double-layer capacitors with ionic liquid electrolyte. *Adv. Funct. Mater.* 22, 827–834. doi: 10.1002/adfm.201101866

Wen, Y., Rufford, T. E., Hulicova-Jurcakova, D., and Wang, L. (2016). Nitrogen and phosphorous co-doped graphene monolith for supercapacitors. *Chem. Sus. Chem.* 9, 513–520. doi: 10.1002/cssc.201501303

Winter, M., and Brodd, R. J. (2004). What are batteries, fuel cells, and supercapacitors? *Chem. Rev.* 104, 4245–4269. doi: 10.1021/cr020730k

Xu, J., Wu, C., Yan, P., Zhang, R., Yue, X., and Ge, S. (2014). Pore characteristics of carbide-derived carbons obtained from carbides with different carbon volume fractions. *Micropor. Mesopor. Mater.* 198, 74–81. doi: 10.1016/j.micromeso.2014.07.019

Xu, J., Yuan, N., Razal, J. M., Zheng, Y., Zhou, X., Ding, J., et al. (2019). Temperature-independent capacitance of carbon-based supercapacitor from −100 to 60°C. *Energy Storage Mater.* 22, 323–329. doi: 10.1016/j.ensm.2019.02.016

Yan, W., Meng, Z., Zou, M., Miao, H., Ma, F., Yu, R., et al. (2020). Neutralization reaction in synthesis of carbon materials for supercapacitors. *Chem. Eng. J.* 381:122547. doi: 10.1016/j.cej.2019.122547

Yun, X., Li, J., Chen, X., Chen, H., Xiao, L., Xiang, K., et al. (2019a). Porous Fe2O3 modified by nitrogen-doped carbon quantum dots/reduced graphene oxide composite aerogel as a high-capacity and high-rate anode material for alkaline aqueous batteries. *ACS Appl. Mater. Interf.* 11, 36970–36984. doi: 10.1021/acsami.9b12827

Yun, X., Wu, S., Li, J., Li, L., Zhou, J., Lu, P., et al. (2019b). Facile synthesis of crystalline RuSe2 nanoparticles as a novel pseudocapacitive electrode material for supercapacitors. *Chem. Commun.* 55, 12320–12323. doi: 10.1039/c9cc06023e

Zhang, H., Zhang, X., Lin, H., Wang, K., Sun, X., Xu, N., et al. (2015). Graphene and maghemite composites based supercapacitors delivering high volumetric capacitance and extraordinary cycling stability. *Electrochim. Acta* 156, 70–76. doi: 10.1016/j.electacta.2015.01.041

Zhou, H., Liu, C., Wu, J.-C., Liu, M., Zhang, D., Song, H., et al. (2019). Boosting the electrochemical performance through proton transfer for the Zn-ion hybrid supercapacitor with both ionic liquid and organic electrolytes. *J. Mater. Chem. A* 7, 9708–9715. doi: 10.1039/C9TA01256G

Zhou, H., Liu, M., Li, Y., Liu, C., Gao, H., Cao, Z., et al. (2018). Carbon nanosponge cathode materials and graphite-protected etched al foil anode for dual-ion hybrid supercapacitor. *J. Electrochem. Soc.* 165, A3100–A3107. doi: 10.1149/2.0681813jes

Zhou, J. H., Sui, Z. J., Zhu, J., Li, P., Chen, D., Dai, Y. C., et al. (2007). Characterization of surface oxygen complexes on carbon nanofibers by TPD, XPS and FT-IR. *Carbon* 45, 785–796. doi: 10.1016/j.carbon.2006.11.019

Zou, K., Cai, P., Liu, C., Li, J., Gao, X., Xu, L., et al. (2019). A kinetically well-matched full-carbon sodium-ion capacitor. *J. Mater. Chem. A* 7, 13540–13549. doi: 10.1039/C9TA03797G

Conflict of Interest: The authors declare that the research was conducted in the absence of any commercial or financial relationships that could be construed as a potential conflict of interest.

frontiers in Chemistry

ORIGINAL RESEARCH
published: 27 February 2020
doi: 10.3389/fchem.2020.00062

Freestanding Needle Flower Structure $CuCo_2S_4$ on Carbon Cloth for Flexible High Energy Supercapacitors With the Gel Electrolyte

*Tian Xie, Jinxiao Xu, Jie Wang, Chuanli Ma, Linghao Su, Fengying Dong and Liangyu Gong**

College of Chemistry and Pharmaceutical Sciences, Qingdao Agricultural University, Qingdao, China

A facile hydrothermal approach was adopted to the direct synthesis of bimetallic sulfide ($CuCo_2S_4$) on carbon cloth (CC) without binders for the supercapacitor's electrodes. A possible formation mechanism was proposed. The prepared bimetallic electrode exhibited a high specific capacitance (Csp) of 1,312 $F{\cdot}g^{-1}$ at 1 $A{\cdot}g^{-1}$, and an excellent capacitance retention of 94% at 5 $A{\cdot}g^{-1}$ over 5,000 cycles. In addition, the asymmetric supercapacitor ($CuCo_2S_4$/CC//AC/CC) exhibited energy density (42.9 $wh{\cdot}kg^{-1}$ at 0.8 $kW{\cdot}kg^{-1}$) and outstanding cycle performance (80% initial capacity retention after 5,000 cycles at 10 $A{\cdot}g^{-1}$). It should be noted that the electrochemical performance of a supercapacitor device is quite stable at different bending angles. Two charged devices in series can light 28 red-colored LEDs (2.0 V) for 5 min. All of this serves to indicate the potentially high application value of $CuCo_2S_4$.

Keywords: flexible electrode, nanoneedles, $CuCo_2S_4$, pseudocapacitance, supercapacitors

OPEN ACCESS

Edited by:
Tang Wei,
Xi'an Jiaotong University, China

Reviewed by:
Bingbing Tian,
Shenzhen University, China
Chengxin Peng,
University of Shanghai for Science and Technology, China

****Correspondence:***
Liangyu Gong
lygong@163.com

Specialty section:
This article was submitted to Electrochemistry, a section of the journal Frontiers in Chemistry

Received: *19 December 2019*
Accepted: *20 January 2020*
Published: *27 February 2020*

Citation:
Xie T, Xu J, Wang J, Ma C, Su L, Dong F and Gong L (2020) Freestanding Needle Flower Structure $CuCo_2S_4$ on Carbon Cloth for Flexible High Energy Supercapacitors With the Gel Electrolyte. Front. Chem. 8:62. doi: 10.3389/fchem.2020.00062

INTRODUCTION

Supercapacitors are extremely valuable for energy storage, owing to their rapid rechargeable ability and extended life cycle (Gao et al., 2015b; He and Chen, 2015). In recent years, they have been widely applied in many fields, such as power backup devices, hybrid electric vehicles, and portable and wearable electronic products (Dong et al., 2015). While flexible electronic products have experienced explosive growth, all electronic devices require flexible and long-life energy storage systems (Hu et al., 2010; Shen et al., 2014; Liu G. et al., 2018). Currently, the main commercial supercapacitors use carbon materials as electrode materials and thus suffer from low-energy density (Dong et al., 2016). Therefore, designing advanced nanostructures with high-energy density and outstanding performance at high-current densities is still given a large amount of attention and holds great appeal (Bao and Li, 2012; Wang et al., 2014; Huang et al., 2016; Xing et al., 2018).

Transition metal compounds, including oxides and sulfides, can provide superior specific capacitance (C_{sp}) due to the rapid faraday redox reaction (Guo et al., 2014; Padmanathan and Selladurai, 2014; Pu et al., 2014; Gao et al., 2015b; Moosavifard et al., 2016). However, the maximum capacitance and energy density of these materials are severely limited by the lower electrical conductivity. Among them, transitional bimetallic sulfides can provide a richer redox reaction,

resulting in a generally superior electrochemical performance (Xiong et al., 2015; Sun et al., 2017; Wang J. et al., 2018; You et al., 2018; Dong et al., 2019). For example, Li et al. supported $NiCo_2S_4$ nanorods on Ni foam, which displayed a 94.96% capacitive retention over 10,000 cycles (Li M. L. et al., 2018; Li X.-X et al., 2018). At the same time, it has been found that transition bimetallic sulfides also possess rich redox couples and enhance the electronic conductivity (Ai et al., 2016; Wang et al., 2017). In recent years, $CuCo_2S_4$ as electrode material has been found to have excellent electronic conductivity, good electrochemical stability, and higher conductivity when compared to its oxide counterparts. In addition, the synergistic effects due to the interaction between diverse metal compounds leads to an enhanced electrochemical energy storage performance, as compared with monometallic sulfides (Shinde et al., 2019). For example, Tian et al. anchored $CuCo_2S_4$ to graphene aerogel through solvent thermal reaction with 668 $F{\cdot}g^{-1}$ at $1A{\cdot}g^{-1}$. Asymmetrical supercapacitors based on $CuCo_2S_4$/GA exhibit a maximum of 22 $Wh{\cdot}kg^{-1}$ (Tian et al., 2018). Guo et al. prepared Co_2CuS_4 on graphene nanosheets, which exhibited C_{sp} of 1,005 $F{\cdot}g^{-1}$ at $1A{\cdot}g^{-1}$ (Guo et al., 2016). In addition, designing nanostructures with large surface areas is important for promoting ion transport in electrochemical processes (Wang et al., 2016; Shang et al., 2018).

In order to adapt to the trend of wearable and flexible supercapacitors, others found it desirable to prepare electrode materials on flexible substrates (Dingshan et al., 2015; He et al., 2018). According to previous reports, carbon fiber, nickel foam, and copper foam are widely applied as conductive substrate (Martti et al., 2009; Yang et al., 2014; Xiao et al., 2015; Sun et al., 2016). Among them, the carbon fiber cloth is considered to be an ideal conductive substrate due to its flexibility, electrical conductivity, and low cost. At the same time, directly growing nanostructured materials on carbon cloth avoids the use of binders, resulting in rapid electro transport (Jiang et al., 2011; Liu et al., 2011; Yuan et al., 2012; Zhang et al., 2012, 2016; Wang et al., 2013).

Here, we confirm that carbon cloth is a conductive substrate that can be used to grow a novel 3D needle-flowerlike $CuCo_2S_4$ nanostructure. As a result, the flowerlike $CuCo_2S_4$ nanostructure exhibits excellent performance (1,312 $F{\cdot}g^{-1}$ at 1 $A{\cdot}g^{-1}$). Beyond that, an asymmetric solid-state device was manufactured. As a result, it's provided a significant energy density of 42.9 $Wh{\cdot}kg^{-1}$ with an initial capacitance retention rate of 80%–even after 5,000 cycles in the 1.6 V-wide working potential window, showing excellent cycling stability.

MATERIALS AND METHODS

Preparation of $CuCo_2S_4$/CC

All reagents were analytical-grade and used without any additional purification. The carbon cloth was purchased from Ce Tech WOS1009. First, a piece of carbon cloth was refluxed at 100°C for 1 h with HNO_3 and subsequently rinsed with deionized water and ethanol. As is typical, $CuCl_2{\cdot}6H_2O$ (2 mmol), $CoCl_2{\cdot}2H_2O$ (4 mmol), urea (30 mmol), and NH_4F (20 mmol) were dissolved into 60 mL DI water and stirred for 10 min. Then, the mixture solution and the treated CC were transferred into 100 mL autoclave. After the hydrothermal reaction (140°C for 6 h), the precursors on carbon cloth were washed with deionized water and ethanol, and then dried at 60°C for 12 h.

Next, thioacetamide (TAA, 5 mmol) was dissolved in 60 mL of absolute ethanol with stirring. Then, the solution and the as-obtained precursor were transferred together to the 100 ml autoclave (140°C for 6 h). Finally, after being washed and dried at 60°C overnight, the carbon cloth of uniform load $CuCo_2S_4$ was obtained. The loading mass of $CuCo_2S_4$ was about 2.3 $mg{\cdot}cm^{-2}$. For comparison, $CuCo_2S_4$ was directly obtained without the placement of a carbon cloth and the CC without the loaded sample is named blank-CC.

Characterization

X-ray diffraction (XRD) patterns were recorded on a Bruker D8. The morphology of samples was studied by scanning electron microscopy (SEM) (JEOL-7500F, Japan) and transmission electron microscopy (TEM) (HITACHI-7650, Japan). Cycling voltammetry (CV), galvanostatic charge-discharge (GCD), and electrochemical impedance spectroscopy (EIS) were performed with a CHI760E (Shanghai CH, China) electrochemical workstation. Additionally, the cycle life was tested on a CT2001A LAND Battery Test System (LAND, Wuhan, China).

Electrochemical Measurements

The electrochemical measurements were carried out in a three-electrode system by using 3 M KOH aqueous solution as the electrolyte, where the $CuCo_2S_4$/CC was directly used as the working electrode, Pt foil was used as the counter electrode, and a saturated calomel electrode (SCE.) was used as the reference electrode. The C_{sp} of materials was calculated through the equation $C_{sp} = I \times \Delta t \,/\, m \times \Delta V$, where I, ρt, m, and V are the discharge current (A), discharge time (s), loading mass (g), and voltage range.

The flexible solid-state asymmetric supercapacitor (FSASC) device was assembled with a $CuCo_2S_4$/CC cathode, active carbon (AC)/CC anode, and PVA/KOH gel electrolyte. The mass ratio between $CuCo_2S_4$/CC and AC/CC was $m^+/m^- = 0.19$, according to charge conservation (Yuan et al., 2018). The AC/CC electrode was produced by mixing AC 80 wt%, acetylene black 10 wt%, and PTFE 10 wt% and then coated onto carbon cloth. The PVA/KOH gel electrolyte was maintained by mixing KOH (3 g) and PVA (3 g) in 30 ml DI water at 80°C for 1 h with stirring. The energy and power densities were measured by using equation $E\ (Wh{\cdot}kg^{-1}) = C_{sp} \times \Delta V^2 \,/\, 2$ and $P\ (W{\cdot}kg^{-1}) = E \,/\, \Delta t$.

RESULTS AND DISCUSSION

As illustrated in **Scheme 1**, the $CuCo_2S_4$/CC was successfully synthesized through a simple two-step process. First, the Cu-Co precursor was directly grown on the CC via a hydrothermal process. Subsequently, the Cu-Co precursor is converted into $CuCo_2S_4$/CC via a sulfurization strategy.

The chemical composition is recorded by XRD (**Figure 1**). The different peaks of 16, 26, 31.2, 37.9, 46.9, 49.9, and 54.8° are identical to the standard diffraction data of $CuCo_2S_4$ (JCPDS No.42-1450) (You et al., 2018). And the broad peaks at 25 and 45° are derived from the CC substrate (Liu and Wu, 2018).

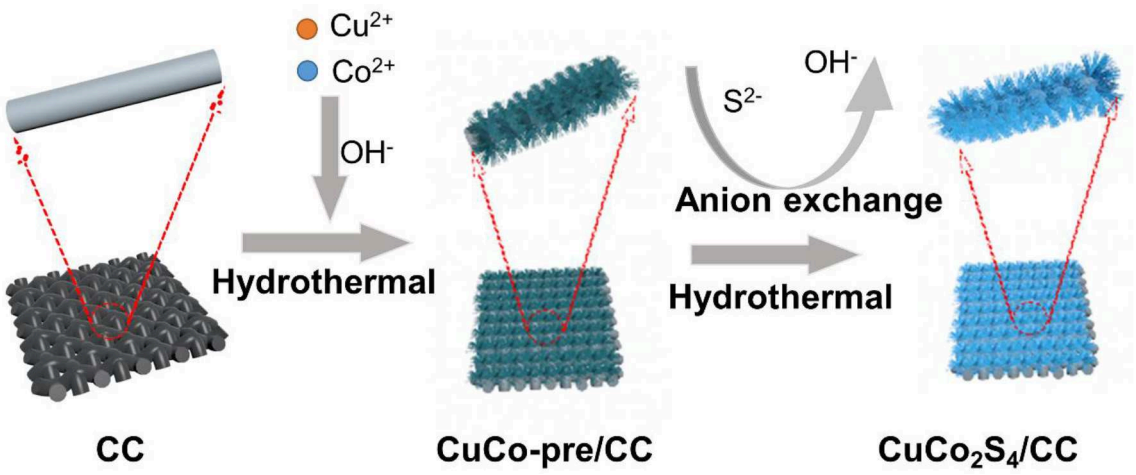

SCHEME 1 | The growth mechanism schematic of $CuCo_2S_4$ on carbon cloth.

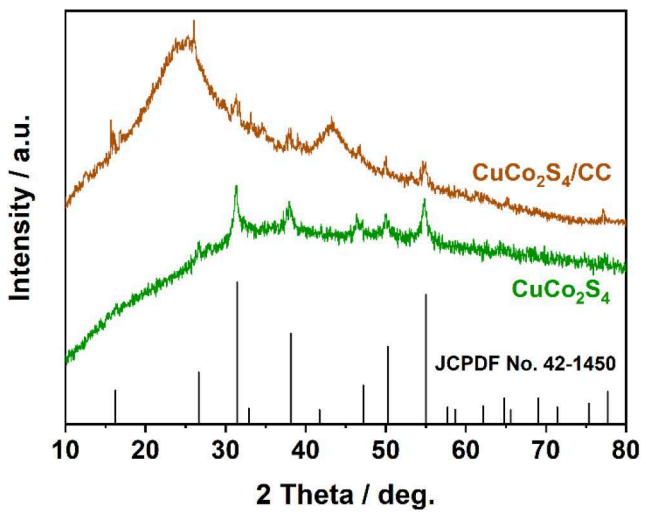

FIGURE 1 | XRD patterns of $CuCo_2S_4$/CC and $CuCo_2S_4$.

Figures 2A–H shows the topographical changes of $CuCo_2S_4$ on carbon cloth. In **Figure 2A**, the $CuCo_2S_4$ was uniformly adhered to the carbon fiber at a reaction time of 2 h. As seen in **Figure 2E**, the flowerlike structure, composed of acicular $CuCo_2S_4$, is supported on the carbon fiber. When the reaction time was extended to 4 h (**Figures 2B,F**), the acicular structure of $CuCo_2S_4$ began to aggregate. When the reaction time was 6 h (**Figures 2C,G**), the acicular structure was further aggregated to form a flowerlike structure. The acicular structure provides more active sites, providing abundant pores, while the surface that is initially aggregated by the needle structure provides a larger reaction area. When the reaction time was extended to 8 h, the flowerlike structure supported on the carbon fiber is composed of agglomerated sheets, which reduces the reactive sites and electrochemical performance (**Figures 2D,H**). The morphological structure of the CoCu-pre and $CuCo_2S_4$ is shown in **Figure S1**. In **Figure S1A**, the needle CuCo-pre constitutes a flowerlike structure and uniformly grows on the carbon fibers. **Figure S1B** clearly shows the flowerlike $CuCo_2S_4$ structure on the carbon fiber; the exchange of anions during vulcanization does not destroy the overall morphology. In contrast, the CuCo-pre and $CuCo_2S_4$ were obtained without adding a carbon cloth substrate (**Figures S1C,D**). It can be seen that both exhibit similar morphologies as those loaded on carbon cloth.

In addition, the microstructure of the $CuCo_2S_4$/CC shown by TEM (**Figure 3A**) further demonstrates that the acicular structure of $CuCo_2S_4$ is attached to the carbon fibers. A HRTEM image shows clear lattice fringes with lattice spacing corresponding to the (113) and (004) planes (**Figure 3B**). The SAED in inset indicates the polycrystalline of the materials. Meanwhile, the TEM and SAED image of $CuCo_2S_4$ shows that it is composed of many primary nano-needles and its polycrystalline (**Figures S1E,F**).

Through the above observations, the growth mechanism of flowerlike $CuCo_2S_4$ on carbon cloth can be preliminarily obtained. First, in an alkaline environment, Cu^{2+} and Co^{2+} ions form a $CuCo(OH)_x$ precursor (Wan et al., 2015; Jayaraman et al., 2017). At this time, the solution becomes a supersaturated solution with a large amount of Cu-Co precursor particles. Due to the high surface energy and thermodynamic instability, the nanoparticles adhere to the carbon fibers to reduce the surface energy. Based on the hydrolysis rate control of NH_4F, the precursors will be oriented to grow into the acicular structure and further assemble into a flowerlike structure (Liu S. et al., 2018). The second step is the vulcanization process. The S^{2-} released by TAA undergoes anion exchange with OH^- to form a $CuCo_2S_4$ flowerlike structure.

The electrochemical properties of $CuCo_2S_4$/CC were measured. **Figure 4A** shows the CV curve of $CuCo_2S_4$/CC, $CuCo_2S_4$ and blank-CC at 10 $mV{\cdot}s^{-1}$. The curve area of $CuCo_2S_4$/CC is larger than that of $CuCo_2S_4$ and blank-CC, which means that $CuCo_2S_4$/CC has a higher specific capacitance.

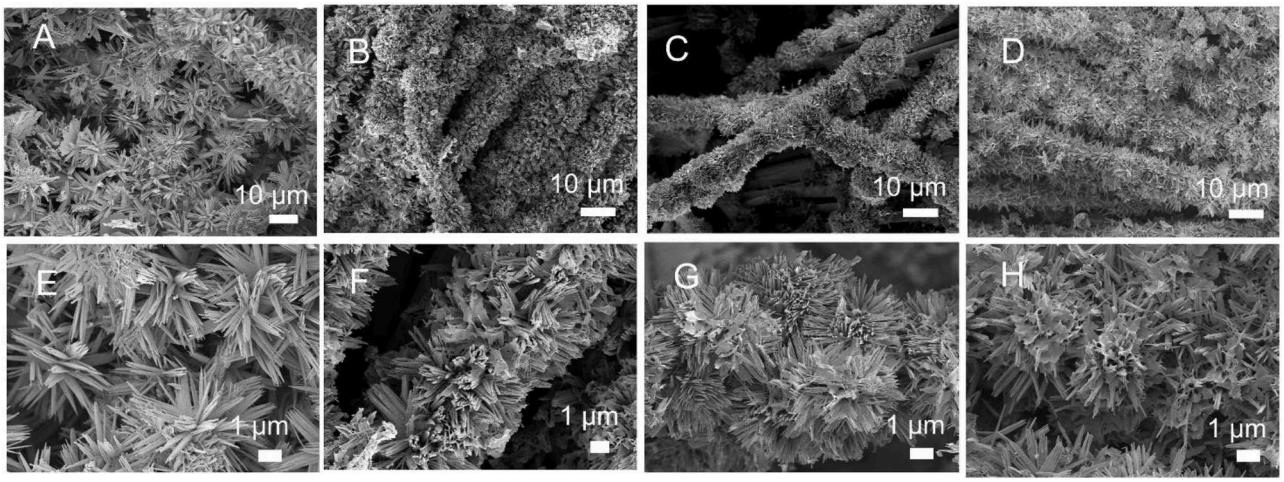

FIGURE 2 | SEM images for $CuCo_2S_4$/CC at different reaction times: 2 h **(A,E)**; 4 h **(B,F)**; 6 h **(C,G)**, and 8 h **(D,H)**.

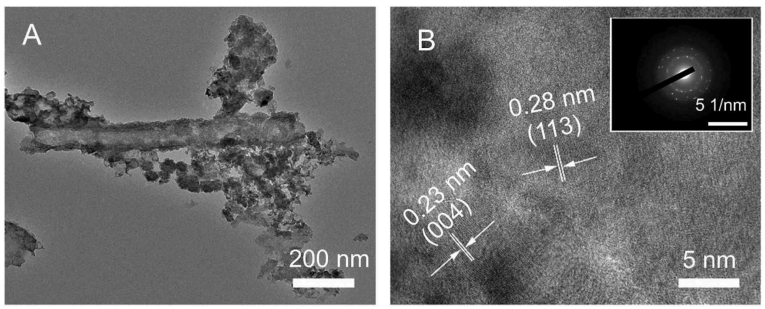

FIGURE 3 | TEM image **(A)**; HRTEM image **(B)**; and SAED pattern (inset) of $CuCo_2S_4$/CC.

Figure 4B is a $CuCo_2S_4$/CC and $CuCo_2S_4$ GCD curves at 1 $A{\cdot}g^{-1}$. Similarly, the discharge time of the $CuCo_2S_4$/CC material is much higher than that of $CuCo_2S_4$. And, the capacitance contribution of blank-CC is negligible. **Figure 4C** shows typical CV curves for $CuCo_2S_4$/CC at 0–0.6 V. Each curve shows a significant redox peak, indicating that the Cu(Co)-S-O/Cu(Co)-S-OH-related faraday reaction was carried out (Jayaraman et al., 2017). As the scan rate increased, the redox peak appeared to shift due to the presence of polarization (Ratha et al., 2017). The possible electrochemical reaction equations are as follows (Kaverlavani et al., 2017; Zhu et al., 2017):

$$CuCo_2S_4 + OH^- + H_2O \leftrightarrow CuSOH + 2CoSOH + e^- \quad (1)$$

$$CuSOH + OH^- \leftrightarrow CuSO + H_2O + e^- \quad (2)$$

$$CoSOH + OH^- \leftrightarrow CoSO + H2O + e^- \quad (3)$$

In order to accurately compare the specific capacitances, the exact C_{sp} was calculated from GCD measures. **Figure 4D** shows the GCD curves of $CuCo_2S_4$/CC from 1 to 10 $A{\cdot}g^{-1}$. From the comparison of C_{sp} graphs of $CuCo_2S_4$/CC and $CuCo_2S_4$ (**Figure 4E**), the discharge-specific capacitance of $CuCo_2S_4$/CC is 1,312, 1,228, 1,116, 1,010, 864, and 820 $F{\cdot}g^{-1}$ at 1, 2, 3, 5, 8, 10 $A{\cdot}g^{-1}$, which is much larger than $CuCo_2S_4$. The specific capacity values were compatible relative to those previously reported (**Table S1**). On the other hand, lower charge transfer resistance (R_{ct}) and Warburg impedance (W) also means that $CuCo_2S_4$/CC can show superior electrochemical performance compared to $CuCo_2S_4$ (**Figure S2**). It is noteworthy that the capacities decrease with an increase in current density, which may be due to the fact that the transport and/or diffusion of electrolyte ions are suppressed in high current density (Brousse et al., 2015). The $CuCo_2S_4$/CC electrode maintained an initial capacity of 94% after cycling 5,000 times at 5 $A{\cdot}g^{-1}$, while the Coulomb efficiency remained almost 100%, indicating excellent cycling stability (**Figure 4F**).

To prove the application potential, the FSASC device was made of $CuCo_2S_4$/CC and AC/CC as the positive and negative electrodes, respectively. **Figure 5A** is the CV curves of $CuCo_2S_4$/CC and AC/CC at 20 $mV{\cdot}s^{-1}$. The detailed electrochemical data of the AC is shown in **Figure S3**. The electrochemical properties of the assembled FSASC were evaluated. The CV and GCD measurements of the ASC device are shown in **Figures 5B,C**, respectively. At the same time, the charging time of the device is higher than the

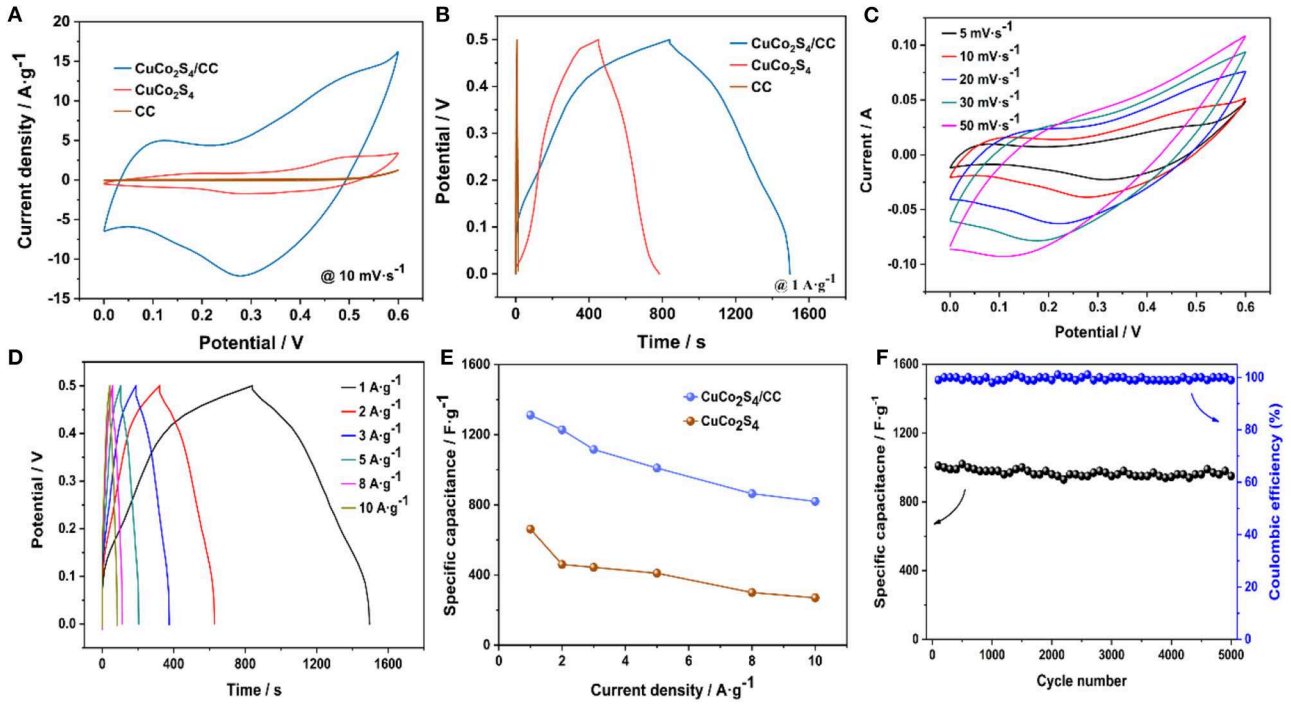

FIGURE 4 | CV curves of $CuCo_2S_4$/CC, $CuCo_2S_4$, and blank-CC at 10 mV·s^{-1} **(A)**; GCD curves of $CuCo_2S_4$/CC, $CuCo_2S_4$, and blank-CC at 1A·g^{-1} **(B)**; CV curves of $CuCo_2S_4$/CC at 5–50 mV·s^{-1} **(C)**; GCD curves of $CuCo_2S_4$/CC at 1–10A·g^{-1} **(D)**; the rate capability of the as-prepared two electrodes **(E)**; Cycling performance at 5A·g^{-1} **(F)**.

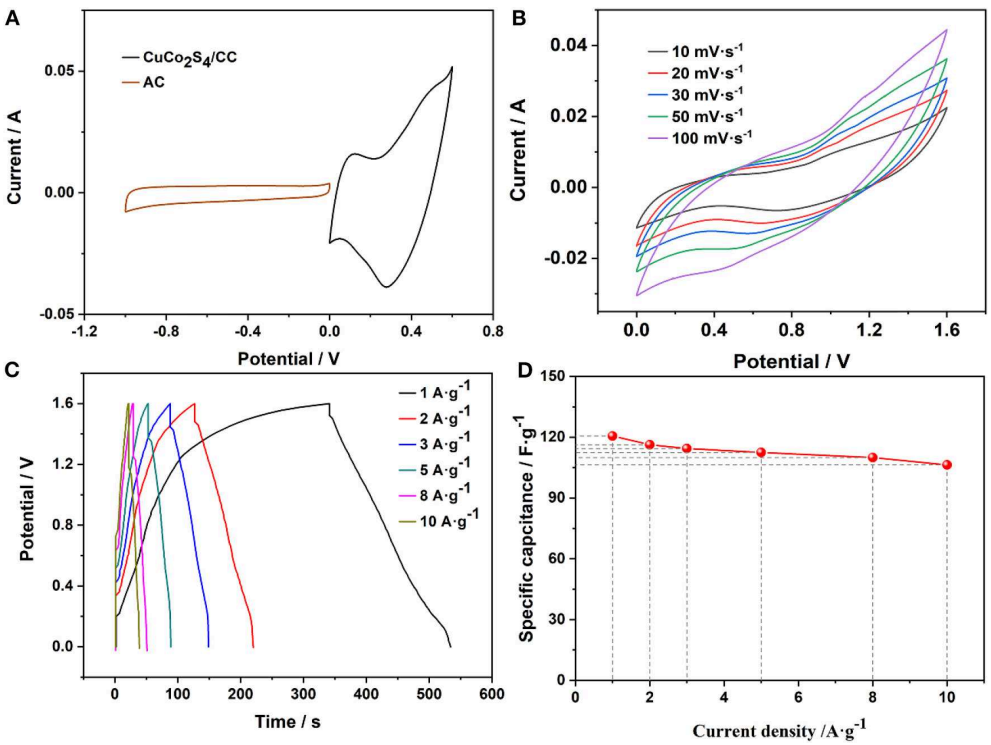

FIGURE 5 | CV curves of the positive and negative **(A)**; CV curves **(B)**; GCD curves **(C)**; and the rate characteristics **(D)** of the device.

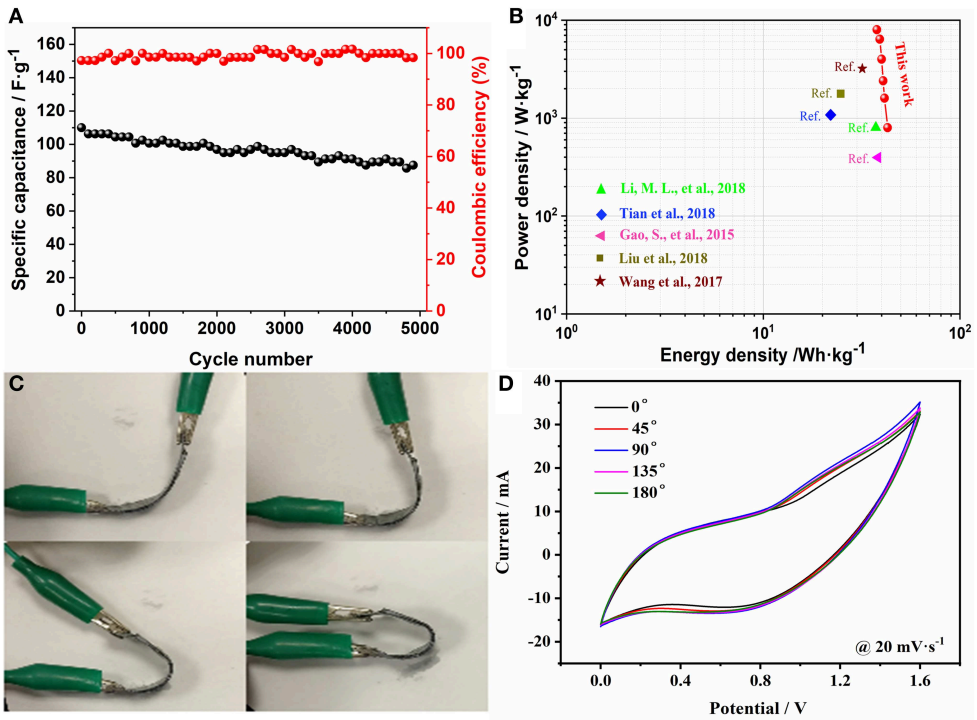

FIGURE 6 | Cycling properties of the device at 10 A·g^{-1} **(A)**; Ragone plot **(B)**; images of asymmetric device at different bending states **(C)**; and the corresponding CV curves **(D)**.

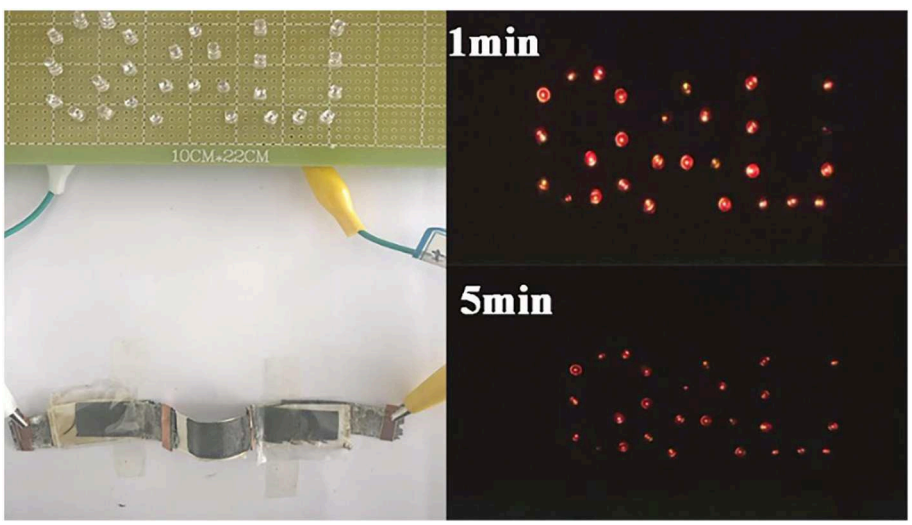

FIGURE 7 | Commercial LED lights powered by three ASC devices connected in series.

discharge time in GCD curves, which may be due to the fact that transport of the electrolyte ion cannot be fully carried out at a low current density (**Figure 5C**). This phenomenon stems from the nature of the gel electrolyte and the inherent properties of the material (Qi et al., 2015; Wang P. et al., 2018). When the current density is 10 A·g^{-1}, a high C_{sp} of 106.3 F·g^{-1} can be delivered, which shows a retention of 88.1% (**Figure 5D**).

The cycle properties of the ASC device were evaluated by cycling 5,000 times at 10 A·g^{-1} (**Figure 6A**). The C_{sp} decreases from 110 to 87.5 F·g^{-1}, which exhibits an excellent retention of 80%. Meanwhile, the coulombic efficiency is almost maintained

at 100%, which indicates that the prepared device has excellent performance. **Figure 6B** shows a maximum energy density of 42.9 $Wh{\cdot}kg^{-1}$ at 0.8 $kW{\cdot}kg^{-1}$. And it's still has 37.8 $Wh{\cdot}kg^{-1}$ at 8 $kW{\cdot}kg^{-1}$. In addition, the assembled FSASC device exhibits outstanding flexibility—the CV curves at different angles proving that the bending has little effect on the device (**Figures 6C,D**).

To demonstrate the practical application potential of the equipment, 28 red LEDs assembled in parallel can be illuminated for more than 5 min (**Figure 7**), which indicates that $CuCo_2S_4$ possess excellent energy storage potential.

CONCLUSIONS

In short, we directly grew needle flower structure $CuCo_2S_4$ on carbon cloth by means of a hydrothermal reaction and vulcanization process; the prepared $CuCo_2S_4$/CC shows an excellent electrochemical performance (1,312 $F{\cdot}g^{-1}$ at 1 $A{\cdot}g^{-1}$ and 94% retention over 5,000 cycles). When used as an electrode material for flexible asymmetric supercapacitors, the device provides higher energy density (maximum of 42.9 $Wh{\cdot}kg^{-1}$) and power density (maximum of 8 $kW{\cdot}kg^{-1}$), long-term cycling stability (80% retention over 5,000 cycles), and superior flexibility. The needle flower structure promotes the transport of electrolyte ions, providing a higher specific capacitance. The rapid transport of ions/electrons on carbon fibers imparts high-rate characteristics to flexible solid-state supercapacitors. This indicates that $CuCo_2S_4$/CC is promising as a flexible supercapacitor electrode material.

DATA AVAILABILITY STATEMENT

All datasets generated for this study are included in the article/**Supplementary Material**.

AUTHOR CONTRIBUTIONS

The manuscript was written through contributions of all authors. All authors have given their approval of the final version of the manuscript.

FUNDING

This work was financially supported by the Natural Science Foundation of Shandong Province (ZR2017LB031).

ACKNOWLEDGMENTS

The authors thank the Analytical and Testing Center of Qingdao Agricultural University for allowing them to use its facilities.

SUPPLEMENTARY MATERIAL

The Supplementary Material for this article can be found online at: https://www.frontiersin.org/articles/10.3389/fchem.2020.00062/full#supplementary-material

REFERENCES

Ai, Z., Hu, Z., Liu, Y., Fan, M., and Liu, P. (2016). Novel 3D flowerlike $CoNi_2S_4$/carbon nanotube composites as high-performance electrode materials for supercapacitors. *N. J. Chem.* 40, 340–347. doi: 10.1039/C5NJ02279G

Bao, L., and Li, X. (2012). Towards textile energy storage from cotton T-shirts. *Adv. Mater.* 24, 3246–3252. doi: 10.1002/adma.201200246

Brousse, T., Bélanger, D., and Long, J. W. (2015). To be or not to be pseudocapacitive? *J. Electrochem. Soc.* 162, A5185–A5189. doi: 10.1149/2.0201505jes

Dingshan, Y., Shengli, Z., Wenchao, J., Kunli, G., Li, W., Xudong, C., et al. (2015). Transforming pristine carbon fiber tows into high performance solid-state fiber supercapacitors. *Adv. Mater.* 27, 4895–4901. doi: 10.1002/adma.201501948

Dong, D., Wu, Z., Wang, J., Fu, G., and Tang, Y. (2019). Recent progress in Co9S8-based materials for hydrogen and oxygen electrocatalysis. *J. Mater. Chem. A* 7, 16068–16088. doi: 10.1039/C9TA04972J

Dong, L., Xu, C., Li, Y., Huang, Z.-H., Kang, F., Yang, Q.-H., et al. (2016). Flexible electrodes and supercapacitors for wearable energy storage: a review by category. *J. Mater. Chem. A* 4, 4659–4685. doi: 10.1039/C5TA10582J

Dong, L., Xu, C., Yang, Q., Fang, J., Li, Y., and Kang, F. (2015). High-performance compressible supercapacitors based on functionally synergic multiscale carbon composite textiles. *J. Mater. Chem. A* 3, 4729–4737. doi: 10.1039/C4TA06494A

Gao, S., Liao, F., Ma, S., Zhu, L., and Shao, M. (2015a). Networklike mesoporous $NiCo_2O_4$ grown on carbon cloth for high-performance pseudocapacitors. *J. Mat. Chem. A* 3, 16520–16527. doi: 10.1039/C5TA02876K

Gao, Z., Yang, W., Wang, J., Song, N., and Li, X. (2015b). Flexible all-solid-state hierarchical $NiCo_2O_4$/porous graphene paper asymmetric supercapacitors with an exceptional combination of electrochemical properties. *Nano Energy* 13, 306–317. doi: 10.1016/j.nanoen.2015.02.036

Guo, D., Luo, Y., Yu, X., Li, Q., and Wang, T. (2014). High performance $NiMoO_4$ nanowires supported on carbon cloth as advanced electrodes for symmetric supercapacitors. *Nano Energy* 8, 174–182. doi: 10.1016/j.nanoen.2014.06.002

Guo, M., Balamurugan, J., Thanh, T. D., Kim, N. H., and Lee, J. H. (2016). Facile fabrication of Co_2CuS_4 nanoparticle anchored N-doped graphene for high-performance asymmetric supercapacitors. *J. Mater. Chem. A* 4, 17560–17571. doi: 10.1039/C6TA07400F

He, S., and Chen, W. (2015). Application of biomass-derived flexible carbon cloth coated with MnO_2 nanosheets in supercapacitors. *J. Power Sources* 294, 150–158. doi: 10.1016/j.jpowsour.2015.06.051

He, Z., Jiang, Y., Li, Y., Zhu, J., Zhou, H., Meng, W., et al. (2018). Carbon layer-exfoliated, wettability-enhanced, SO_3H^- functionalized carbon paper: a superior positive electrode for vanadium redox flow battery. *Carbon* 127, 297–304. doi: 10.1016/j.carbon.2017.11.006

Hu, L., Pasta, M., Mantia, F. L., Cui, L., Jeong, S., Deshazer, H. D., et al. (2010). Stretchable, porous, and conductive energy textiles. *Nano Lett.* 10, 708–714. doi: 10.1021/nl903949m

Huang, Z., Zhang, Z., Qi, X., Ren, X., Xu, G., Wan, P., et al. (2016). Wall-like hierarchical metal oxide nanosheet arrays grown on carbon cloth for excellent supercapacitor electrodes. *Nanoscale* 8, 13273–13279. doi: 10.1039/C6NR04020A

Jayaraman, B., Chao, L., Peera, S. G., Kim, N.H., and Lee, J. H. (2017). High-energy asymmetric supercapacitors based on free-standing hierarchical Co-Mo-S nanosheets with enhanced cycling stability. *Nanoscale* 9, 13747–13759. doi: 10.1039/C7NR03763E

Jiang, H., Zhao, T., Ma, J., Yan, C., and Li, C. (2011). Ultrafine manganese dioxide nanowire network for high-performance supercapacitors. *Chem. Commun.* 47, 1264–1266. doi: 10.1039/C0CC04134C

Kaverlavani, S. K., Moosavifard, S. E., and Bakouei, A. (2017). Designing graphene-wrapped nanoporous $CuCo_2O_4$ hollow spheres electrodes

for high-performance asymmetric supercapacitors. *J. Mater. Chem. A* 5, 14301–14309. doi: 10.1039/C7TA03943C

Li, M. L., Xiao, K., Su, H., Li, N., Cai, Y. P., Liu, Z. Q., et al. (2018). $CuCo_2S_4$ nanosheets coupled with carbon nanotube heterostructures for highly efficient capacitive energy storage. *ChemElectroChem* 5, 2496–2502. doi: 10.1002/celc.201800329

Li, X.-X., Wang, X.-T., Xiao, K., Ouyang, T., Li, N., and Liu, Z.-Q. (2018). *In situ* formation of consubstantial $NiCo_2S_4$ nanorod arrays toward self-standing electrode for high activity supercapacitors and overall water splitting. *J. Power Sources* 402, 116–123. doi: 10.1016/j.jpowsour.2018.09.021

Liu, C., and Wu, X. (2018). $NiCo_2S_4$ nanotube arrays grown on flexible carbon fibers as battery-type electrodes for asymmetric supercapacitors. *Mater. Res. Bull.* 103, 55–62. doi: 10.1016/j.materresbull.2018.03.014

Liu, G., Wang, B., Liu, T., Wang, L., Luo, H., Gao, T., et al. (2018). 3D self-supported hierarchical core/shell structured $MnCo_2O_4$@CoS arrays for high-energy supercapacitors. *J. Mat. Chem. A* 6, 1822–1831. doi: 10.1039/C7TA10140F

Liu, R., Duay, J., and Lee, S. B. (2011). Heterogeneous nanostructured electrode materials for electrochemical energy storage. *Chem. Commun.* 47, 1384–1404. doi: 10.1039/C0CC03158E

Liu, S., Yin, Y., Hui, K. S., Hui, K. N., Lee, S. C., and Jun, S. C. (2018). High-performance flexible quasi-solid-state supercapacitors realized by molybdenum dioxide@nitrogen-doped carbon and copper cobalt sulfide tubular nanostructures. *Adv. Sci.* 5:1800733. doi: 10.1002/advs.201800733

Martti, K., Chan, C. K., Ma, J., Yi, C., and George, G. (2009). Printable thin film supercapacitors using single-walled carbon nanotubes. *Nano Lett.* 9, 1872–1876. doi: 10.1021/nl8038579

Moosavifard, S. E., Fani, S., and Rahmanian, M. (2016). Hierarchical $CuCo_2S_4$ hollow nanoneedle arrays as novel binder-free electrodes for high-performance asymmetric supercapacitors. *Chem. Commun.* 52, 4517–4520. doi: 10.1039/C6CC00215C

Padmanathan, N., and Selladurai, S. (2014). Controlled growth of spinel $NiCo_2O_4$ nanostructures on carbon cloth as a superior electrode for supercapacitors. *RSC Adv.* 4:8341. doi: 10.1039/c3ra46399k

Pu, J., Wang, T., Wang, H., Tong, Y., Lu, C., Kong, W., et al. (2014). Direct growth of $NiCo_2S_4$ nanotube arrays on nickel foam as high-performance binder-free electrodes for supercapacitors. *Chempluschem* 79, 577–583. doi: 10.1002/cplu.201300431

Qi, J. L., Wang, X., Lin, J. H., Zhang, F., Feng, J. C., and Fei, W.-D. (2015). A high-performance supercapacitor of vertically-oriented few-layered graphene with high-density defects. *Nanoscale* 7, 3675–3682. doi: 10.1039/C4NR07284G

Ratha, S. K.,Samantara, A., Singha, K. K., Sadashiv, A., Gangan, Chakraborty, B., et al. (2017). Urea-assisted room temperature stabilized metastable beta-$NiMoO_4$ experimental and theoretical insights into its unique bifunctional activity toward oxygen evolution and supercapacitor. *ACS Appl. Mater. Interfaces* 9, 9640–9653. doi: 10.1021/acsami.6b16250

Shang, Y., Xie, T., Ma, C., Su, L., Gai, Y., Liu, J., et al. (2018). Synthesis of hollow $ZnCo_2O_4$ microspheres with enhanced electrochemical performance for asymmetric supercapacitor. *Electrochim. Acta* 286, 103–113. doi: 10.1016/j.electacta.2018.08.025

Shen, L., Che, Q., Li, H., and Zhang, X. (2014). Mesoporous $NiCo_2O_4$ nanowire arrays grown on carbon textiles as binder-free flexible electrodes for energy storage. *Adv. Funct. Mater.* 24, 2630–2637. doi: 10.1002/adfm.201303138

Shinde, S. K., Ramesh, S., Bathula, C., Ghodake, G. S., Kim, D. Y., Jagadale, A. D., et al. (2019). Novel approach to synthesize $NiCo_2S_4$ composite for high-performance supercapacitor application with different molar ratio of Ni and Co. *Sci. Rep.* 9, 1–10. doi: 10.1038/s41598-019-50165-5

Sun, H., Xie, S., Li, Y., Jiang, Y., Sun, X., Wang, B., et al. (2016). Large-area supercapacitor textiles with novel hierarchical conducting structures. *Adv. Mater* 28, 8431–8438. doi: 10.1002/adma.201602987

Sun, W., Wang, Y., Wu, H., Wang, Z., Rooney, D., and Sun, K. (2017). 3D free-standing hierarchical $CuCo_2O_4$ nanowire cathodes for rechargeable lithium-oxygen batteries. *Chem. Commun.* 53, 8711–8714. doi: 10.1039/C7CC02621H

Tian, Z., Wang, X., Li, B., Li, H., and Wu, Y. (2018). High rate capability electrode constructed by anchoring $CuCo_2S_4$ on graphene aerogel skeleton toward quasi-solid-state supercapacitor. *Electrochem. Acta* 298, 321–329. doi: 10.1016/j.electacta.2018.12.103

Wan, H., Liu, J., Ruan, Y., Lv, L., Peng, L., Ji, X., et al. (2015). Hierarchical configuration of $NiCo_2S_4$ nanotube@Ni-Mn layered double hydroxide arrays/three-dimensional graphene sponge as electrode materials for high-capacitance supercapacitors. *ACS Appl. Mater. Interfaces* 7, 15840–15847. doi: 10.1021/acsami.5b03042

Wang, G., Wang, H., Lu, X., Ling, Y., Yu, M., Zhai, T., et al. (2014). Solid-state supercapacitor based on activated carbon cloths exhibits excellent rate capability. *Adv. Mater. 26*, 2676-2682, 2615. doi: 10.1002/adma.201304756

Wang, J., Liang, J., Wu, J., Xuan, C., Wu, Z., and Guo, X. (2018). Coordination effect of network NiO nanosheet and a carbon layer on the cathode side in constructing a high-performance lithium-sulfur battery. *J. Mater. Chem. A* 6, 6503–6509. doi: 10.1039/C8TA00270C

Wang, J.-G., Jin, D., Zhou, R., Shen, C., Xie, K., and Wei, B. (2016). One-step synthesis of $NiCo_2S_4$ ultrathin nanosheets on conductive substrates as advanced electrodes for high-efficient energy storage. *J. Power Sources* 306, 100–106. doi: 10.1016/j.jpowsour.2015.12.014

Wang, P., Zhang, Y., Yin, Y., Fan, L., Zhang, N., and Sun, K. (2018). *In Situ* synthesis of $CuCo_2S_4$@N/S-doped graphene composites with pseudocapacitive properties for high-performance lithium-ion batteries. *ACS Appl. Mater. Interfaces* 10, 11708–11714. doi: 10.1021/acsami.8b00632

Wang, Q., Wang, X., Liu, B., Yu, G., Hou, X., Chen, D., et al. (2013). $NiCo_2O_4$ nanowire arrays supported on Ni foam for high-performance flexible all-solid-state supercapacitors. *J. Mat. Chem. A* 1:2468. doi: 10.1039/c2ta01283a

Wang, Y., Yang, D., Zhou, T., Pan, J., Wei, T., and Sun, Y. (2017). Oriented $CuCo_2S_4$ nanograss arrays/Ni foam as an electrode for a high-performance all-solid-state supercapacitor. *Nanotechnology* 28:465402.

Xiao, F., Yang, S., Zhang, Z., Liu, H., Xiao, J., Wan, L., et al. (2015). Scalable synthesis of freestanding sandwich-structured graphene/polyaniline/graphene nanocomposite paper for flexible all-solid-state supercapacitor. *Sci. Rep.* 5:9359. doi: 10.1038/srep09359

Xing, L., Dong, Y., Hu, F., Wu, X., and Umar, A. (2018). Co_3O_4 nanowire@NiO nanosheet arrays for high performance asymmetric supercapacitors. *Dalton Trans.* 47, 5687–5694. doi: 10.1039/C8DT00750K

Xiong, X., Waller, G., Ding, D., Chen, D., Rainwater, B., Zhao, B., et al. (2015). Controlled synthesis of $NiCo_2S_4$ nanostructured arrays on carbon fiber paper for high-performance pseudocapacitors. *Nano Energy* 16, 71–80. doi: 10.1016/j.nanoen.2015.06.018

Yang, Y., Zhiwei, P., Gunuk, W., Gedeng, R., Xiujun, F., Lei, L., et al. (2014). Three-dimensional thin film for lithium-ion batteries and supercapacitors. *ACS Nano* 8, 7279–7287. doi: 10.1021/nn502341x

You, H., Zhang, L., Jiang, Y., Shao, T., Li, M., and Gong, J. (2018). Bubble-supported engineering of hierarchical $CuCo_2S_4$ hollow spheres for enhanced electrochemical performance. *J. Mater. Chem. A* 6, 5265–5270. doi: 10.1039/C7TA07890K

Yuan, C., Li, J., Hou, L., Zhang, X., Shen, L., and Lou, X. W. D. (2012). Ultrathin mesoporous $NiCo_2O_4$ nanosheets supported on Ni foam as advanced electrodes for supercapacitors. *Adv. Funct. Mater.* 22, 4592–4597. doi: 10.1002/adfm.201200994

Yuan, X., Tang, B., Sui, Y., Huang, S., Qi, J., Pu, Y., et al. (2018). $CuCo_2S_4$ nanotubes on carbon fiber papers for high-performance all-solid-state asymmetric supercapacitors. *J. Mat. Sci. Mat. Elect.* 29, 8636–8648. doi: 10.1007/s10854-018-8878-6

Zhang, G. Q., Wu, H. B., Hoster, H. E., Chan-Park, M. B., and Lou, X. W. (2012). Single-crystalline $NiCo_2O_4$ nanoneedle arrays grown on conductive

substrates as binder-free electrodes for high-performance supercapacitors. *Energy Environ. Sci.* 5:9453. doi: 10.1039/c2ee22572g

Zhang, Y., Hu, Z., An, Y., Guo, B., An, N., Liang, Y., et al. (2016). High-performance symmetric supercapacitor based on manganese oxyhydroxide nanosheets on carbon cloth as binder-free electrodes. *J. Power Sources* 311, 121–129. doi: 10.1016/j.jpowsour.2016.02.017

Zhu, J., Tang, S., Wu, J., Shi, X., Zhu, B., and Meng, X. (2017). Wearable high-performance supercapacitors based on silver-sputtered textiles with $FeCo_2S_4$-$NiCo_2S_4$ composite nanotube-built multitripod architectures as advanced flexible electrodes. *Adv. Ene. Mat.* 7:1601234. doi: 10.1002/aenm.201601234

Conflict of Interest: The authors declare that the research was conducted in the absence of any commercial or financial relationships that could be construed as a potential conflict of interest.

frontiers in Chemistry

ORIGINAL RESEARCH
published: 31 March 2020
doi: 10.3389/fchem.2020.00232

Ion Liquid Modified GO Filler to Improve the Performance of Polymer Electrolytes for Li Metal Batteries

Zhongliang Hu, Xiaojing Zhang, Jilei Liu and Yirong Zhu**

Department of Inorganic Nonmetallic Material, College of Metallurgy and Material Engineering, Hunan University of Technology, Zhuzhou, China

Polymer electrolytes for Li metal batteries (LMBs) should be modified to improve their ionic conductivity and stability against the lithium electrode. In this study, graphene oxide (GO) was modified by ion liquid (IL), and the IL modified GO (GO-IL) had been used as a filler for polyethylene oxide (PEO). The obtained solid polymer electrolyte (SPE) is of high ionic conductivity, low crystallinity and excellent stability against the lithium electrode. The PEO/GO-IL was characterized by various techniques, and its structure and performance were analyzed in detail. By addition of 1% GO-IL, the ionic conductivity of the PEO/GO-IL SPE reaches 1.8×10^{-5} S cm^{-1} at 25°C, which is 10 times higher than PEO (1.7×10^{-6} S cm^{-1}), and the current density for stable Li plating/stripping in PEO/GO-IL can be increased to 100 μA cm^{-2} at 60°C. $LiFePO_4$/Li cell (using PEO/GO-IL SPE) tests indicated that the initial discharge capacity can reach ∼145 mA h g^{-1} and capacity retention can maintain 88% even after 100 cycles at a rate of 0.1C and at 60°C. Our creative work could provide a useful method to develop SPEs with excellent performance, thus accelerating the commercial application of LMBs.

Keywords: graphene oxide, ionic liquid, polymer electrolyte, Li metal anode, Li metal batteries, rechargeable batteries

OPEN ACCESS

Edited by:
Hongshuai Hou,
Central South University, China

Reviewed by:
Jianmin Ma,
Hunan University, China
Yongchang Liu,
University of Science and Technology Beijing, China

****Correspondence:***
Zhongliang Hu
david10103@sina.com
Yirong Zhu
zhuyirong2004@163.com

Specialty section:
This article was submitted to Electrochemistry, a section of the journal Frontiers in Chemistry

Received: *09 January 2020*
Accepted: *10 March 2020*
Published: *31 March 2020*

Citation:
Hu Z, Zhang X, Liu J and Zhu Y (2020) Ion Liquid Modified GO Filler to Improve the Performance of Polymer Electrolytes for Li Metal Batteries. Front. Chem. 8:232. doi: 10.3389/fchem.2020.00232

INTRODUCTION

Li metal anodes have a high theoretical capacity (3,860 mA h g^{-1}) and extremely low redox potential (∼3.04 V vs. standard hydrogen electrodes), so Li metal batteries (LMBs) have been thought as promising secondary power sources for next generation of cutting-edge devices such as electric vehicles, autonomous aircrafts and smart grids (Zhang et al., 2016; Cheng et al., 2017; Wang et al., 2019; Cai et al., 2020; Wu et al., 2020; Zhu et al., 2020; Liao et al., in press). However, Li dendrite growth would happen during Li plating/stripping, probably resulting in short circuit and performance deterioration (Xu et al., 2014; Gao et al., 2019; Yan et al., 2020). In addition, liquid organic electrolytes commonly used in Li ion batteries are flammable and easy-leakage, and hence they would bring more severe safety problem when used in LMBs (Fu et al., 2016). Therefore, solid electrolytes have attracted increasing attention owing to their non-flammability, high safety, and good flexibility (Fan et al., 2018; Zhang et al., 2018).

At present mainly two kinds of solid electrolytes with quite different characteristics have been explored, which can be classified into inorganic electrolytes and polymer electrolytes (Fu et al., 2016). Although inorganic electrolytes have high ionic conductivities (∼10^{-3} S cm^{-1}) at room temperature, they are stiff and fragile, resulting in their poor processability and huge interfacial resistance between them and Li metal anodes. On the contrary, solid polymer electrolytes (SPEs) containing lithium salts can be easily processed into a membrane owing to their

properties of flexibility and stretchability. The commonly investigated polymers as SPEs include poly(ethylene oxide) (PEO) (Ito et al., 1987), polyacrylonitrile (PAN) (Slane and Salomon, 1995), poly(methyl methacrylate) (PMMA) (Appetecchi et al., 1995), and poly(vinylidene fluoride-co-hexafluoropropene) (PVDF-HFP) (Boudin et al., 1999). Among them, PEO has been considered as the most appropriate polymer to prepare SPEs because PEO molecule has rich lone pair electrons in its O atoms, thereby endowing it with strong coordination ability (Mohanta et al., 2018). Unfortunately, the ionic conductivity of PEO is relatively low ($\sim 10^{-6}$ S cm^{-1} at room temperature) (Zhang Q. et al., 2017), and obviously it can not reach the required value ($>10^{-5}$ S cm^{-1}) for SPEs of LMBs at ambient and moderate temperature.

Li ions can transport along with the PEO chains, so the ionic conductivity of PEO can be enhanced by various means of lowing its crystallization, including adding plasticizers (Zhang D. et al., 2017), mixing with other co-polymers (Puthirath et al., 2017) and introducing inorganic particles (Zhang J. et al., 2017). The investigation conducted by Cui's group demonstrated that the ion transport in polymers can be effectively ameliorated and their good physicochemical properties are well-maintained by incorporating inorganic fillers into polymers (Lin et al., 2015).

Recently, due to its unique structure and special characteristics, graphene oxide (GO) has been regarded as a promising active nanofiller to improve the performance of SPEs. GO has rich oxygen-containing groups (epoxy, hydroxyl, carboxyl, etc), and these groups can attract Li ions by acid-base interactions, consequently further promoting the dissociation of the lithium salt into free ions. Furthermore, GO can facilitate creating continuous ion channels within polymer electrolytes (Shim et al., 2014). The investigation conducted by Ardebili indicated that addition of 1% GO filler can induce 260% increase in tensile strength, and significantly improve thermo-mechanical stability of the polymer electrolyte (Yuan et al., 2014). However, GO tends to restack at high temperature owing to strong interlayer interaction, thus drastically expediting the capacity fading and greatly lowing the coulombic efficiencies (Yang et al., 2013).

On the other hand, recently the incorporating ionic liquids (ILs) into the polymer electrolytes becomes a popular approach to enhance their conductivity (Shin et al., 2005). Their beneficial properties such as non-volatility, non-flammability, high conductivity and high thermal stability can make them be excellent dopants for polymer electrolytes (Kar et al., 2019). We conceived that the filler of IL modified GO can well-improve the performance of PEO. Firstly, GO can coordinate with oxygen atoms in PEO chains, thereby effectively reducing PEO's crystallization and weakening the interactions between PEO and ions as well as those among various ions (Lee et al., 2015). Secondly, the cations in ILs can also lower the interaction between Li^+ and PEO, thus promoting the migration of more lithium ions (Long et al., 2016). Finally, ILs can inhibit the aggregation of GO sheets by reacting IL-NH_2 with GO (Lin et al., 2014). The IL modified filler is expected to not only sharply enhance Li ion migration number but also greatly increase mechanical strength of SPEs.

In this work, 1-(3-aminopropyl)-3-methylimi-dazolium bromide (IL-NH_2), and graphite oxide were used as precursors to synthesize IL-GO filler, which was adopted to modify PEO. The resultant PEO/GO-IL electrolyte possesses a high ionic conductivity at 25°C (1.8×10^{-5} S cm^{-1}), can effectively suppress the growth of Li dendrites on Li metal anode, and the LMBs with PEO/GO-IL electrolyte display good performance. The study could provide a methodlogy to solve the dilemma of LMBs by designing novel SPEs with excellent performance.

EXPERIMENTAL

Materials

Graphite powders (100 mesh, Nanjin XFNANo), $LiFePO_4$ cathode slurry (MTI Co.), Lithium bis(trifluoromethanesulfonyl) imide (LiTFSI, Alfa Aesar), Poly(ethylene oxide) (PEO, Mw=1000000, Sigma), 1-(3-aminopropyl)-3-methylimidazolium bromide (Lanzhou Institute of Chemical Physics), Potassium permanganate ($KMnO_4$, Sinopharm), Sulphuric acid (H_2SO_4, concentrated, Sinopharm), Hydrogen peroxide (H_2O_2, Sinopharm), Potassium hydroxide (KOH, Sinopharm), Sodium nitrate ($NaNO_3$, Sinopharm).

Preparation of Graphite Oxide

Graphite oxide was prepared following the Hummers' method (Hummers and Offeman, 1958). Briefly, 4 g of graphite powder and 4 g of $NaNO_3$ were put into a flask, and then 200 mL of concentrated H_2SO_4 was added into the flask at 0°C under vigorous stirring. Atfer 24 g of $KMnO_4$ was gradually added, the mixture solution was first stirred at 0°C for 2 h and then at 35°C for 2 h. Subsequently 120 mL of distilled water was slowly dropped to cause an increase in temperature to 98°C and this temperature was held for 25 min. After 200 mL of distilled water was again added into the mixture solution, 30 mL H_2O_2 was added, ensuring that the residual permanganate and manganese dioxide were reduced to manganese sulfate. Finally, the reaction product was repeatedly washed with distilled water, centrifuged until the supernatant solution became neutral. The graphite oxide was collected, dried and preserved in a desiccator.

Preparation of GO-IL Filler

IL-GO was synthesized by an epoxide ring-opening reaction between GO and IL-NH_2 (Yang et al., 2009; Lin et al., 2014). Firstly, 20 mg of IL-NH_2 and 20 mg of KOH were successively added into 20 mL of graphie oxide (0.5 mg/mL) solution, and the obtained turbid solution had been treated by ultrasonication until it became a homogeneous solution. Subsequently the mixture solution was transferred into a water bath to reflux at 80°C for 24 h. The solid reaction product was centrifuged and washed with ethanol to remove the unreacted IL-NH_2. Finally 10 g of the solid product and 50 mg of LiTFSI were successively added into 20 mL of distilled water, and the mixture solution reacted at 50°C for 8 h under stirring. After centrifugation and washing with distilled water, the final GO-IL filler was obtained.

FIGURE 1 | Sketch of the synthesis processes of GO-IL.

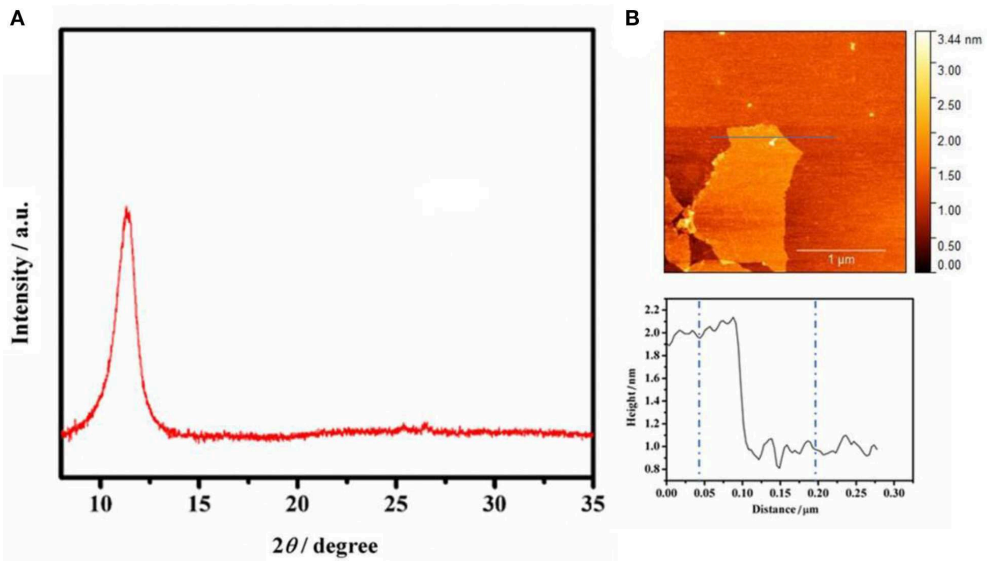

FIGURE 2 | (A) XRD spectrum of graphite oxide. **(B)** AFM image of GO (0.25 mg mL^{-1} GO water solution) on freshly cleaved mica surface through drop-casting, and height profiles along the line shown in AFM image.

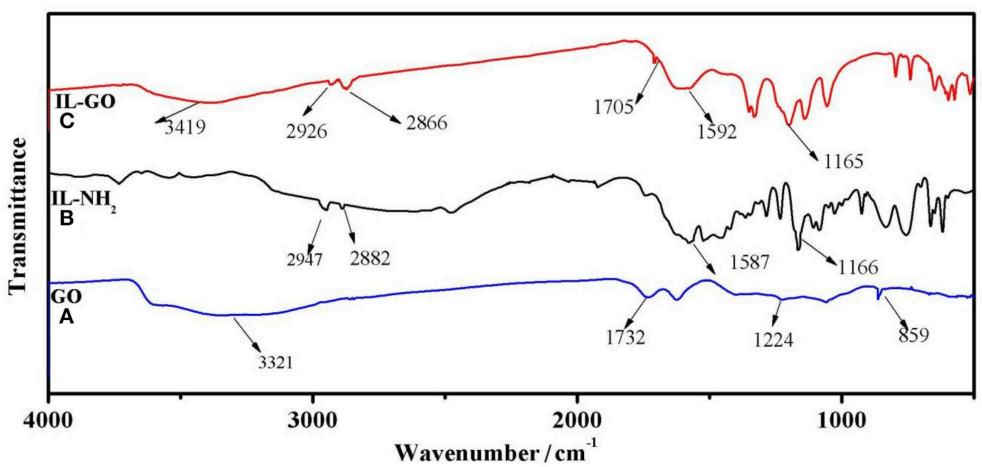

FIGURE 3 | FT-IR spectra of (A) GO,(B) IL-NH_2, and (C) GO-IL.

Preparation of Electrode

The cathode slurry (the weight ratio of $LiFePO_4$, Super P and PVDF is 8: 1: 1, NMP solvent) was evenly coated on an aluminum foil and then dried at room temperature to form a film. The loading mass of slurry in the film was ensured to be 2.5∼3.0 mg cm^{-2}, and as-obtained $LiFePO_4$ (LFP) material was used as a cathode of LMB for later electrochemical tests.

Preparation of PEO/GO-IL SPE

The PEO/GO-IL SPE was prepared by solvent casting technique. 10 mg of the IL-GO filler was added into 10 g of absolute acetonitrile. After 2 h ultrasonication and subsequent 12 stirring, the mixture solution become homogeneous. Then, 800 mg of PEO and LiTFSI (the molar ratio of EO and Li is 20: 1) were added into the above solution and stirred for 12 h, resulting in a uniform and brown slurry. The above slurry was spread on a round dish and heated at 45°C overnight to evaporate acetonitrile. Finally, the resultant membrane was peeled off from the dish and dried under vacuum at 45°C for 12 h to obtain the PEO/GO-IL SPE.

Materials Characterization and Electrochemical Measurements

The powder X-ray diffraction (XRD) patterns were collected using a Rigaku D/max-2500 with Cu Ka radiation. Atomic force microscope (AFM) images were obtained with a Digital Instruments nanoscope IIIa (Multimode,Veeco), operating in tapping mode. Fourier transform infrared (FTIR) spectra were recorded using a FTIR spectrometer (VERTEX 70v spectrometer, Bruker) in the wave number range of 400–4,000 cm^{-1}. Scanning electronic microscopy (SEM) images were performed using a Hitachi SU8020 electron microscopy.

The cells were assembled in an argon-filled glove box. The half-cells were charged and discharged with a constant current between 2.5 V and 4.0 V. The charge/discharge cycling studies were performed on a battery test system (LAND CT2001, China). Electrochemical impedance spectra tests (EIS) were carried out in the frequency ranging from 0.1 to 100 KHz in an electrochemical workstation (Autolab). Linear sweep voltammetry (LSV) was conducted in an electrochemical workstation (Interface-1000E, Gamry) using Li/composite/stainless steel cells and the sweeping voltage ranged from 2.6 to 6.0 V with a scanning rate of 10 mV s^{-1}.

RESULTS AND DISCUSSIONS

The sketch of the synthesis processes of GO-IL filler is shown in **Figure 1**. The graphite oxide prepared by Hummers' approach can act as a good precursor for GO and it can easily form GO solution under ultrasonication when dispersed in alkaline solution. The GO reacted with IL-NH_2 by epoxide ring-opening reaction between epoxy groups and -NH_2 groups in the precursors (Yang et al., 2009), and then reacted with LiTFSI by anion-exchange, forming the GO-IL filler.

Figure 2A shows the XRD pattern of graphite oxide, the precursor of GO. A peak at 12.2° can be clearly observed, which can be attributed to the (001) crystal plane of graphite oxide. The XRD characterization demonstrates that graphite oxide has a good crystalline structure. However, when it is dispersed in water or a base solution, it can easily dissociate

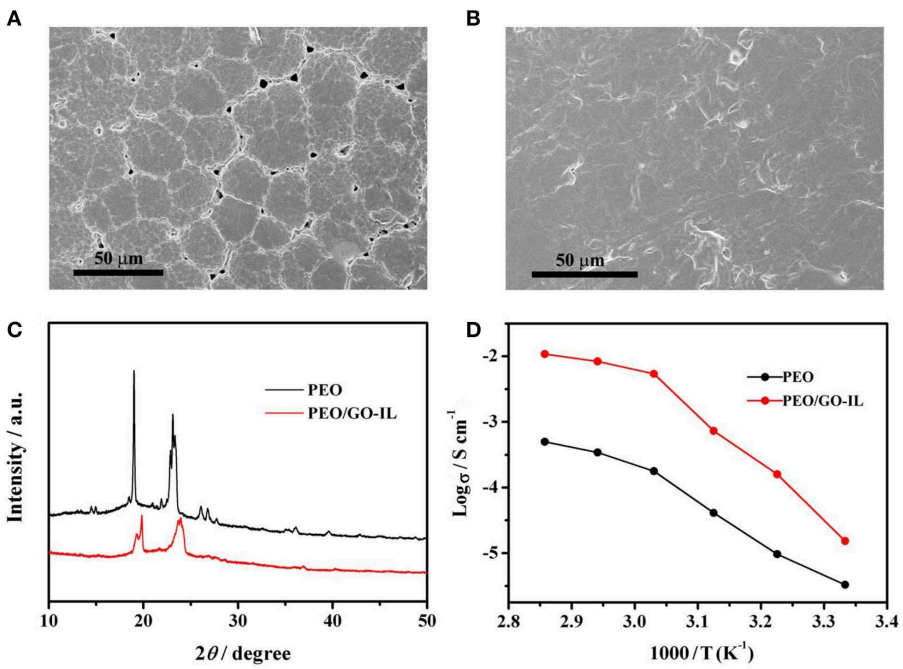

FIGURE 4 | SEM images of **(A)** PEO, **(B)** PEO/GO-IL, **(C)** XRD patterns of PEO and PEO/GO-IL, **(D)** ion conductivity vs. temperature of PEO and PEO/GO-IL.

into single layer of graphene oxide, which was proved by AFM characterization. **Figure 2B** presents the AFM image and corresponding height profile of GO, and the thickness of GO is ∼1.05 nm, indicating that GO is of single layer (Zhu et al., 2010).

Figure 3 displays the FTIR spectra of GO, IL-NH_2, and IL-GO. For GO, the peak at 1,732 cm^{-1} can be attributed to the stretching vibration of carboxyl groups of GO. The peak at ∼859 cm^{-1} comes from epoxy groups, and the broad peak centered at 3,321 cm^{-1} can be ascribed to the stretching vibration of hydroxyl groups of GO. For IL-NH_2, The peak at ∼2,947 and 2,882 cm^{-1} can be assigned to the stretching vibrations of methylene and methyl, respectively. The peak at 1,587 cm^{-1} is due to imidazolium cations. For GO-IL, several new peaks at 2,926, 2,866, and 1,592 cm^{-1} can be observed, inferring that GO has been successfully bonded with IL-NH_2. In addition, the peak belonging to epoxy groups of GO disappears in GO-IL, further demonstrating GO has successfully reacted with IL-NH_2.

The AFM image in **Figure 2** has fully proved that the GO is of single layer with a small size and the nanostructured GO-IL filler can be evenly distributed in PEO matrix. The SEM images of PEO and PEO/GO-IL are presented in **Figure 4**. Obviously, there exist very clear grain boundaries in PEO, and in some places the PEO crystals are evenly separated from each other by some pores, indicating that PEO has a good crystalline texture. In contrast, PEO/GO-IL does not exhibit any crystal boundaries (**Figure 4B**), and instead a smooth and uniform surface is presented, inferring that the crystallinity of PEO has been effectively lowed.

The XRD patterns of PEO and PEO/GO-IL are displayed in **Figure 4C**. Both samples have peaks at $2\theta = 19.2$ and 23.3°, which can be ascribed to the characteristic peaks of PEO. However, in contrast to PEO, PEO/GO-IL presents much broader and weaker peaks, indicating that the crystallinity of PEO in PEO/GO-IL has deteriorated greatly. Therefore, the XRD results further proved that the addition of GO/IL fillers can significantly low the crystallinity of PEO, in good agreement with SEM results.

The evolutions of the ionic conductivity with temperature were investigated and the results are presented in **Figure 4D**. Obviously, PEO/GO-IL (1.8×10^{-5} S cm^{-1}) has a much higher ionic conductivity than PEO (1.7×10^{-6} S cm^{-1}) at 25°C, and it can be due to two reasons. Firstly, the addition of GO-IL decreased the crystallinity of PEO, which was beneficial to enhancing the ionic conductivity. Secondly, GO can dissociate lithium salt into free ions and facilitate creating continuous ion channels within polymer electrolytes (Shim et al., 2014). The structure variation of PEO in the electrolyte can be attributed to the addition of GO-IL, in which IL-NH_2 has reacted with GO by covalent bonding, thereby inhibiting the agglomeration of GO sheets. In this study, GO-IL can promptly increase the ionic conductivity at a low content. Unfortunately, when the content of GO-IL is >1%, the ionic conductivity will no longer improve and even decrease slightly with further increasing the GO-IL content. Hence the optimal content of GO-IL is 1%. The utilization of IL to modify GO via chemical bonding can make good use of the advantages of GO and IL, and it has be proved to be a promising way to enhance the performance of SPEs.

LSV has been performed to investigate the electrochemical stability of the electrolytes at 30°C and the results are shown in **Figure 5A**. For PEO, the oxidation stage starts at 4.0 V. In contrast, for PEO/GO-IL, there is no oxidation current until 4.48 V. The wide electrochemical window of PEO/GO-IL is very related to its modified structure. In this study, the IL-NH_2 was grafted to GO sheets by covalent bonding, thus the agglomeration of GO can be effectively prevented and the role of GO in the composites can be well-performed. On the other hand, the addition of GO-IL filler further reduces the crystallinity of PEO. Suppression of lithium dendrite growth is crucial for the application of LMBs. Li/(PEO/GO-IL)/Li symmetrical cells were used to investigate the cycling performance and the tests were carried out under galvanostatic condition at 30°C. As shown in **Figure 5B**, the cells with PEO/GO-IL electrolyte can be well-charged/discharged sequentially for more than 300 h with negligible cell voltage loss at 0.1 mA cm^{-2}. In contrast, for PEO,

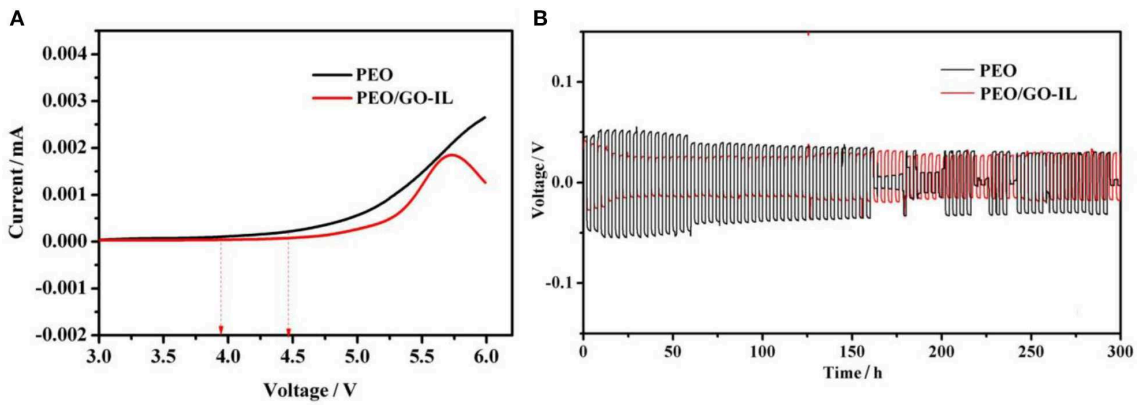

FIGURE 5 | (A) Linear sweep voltammetry scans for PEO and PEO/GO-IL. **(B)** Galvanostatic cycles under 0.1 mA cm^{-2} for PEO and PEO/GO-IL (each cycle time is 4 h).

the voltage is unstable and decreases fast, and a short circuit would happened upon charging/discharging within ∼150 h.

Solid-state LFP/Li cells with PEO and PEO/GO-IL electrolytes were assembled to verify their electrochemical performances and the electrochemical experiments were performed under different rates at 60°C. In cells using PEO/GO-IL electrolyte, polarization voltage increases slightly and the coulomb efficiency remains at 90% at 1C (**Figure 6A**), and the initial discharge capacity is 145 mA h g^{-1}at 0.1C. In contrast, the charge/discharge curves become very rough in cells using PEO electrolyte, indicating that the internal lithium ion channel in PEO collapsed quickly when charged/discharged at 1C (**Figure 6B**). The great performance difference between PEO/GO-IL and PEO indicates that GO can act as a role to support the lithium ion channel in polymer.

The cycle performance of the cells with PEO/GO-IL electrolyte is evaluated at a rate of 0.1C at 60°C (**Figure 6C**). The cell delivers the relatively smooth charge/discharge curves and high coulombic efficiency, inferring that electrode/electrolyte interface is very compatible during charge/discharge process. Moreover, the capacity retention is as high as 88% after 100 cycles (**Figure 6C**), manifesting considerable electrochemical stability of PEO/GO-IL electrolyte.

CONCLUSION

Novel PEO/GO-IL SPE has been developed by using GO-IL filler. The GO-IL filler is of high ionic conductivity, low crystallinity and excellent stability against the lithium anode electrode. By addition of 1% GO-IL filler, the crystallinity of PEO is significantly lowered and its performance is greatly improved. The ionic conductivity of PEO/GO-IL can reach 1.8 × 10^{-5} S cm^{-1} at 25°C and the electrolyte can effectively suppress the Li dendrite growth against Li anode electrode. Moreover, the current density for stable Li plating/stripping in the PEO/GO-IL solid electrolyte can increase to 0.1 mA cm^{-2}. The investigation in this study indicated that the performance of SPEs can be greatly improved by using the fillers with excellent properties and they can effectively solve the problems of the safety and performance deterioration of Li metal anode, thus accelerating the application of LMBs.

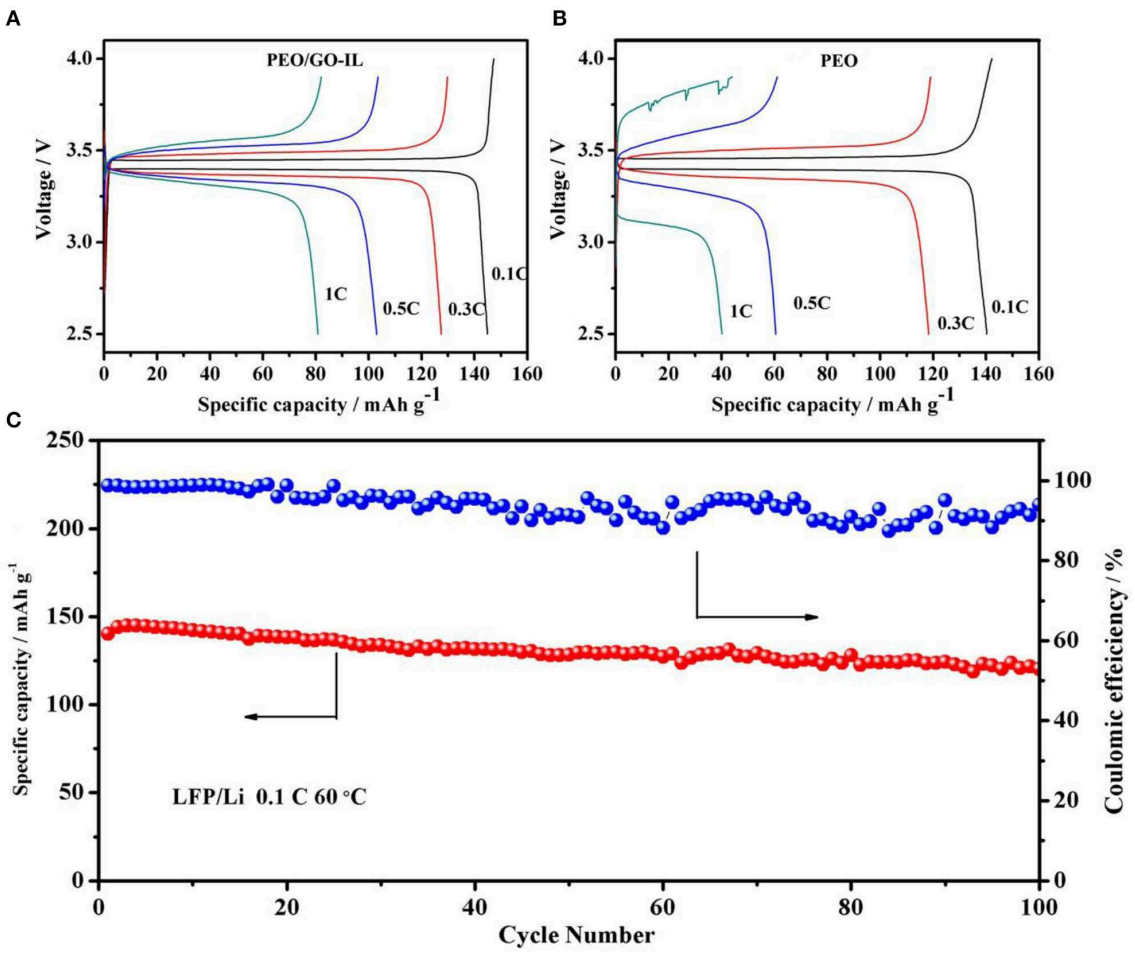

FIGURE 6 | (A) Charge/discharge curves of cells with PEO/GO-IL at the 0.1C, 0.3C, 0.5C, 1C. **(B)** Charge/discharge curves of cells with PEO at the 0.1C,0.3C, 0.5C, 1C. **(C)** Cycling performance of cells based on PEO/GO-IL electrolyte at 0.1C at 60°C.

DATA AVAILABILITY STATEMENT

The datasets generated for this study are available on request to the corresponding author.

AUTHOR CONTRIBUTIONS

ZH and XZ conducted the most experiments. JL and YZ performed the characterization and data analysis. All authors involved the analysis of experimental data and manuscript preparation.

ACKNOWLEDGMENTS

The authors would like to acknowledge the financial support from the National Natural Science Foundation of China (Nos. 21576075 and 21376069).

REFERENCES

Appetecchi, G. B., Croce, F., and Scrosati, B. (1995). Kinetics and stability of the lithium electrode in poly(methylmethacrylate)-based gel electrolytes. *Electrochim. Acta* 40, 991–997. doi: 10.1016/0013-4686(94)00345-2

Boudin, F., Andrieu, X., Jehoulet, C., and Olsen, I. (1999). Microporous PVDF gel for lithium-ion batteries. *J. Power Sourc.* 81–82, 804–807. doi: 10.1002/cssc.201802370

Cai, P., Zou, K., Deng, X., Wang, B., Zou, G., Hou, H., et al. (2020). Defect rich hierarchical porous carbon for high power supercapacitors. *Front. Chem.* 8:43. doi: 10.3389/fchem.2020.00043

Cheng, X., Zhang, R., Zhao, C., and Zhang, Q. (2017). Toward safe lithium metal anode in rechargeable batteries: a review. *Chem. Rev.* 117, 10403–10473. doi: 10.1021/acs.chemrev.7b00115

Fan, L., Wei, S., Li, S., Li, Q., and Lu, Y. (2018). Recent progress of the Solid-state electrolytes for high-energy metal-based batteries. *Adv. Energy Mater.* 8:1702657. doi: 10.1002/aenm.201702657

Fu, X., Yu, D., Zhou, J., Li, S., Gao, X., Han, Y., et al. (2016). Inorganic and organic hybrid solid electrolytes for lithium-ion batteries. *Crystengcomm* 18, 4236–4258. doi: 10.1039/C6CE00171H

Gao, Y., Yan, Z., Gray, J. L., He, X., Wang, D., Chen, T., et al. (2019). Polymer-inorganic solid-electrolyte interphase for stable lithium metal batteries under lean electrolyte conditions. *Nat. Mater.* 18, 384–389. doi: 10.1038/s41563-019-0305-8

Hummers, W. S., and Offeman, R. E. (1958). Preparation of graphite oxide. *J. Am. Chem. Soc.* 80, 1339–1339. doi: 10.1021/ja01539a017

Ito, Y., Kanehori, K., Miyauchi, K., and Kudo, T. (1987). Ionic conductivity of electrolytes formed from PEO-$LiCF_3SO_3$ complex low molecular weight poly(ethylene glycol). *J. Mater. Sci.* 22, 1845–1849. doi: 10.1007/BF01132415

Kar, M., Tutusaus, O., MacFarlane, D. R., and Mohtadi, R. (2019). Novel and versatile room temperature ionic liquids for energy storage. *Energy Environ. Sci.* 12, 566–571. doi: 10.1039/C8EE02437E

Lee, Y., Bae, J. W., Thi, T. T. H., Park, K. M., and Park, K. D. (2015). Injectable and mechanically robust 4-arm PPO-PEO/graphene oxide composite hydrogels for biomedical applications. *Chem. Commun.* 51, 8876–8879. doi: 10.1039/c5cc02511g

Liao, J., Ni, W., Wang, C., and Ma, J. (in press). Layer-structured niobium oxides and their analogues for advanced hybrid capacitors. *Chem. Eng. J.* 123489 doi: 10.1016/j.cej.2019.123489

Lin, B., Shang, H., Chu, F., Ren, Y., Yuan, N., and Jia, B., et. al. (2014). Ionic liquid-tethered graphene oxide/ionic liquid electrolytes for highly efficient dye sensitized solar cells. *Electrochim. Acta* 134, 209–214. doi: 10.1016/j.electacta.2014.03.064

Lin, D., Liu, W., Liu, Y., Lee, H. R., Hsu, P. C., and Liu, K., et. al. (2015). High ionic conductivity of composite solid polymer electrolyte via *in situ* synthesis of monodispersed SiO_2 nanospheres in poly (ethylene oxide). *Nano Lett.* 16, 459–465. doi: 10.1021/acs.nanolett.5b04117

Long, L., Wang, S., Xiao, M., and Meng, Y. (2016). Polymer electrolytes for lithium polymer batteries. *J. Mater. Chem. A* 4, 10038–10069. doi: 10.1039/C6TA02621D

Mohanta, J., Padhi, D. K., and Si, S. (2018). Li-ion conductivity in PEO-graphene oxide nanocomposite polymer electrolytes: a study on effect of the counter anion. *J. Appl. Polym. Sci.* 135:46336. doi: 10.1002/app.46336

Puthirath, A. B., Patra, S., Pal, S., Manoj, M., Balan, A. P., and Jayalekshmi, S. (2017). Transparent flexible lithium ion conducting solid polymer electrolyte. *J. Mater. Chem. A* 5, 11152–11162. doi: 10.1039/C7TA02182H

Shim, J., Kim, D. G., Kim, H. J., Lee, J. H., Baik, J. H., and Lee, J. C. (2014). Novel composite polymer electrolytes containing poly (ethylene glycol)-grafted graphene oxide for all-solid-state lithium-ion battery applications. *J. Mater. Chem. A* 2, 13873–13883. doi: 10.1039/C4TA02667E

Shin, J. H., Henderson, W. A., Appetecchi, G. B., Alessandrini, F., and Passerini, S. (2005). Recent developments in the ENEA lithium metal battery project. *Electrochim. Acta* 50, 3859–3865. doi: 10.1016/j.electacta.2005.02.049

Slane, S., and Salomon, M. (1995). Composite gel electrolyte for rechargeable lithium batteries. *J. Power Sourc.* 55, 7–10. doi: 10.1016/0378-7753(94)02148-V

Wang, X., Zhai, H., Qie, B., Cheng, Q., Li, A., Borovilas, J., et al. (2019). Rechargeable solid-state lithium metal batteries with vertically aligned ceramic nanoparticle/polymer composite electrolyte. *Nano Energy* 60, 205–212. doi: 10.1016/j.nanoen.2019.03.051

Wu, D., Zhang, W., Fang, Y., and Ma, J. (2020). Necklace-like carbon nanofibers encapsulating V3S4 microspheres for ultrafast and stable potassium-ion storage. *J. Mater. Chem. A* 8, 2618–2626. doi: 10.1039/C9TA12859J

Xu, W., Wang, J., Ding, F., Chen, X., Nasybulin, E., Zhang, Y., et al. (2014). Lithium metal anodes for rechargeable batteries. *Energy Environ. Sci.*7, 513–537. doi: 10.1039/C3EE40795K

Yan, Z., Yang, Q., Wang, Q., and Ma, J. (2020). Nitrogen doped porous carbon as excellent dual anodes for Li- and Na-ion batteries. *Chin. Chem. Lett.* 31, 583–588. doi: 10.1016/j.cclet.2019.11.002

Yang, H., Shan, C., Li, F., Han, D., Zhang, Q., and Niu, L. (2009). Covalent functionalization of polydisperse chemically-converted graphene sheets with amine-terminated ionic liquid. *Chem. Commun.* 134, 3880–3882. doi: 10.1039/b905085j

Yang, X., Zhang, F., Zhang, L., Zhang, T., Huang, Y., and Chen, Y. (2013). A high-performance graphene oxide-doped ion gel as gel polymer electrolyte for all-solid-state supercapacitor applications. *Adv. Funct. Mater.* 23, 3353–3360. doi: 10.1002/adfm.201203556

Yuan, M., Erdman, J., Tang, C., and Ardebili, H. (2014). High performance solid polymer electrolyte with graphene oxide nanosheets. *RSC Adv.* 4, 59637–59642. doi: 10.1039/C4RA07919A

Zhang, D., Zhang, L., Yang, K., Wang, H., Yu, C., Xu, D., et al. (2017). Superior blends solid polymer electrolyte with integrated hierarchical architectures for all-solid-state lithium-ion batteries. *ACS Appl. Mater. Interfaces* 9, 36886–36896. doi: 10.1021/acsami.7b12186

Zhang, J., Zang, X., Wen, H., Dong, T., Chai, J., and Li, Y., et. al. (2017). High-voltage and free-standing poly (propylene carbonate) /$Li_{6.75}La_3Zr_{1.75}Ta_{0.25}O_{12}$ composite solid electrolyte for wide temperature range and flexible solid lithium ion battery. *J. Mater. Chem. A* 5, 4940–4948. doi: 10.1039/C6TA10066J

Zhang, Q., Liu, K., Ding, F., and Liu, X. (2017). Recent advances in solid polymer electrolytes for lithium batteries. *Nano Res.* 10, 4139–4174. doi: 10.1007/s12274-017-1763-4

Zhang, R., Cheng, X., Zhao, C., Peng, H., Shi, J., Huang, J., et al. (2016). Conductive nanostructured scaffolds render low local current density to inhibit

lithium dendrite growth. *Adv. Mater.* 28, 2155–2162. doi: 10.1002/adma.201504117

Zhang, Z., Shao, Y., Lotsch, B., Hu, Y. S., Li, H., Janek, J., et al. (2018). New horizons for inorganic solid state ion conductors. *Energy Environ. Sci.* 11, 1945–1976. doi: 10.1039/C8EE01053F

Zhu, Y., Li, J., Yun, X., Zhao, G., Ge, P., Zou, G., et al. (2020). Graphitic carbon quantum dots modified nickel cobalt sulfide as cathode materials for alkaline aqueous batteries. *Nano Micro Lett.* 12:16. doi: 10.1007/s40820-019-0355-0

Zhu, Y., Murali, S., Cai, Y., Li, X., Suk, J. W., Potts, J. R., et al. (2010). Graphene and graphene oxide: synthesis, properties, and applications. *Adv. Mater.* 22, 3906–3924. doi: 10.1002/adma.201001068

Conflict of Interest: The authors declare that the research was conducted in the absence of any commercial or financial relationships that could be construed as a potential conflict of interest.

frontiers in Chemistry

ORIGINAL RESEARCH
published: 02 April 2020
doi: 10.3389/fchem.2020.00241

Sulfur-Doped and Bio-Resin-Derived Hard Carbon@rGO Composites as Sustainable Anodes for Lithium-Ion Batteries

Qinyuan Huang, Jinbo Hu, Shujing Wen, Xiang Zhang, Gonggang Liu, Shanshan Chang* and Yuan Liu*

College of Materials Science and Engineering, Central South University of Forestry and Technology, Changsha, China

Hard carbon derived from fossil products is widely used as anode material for lithium-ion batteries. However, there are still several main shortcomings such as high cost, and poor rate performance, which restrict its wide application. Then tremendous efforts have been devoted to developing biomaterials in the battery applications. Recently, especially agricultural and industrial by-products have attracted much attention due to the electric double-layer capacitors. Herein, we report the sulfur-doped hard carbon (SHC) materials from the tannin-furanic resins (TF-Resin) of the derived agricultural by-products, followed by enveloping rGO on its surface through the hexadecyl trimethyl ammonium bromide. SHC provides sites for the storage of lithium, while the rGO layers can offer a highly conductive matrix to achieve good contact between particles and promote the diffusion and transport of ions and electrons. As a result, the SHC@rGO shows excellent lithium storage performance with initial discharge capacity around 746 mAh g^{-1} at a current density of 50 mA g^{-1}, and shows superb stability keeping capacity retention of 91.9% after 200 cycles. Moreover, even at a high current density of 2,000 mAg^{-1}, SHC@rGO still delivers a specific capacity of 188 mAg^{-1}. These desired promising properties are active to the implement in the possible practical application.

Keywords: bio-resin-derived hard carbon, tannin–furanic resins, sulfur-doped, rGO, lithium-ion battery

OPEN ACCESS

Edited by:
Weijie Li,
University of Wollongong, Australia

Reviewed by:
Xing-Long Wu,
Northeast Normal University, China
Xianhong Rui,
Guangdong University of Technology, China

****Correspondence:***
Jinbo Hu
hjb1999@hotmail.com
Shanshan Chang
changelxy@hotmail.com

Specialty section:
This article was submitted to Electrochemistry, a section of the journal Frontiers in Chemistry

Received: *14 January 2020*
Accepted: *13 March 2020*
Published: *02 April 2020*

Citation:
Huang Q, Hu J, Wen S, Zhang X, Liu G, Chang S and Liu Y (2020) Sulfur-Doped and Bio-Resin-Derived Hard Carbon@rGO Composites as Sustainable Anodes for Lithium-Ion Batteries. Front. Chem. 8:241. doi: 10.3389/fchem.2020.00241

INTRODUCTION

Nowadays, lithium-ion batteries (LIBs) have been widely used with energy storage systems and portable digital devices because of their long cycle stability and high energy density (Etacheri et al., 2011; Wang et al., 2014). With a high demand for LIBs, the preparation of low-cost, environmentally friendly, and high-performance anode materials has been substantially researched in recent years (Liao et al., 2012). Various carbonaceous materials, such as graphitic carbon (Funabiki et al., 1999; Song et al., 2011), amorphous carbon (hard carbon) (Zhang et al., 2015, 2016, 2017) and soft carbon (Chae et al., 2014; Huang et al., 2018; Wang et al., 2018)), nanostructured carbon (graphene) (Raccichini et al., 2016; Ferguson et al., 2017), and carbon nanotubes (Liu et al., 2018; Yuan et al., 2018) have been widely investigated for their LIBs applications. Among all the anode materials for LIBs, graphitic material is the most commercially unitized because of its low cost, low potential (≈0.2 V vs. Li/Li^+), and optimal electrical conductivity (Han et al., 2015). Nevertheless, graphite anode is far from meeting the demands for high energy/power density as a result of its limited capacity (372 mAh g^{-1}) and inferior rate performance (Ge et al., 2018).

Alternatively, majority of researchers have taken notice of hard carbon because of its high specific capacity (740 mAh g^{-1}) (Fey and Chen, 2001). As well-known, the precursors for preparing hard carbon are mainly petrochemical raw materials, such as a phenolic resin (Liu et al., 1996), high molecular polymers (Piotrowska et al., 2013), asphalt (Larcher et al., 1999; Mochida et al., 2001), etc. These raw materials are non-renewable substances, and the price is volatile because of fluctuations in international oil prices. Also, carbonization of these products often causes environmental issue such as the release of formaldehyde or other toxic carcinogens. Fortunately, biomass is a rich and renewable potentially green material. A large amount of biomass with little or no economic value can be used as a cheap and effective source of carbon precursors to produce materials that are environmentally and economically of high added value. Most natural resources have been reported including bamboo chopsticks (Jiang et al., 2014), wood (Zhang et al., 2019), soybean (Xu et al., 2015), wheat flour (Lim et al., 2017), corn cob (Liu et al., 2016), peanut shells (Ding et al., 2015), cherry stones (Arrebola et al., 2010), silk (Hou et al., 2015), coconut oil (Gaddam et al., 2016), and mangrove (Liu et al., 2010), were widely used as electrodes for energy storage applications. However, the lower conductivity of hard carbon than that of graphitizable carbons is another defect, which results in poor rate performance. In order to tackle these problems, great efforts have been made to adjust the surface structure of hard carbon, such as the construction of hybrid anodes (Guo et al., 2008), thermal carbon coatings (Ohzawa et al., 2005; Lee et al., 2007), and vacuum and oxidation treatments (Fujimoto et al., 2010; Liu et al., 2010). Although these surface modification methods may improve the coulombic efficiency of hard carbon, their rate performance and cyclability are far from satisfactory. Moreover, the further modification optimization of hard carbon materials is quite meaningful for practical application.

Corn cob and wood bark are abandoned agricultural byproducts and are generally burnt, which not only leads to air pollution but also wastes resources. To date, tannin–furanic resins have received great attention because of tannin and furfural alcohol, which are extracted from wood bark and corn cob (Tondi and Pizzi, 2009; Meikleham and Pizzi, 2010). Thus far, the synthesis of resins without formaldehyde has been an attractive focus (Tondi et al., 2009; Li et al., 2013). With the development of technology, possible applications of the natural tannin–furanic resin were recently presented (Tondi et al., 2016). It is active that the epoxy novolac resin as the hard carbon source and coated rGO for LIBs have shown the outstanding stability and rate capability due to via constructing the conductive network (Zhang et al., 2015). Herein, we report the synthesis of SHC materials derived from the biomass TF-resin with the carbonization method and enveloped with the rGO on its surface through the hexadecyl trimethyl ammonium bromide. SHC provides active sites for the storage of lithium, whereas the rGO layer can offer a highly conductive matrix to achieve contact between particles and promote the diffusion and transport of ions and electrons. As a result, the SHC@rGO shows excellent lithium storage performance with an initial discharge capacity of approximately 746 mAh g^{-1} at a current density of 50 mA g^{-1}, and shows superb stability keeping a capacity retention of 91.9% after 200 cycles. Furthermore, even at a high current density of 2,000 mA g^{-1}, SHC@rGO still delivers specific capacity of 188 mA g^{-1}. This study compares the following petrochemical raw materials: (i) tannins and furfuryl alcohol raw materials, which have the advantages of environmental friendliness, low-cost, and renewability; (ii) the full biomass-derived hard carbon, which has optimal electrochemical properties; and (iii) it provides a reference for the application of the full biomass resin materials in energy storage materials.

EXPERIMENTAL SECTION

Tannin extract (60 g), furfuryl alcohol (180 g), 100 mL deionized water, and 8 mL p-toluene sulfonic acid (65 wt%), which acted as the hardener, were mixed at room temperature. The precursor was treated at 60°C for 1 h in a rotary evaporator and then cured in the drying box at 60, 100, and 150°C for 2, 1, and 24 h, respectively. The cured precursor was heated at 500°C for 1 h with 3°C min^{-1} and then ground to powders after cooling under the argon atmosphere. Finally, the sample was heated at 1,000°C under the argon flow for 1 h with a ramp rate of 10°C min^{-1} to prepare the SHC.

SHC (2 g) and GO (0.4 g) were sonicated for 0.5 h in 120 mL (20 wt%) ethanol to disperse GO sheets and SHC powders. The 0.1 g hexadecyl trimethyl ammonium bromide was dissolved in the resulting suspended liquid through magnetic stirring for 5 h at room temperature. The suspension was vacuum filtered, dried in air at 100°C, and then heated to 1,000°C under argon flow for 1 h at a heating rate of 10°C min^{-1} in a vacuum tube furnace to prepare the SHC@rGO.

MATERIAL CHARACTERIZATION

The morphologies of the sample were investigated with a scanning electron microscope (SEM). The morphology and microstructure of the SHC@rGO sample were characterized by transmission electron microscopy (TEM F20) and scanning transmission electron microscopy equipped with an energy dispersive spectrometer (EDS). The X-ray photoelectron spectra (XPS) were obtained by a Thermo Fisher Scientific ESCALAB 250Xi spectrometer. X-ray diffraction (XRD) was recorded on an XD-2X X-ray diffractometer with Cu–Kα radiation ($\lambda = 1.5406$ A, 30 KV, 20 mA) at the scan rate of 8°C min^{-1}. Raman spectra were collected using a Raman spectrometer (Alpha300-R) with 532 nm. Nitrogen adsorption and desorption isotherms were determined through nitrogen physisorption on a Micro Active for an ASAP 2460 analyzer. Comprehensive thermal analysis (TG-DSC) was obtained using a SETARAM AETSYS-24 comprehensive thermal analysis instrument, starting from room temperature to 1,200°C at a heating rate of 10°C min^{-1} under an N_2 gas atmosphere.

ELECTROCHEMICAL TESTING

Electrochemical measurements were performed using a 2016 coin-type battery using lithium metal as the anode. The working electrode was composed of active materials (SHC and SHC@rGO), the conductivity material (super P), and the binder (PVDF) in a weight ratio of 8:1:1 dissolved in N-methyl pyrrolidinone. The slurry was then spread evenly on the copper foil and dried in a vacuum oven at 120°C for 12 h. After drying, the electrode was cut into a disc with a diameter of 12 mm. The carrying mass of SHC@rGO on the anode is 0.55–0.66 mg·cm^{-2}. The mass loads of rGO in SHC@rGO is 0.11–0.13 mg·cm^{-2}. A solution of 1 M $LiPF_6$ in ethylene carbonate, diethyl carbonate, and dimethyl carbonate (1:1:1 by volume ratio) was used as an electrolyte, and a polypropylene film was used as a separator. The cycling and rate performance of SHC and SHC@rGO were tested on a land battery test system at 25°C. Cyclic voltammetry (CV) and electrochemical impedance spectroscopy (EIS) measurements were performed on an Ivium electrochemical workstation.

RESULTS AND DISCUSSION

Figure 1 shows the schematic illustration for the synthesis of SHC and SHC@rGO materials derived from the biomass TF-Resin. Firstly, TF-Resin precursors were obtained a simple solidify method (see Experimental Section for detail). Subsequently, the obtained TF-Resin precursors were calcinated under Ar atmosphere to prepare SHC. Finally, the SHC@rGO was obtained after enveloped with the rGO on its surface through the hexadecyl trimethyl ammonium bromide and assembled into a 2016 Coin battery.

Figure 2 shows the SEM images of SHC and SHC@rGO. It can be seen that SHC sample presents irregular morphology and the surface is non-porosity and glossy (**Figures 2A,B**). The SHC@rGO sample consists of irregular HC particles and lamellar reduced graphene oxide (rGO) with a wrinkled surface (**Figures 1C,D**). which is help construct the conductive network and guaranteeing fast electron conduction.

The microstructure of SHC@rGO composites was further studied by TEM and high-resolution TEM (HRTEM). As presented in **Figure 3A**, the SHC is partially wrapped by corrugated graphene nanosheets. It can be known that winkled rGO is well bonded to SHC particles due to van der Waals force between graphene sheets and SHC, which is beneficial to transport electrons and lithium ions. HRTEM image of SHC@rGO sample taken on the edges of rGO is shown in **Figure 3B**. The rGO consists of several stacked layers and its thickness is <5 nm. Graphene coating can effectively promote the transmission rate of electrons and ions and maintain the integrity of the conductive network, which contribute to improved electrochemical performance. The EDS mapping of SHC is shown in **Figure 3C**. The EDS element mapping of C and S confirms that the S element is evenly distributed throughout the hard carbon.

To determine the doping level and bonding configuration of S, we performed the XPS analyzation of SHC@rGO. As presented in **Figure 4A**, the predominant peaks at 165.0, 228.0, 285.0, 402.0, and 532.0 eV are assigned to S 2p, S 2s, C 1s, N 1s, and O 1s, respectively. The S 2p spectra (**Figure 4B**) showed three

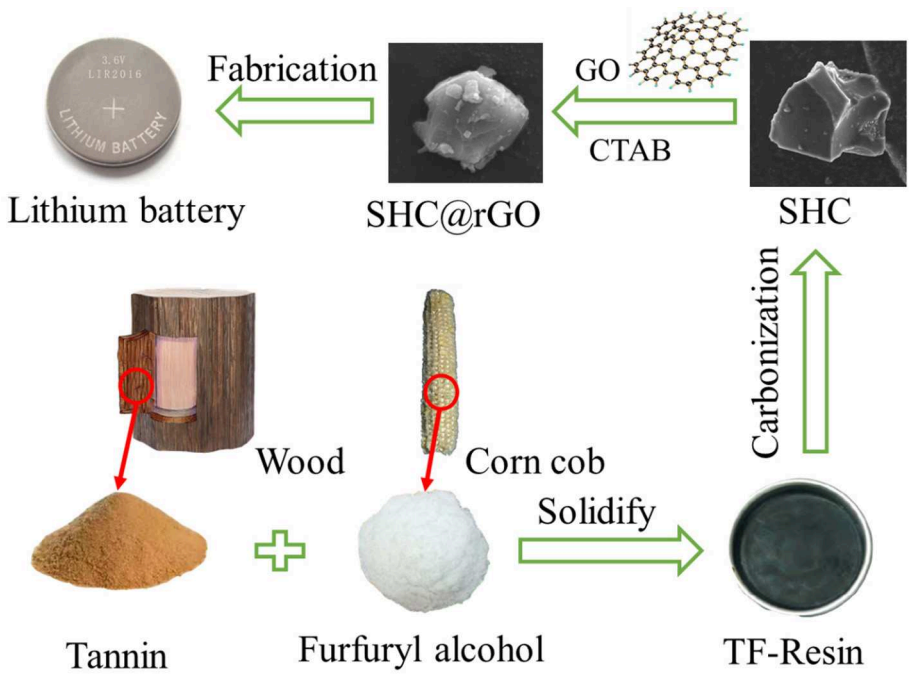

FIGURE 1 | Schematic illustration of the preparation of SHC and SHC@rGO.

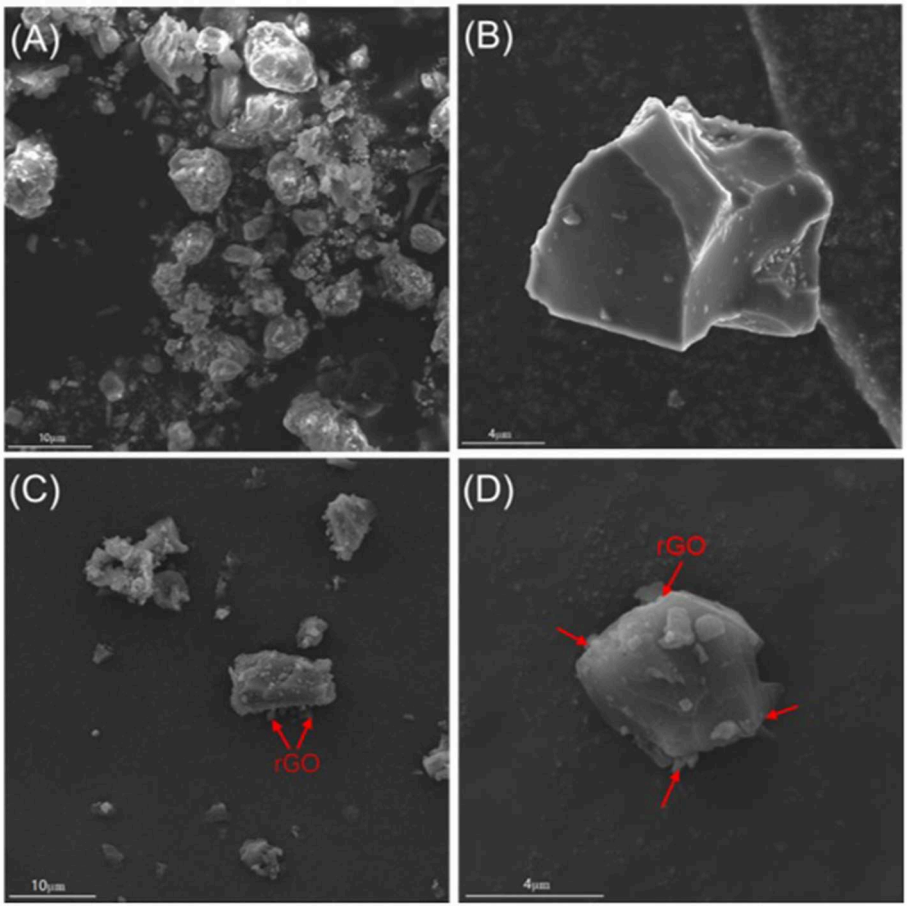

FIGURE 2 | SEM images of SHC **(A,B)** and SHC@rGO **(C,D)** composites.

peaks at 164.1, 165.3, and 169.2 eV. The former two peaks are assigned to the thiophene-S groups (–C–S–C–), and the third peak corresponds to the –C–SOx groups ($X = 2$–4) (Choi et al., 2011; Kiani et al., 2019). The XPS results indicate that the S atom has been chemically bonded to the SHC.

The XRD patterns of the SHC and SHC@rGO samples are presented in **Figure 5A**. It can be seen that the XRD patterns of SHC and SHC@rGO are both composed of wide diffraction peaks at 22°-26°and 44°-45° 2θ corresponding to (002) and (100), respectively, which are typical of carbonaceous materials with an amorphous-like structures (Inagaki et al., 2001). The D_{002} values of SHC and SHC@rGO are summarized in **Table S1**. SHC@rGO (0.351 nm) exhibits smaller average interlayer distance than SHC (0.380 nm), which is induced by rGO addition, because of the graphene oxide is reduced at high temperature to form a layered structure with decreasing interlayer spacing.

Figure 5B shows the Raman spectra of SHC and SHC@rGO. The characteristic peaks of the two samples are similar. The D-bands peak at about 1,340 cm^{-1} and the G-bands peak at about 1,590 cm^{-1}. Peak D-bands and G-bands represent sp^3 hybridization and sp^2 hybridization, respectively. The ratio of the integrated areas of the two peaks can manifest the degree of order of carbon materials. The I_D/I_G of the SHC and SHC@rGO is 1.13 and 1.08, respectively (Ferrari and Robertson, 2000). It was shown that the carbon atoms in sp^2 hybridization increased after graphene was added, the structure order and graphitization degree of the materials increased. This result was consistent with the results of XRD.

The nitrogen adsorption-desorption isotherm test (77 K) is an important tool of characterizing the specific surface area and pore volume of porous materials. **Figure 5C** shows the N_2 adsorption-desorption curve and the pore size distribution based on the BJH (Barrett-Joiner-Halenda) model of SHC and SHC@rGO. It can be seen that the N_2 adsorption isotherm of SHC and SHC@rGO belong to the III type isotherm. The calculated pore size distributions from the adsorption branches using the density functional theory (DFT) (inset of **Figure 5C**) model for SHC and SHC@rGO, suggest the characteristics of mesoporosity and microporosity. The specific surface area S_{BET} and pore volume data are listed in **Table S1**. It can be seen from the table that the BET specific surface area increases from 11.21 $m^2\ g^{-1}$ of SHC to 21.02 $m^2\ g^{-1}$ of SHC@rGO, the pores volume remains basically comparative. For these two samples, the mesopore volume accounts for more than 90% of the total pore volume.

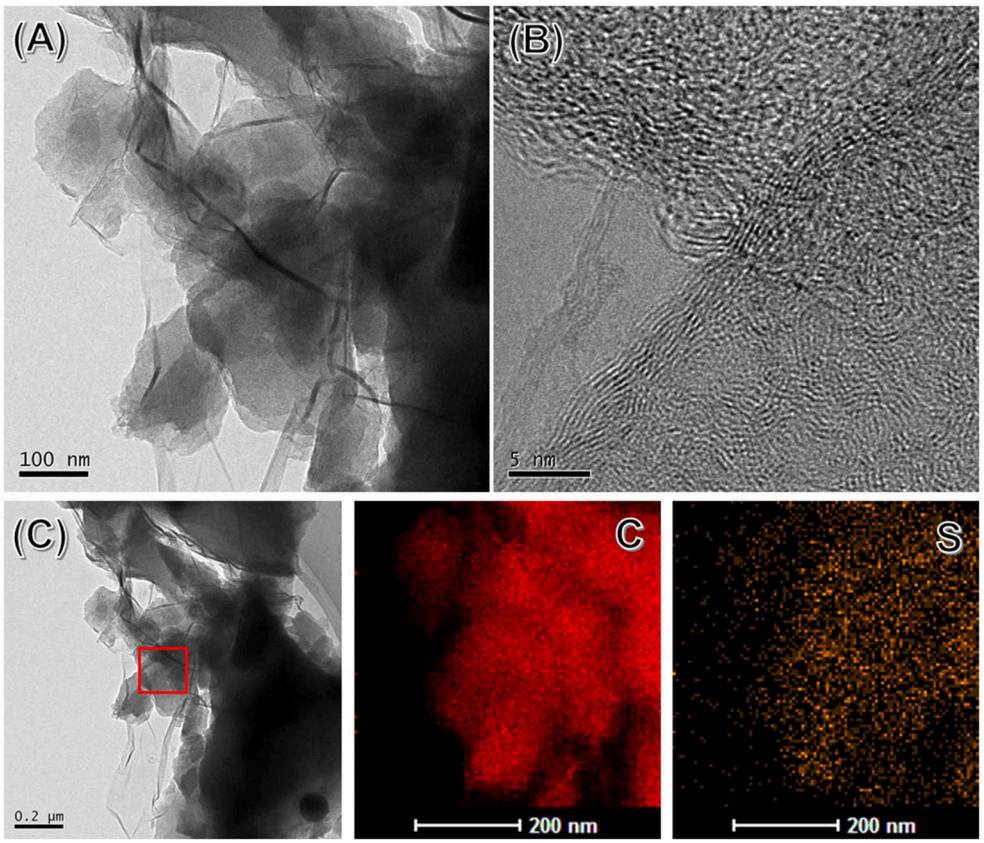

FIGURE 3 | A TEM **(A)**, HRTEM image **(B)**, and EDS elemental mapping **(C)** of SHC@rGO.

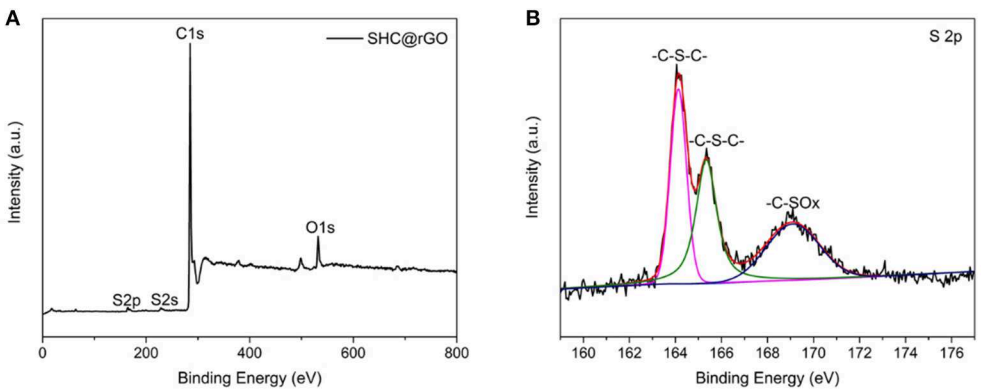

FIGURE 4 | XPS spectra of SHC@rGO composite and survey spectrum **(A)** and S 2p spectra **(B)**.

Figure 5D shows the TG/DSC curves for GO and SHC@rGO. The TG/DSC of pure SHC curve is not shown because it has no heat loss and exotherm. It can be seen that GO has a distinct exothermic peak at 190°C with significant thermal weight loss, which is caused by the volatilization of a large number of water molecules adsorbed on GO. The thermogravimetric curve of SHC@rGO showed a slight decrease due to the small proportion of GO in the SHC@rGO mixture. When the temperature increases from 254 to 388°C, the DSC curve of GO shows a taro peak with a slight thermal weight loss, indicating a moderate exothermic reaction, which is ascribed to escape of the large number of H atoms in GO. When the temperature is at 781 and 1,000°C, there is a significant endothermic peak with obvious thermal weight loss, the TG curve still slightly decreases, which is caused by the large amount of O atoms in GO continuously escaping at high temperature. It also shows that GO can be

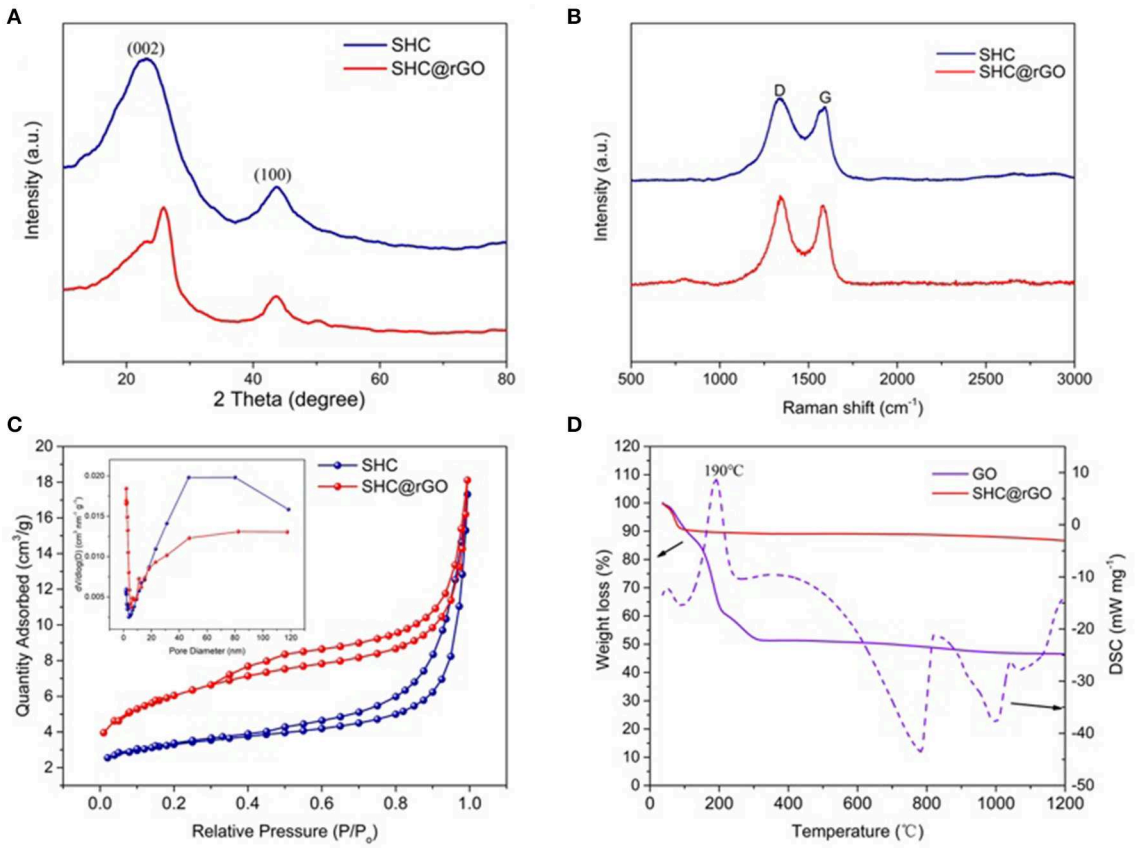

FIGURE 5 | (A) XRD patterns of SHC and SHC@rGO, **(B)** Raman spectra of SHC and SHC@rGO, **(C)** calculated pore size distribution and nitrogen adsorption isotherms (insert C) for SHC and SHC@rGO, and **(D)** TGA curve of the decomposition of SHC and SHC@rGO composite (Atmosphere: N_2, heating rate: 10°C min^{-1}).

reduced at high temperatures. When the pyrolysis temperature is 1,200°C, the residual mass ratio of GO and SHC@rGO are 46.6 and 86.6%, respectively. Assuming that the mass of SHC does not change, the theoretical calculation shows that the residual mass ratio of SHC@rGO is 88.3%, which is basically consistent with the experimental results. It indicates that at high temperatures, most of the H and O atoms in the GO are removed.

The electrochemical profiles of SHC and SHC@rGO are characterized by coin half cells, which are composed of SHC or SHC@rGO as an anode, a lithium metal as counter electrodes, electrolyte, and a Celgard 2,400 separator. **Figure 6** shows the initial two CV curves of SHC and SHC@rGO between 0 and 3 V at a sweep rate of 0.1 mV s^{-1}. It can be seen that cathode reduction peaks appear at 0.70–0.75 V in the first cycle and disappear in the subsequent cycle (**Figure 6B**). These reduction peaks suggest that the solid electrolyte interphase (SEI) layer being formed on the surface of the carbon materials during the first lithium intercalation (Buqa et al., 2006). Cathodic current peaks reach 0.21 V because of irreversible side reactions of lithium with absorbed species or surface functional groups, a weak reduction peak was found in two samples during the first discharge process but disappeared in the second cycle (**Figure 6B**), which contributes to part of capacity loss leading to large irreversible capacity (Zhang et al., 2014). In addition, the anodization peak potential of SHC@rGO was lower than that of pure SHC, indicating that when graphene is added to the hard carbon material, lithium-ions are more easily deintercalated in the hard carbon material during the charge/discharge process, which will be beneficial to improve its electrochemical performance. Therefore, the graphene in SHC@rGO not only provides electronic conductivity but also improves the reversible migration ability of lithium-ions in materials.

The initial galvanostatic discharge/charge curves of SHC and SHC@rGO at a current density of 50 mA g^{-1} are shown in **Figure 7A**. The charging and discharging processes correspond to the lithium removal and insertion process, respectively. It can be seen that the shape of the first charge-discharge curves of SHC and SHC@rGO is analogical, indicating that the lithium intercalation/deintercalation mechanism of SHC has not been changed after modification by wrapped GO. It can be seen that the specific capacity of SHC and SHC@rGO for the initial discharge capacities are 605 and 746 mAh g^{-1}, and the charge capacities are 321 and 486 mAh g^{-1}, respectively. The first irreversible specific capacity of SHC and SHC@rGO are 284 and 260 $mAhg^{-1}$, and the initial Coulomb efficiency (ICE) of SHC and SHC@rGO are 53.1% and 65.1%, respectively.

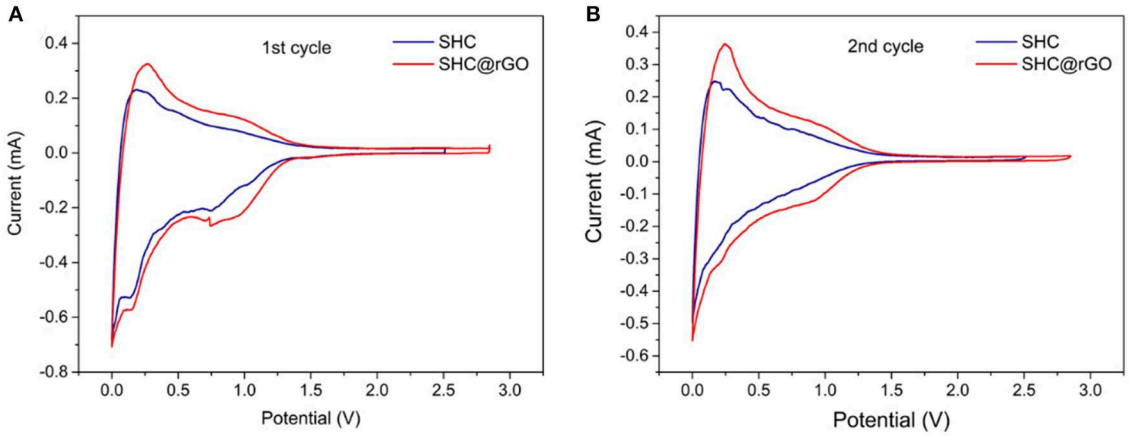

FIGURE 6 | (A) CV curves of SHC and SHC@rGO in the first cycle and **(B)** CV curves of SHC and SHC@rGO in the second cycle.

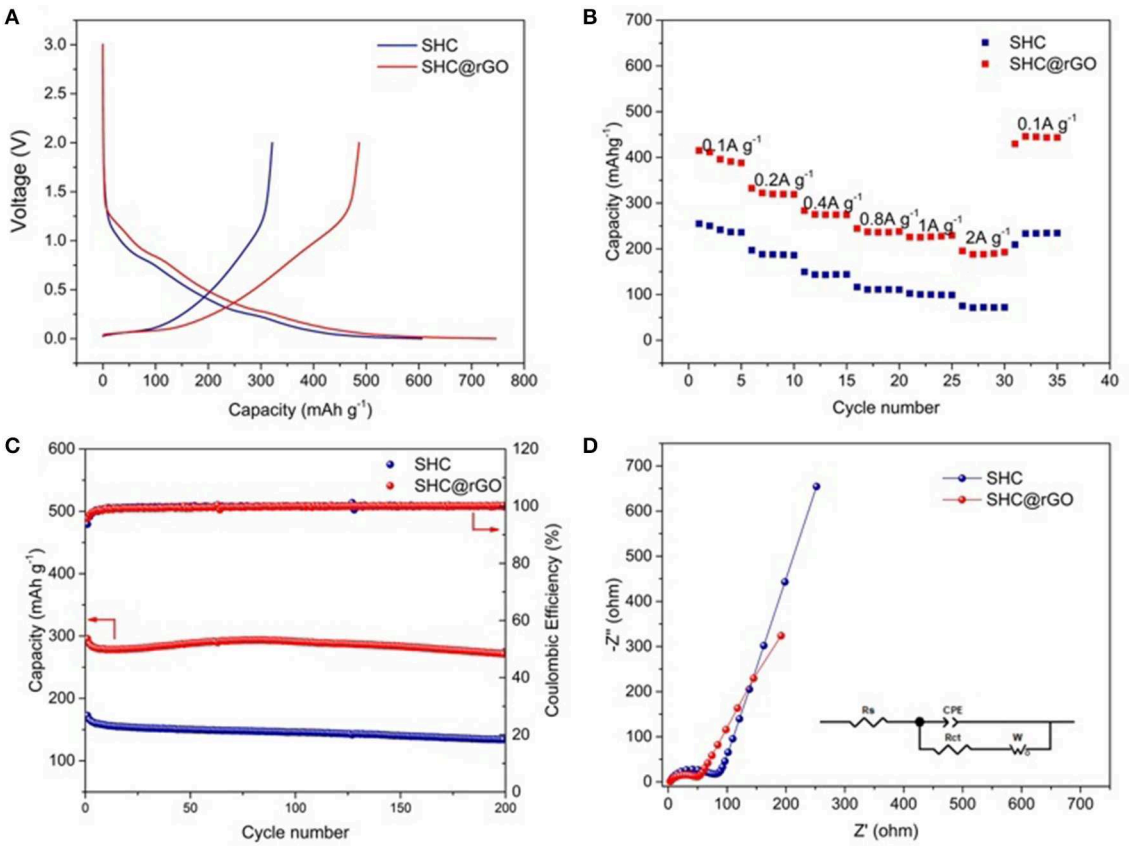

FIGURE 7 | (A) Charge and discharge curves of SHC and SHC@rGO at a current density of 50 mA g^{-1} between 0 and 3 V, **(B)** ratio performance patterns of SHC and SHC@rGO with the charge/discharge current densities in the 100–2000 mA g^{-1} range, **(C)** cycle stability curves of SHC and SHC@rGO at 400 mA g^{-1}, and **(D)** Nyquist plots of SHC and SHC@rGO at the potential of 0.1 V vs. Li/Li^+ over the frequency range from 100 kHz to 0.01 Hz.

Unfortunately, the pure SHC electrodes show low ICE at the same current density, similar to previous reports about hard carbon material (Zhang et al., 2015). The battery of the low ICE is probably attributed to the following two major reasons. Primarily, the decomposition of electrolyte during the initial charge/discharge process has significantly displayed in the battery formulation of SHC derived the resin. Secondly, the formation of an irreversible solid electrolyte interface (SEI) on the surface of

anode could also lead to a low ICE (Liu et al., 2016), consistent with the CV results. Nevertheless, it is active that the ICE can be improved from 53.1 to 65.1% owing to the presence of rGO in SHC@rGO. The ICE improvement of SHC@rGO was ascribed to the crucial rGO, which can construct the conductive network and promote the transport of Li^+ ions in the electrolyte. Therefore, the SHC would be progressively modified in the prospective battery.

The rate performance of SHC and SHC@rGO prepared at different current densities are shown in **Figure 7B**. The rate performance of SHC@rGO is superior to that of SHC under different current densities from 0.1 A g^{-1} (410 mAh g^{-1}) to 2 A g^{-1} (188 mAh g^{-1}). When the current rate decreased from 2 A g^{-1} to 0.1 A g^{-1}after the 25th rate cycle corresponding to discharge capacity of 444.7 mAh g^{-1}. As for SHC, a much lower rate capacity was delivered at varied current densities. Both the capacity of SHC and SHC@rGO increased when the current density returned to 0.1 A g^{-1}, this phenomenon can be confirmed by the electrolyte infiltration and electrode material activation during different current charge/discharge processes. **Table S2** lists TF-resin prepared in this work vs. other hard carbons derived from epoxy novolac resin (Zhang et al., 2014), pitch (Kim et al., 2016), and polyphenylene sulfide (Luo et al., 2018), which demonstrates that the SHC derived from TF-resin deliver better discharge capacity and rate performance.

Cycle stability of SHC and SHC@rGO was estimated at the current density of 400 mA g^{-1} (**Figure 7C**). It can be inferred that from this cyclic performance, SHC and SHC@rGO delivered 134.1 and 271.8 mAh g^{-1} capacity after 200 cycles with the Coulombic efficiency near 100%, keeping capacity retention of 77.7 and 91.9%, respectively. Therefore, the SHC@rGO hybrid anode shows obviously higher cycling stability and reversible capacity, which are S-doping hard carbon provides active sites for the storage of lithium, while the rGO layers offer a highly conductive matrix and high contact area can lead to effective contact with the electrolyte into the electrode and quickly transport ions into the deeper parts of the SHC@rGO particles and graphite layer. A comparison of hard carbon prepared in this work with other biomass-derived carbons is shown in **Table S3**, which demonstrates that the prepared hard carbon delivers better rate capabilities and cycling performance.

The EIS measurements of SHC and SHC@rGO were tested (**Figure 5D**). The plots consist of a semicircle in the high-frequency region and a straight line in the low-frequency region. the straight line and the semicircle corresponding to Warburg diffusion impedance (W) and charge transfer resistance (Rct), respectively (Pan et al., 2018). Based on equivalent electric circuit, the Rct of SHC and SHC@rGO are 65.34 and 50.49Ω, respectively. The lower Rct of SHC@rGO was attributed to the presence of conductive rGO able to constructing the conductive network and facilitate the transport of Li^+ ions, resulting in a superior electrochemical performance.

CONCLUSION

In summary, biomass TF resin-derived SHC and SHC@rGO composite material was prepared as the anode material for lithium-ion battery. It is demonstrated that the rGO networks are enveloped on SHC constructing the desired microstructure. Compared with the biomass-derived pure SHC, the SHC@rGO composites show enhanced conductivity offered by rGO networks and large Li ion storage sites supported by SHC. As a consequence, SHC@rGO composite exhibits a superior electrochemical rate performance and reversible capacity. Based on this study, a new biomass derived hard carbon composites with superior electrochemical properties is reported, which is promising for low-cost and eco-friendly anode material of LIBs.

DATA AVAILABILITY STATEMENT

All datasets generated for this study are included in the article/**Supplementary Material**.

AUTHOR CONTRIBUTIONS

JH, XZ, SC, and YL: conceived and designed the experiments. QH, SW, and JH: performed the experiment. SC, JH, and XZ: supervised the work. QH, JH, and YL: wrote the paper. JH, GL, and XZ: revised the paper. JH and YL: contributed equally. All authors reviewed and approved the final manuscript.

FUNDING

The research was funded by the National Key Research and Development Program of China (2017YFB1303901; to JH) and the Scientific research project of Hunan Provincial Department of Education (19A505; to JH).

ACKNOWLEDGMENTS

The authors thank Priof. Xiaobo JI from Central South University in China for the analysis.

SUPPLEMENTARY MATERIAL

The Supplementary Material for this article can be found online at: https://www.frontiersin.org/articles/10.3389/fchem.2020.00241/full#supplementary-material

REFERENCES

Arrebola, J. C., Caballero, A., Hernán, L., Morales, J., Olivares-Marín, M, and Gómez-Serrano, V. (2010). Improving the performance of biomass-derived carbons in li-ion batteries by controlling the lithium insertion process. *J. Electrochem. Soc.* 157, A791–A797. doi: 10.1149/1.3425728

Buqa, H., Würsig, A., Vetter, J., Spahr, M. E., Krumeich, F., and Novák, P. (2006). SEI film formation on highly crystalline graphitic materials in lithium-ion batteries. *J. Power Sour.* 153, 385–390. doi: 10.1016/j.jpowsour.2005.05.036

Chae, J. E., Annaka, K., Hong, K., Lee, S.-I., Munakata, H., Kim, S.-S., et al. (2014). Electrochemical characterization of phosphorous-doped soft carbon using single particle for lithium battery anode. *Electrochim. Acta* 130, 60–65. doi: 10.1016/j.electacta.2014.03.009

Choi, C. H., Park, S. H., and Woo, S. I. (2011). Heteroatom doped carbons prepared by the pyrolysis of bio-derived amino acids as highly active catalysts for oxygen electro-reduction reactions. *Green Chem.* 13, 406–412. doi: 10.1039/C0GC00384K

Ding, J., Wang, H. L., Li, Z., Cui, K., Karpuzov, D., Tan, X. H., et al. (2015). Peanut shell hybrid sodium ion capacitor with extreme energy-power rivals lithium ion capacitors. *Energy Environ. Sci.* 8, 941–955. doi: 10.1039/C4EE02986K

Etacheri, V., Marom, R., Elazari, R., Salitra, G., and Aurbach, D. (2011). Challenges in the development of advanced Li-ion batteries: a review. *Energy Environ. Sci.* 4, 3243–3262. doi: 10.1039/c1ee01598b

Ferguson, D., Searles, D. J., and Hankel, M. (2017). Biphenylene and phagraphene as lithium ion battery anode materials. *ACS Appl. Mater. Interfaces* 9, 20577–20584. doi: 10.1021/acsami.7b04170

Ferrari, A. C., and Robertson, J. (2000). Interpretation of Raman spectra of disordered and amorphous carbon. *Phys. Rev. B* 61, 14095–14107. doi: 10.1103/PhysRevB.61.14095

Fey, T. K., and Chen, C. L. (2001). High-capacity carbons for lithium-ion batteries prepared from rice husk. *J. Power Sour.* 97, 47–51. doi: 10.1016/S0378-7753(01)00504-3

Fujimoto, H., Tokumitsu, K., Mabuchi, A., Chinnasamy, N., and Kasuh, T. (2010). The anode performance of the hard carbon for the lithium ion battery derived from the oxygen-containing aromatic precursors. *J. Power Sour.* 195, 7452–7456. doi: 10.1016/j.jpowsour.2010.05.041

Funabiki, A., Inaba, M., Abe, T., and Ogumi, Z. (1999). Nucleation and phase-boundary movement upon stage transformation in lithium–graphite intercalation compounds. *Electrochim. Acta* 45, 865–871. doi: 10.1016/S0013-4686(99)00290-X

Gaddam, R. R., Yang, D., Narayan, R., Raju, K., Kumar, N. A., and Zhao, X. S. (2016). Biomass derived carbon nanoparticle as anodes for high performance sodium and lithium ion batteries. *Nano Energy* 26, 346–352. doi: 10.1016/j.nanoen.2016.05.047

Ge, C., Fan, Z., Zhang, J., Qiao, Y., Wang, J., and Ling, L. (2018). Novel hard carbon/graphite composites synthesized by a facile in situ anchoring method as high-performance anodes for lithium-ion batteries. *RSC Adv.* 8, 34682–34689. doi: 10.1039/C8RA07170E

Guo, B., Shu, J., Tang, K., Bai, Y., Wang, Z., and Chen, L. (2008). Nano-Sn/hard carbon composite anode material with high-initial coulombic efficiency. *J. Power Sour.* 177, 205–210. doi: 10.1016/j.jpowsour.2007.11.003

Han, Y.-J., Kim, J., Yeo, J.-S., An, J. C., Hong, I.-P., Nakabayashi, K., et al. (2015). Coating of graphite anode with coal tar pitch as an effective precursor for enhancing the rate performance in Li-ion batteries: effects of composition and softening points of coal tar pitch. *Carbon* 94, 432–438. doi: 10.1016/j.carbon.2015.07.030

Hou, J., Cao, C., Idrees, F., and Ma, X. (2015). Hierarchical porous nitrogen-doped carbon nanosheets derived from silk for ultrahigh-capacity battery anodes and supercapacitors. *ACS Nano* 9, 2556–2564. doi: 10.1021/nn506394r

Huang, F., Zhao, Q., Yang, J., Zhang, H., Huo, W., and Xu, F. (2018). Spherical mesophase soft carbon materials with micro-nano composite structure and their applications in lithium-ion batteries. *Energy Sour. Part A: Recovery Utilization Environ. Effects* 40, 1–6. doi: 10.1080/15567036.2018.1486897

Inagaki, M., Fujita, K., Takeuchi, Y., Oshida, K., Iwata, H., and Konno, H. (2001). Formation of graphite crystals at 1000–1200°C from mixtures of vinyl polymers with metal oxides. *Carbon* 39, 921–929. doi: 10.1016/S0008-6223(00)00210-4

Jiang, J., Zhu, J. H., Ai, W., Fan, Z. X., Shen, X. N., and Zou, C. J. (2014). Evolution of disposable bamboo chopsticks into uniform carbon fibers: a smart strategy to fabricate sustainable anodes for Li-ion batteries. *Energy Environ. Sci.* 7, 2670–2679. doi: 10.1039/C4EE00602J

Kiani, M., Zhang, J., Chen, J., Luo, Y., Chen, Y., Fan, J., et al. (2019). Facile synthesis of magnesium ferrite nanoparticles supported on nitrogen and sulfur co-doped carbon black as an efficient electrocatalyst for oxygen reduction reaction. *J. Nanoparticle Res.* 21. doi: 10.1007/s11051-019-4539-9

Kim, B.-H., Kim, J.-H., Kim, J.-G., Bae, M.-J., Im, J. S., Lee, C. W., et al. (2016). Electrochemical and structural properties of lithium battery anode materials by using a molecular weight controlled pitch derived from petroleum residue. *J. Ind. Eng. Chem.* 41, 1–9. doi: 10.1016/j.jiec.2016.07.006

Larcher, D., Mudalige, C., Gharghouri, M., and Dahn, J. R. (1999). Electrochemical insertion of Li and irreversibility in disordered carbons prepared from oxygen and sulfur-containing pitches. *Electrochim. Acta* 44, 4069–4072. doi: 10.1016/S0013-4686(99)00167-X

Lee, J.-H., Lee, H.-Y., Oh, S.-M., Lee, S.-J., Lee, K.-Y., and Lee, S.-M. (2007). Effect of carbon coating on electrochemical performance of hard carbons as anode materials for lithium-ion batteries. *J. Power Sour.* 166, 250–254. doi: 10.1016/j.jpowsour.2006.12.078

Li, X., Nicollin, A., Pizzi, A., Zhou, X., Sauget, A., and Delmotte, L. (2013). Natural tannin–furanic thermosetting moulding plastics. *RSC Adv.* 3, 17732–17740. doi: 10.1039/c3ra43095b

Liao, X., Ji, Y., and Gao, L. (2012). Electrochemical study on lithium iron phosphate/hard carbon lithium-ion batteries. *J. Solid State Electrochem.* 16, 423–428. doi: 10.1007/s10008-011-1387-7

Lim, D. G., Kim, K., Razdan, M., Diaz, R., Osswald, S., and Pol, V. G. (2017). Lithium storage in structurally tunable carbon anode derived from sustainable source. *Carbon* 121, 134–142. doi: 10.1016/j.carbon.2017.05.079

Liu, D.-S., Liu, D.-H., Hou, B.-H., Wang, Y.-Y., Guo, J.-Z., Ning, Q.-L., et al. (2018). 1D porous MnO@N-doped carbon nanotubes with improved Li-storage properties as advanced anode material for lithium-ion batteries. *Electrochim. Acta* 264, 292–300. doi: 10.1016/j.electacta.2018.01.129

Liu, P., Li, Y. M., Hu, Y. S., Li, H., Chen, L. Q., and Huang, X. J. (2016). A waste biomass derived hard carbon as a high-performance anode material for sodium-ion batteries. *J. Mater. Chem. A* 4, 13046–13052. doi: 10.1039/C6TA04877C

Liu, T., Luo, R., Qiao, W., Yoon, S.-H., and Mochida, I. (2010). Microstructure of carbon derived from mangrove charcoal and its application in Li-ion batteries. *Electrochim. Acta* 55, 1696–1700. doi: 10.1016/j.electacta.2009.10.051

Liu, Y., Xue, J. S., Zheng, T., and Dahn, J. R. (1996). Mechanism of lithium insertion in hard carbons prepared by pyrolysis of epoxy resins. *Carbon* 34, 193–200. doi: 10.1016/0008-6223(96)00177-7

Luo, D., Chen, M., Xu, J., Yin, X., Wu, J., Chen, S., et al. (2018). Polyphenylene sulfide nonwoven-based composite separator with superior heat-resistance and flame retardancy for high power lithium ion battery. *Compos. Sci. Technol.* 157, 119–125. doi: 10.1016/j.compscitech.2018.01.023

Meikleham, N. E., and Pizzi, A. (2010). Acid- and alkali-catalyzed tannin-based rigid foams. *J. Appl. Polym. Sci.* 53, 1547–1556. doi: 10.1002/app.1994.070531117

Mochida, I., Ku, C.-H., and Korai, Y. (2001). Anodic performance and insertion mechanism of hard carbons prepared from synthetic isotropic pitches. *Carbon* 39, 399–410. doi: 10.1016/S0008-6223(00)00137-8

Ohzawa, Y., Yamanaka, Y., Naga, K., and Nakajima, T. (2005). Pyrocarbon-coating on powdery hard-carbon using chemical vapor infiltration and its electrochemical characteristics. *J. Power Sour.* 146, 125–128. doi: 10.1016/j.jpowsour.2005.03.009

Pan, Q., Zheng, F., Wu, Y., Ou, X., Yang, C., and Xiong, X. (2018). MoS2-covered SnS nanosheets as anode material for lithium-ion batteries with high capacity and long cycle life. *J. Mater. Chem. A* 6, 592–598. doi: 10.1039/C7TA08346G

Piotrowska, A., Kierzek, K., Rutkowski, P., and Machnikowski, J. (2013). Properties and lithium insertion behavior of hard carbons produced by pyrolysis of various polymers at 1000°C. *J. Anal. Appl. Pyrolysis* 102, 1–6. doi: 10.1016/j.jaap.2013.04.011

Raccichini, R., Varzi, A., Chakravadhanula, V. S. K., Kübel, C., and Passerini, S. (2016). Boosting the power performance of multilayer graphene as lithium-ion battery anode via unconventional doping with in-situ formed Fe nanoparticles. *Sci. Rep.* 6:23585. doi: 10.1038/srep23585

Song, M.-K., Park, S., Alamgir, F. M., Cho, J., and Liu, M. (2011). Nanostructured electrodes for lithium-ion and lithium-air batteries: the latest developments, challenges, and perspectives. *Mater. Sci. Eng. R Rep.* 72, 203–252. doi: 10.1016/j.mser.2011.06.001

Tondi, G., Link, M., Kolbitsch, C., Lesacher, R., and Petutschnigg, A. (2016). Pilot plant up-scaling of tannin foams. *Ind. Crops Prod.* 79, 211–218. doi: 10.1016/j.indcrop.2015.11.013

Tondi, G., and Pizzi, A. (2009). Tannin-based rigid foams: characterization and modification. *Ind. Crops Prod.* 29, 356–363. doi: 10.1016/j.indcrop.2008.07.003

Tondi, G., Zhao, W., Pizzi, A., Du, G., Fierro, V., and Celzard, A. (2009). Tannin-based rigid foams: a survey of chemical and physical properties. *Bioresour. Technol.* 100, 5162–5169. doi: 10.1016/j.biortech.2009.05.055

Wang, D., Zhou, J., Li, Z., Li, J., Hou, L., and Gao, F. (2018). Uniformly expanded interlayer distance to enhance the rate performance of soft carbon for lithium-ion batteries. *Ionics* 25, 1531–1539. doi: 10.1007/s11581-018-2646-8

Wang, F., Li, W., Hou, M., Li, C., Wang, Y., and Xia, Y.-Y. (2014). Sandwich-like Cr2O3-graphite intercalation composites as high-stable anode materials for lithium-ion batteries. *J. Mater. Chem. A*, 3:1703. doi: 10.1039/C4TA05072J

Xu, G., Han, J., Ding, B., Nie, P., Pan, J., and Dou, H. (2015). Biomass-derived porous carbon materials with sulfur and nitrogen dual-doping for energy storage. *Green Chem.* 17, 1668–1674. doi: 10.1039/C4GC02185A

Yuan, W., Qiu, Z., Chen, Y., Zhao, B., Liu, M., and Tang, Y. (2018). A binder-free composite anode composed of CuO nanosheets and multi-wall carbon nanotubes for high-performance lithium-ion batteries. *Electrochim. Acta* 267, 150–160. doi: 10.1016/j.electacta.2018.02.081

Zhang, X., Fan, C., Li, L., Zhang, W., Zeng, W., He, X., et al. (2014). Hard carbon wrapped in graphene networks as lithium ion battery anode. *Electrochim. Acta* 149, 94–100. doi: 10.1016/j.electacta.2014.10.094

Zhang, X., Fan, C. L., and Han, S. C. (2017). Improving the initial coulombic efficiency of hard carbon-based anode for rechargeable batteries with high energy density. *J. Mater. Sci.* 52, 10418–10430. doi: 10.1007/s10853-017-1206-3

Zhang, X., Han, S. C., Fan, C. L., Li, L. F., and Zhang, W. H. (2015). Hard carbon enveloped with graphene networks as lithium ion battery anode. *Mater. Lett.* 138, 259–261. doi: 10.1016/j.matlet.2014.10.023

Zhang, X., Han, S. C., Xiao, P. G., Fan, C. L., and Zhang, W. H. (2016). Thermal reduction of graphene oxide mixed with hard carbon and their high performance as lithium ion battery anode. *Carbon* 100, 600–607. doi: 10.1016/j.carbon.2016.01.033

Zhang, X., Hu, J., Chen, X., Zhang, M., Huang, Q., Du, X., et al. (2019). Microtubular carbon fibers derived from bamboo and wood as sustainable anodes for lithium and sodium ion batteries. *J. Porous Mater.* 26, 1821–1830. doi: 10.1007/s10934-019-00781-3

Conflict of Interest: The authors declare that the research was conducted in the absence of any commercial or financial relationships that could be construed as a potential conflict of interest.

frontiers in Chemistry

ORIGINAL RESEARCH
published: 23 April 2020
doi: 10.3389/fchem.2020.00309

β-FeOOH Interlayer With Abundant Oxygen Vacancy Toward Boosting Catalytic Effect for Lithium Sulfur Batteries

Yingying Li[1], Xifei Li[1,2,3], Youchen Hao[2], Alibek Kakimov[2], Dejun Li[1], Qian Sun[4], Liang Kou[5], Zhanyuan Tian[5], Le Shao[5], Cheng Zhang[5], Jiujun Zhang[2,6] and Xueliang Sun[1,2,4]*

[1] Tianjin International Joint Research Centre of Surface Technology for Energy Storage Materials, Energy & Materials Engineering Centre, College of Physics and Materials Science, Tianjin Normal University, Tianjin, China, [2] Xi'an Key Laboratory of New Energy Materials and Devices, Institute of Advanced Electrochemical Energy & School of Materials Science and Engineering, Xi'an University of Technology, Xi'an, China, [3] State Center for International Cooperation on Designer Low-Carbon & Environmental Materials (CDLCEM), Zhengzhou University, Zhengzhou, China, [4] Department of Mechanical and Materials Engineering, University of Western Ontario, London, ON, Canada, [5] Shaanxi Coal Chemical Industry Technology Research Institute Co., Ltd., Xi'an, China, [6] Department of Chemistry, College of Sciences/Institute for Sustainable Energy, Shanghai University, Shanghai, China

OPEN ACCESS

Edited by:
Hongshuai Hou,
Central South University, China

Reviewed by:
Qiaobao Zhang,
Xiamen University, China
Xunhui Xiong,
South China University of Technology, China

***Correspondence:**
Xifei Li
xfli2011@hotmail.com

Specialty section:
This article was submitted to Electrochemistry, a section of the journal Frontiers in Chemistry

Received: 25 February 2020
Accepted: 27 March 2020
Published: 23 April 2020

Citation:
Li Y, Li X, Hao Y, Kakimov A, Li D, Sun Q, Kou L, Tian Z, Shao L, Zhang C, Zhang J and Sun X (2020) β-FeOOH Interlayer With Abundant Oxygen Vacancy Toward Boosting Catalytic Effect for Lithium Sulfur Batteries. Front. Chem. 8:309. doi: 10.3389/fchem.2020.00309

Due to the shuttle effect and low conductivity of sulfur (S), it has been challenging to realize the application of lithium-sulfur (Li-S) batteries with high performance and long cyclability. In this study, a high catalytic active CNTs@FeOOH composite is introduced as a functional interlayer for Li-S batteries. Interestingly, the existence of oxygen vacancy in FeOOH functions electrocatalyst and promotes the catalytic conversion of intercepted lithium polysulfides (LiPS). As a result, the optimized CNTs@FeOOH interlayer contributed to a high reversible capacity of 556 mAh g^{-1} at 3,200 mA g^{-1} over 350 cycles. This study demonstrates that enhanced catalytic effect can accelerate conversion efficiency of polysulfides, which is beneficial of boosting high performance Li-S batteries.

Keywords: CNTs@FeOOH, oxygen vacancy, catalytic effect, polysulfides, Li-S batteries

INTRODUCTION

Currently, Li-S batteries have received extensive attention due to their high theoretical capacity (1,675 mAh g^{-1}), high energy density (2,600 Wh kg^{-1}) (Ji and Nazar, 2010; Manthiram et al., 2013), low cost and environmental friendliness (Nazar et al., 2014; Yang et al., 2018). Considering the low conductivity of S ($\sigma = 5.0 \times 10^{-30}$ S cm^{-1}) and the shuttle effect of LiPS, research on Li-S batteries is strongly delayed and thus hardly meets actual needs (Zhang, 2013; Rosenman et al., 2015).

To solve these problems, many pioneering works are using a porous carbon-based host, a functional interlayer, absorptable polar composites [such as CoS_2/C (Yuan et al., 2016), MnO_2/GO/CNT (Kong et al., 2017), S@TiO_2 (Wei Seh et al., 2013) etc.] and a catalytic effect on LiPS conversion. Among them, carbon-based hybrid materials with absorbility to LiPS have always shown attractive characteristics (Tang and Hou, 2018). For instance, Pang and Nazar obtained C_3N_4 by pyrolysis of melamine, which has rich pyridine nitrogen adsorption sites. This can lead to the fact that the sulfur electrode with ultra-low long-term capacity fades out by 0.04% for a cycle over 1,500 cycles at a practical rate of 0.5C (Pang and Nazar, 2016). However, it should be noted that absorbed LiPS is easy to release, because these materials are soluble in the electrolyte. Thus,

a more efficient strategy is urgently needed to meet this problem. Catalyst has been employed to accelerate the transformation of LiPS from liquid to solid, which corresponds to the transmission from long-chain Li_2S_6 to short-chain Li_2S. We strongly believe that this is an alternative option to modify Li-S batteries by introducing catalytic materials to catalyze the conversion of LiPS into insoluble products. Yang group reported the Fe_3C/Fe-N_x@NPCN modified separator, due to the catalytic effect of Fe_3C to LiPS, the modified batteries yielded a high capacity of 1,517 mAh g^{-1} at 0.1C and displayed a capacity decay rate of 0.034% per cycle after 500 cycles at 1C (Yang et al., 2019). Bian et al. took multi-functional porous carbon nanofibers (g-C_3N_4@PCNF) as the sulfur host, in which g-C_3N_4 contributed to rapid oxidation-remediation conversion of S species and slowed down LiPS yield. Consequently, the g-C_3N_4@PCNF/S cathode achieves good flexibility and excellent cycling retention, e.g., long cycling with decay power of only 0.056% per cycle for 500 cycles at 1.0 A g^{-1} (Bian et al., 2019). In addition, Lee and coworkers have demonstrated that catalytic activity in anoxic sites is higher than in saturated sites as the oxygen vacancy can contribute to the transformation of electrons and the formation of S^{3-} radicals (Lin et al., 2018). Therefore, we are inspired to develop more powerful carbon-based composites with better catalytic effect for LiPS.

As previously reported, FeOOH with abundant oxygen vacancies (Zhang et al., 2018) can be a promising candidate as the catalyst for LiPS. We propose using CNTs@FeOOH composite materials to enhance the stability of Li-S batteries. On the one hand, FeOOH is efficient to catalyze the transformation of polysulfides; on the other hand, CNTs provide a fast electron transport channel, which ensures the sustainability of the reaction under high current and reduces the occurrence of polarization. As a result, the obtained electrodes maintained a high reversible capacity of 556 mAh g^{-1} at 2C for 350 cycles. This work plays a significant contribution to the development of Li-S batteries with high performance and long lifespan.

EXPERIMENTAL SECTION

Synthesis of CNTs@FeOOH Composite and Separator

As reported in our previous work (Hao et al., 2019), CNTs@FeOOH composites with various mass ratio can be obtained by controlling the content of iron source. For comparison, the pure FeOOH phase was synthesized under the same conditions without adding CNTs.

CNTs@FeOOH composites were homogenized into paste by N, N-2-methyl pyrrolidone, the slurry was evenly coated on the polypropylene separator (PP separator). The CNTs@FeOOH-coated separator was dried overnight in vacuum at 40°C and then cut into circular disks (16 mm). CNTs and pure FeOOH phase were wrapped on the separator surface by the same method as the control experiment.

Preparation of the Pure Sulfur Cathode

The commercial S powder, acetylene black and polyvinylidene fluoride binder (PVDF) with a mass ratio of 55:30:15 were mixed into N-methyl-2-pyrrolidone (NMP) solvent and stirred on an electromagnetic stirrer for 24 h to obtain the slurry. The slurry was then cast on Al foil and dried overnight in a vacuum oven at 60°C. The load mass of S is about 0.8 mg cm^{-2}. And the lithium foil was used as the anode electrode.

Materials Characterization

X-ray diffraction (XRD) spectra were tested by Bruker AXS D8 Advance diffractometer with Cu/Kα radiation. Thermogravimetric analysis (TGA, Pyris Diamond6000 TG/DTA, PerkinElmer Co., America) was performed to confirm the FeOOH content in composites. The morphologies of as-obtained samples were measured by a field-emission scanning electron microscope (SEM Hitach SU8010) and JEOLJEM-3000F transmission electron microscope (TEM). The composition of the elements on the composites surface was verified by X-ray photoelectron spectroscopy (XPS PHI5000 Versa Probe).

Electrochemical Characterizations

Electrochemical performance was studied using CR2032 coin-typed cells assembled in an argon filled glovebox. 1.0 M lithium bis-trifluoromethanesulfonylimide (LiTFSI) in 1,3-dioxolane (DOL) and 1,2-dimethoxyethane (DME) at a volume ratio of 1: 1 with 1 wt% $LiNO_3$ additive was utilized as electrolyte. Galvanostatic charge/discharge characteristics were tested on the LAND CT2001A battery tester. Princeton Applied Research Versa STAT4 was used to perform cyclic voltammetry at a scanning rate of 0.1 mV s^{-1}. Electrochemical impedance spectroscopy (EIS) was performed on Princeton Applied Research Versa STAT4. The frequency range was 0.01 Hz−100 kHz amplitude of AC was 5.0 mV. All electrochemical tests were performed in the range of 1.7–2.8 V.

RESULTS AND DISCUSSION

The morphologies of CNTs, bare FeOOH and CNTs@FeOOH composites were visualized via scanning electron microscope (SEM). As depicted in **Figures 1a–c**, an increasingly obvious stick-like FeOOH being grown on the surface of CNTs (denoted as CNTs@FeOOH-I, II, and III, respectively). Compared to pure CNTs and FeOOH in **Figure S1**, the formation of rod-shaped FeOOH may induced by the reaction conditions. In addition, the X-ray diffraction (XRD) patterns of all samples are compared in **Figure 1d**. The peaks of pure FeOOH are located at $2\theta = 11.925°$, 16.901°, 26.874°, 34.185°, 35.311°, 39.386°, 46.656°, 52.349°, 56.158°, 61.278°, 64.718°, and 68.117° are attributed to the (110), (200), (130), (400), (211), (301), (411), (600), (251), (002), (541), and (132) reflection planes of β-FeOOH (JCPDS 75-1594). The FeOOH peaks become more evident with increasing FeOOH content and no impurity phase is detected. Transmission electron microscope (TEM) images of CNTs@FeOOH-II, demonstrated that FeOOH particles are uniformly adhered on the surface of CNTs, which consistent well with the results of SEM (see **Figures S2a,b**). The selected area electron diffraction pattern of the CNTs@FeOOH-II nanomaterials shows diffraction rings characteristic of FeOOH and CNTs (see **Figure S2c**), while the image of high resolution TEM in **Figure S2d** indicates lattice

fringes corresponding to (110), (200), (211), and (330) planes. The results are consistent with those of XRD spectrums. Besides, thermogravimetric analysis (TGA) was used to calculate the proportion of components in various composites (Zhang et al., 2017). As shown in **Figure 1e**, the FeOOH content is measured as 24.8, 45.7, and 71.5 wt% for the composites CNTs@FeOOH-I, II, and III, respectively.

X-ray photoelectron spectroscopy (XPS) was employed to investigate the composition of elements on the surface of CNTs@FeOOH nanocomposites and the chemical states of various bond elements. The result shown the presence of Fe, O, and C atoms at the CNTs@FeOOH sheet surface (**Figure S3a**). The binding energy peak observed in the high-resolution C 1s profile at 284.9 eV (**Figure S3b**) can be attributed to graphite carbon in carbon nanotubes. The peak at 285.4 eV belongs to epoxy and hydroxyl (Beamson et al., 1994). The other two peaks are caused by carbonyl (C=O, 288.7 eV) and the oxygenated carbons of carboxyl (O-C=O, 291.2 eV) (Gardella et al., 1986; Kokai, 1990). These peaks reveal the existence of oxygen-containing functional groups on the surface of CNTs (Zhang et al., 2017). Meanwhile, the finescanned Fe 2p XPS spectra of that sample was also shown in **Figure S3c**, and the Fe 2p3/2 and Fe 2p1/2 peaks located at 711.0 and 724.9 eV could be indexed to Fe^{3+} and Fe^{2+}, respectively, and satellite peaks at 719.4 and 733.9 eV correspond well with FeOOH (Tan et al., 1990). In addition, the O 1s peaks (**Figure 1f**) can be assigned to Fe-O-Fe (529.5 eV), Fe-O-H (530.1 eV), and H-O-H bonds (531.2 eV). It is worthwhile to point out that the peak at 531.2 eV is attributed to defect sites with low oxygen coordination (Zhang et al., 2019). According to previous reports, surface oxygen vacancies are involved in the LiPS transformation reaction, which significantly improves the kinetics of the reaction, thus contributing to the fast LiPS transformation at high rate.

According to the previous paper, the shuttle effect of polysulfides can be diminished with an additional intermediate layer (Fan et al., 2019). In this work, various composites of CNTs@FeOOH were coated on the surface of the PP separator as a functional interlayer to study their effect on Li-S batteries. **Figure S4a** shows a schematic representation of conventional PP-separator Li-S structures and advanced Li-S batteries with functional CNTs@FeOOH layers. The surface morphology of the modified interlayer is shown in **Figures 2a–c**, the preserved porous structure will facilitate electrolyte penetration and lithium ions (Li^+) transfer. **Figure 2d** and **Figures S4b,c** show the cross-sectional appearance, and the thickness of the interlayer is about 20 um.

Coin-typed cells with different separators were assembled to evaluate electrochemical performances. **Figure S4d** exhibits the cycling performance of all Li-S cells with PP separator, CNTs, pure FeOOH and three proportional composites interlayer at 0.2C (1C = 1,675 mA g^{-1}) between 1.7 and 2.8 V. After 100 cycles, CNTs@FeOOH-II revealed the best cyclability of 662.1 mAh g^{-1}, which indicates a good synergistic effect between CNTs and FeOOH.

In order to explore the lithium diffusion properties and investigate the role of composite materials in Li-S batteries, we performed cyclic voltammetry (CV) measurements under various scanning rates ranging from 0.1 to 0.5 mV s^{-1} between 1.7 and 2.8 V (vs. Li/Li^+). As shown in **Figures 3A–D**, all curves show typical reduction/oxidation reaction of S cathode, with two

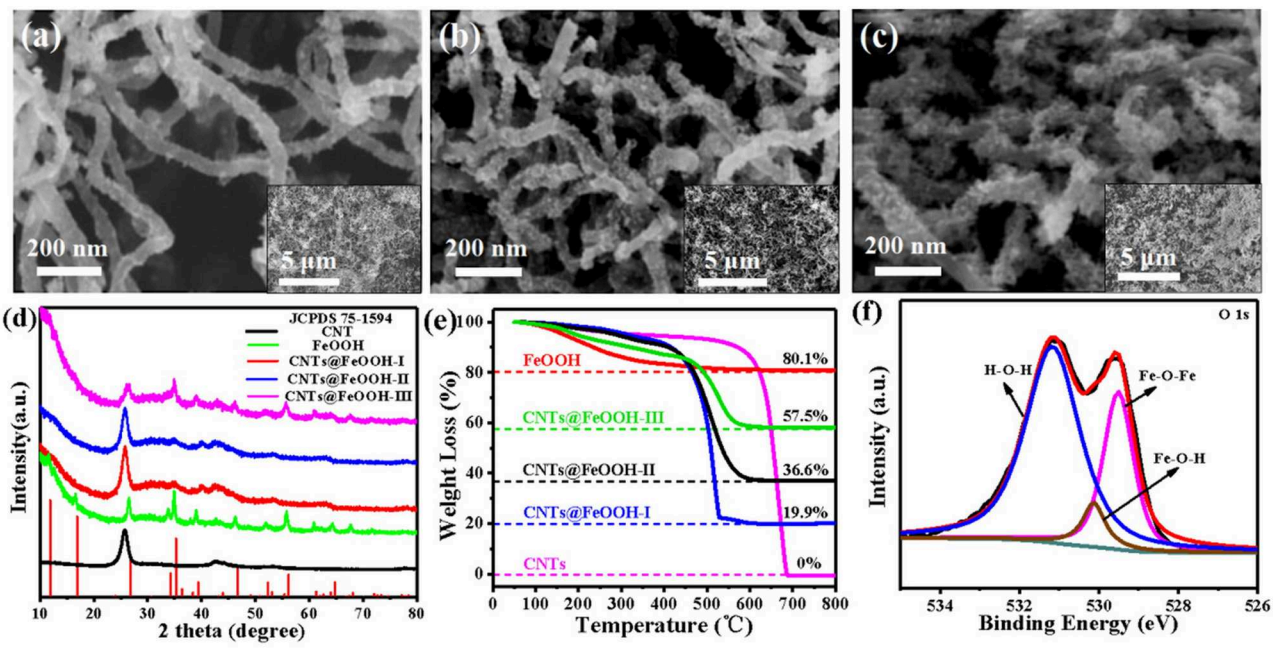

FIGURE 1 | SEM images of **(a)** CNTs@FeOOH-I, **(b)** CNTs@FeOOH-II, **(c)** CNTs@FeOOH-III; **(d)** XRD, and **(e)** TGA of carboxylic CNTs, bare FeOOH and CNTs@FeOOH compounds with different proportions; **(f)** XPS spectra results of CNTs@FeOOH-II compounds: O 1s core-level spectrum.

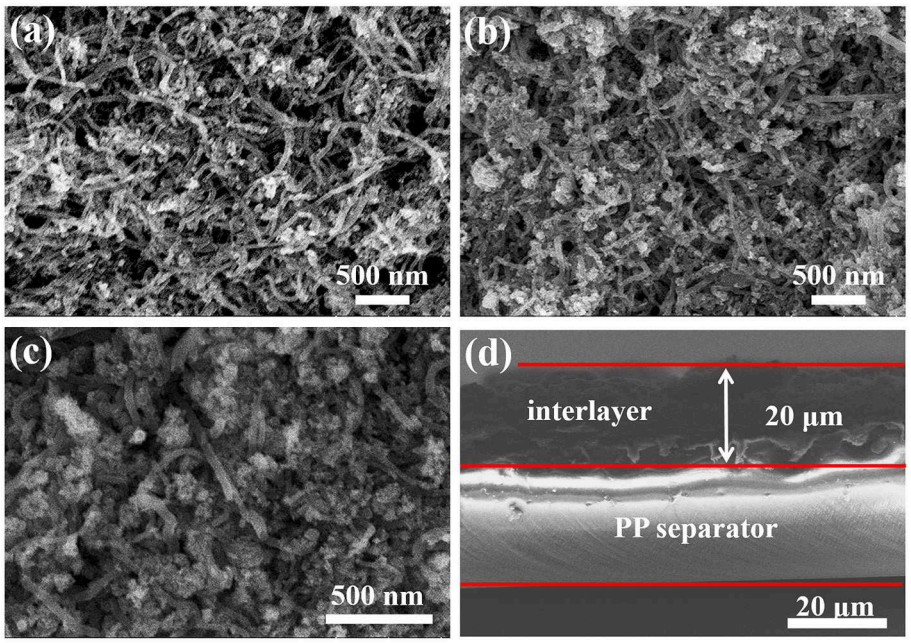

FIGURE 2 | Surface morphology of **(a)** CNTs@FeOOH-I, **(b)** CNTs@FeOOH-II, **(c)** CNTs@FeOOH-III, and **(d)** cross section of CNTs@FeOOH-II interlayer.

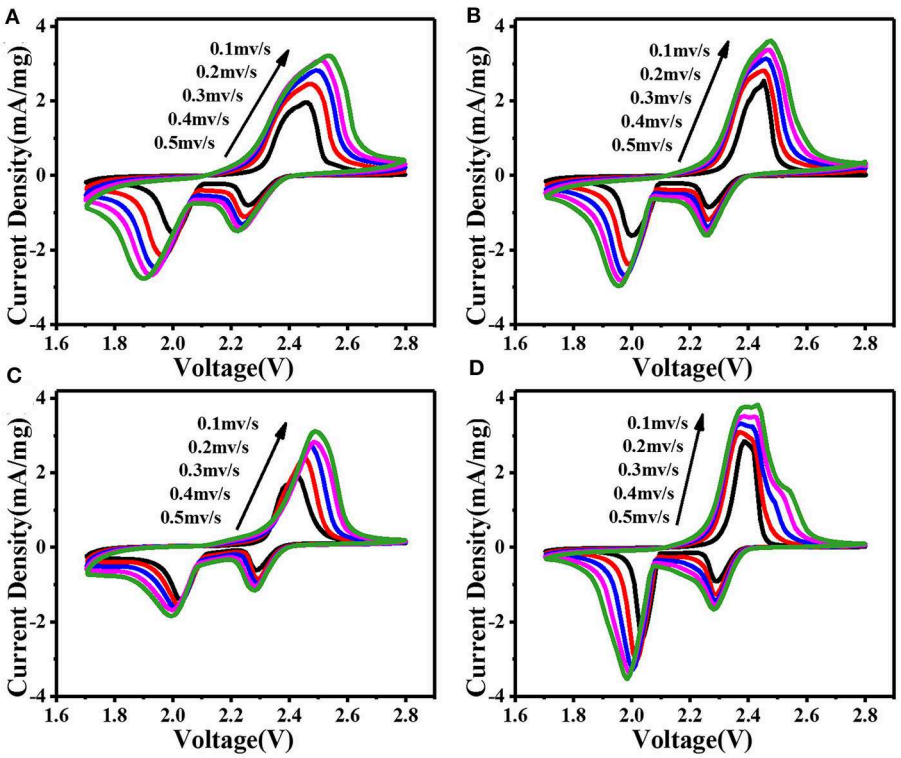

FIGURE 3 | CV curves at various scan rates: the battery with **(A)** PP, **(B)** CNTs, **(C)** FeOOH, and **(D)** CNTs@FeOOH-II separator, respectively.

distinct cathode peaks and one anode peak. The cathode peak at about 2.3 V corresponds to the transformation of sulfur bonding with Li^+ into soluble long-chain polysulfide [Li_2S_x (x = 4–8)]. Furthermore, the cathode peak around 2.0 V corresponds to the transformation of long-chain polysulfide into insoluble Li_2S or Li_2S_2 (Chung et al., 2016). In subsequent anode scanning, the

oxidation peak at ∼2.4 V corresponds to its reverse process. According to the relationship between CV scanning rate ($\nu^{0.5}$) and peak current (Ip), the lithium diffusion performance can be estimated using the classical Randles Sevcik equation:

$$Ip = (2.69\times10^5)n^{1.5}SD_{Li+}{}^{0.5}\,C_{Li}\nu^{0.5} \quad (1)$$

where, Ip-peak current (A), n-number of electrons per type of reaction ($n = 1$), S-electrode area (S = 1.13 cm^2), D_{Li+}-diffusion coefficient of lithium ion ($cm^2\ s^{-1}$), C_{Li+}-initial concentration of lithium ion in the cathode ($C_{Li+} = 1\ mol\ cm^{-3}$), ν-potential scanning rate ($V\ s^{-1}$) (Tao et al., 2016). The n, S, and C_{Li+} are constant in our battery system. The slope of the curve in **Figure S5a** is positively correlated with the corresponding Li^+ diffusion. The calculated results show that the modified CNTs@FeOOH-II had the greatest diffusion capacity of Li 4.40 × 10^{-12}, better than intact (2.08 × 10^{-12}). Typically, the PP separator has difficulty catching soluble LiPS, which tends to dissolve in electrolytes in large quantities. As a result increasing viscosity of electrolyte leads to slower diffusion of Li^+. On the contrary, since CNTs@FeOOH-II material can accelerate the conversion of LiPS to Li_2S_2 or Li_2S, it is easier to increase the diffusion rate of Li^+ in modified cells.

The discharge process in Li-S batteries can be expressed as follows:

$$S_8 + 2e^- \leftrightarrow S_8^{2-} \quad (2)$$

$$3S_8 + 2e^- \leftrightarrow 4S_6^{2-} \quad (3)$$

$$2S_6^{2-} + 2e^- \leftrightarrow 3S_4^{2-} \quad (4)$$

$$S_4^{2-} + 4Li^+ + 2e^- \leftrightarrow 2Li_2S_2 \quad (5)$$

$$Li_2S_2 + 2Li^+ + 2e^- \leftrightarrow 2Li_2S \quad (6)$$

The theoretical discharge capacity of Li-S battery at different stages is calculated by referring the number of electrons transferred. The details are given in **Table 1** and specific formulas are given below (Diao et al., 2013):

$$q = nF/M \quad (7)$$

Among them, q is the specific discharge capacity, mAh g^{-1}; n is the number of transfer electrons per mole mass, mol^{-1}; F is the amount of electricity owned by 1 M electrons, 26.8 Ah; M is the molar mass of elemental sulfur, 32 g mol^{-1} (Diao et al., 2013). Here, the discharge capacity of $S_8 \rightarrow S_4^{2-}$ is recorded as S_1, and that of $S_8 \rightarrow Li_2S$ as S_2. Accordingly, $S_1 : S_2$ is approach to 1:3. **Figures 4A–D** shows the discharge curve of the PP separator and various barrier interlayers circulating for 200 cycles at 2C. The calculated results show that the capacity ratio of CNTs@FeOOH-II (1:2.44) is closest to the theoretical value, higher than 1:2.26, 1:2.27, and 1:1.74 of PP separator, CNTs and FeOOH, respectively, which indicates the enhanced transformation ability of CNTs@FeOOH-II to polysulfide ions at high current density.

TABLE 1 | The relationship between DOD and the discharge specific capacity.

Discharge products	Transfer electron number/n (mol•mol^{-1} S)	Depth of discharge DOD	Discharge specific capacity/q (mAh g^{-1})
$S_8 \rightarrow S_8^{2-}$	0.25	12.5%	210
$S_8 \rightarrow S_6^{2-}$	0.33	16.7%	280
$S_8 \rightarrow S_4^{2-}$	0.5	25.0%	420
$S_8 \rightarrow Li_2S_2$	1	50.0%	840
$S_8 \rightarrow Li_2S$	2	100.0%	1,680

Figure 4E compares the cyclic characteristics of the batteries with PP separator, CNTs, pure phase FeOOH and CNTs@FeOOH-II separator in a voltage range of 1.7–2.8 V at 2C. The initial discharge capacities are 870.6, 1,093, 1326.4, and 1121.9 mAh g^{-1}, respectively, show that CNTs@FeOOH-II interlayer can strengthen the utilization of S upon cycling. After 350 cycles, CNTs@FeOOH-II maintained a high reversible capacity of 556 mAh g^{-1}. In detail, although CNTs have good electrical conductivity, the weak van der Waals interactions between polar LiPS and non-polar carbon materials results in slow release of S-active substances from carbon materials and obvious capacity decay during long cycle (Song et al., 2016). Simultaneously, it is remarkable that the highest reversible capacity of 1326.4 mAh g^{-1} can be obtained for pure FeOOH group. This can be explained by the presence of oxygen vacancies in FeOOH, which makes it electrocatalytic and prompts the rapid conversion of long-chain LiPS to solid Li_2S_2 and Li_2S. Since 75% of the discharge capacity (1,254 mAh g^{-1}) occurs in this conversion process, an enhanced reaction kinetics is beneficial for increasing the reversible capacity (Lim et al., 2019). However, since previous studies have shown that the absorption of LiPS by insulating interlayer is considered to be a "death zone" without transferring electrons during cycling (Hao et al., 2017). The fading trend in the battery with FeOOH interlayer mainly result from its low conductivity (10^{-5} S cm^{-1}). Compared with relevant studies (**Table S1**), the introduction of this functional interlayer delivered better performance improvement for Li-S batteries.

The existence of functional interlayer can be used both as a conductive top current collector and as a physical barrier to polysulfide diffusion and lithium (Li) metal, debase the corrosion of Li metal. In case of rate performance (**Figure S5b**), CNTs@FeOOH-II composites exhibit high discharge capacity of 1292.6, 957.5, 802.3, and 630.8 mAh g^{-1} at various rates from 0.2 to 2C, which is more satisfactory than CNTs and FeOOH. In particular, when the rate was restored to 0.2C, the specific capacity of the battery returned to 972.5 mAh g^{-1}. These results confirm that CNTs@FeOOH-II interlayer enhances the stability

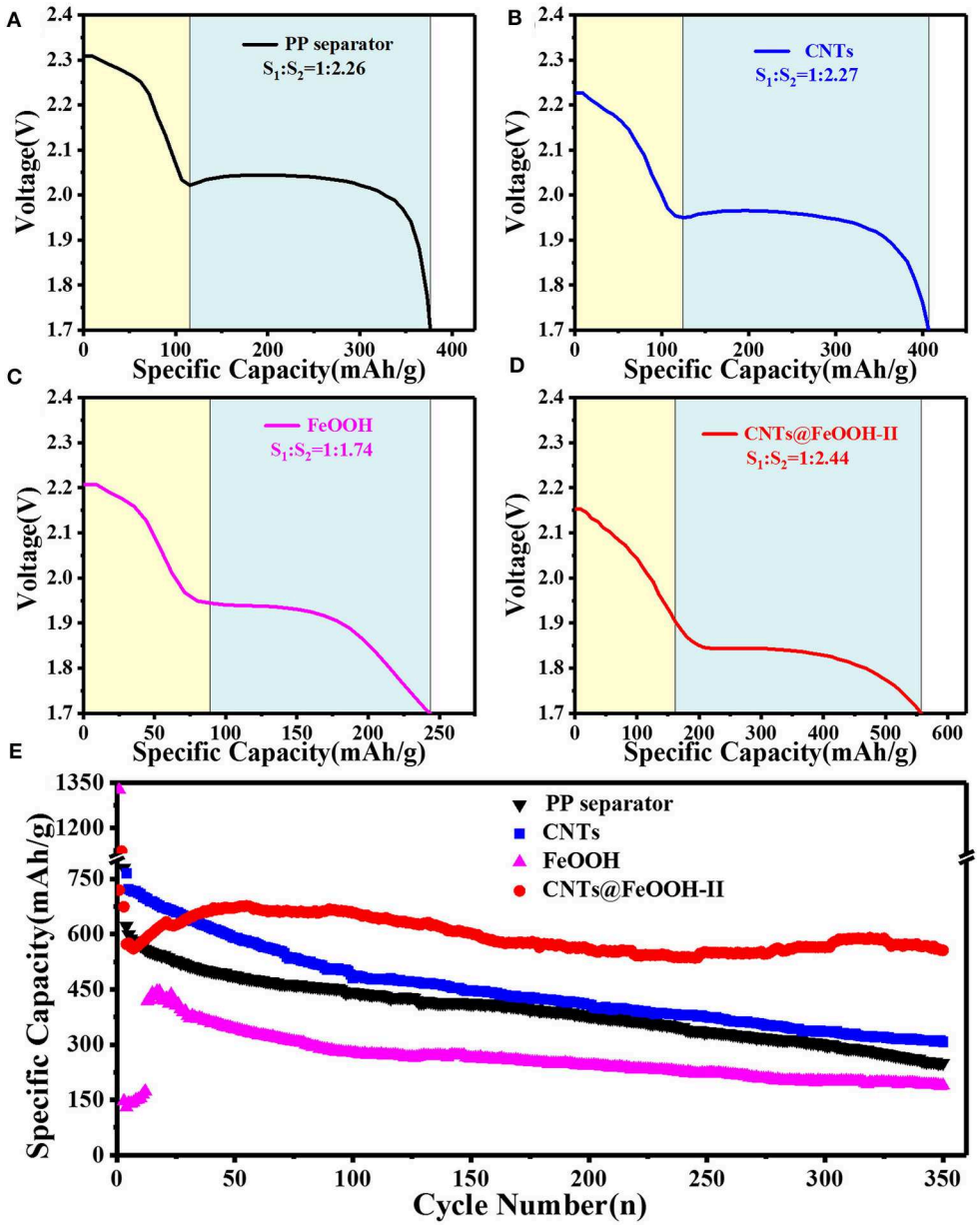

FIGURE 4 | The 200th cycle Discharge profiles of the battery with **(A)** PP separator, **(B)** CNTs, **(C)** FeOOH, and **(D)** CNTs@FeOOH-II separator, respectively, at 3,200 mAh g^{-1}; **(E)** cycle performance at 3,200 mAh g^{-1}.

of S electrode. The presence of FeOOH in CNTs@FeOOH-II composite can enhance the rapid transformation of polysulfide ions and the hysteretic conversion kinetics of Li-S batteries, thus improving the rate capability of Li-S batteries.

The electrocatalytic effects of the different interlayers on PP separator were studied by electrochemical impedance spectroscopy (EIS). In **Figure 5** shows the Nyquist plots when discharges up to 2.1 V after 10, 30, 50 cycles, respectively. Each plot consists of one oblique line in a low frequency region and one or two compressed semicircles in a medium and high frequency region. The corresponding equivalent circuit model is shown in **Figure 5A**. In the equivalent circuit, R_s represents the ohmic resistance of the reaction system; R_f is related to the resistance of the solid electrolyte interface (SEI), corresponding to a semicircle of the high frequency region; R_{ct} represents the charge transfer resistance, corresponding to a semicircle of the mid-frequency region, the diameter of the semicircle is the size of R_{ct}, the larger the diameter, the greater the impedance, the more unfavorable to the high performance; CPE-double layer electrode/electrolyte capacitance; W characterizes the Warburg diffusion impedance of the electrode, which corresponds to an oblique line in the low frequency band, it characterizes the diffusion rate of Li^+ in the

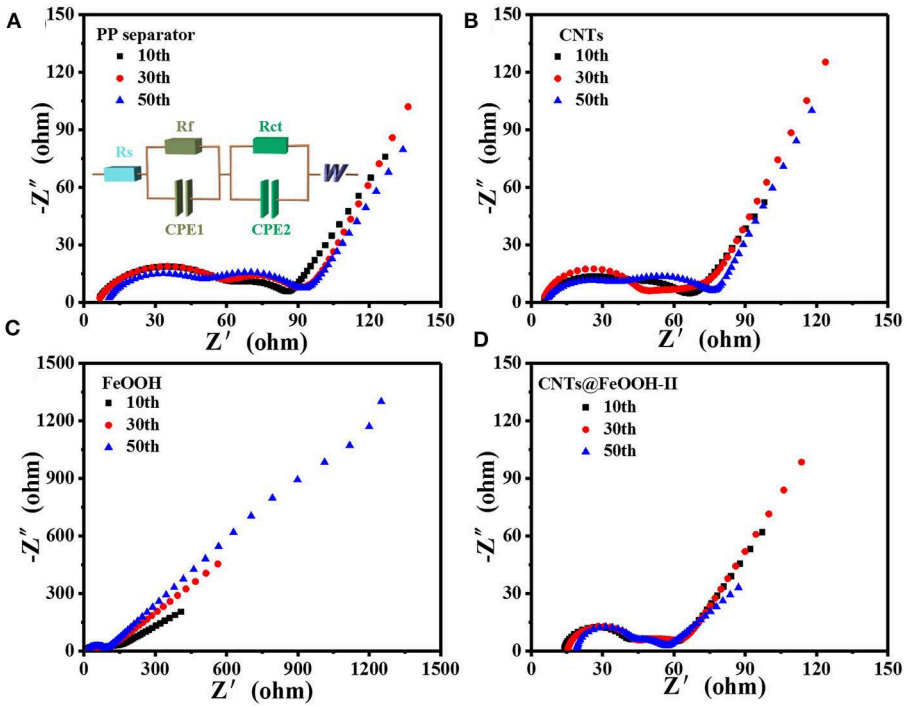

FIGURE 5 | Nyquist plots of **(A)** PP separator, **(B)** CNTs, **(C)** FeOOH, and **(D)** CNTs@FeOOH-II.

TABLE 2 | The comparison of Rct values of different interlayer and PP separator.

Samples	10th	30th	50th
PP separator	24.07	22.55	34.15
CNTs	22.46	18.2	37.12
FeOOH	48.49	28.68	54.96
CNTs@FeOOH-II	19.24	15.94	21.64

material, the larger the slope, the better the high performance (Hu et al., 2018).

The fitting values of R_{ct} were exhibited in **Table 2**, the S electrode with CNTs@FeOOH-II interlayer endowed the lowest R_{ct} value after several charge-discharge cycles. The results are in good accordance with the results of the electrochemical cycle test. The conductivity of CNTs@FeOOH-II was measured by four-point probe method, which is about 4.6 S cm^{-1}. High conductivity of CNTs@FeOOH-II may accelerate electron transfer and reduce electrochemical polarization. This further indicates that electrocatalytic materials with high conductivity and faster electron and ion transfer rates can improve the electrochemical performance of Li-S batteries.

CONCLUSION

In conclusion, FeOOH combined with CNTs with excellent catalytic ability is applied for high performance Li-S batteries. Compared to the pristine samples, the modified battery exhibited a good performance of 556 mAh g^{-1} at 3,200 mA g^{-1} for 350 cycles. CNTs@FeOOH-II plays the following main roles: (i) oxygen vacancies in FeOOH promote the rapid transformation of polysulfide ions, thus enhancing the reaction kinetics; (ii) the presence of FeOOH can effectively adsorb soluble polysulfides, which sluggishs the further diffusion to the anode; (iii) CNTs@FeOOH-II with high electric conductivity can be used as a "vice-electrode" to accelerate electron transfer and thus improve the rate capability. Therefore, for a high performance of Li-S battery, it is necessary to consider the high conductivity, adsorption, and fast conversion of LiPS.

DATA AVAILABILITY STATEMENT

All datasets generated for this study are included in the article/**Supplementary Material**.

AUTHOR CONTRIBUTIONS

YL, XL, and YH contributed conception and design of the study. YL organized the database, performed the statistical analysis, and wrote the first draft of the manuscript. All authors contributed to manuscript revision, read, and approved the submitted version.

FUNDING

This research was supported by the Natural Science Basic Research Plan in Shaanxi Province of China

(2019JLP-04), the National Natural Science Foundation of China (51672189), Xi'an Science and Technology Project of China [201805037YD15CG21(20)], and Tianjin Science and Technology Project (18PTZWHZ00020).

SUPPLEMENTARY MATERIAL

The Supplementary Material for this article can be found online at: https://www.frontiersin.org/articles/10.3389/fchem.2020.00309/full#supplementary-material

REFERENCES

Beamson, G., Clark,DT., Hayes, N. W., and Law, D. S. L. (1994). Effect of crystallinity on the XPS spectrum of poly(ethylene terephthalate). *Surface Sci. Spectra* 3, 357–365. doi: 10.1116/1.1247788

Bian, Z., Yuan, T., Xu, Y., Pang, Y., Yao, H., Li, J., et al. (2019). Boosting Li–S battery by rational design of freestanding cathode with enriched anchoring and catalytic N-sites carbonaceous host. *Carbon* 150, 216–223. doi: 10.1016/j.carbon.2019.05.022

Chung, S. H., Chang, C. H., and Manthiram, A. (2016). A carbon-cotton cathode with ultrahigh-loading capability for statically and dynamically stable lithium-sulfur batteries. *ACS Nano* 10, 10462–10470. doi: 10.1021/acsnano.6b06369

Diao, Y., Xie, K., Hong, X., and Xiong, S. (2013). Analysis of the sulfur cathode capacity fading mechanism and review of the latest development for Li-S battery. *Acta Chim. Sin.* 71, 508–518. doi: 10.6023/A12121024

Fan, L., Li, M., Li, X., Xiao, W., Chen, Z., and Lu, J. (2019). Interlayer material selection for lithium-sulfur batteries. *Joule* 3, 361–386. doi: 10.1016/j.joule.2019.01.003

Gardella, J. A., Jr., Ferguson, S. A., and Chin, R. L. (1986). $\pi^* \leftarrow \pi$ shakeup satellites for the analysis of structure and bonding in aromatic polymers by X-ray photoelectron spectroscopy. *Soc. Appl. Spectrosc.* 40, 224–232. doi: 10.1366/0003702864509565

Hao, Y., Li, X., Liu, W., Maleki Kheimeh Sari, H., Qin, J., and Li, Y. (2019). Asynchronous reactions of "self-matrix" dual-crystals effectively accommodating volume expansion/shrinkage of electrode materials with enhanced sodium storage. *Chem. Commun.* 55, 9076–9079. doi: 10.1039/C9CC03406D

Hao, Y., Xiong, D., Liu, W., Fan, L., Li, D., and Li, X. (2017). Controllably designed "vice-electrode" interlayers harvesting high performance lithium sulfur batteries. *ACS Appl. Mater. Interfaces* 9, 40273–40280. doi: 10.1021/acsami.7b12710

Hu, N., Lv, X., Dai, Y., Fan, L., Xiong, D., and Li, X. (2018). SnO_2/reduced graphene oxide interlayer mitigating the shuttle effect of Li-S batteries. *ACS Appl. Mater. Interfaces* 10, 18665–18674. doi: 10.1021/acsami.8b03255

Ji, X., and Nazar, L. F. (2010). Advances in Li–S batteries. *J. Mater. Chem.* 20, 9821–9826. doi: 10.1039/b925751a

Kokai, F. (1990). X-ray photoelectron spectroscopy studies on modified poly(ethylene terephthalate) surfaces after KrF laser ablation. *Jap. J. Appl. Phys.* 29, 158–161. doi: 10.1143/JJAP.29.158

Kong, W. B., Yan, L. J., Luo, Y. F., Wang, D. T., Jiang, K. L., Li, Q. Q., et al. (2017). Ultrathin MnO_2/Graphene Oxide/Carbon nanotube interlayer as efficient polysulfide-trapping shield for high-performance Li-S batteries. *Adv. Funct. Mater.* 27:1606663. doi: 10.1002/adfm.201606663

Lim, W. G., Kim, S., Jo, C., and Lee, J. (2019). A comprehensive review of materials with catalytic effects in Li-S batteries: enhanced redox kinetics. *Angew. Chem. Int. Ed. Engl.* 58, 18746–18757. doi: 10.1002/anie.201902413

Lin, H., Zhang, S., Zhang, T., Ye, H., Yao, Q., Zheng, G. W., et al. (2018). Elucidating the catalytic activity of oxygen deficiency in the polysulfide conversion reactions of lithium-sulfur batteries. *Adv. Energy Mater.* 8:1801868. doi: 10.1002/aenm.201801868

Manthiram, M., Fu, Y., and Su, Y. S. (2013). Challenges and prospects of lithium sulfur batteries. *Accunts Chem. Res.* 46, 1125–1134. doi: 10.1021/ar300179v

Nazar, L. F., Cuisinier, M., and Pang, Q. (2014). Lithium-sulfur batteries. *MRS Bull.* 39, 436–442. doi: 10.1557/mrs.2014.86

Pang, Q., and Nazar, L. F. (2016). Long-life and high-areal-capacity Li-S batteries enabled by a light-weight polar host with intrinsic polysulfide adsorption. *ACS Nano* 10, 4111–4118. doi: 10.1021/acsnano.5b07347

Rosenman, A., Markevich, E., Salitra, G., Aurbach, D., Garsuch, A., and Chesneau, F. F. (2015). Review on Li-sulfur battery systems: an integral perspective. *Adv. Energy Mater.* 5:1500212. doi: 10.1002/aenm.201500212

Song, J., Yu, Z., Gordin, M. L., and Wang, D. (2016). Advanced sulfur cathode enabled by highly crumpled nitrogen-doped graphene sheets for high-energy-density lithium-sulfur batteries. *Nano Lett.* 16, 864–870. doi: 10.1021/acs.nanolett.5b03217

Tan, B. J., Klabunde, K. J., and Sherwood, P. A. (1990). X-ray photoelectron spectroscopy studies of solvated metal atom dispersed catalysts. Monometallic iron and bimetallic iron-cobalt particles on alumina. *Chem. Mater.* 2, 186–191. doi: 10.1021/cm00008a021

Tang, T., and Hou, Y. (2018). Multifunctionality of carbon-based frameworks in lithium sulfur batteries. *Electrochem. Energy Rev.* 1, 403–432. doi: 10.1007/s41918-018-0016-x

Tao, X., Wang, J., Liu, C., Wang, H., Yao, H., Zheng, G., et al. (2016). Balancing surface adsorption and diffusion of lithium-polysulfides on nonconductive oxides for lithium-sulfur battery design. *Nat. Commun.* 7:11203. doi: 10.1038/ncomms11203

Wei Seh, Z., Li, W., Cha, J. J., Zheng, G., Yang, Y., McDowell, M. T., et al. (2013). Sulphur-TiO_2 yolk-shell nanoarchitecture with internal void space for long-cycle lithium-sulfur batteries. *Nat. Commun.* 4:1331. doi: 10.1038/ncomms2327

Yang, H., Yang, Y., Zhang, X., Li, Y., Qaisrani, N. A., Zhang, F., et al. (2019). Nitrogen-doped porous carbon networks with active Fe-Nx sites to enhance catalytic conversion of polysulfides in lithium-sulfur batteries. *ACS Appl. Mater. Interfaces* 11, 31860–31868. doi: 10.1021/acsami.9b08962

Yang, X., Li, X., Adair, K., Zhang, H., and Sun, X. (2018). Structural design of lithium–sulfur batteries: from fundamental research to practical application. *Electrochem. Energy Rev.* 1, 239–293. doi: 10.1007/s41918-018-0010-3

Yuan, Z., Peng, H. J., Hou, T. Z., Huang, J. Q., Chen, C. M., Wang, D. W., et al. (2016). Powering lithium-sulfur battery performance by propelling polysulfide redox at sulfiphilic hosts. *Nano Lett.* 16, 519–527. doi: 10.1021/acs.nanolett.5b04166

Zhang, B., Huang, X., Hu, H., Chou, L., and Bi, Y. (2019). Defect-rich and ultrathin CoOOH nanolayers as highly efficient oxygen evolution catalysts for photoelectrochemical water splitting. *J. Mater. Chem. A* 7, 4415–4419. doi: 10.1039/C8TA12012A

Zhang, B., Wang, L., Zhang, Y., Ding, Y., and Bi, Y. (2018). Ultrathin FeOOH nanolayers with abundant oxygen vacancies on $BiVO_4$ photoanodes for efficient water oxidation. *Angew. Chem. Int. Ed. Engl.* 57, 2248–2252. doi: 10.1002/anie.201712499

Zhang, E., Wang, B., Yu, X., Zhu, J., Wang, L., Lu, B., (2017). β-FeOOH on carbon nanotubes as A Cathode material for Na-ion batteries. *Energy Storage Mater.* 8, 147–152. doi: 10.1016/j.ensm.2017.05.012

Zhang, S. S. (2013). Liquid electrolyte lithium/sulfur battery: fundamental chemistry, problems, and solutions. *J. Power Sourc.* 231, 153–162. doi: 10.1016/j.jpowsour.2012.12.102

Conflict of Interest: LK, ZT, LS, and CZ were employed by the company Shaanxi Coal Chemical Industry Technology Research Institute Co., Ltd.

The remaining authors declare that the research was conducted in the absence of any commercial or financial relationships that could be construed as a potential conflict of interest.

frontiers in Chemistry

ORIGINAL RESEARCH
published: 05 May 2020
doi: 10.3389/fchem.2020.00316

Biomass-Derived P/N-Co-Doped Carbon Nanosheets Encapsulate Cu_3P Nanoparticles as High-Performance Anode Materials for Sodium–Ion Batteries

Yanyou Yin[1], *Yu Zhang*[1], *Nannan Liu*[1], *Bing Sun*[2]* *and Naiqing Zhang*[1,3]*

[1] State Key Laboratory of Urban Water Resource and Environment, Harbin Institute of Technology, Harbin, China, [2] Faculty of Science, Center for Clean Energy Technology, School of Mathematical and Physical Science, University of Technology Sydney, Sydney, NSW, Australia, [3] Harbin Institute of Technology, Academy of Fundamental and Interdisciplinary Sciences, Harbin, China

Biomass-derived approaches have been accepted as a practical way for the design of transitional metal phosphides confined by carbon matrix (TMPs@C) as energy storage materials. Herein, we successfully synthesize P/N-co-doped carbon nanosheets encapsulating Cu_3P nanoparticles (Cu_3P@P/N-C) by a feasible aqueous reaction followed by a phosphorization procedure using sodium alginate as the biomass carbon source. Cu-alginate hydrogel balls can be squeezed into two-dimensional (2D) nanosheets through a freeze–drying process. Then, Cu_3P@P/N-C was obtained after the phosphorization procedure. This rationally designed structure not only improved the kinetics of ion/electron transportation but also buffered the volume expansion of Cu_3P nanoparticles during the continuous charge and discharge processes. In addition, the 2D P/N co-doped carbon nanosheets can also serve as a conductive matrix, which can enhance the electronic conductivity of the whole electrode as well as provide rapid channels for electron/ion diffusion. Thus, when applied as anode materials for sodium-ion batteries, it exhibited remarkable cycling stability and rate performance. Prominently, Cu_3P@P/N-C demonstrated an outstanding reversible capacity of 209.3 mAh g^{-1} at 1 A g^{-1} after 1,000 cycles. Besides, it still maintained a superior specific capacity of 118.2 mAh g^{-1} after 2,000 cycles, even at a high current density of 5 A g^{-1}.

Keywords: sodium-ion batteries, biomass, Cu_3P, P/N-co-doped carbon, nanosheets

OPEN ACCESS

Edited by:
Weijie Li,
University of Wollongong, Australia

Reviewed by:
Xiaodong Guo,
Sichuan University, China
Dongjiang Yang,
Qingdao University, China

***Correspondence:**
Bing Sun
bing.sun@uts.edu.au
Naiqing Zhang
znqmww@163.com

Specialty section:
This article was submitted to Electrochemistry, a section of the journal Frontiers in Chemistry

Received: *17 February 2020*
Accepted: *30 March 2020*
Published: *05 May 2020*

Citation:
Yin Y, Zhang Y, Liu N, Sun B and Zhang N (2020) Biomass-Derived P/N-Co-Doped Carbon Nanosheets Encapsulate Cu_3P Nanoparticles as High-Performance Anode Materials for Sodium–Ion Batteries. Front. Chem. 8:316. doi: 10.3389/fchem.2020.00316

INTRODUCTION

In recent years, lithium-ion batteries (LIBs) have been widely applied from portable electronic devices to electric vehicles (Zou et al., 2017, 2019; Qiu et al., 2019). However, the shortage of lithium sources limited the further development of LIBs (Wang et al., 2018a; Wu C. et al., 2018). Over the past few years, sodium-ion batteries (SIBs), owing to their low cost of production and earth-abundant sodium sources, show tremendous potential as a promising replacement of LIBs for large-scale energy storage applications (Kundu et al., 2015; Larcher and Tarascon, 2015; Zhang et al., 2016, 2018; Song et al., 2018; Xiao et al., 2018, 2020). However, when compared with LIBs, SIBs are

still an immature technology that is confronted with a lot of challenges, such as low specific energy, poor cycleability, and low power density (Wessells et al., 2011; Lotfabad et al., 2014; Li and Zhou, 2018). Anode, as the main component of SIBs, has a great influence on the overall electrochemical performance. In recent years, red phosphorus has been regarded as one of promising SIB anode materials owing to its comparatively low redox potential (∼0.4 V vs. Na/Na^+) and extremely high theoretical specific capacity (2,596 mAh g^{-1}) (Kim et al., 2013; Qian et al., 2013; Zhou et al., 2017; Hu et al., 2018; Wu Y. et al., 2018). However, the low electrical conductivity (∼10^{-14} S cm^{-1}) and the huge volume expansion (∼490%) during the continuous Na^+ insertion/extraction process make red phosphorus suffer from inferior cycling stability and rate performance (Sun et al., 2014; Wang et al., 2018b). Fortunately, forming transition metal phosphides (TMPs) by combining red phosphorus with conductive transition metals has been proven to be an efficient way to enhance the electronic conductivity and reduce the volume change of phosphorus-based anode materials (Fullenwarth et al., 2014; Pramanik et al., 2015; Fan et al., 2016; Wang X. et al., 2017; Zhang et al., 2017; Liu et al., 2018).

Transitional metal phosphides (TMPs, M = Fe, Cu, Co, etc.) have drawn tremendous attention because of their high specific capacity and safe operating potential (Kim et al., 2013; Qian et al., 2013; Sun et al., 2014; Zhou et al., 2017; Hu et al., 2018; Wu Y. et al., 2018). Particularly, copper phosphide-based anode materials for SIBs have a low reduction potential (0.015–0.4 V *vs*. Na^+/Na) and comparatively high specific capacity (Fan et al., 2016; Kong et al., 2018). However, similar to other conversion-type SIB anode materials, the volume expansion during the charge/discharge process has not been entirely overcome, and its diffusion kinetics is comparatively weak (Ge et al., 2017; Miao et al., 2017; Wang J. et al., 2017).

Fortunately, several effective strategies revealed promising potential ability in boosting the sodium storage performance of TMP anode materials. For example, constructing nanostructured materials, such as nanospheres and nanoparticles, can not only improve the reaction kinetics by shortening the diffusion distance of Na ions within the solid state but also relieve the mechanical strain generated by the large volume change during the conversion reaction (Xu et al., 2012; Ma et al., 2018). In addition, combining TMPs with conductive carbon matrices can also buffer the huge volume expansion and enhance the electronic conductivity of the electrode, thus resulting in better sodium storage performance (Qian et al., 2014; Li et al., 2017; Zhang et al., 2019). For instance, Cu_3P/reduced graphene oxide nanocomposite synthesized by Tong et al. showed superior cycling stability and good rate capability (Liu et al., 2016). The carbon-confined Cu_3P nanoparticles prepared by Zhou et al. exhibited superior cycling stability with a high capacity of 159 mAh g^{-1} at 1.0 A g^{-1} over 100 cycles (Kong et al., 2018). Although much progress has been achieved by reducing the particle size of Cu_3P as well as introducing conductive carbon, it still remains a major challenge to develop a scalable and inexpensive method for practical application.

Biomass-derived carbon, profiting from its economy, environmental benignity, and sustainability, has attracted increasing attention (Moreno et al., 2014; Wu et al., 2017). Among them, sodium alginate has high availability and biodegradability, is non-toxic, and of low price (Comaposada et al., 2015). In particular, sodium alginate can cross-link with di- or trivalent ions (Marcos et al., 2016), thus making it a proper carbon source to synthesize TMP anode materials combined with conductive carbon matrices.

Herein, we present the preparation of Cu_3P nanoparticles encapsulated in P/N-co-doped carbon nanosheets (Cu_3P@P/N-C) through a feasible aqueous reaction followed by a phosphorization procedure. Cu_3P nanoparticles are well-dispersed and encapsulated in two-dimensional (2D) carbon nanosheets, which can not only buffer the large volume expansion but also prevent the agglomeration of Cu_3P nanoparticles, thereby maintaining the integrity of the whole electrode. Furthermore, the 2D carbon nanosheet structure can shorten the Na^+ diffusion path, provide more active sites of Na^+, as well as enhance the electronic conductivity of the entire electrode. Benefiting from these advantages mentioned above, Cu_3P@P/N-C exhibited a long cycle life and outstanding rate performance when applied as anode for SIBs. Cu_3P@P/N-C anode materials demonstrated a long cycle life (209.3 mAh g^{-1} at 1 A g^{-1} after 1,000 cycles) and excellent rate performance (118.2 mAh g^{-1} even at a high current density of 5 A g^{-1} after 2,000 cycles).

EXPERIMENTAL SECTION

Materials

All materials in the experiment were used without further purification. $Cu(NO_3)_2{\cdot}3H_2O$ (ACS, 98.0–102.0%) was purchased from Aladdin. Sodium alginate (AR) was purchased from Aladdin. Red phosphorus (AR) was purchased from Kermel. Argon gases were supplied in cylinders by Qinghuaqiti with 99.999% purity.

Preparation of Cu-Alginate Gel

Sodium alginate (1.0 g) was dispersed in 50 ml distilled water to form an aqueous solution. $Cu(NO_3)_2{\cdot}3H_2O$ (2.0 g) was also dispersed in 50 ml distilled water to form an aqueous solution. Then, the sodium alginate aqueous solution was dropped slowly by a disposable plastic dropper into $Cu(NO_3)_2{\cdot}3H_2O$ aqueous solution to form Cu-alginate hydrogel under magnetic stirring at room temperature. The obtained hydrogel was separated from the solution after 6 h and washed with deionized water several times. The as-prepared Cu-alginate hydrogel was frozen by liquid nitrogen and then dried through freeze–drying for 24 h to obtain Cu-alginate aerogel.

Preparation of Cu_3P@P/N-C

In a typical synthesis of Cu_3P@P/N-C, Cu-aerogel was kept at 300°C for 1 h at a heating rate of 2°C min^{-1} under air atmosphere. After cooling to room temperature, the CuO@C nanosheets aerogel was collected (**Figure S1**). One hundred milligrams of the obtained CuO@C nanosheet aerogel and 200 mg red phosphorus were put into two separate ceramic boats in a tube furnace and then were heated to 800°C for 2 h under

Ar atmosphere with a heating rate of 5°C min^{-1} to produce Cu_3P@P/N-C. After cooling to room temperature, the sample was washed with deionized water three times by centrifugation and dried at 60°C in vacuum oven for 12 h.

Morphology and Structural Characterization

The morphology of the obtained samples was characterized by a field-emission scanning electron microscope (Hitachi Limited SU-8010) and transmission electron microscopy (JEOL-2100FS). The X-ray diffraction (XRD) pattern was determined by PANalytical X'Pert PRO (PANalytical X'Pert PRO, monochromated Cu Kα radiation 40 mA, 40 kV) to characterize the crystal structure. X-ray photoelectron spectroscopy (XPS) was performed with a Thermo Fisher Scientific K-Alpha (Fisher Scientific Ltd., Nepean, ON).

Electrochemical Measurements

The anode slurry was prepared by mixing 70 wt% active materials, 20 wt% Super-P, and 10 wt% polyvinylidene fluoride (PVDF) by a high-speed electric agitator for 12 h. The slurry was pressed onto a cleaned copper foil by a doctor-balding method and dried in a vacuum oven at 80°C for 12 h. The performance of the SIBs was tested using standard 2032-type coin cells in an argon-filled glove box. The separator was glass fiber (GF/D) from Whatman, and sodium foils were used as the counter and reference electrodes. The electrolyte was 1.0 M $NaClO_4$ in diethylene glycol dimethyl ether (Diglyme). The active material loading of the electrode was 0.5–0.8 mg cm^{-2}. The cells were galvanostatically charged and discharged over a cutoff voltage window of 0.01–3.00 V at room temperature on a battery test system (Shenzhen Neware Electronic Co., China). Cyclic voltammetry behavior was studied by the CHI 650d electrochemical workstation at a scan rate of 0.1 mV s^{-1}.

RESULTS AND DISCUSSION

The carbon source we chose is sodium alginate. Sodium alginate is a natural polysaccharide extracted from brown seaweeds and some kinds of bacteria, which consists of a linear copolymer of (1–4)-linked β-D-mannuronic acid (M) and α-L-guluronic acid (G) in alternating blocks. Sodium alginate has high availability and biodegradability and low price. Its aqueous solution has a high viscosity and is non-toxic, which makes it widely useful as food thickeners, stabilizers, emulsifiers, etc. (Comaposada et al., 2015; Zou et al., 2018). In particular, sodium alginate can cross-link with di- or trivalent ions to form the uniform, transparent, water-insoluble, and thermo-irreversible gels at room temperature (Marcos et al., 2016). **Scheme 1** exhibits the typical synthesis of Cu_3P@P/N-C. Sodium alginate aqueous solution was added dropwise into $Cu(NO_3)_2{\cdot}3H_2O$ aqueous solution to form Cu-alginate hydrogel balls. During the freezing process by liquid nitrogen, subsequently, the growth of the ice crystals squeezed the Cu-alginate macromolecules into 2D nanosheets. Then, the sample was dried by freeze drying. In the end, after the phosphorization procedure, Cu_3P@P/N-C was obtained.

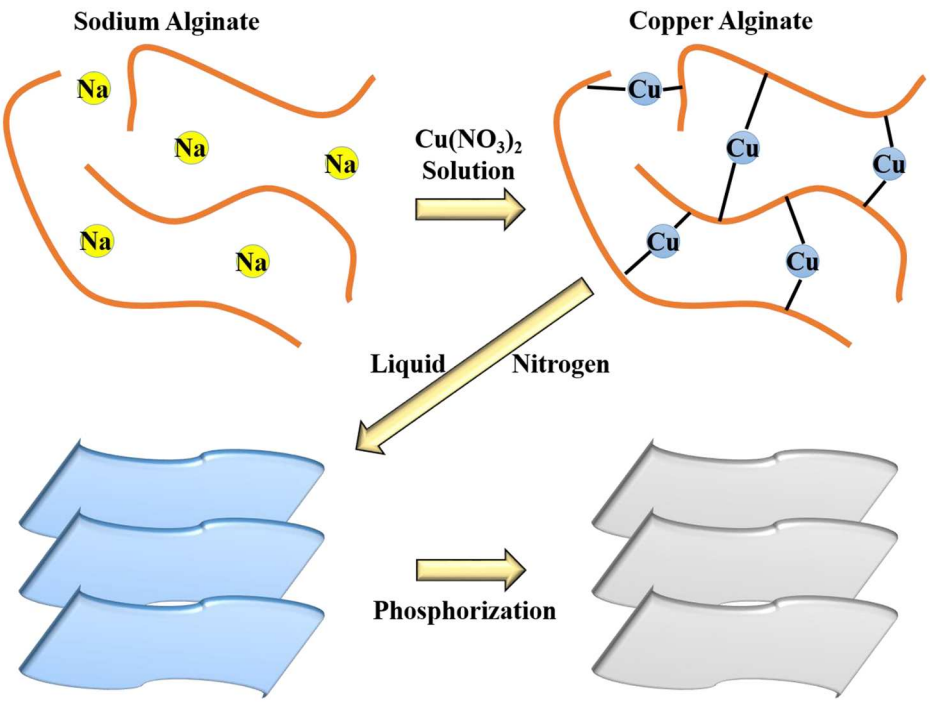

SCHEME 1 | Schematic illustration of the synthesis process of Cu_3P@P/N-C.

As shown in **Figure 1a**, the crystal structure and composition of the as-prepared samples were first tested by XRD measurements. There are several diffraction peaks in the XRD pattern of Cu_3P@P/N-C at 36.0, 39.1, 41.6, 45.1, 46.1, and 47.3°. These peaks can be indexed to the (112), (202), (211), (300), (113), and (212) lattice planes of Cu_3P crystalline (PDF#71-2261), matching well with a formerly reported study (Wang R. et al., 2018). In addition, there is a broad peak at around 24.7°, corresponding to the (002) plane of amorphous carbon. There are no other crystalline phases observed, which suggests that the as-prepared Cu_3P@P/N-C has high purity.

The morphologies of the Cu-alginate aerogel and Cu_3P@P/N-C were investigated by scanning electron microscopy (SEM). **Figure S2** exhibits the typical 2D nanosheet morphology of Cu-alginate aerogel. And as shown in **Figures 1b–d**, the 2D nanosheet morphology remained well after the phosphorization procedure. **Figure 1e** displays the typical energy-dispersive X-ray (EDX) mappings of Cu_3P@P/N-C, where P, N, Cu, and C elements were observed, suggesting the homogeneous distribution of these several elements. The distribution of P element was uniform, indicating that P not only came from Cu_3P but also doped in the carbon nanosheets. The typical 2D nanosheet morphology was also confirmed by the transmission electron microscopy (TEM) image of Cu_3P@P/N-C (**Figures 1f, g**). The Cu_3P nanoparticles with sizes of around 30 nm distributed uniformly as well as encapsulated in P/N-co-doped carbon nanosheets, which can not only provide rapid diffusion channels for the electron/ion but also prevent Cu_3P nanoparticles from agglomeration. **Figure 1h** shows the high-resolution transmission electron microscopy (HRTEM) image in which the lattice fringes can be observed distinctly. The distance of these lattice fringes is 0.20 nm, matching well with the Cu_3P crystalline (300) lattice plane (Liu et al., 2016), verifying the existence of the Cu_3P nanoparticles.

Furthermore, the X-ray photoelectron energy spectra (XPS) measurement was applied to study the detailed chemical states of Cu_3P@P/N-C. As shown in **Figure 2A**, the signals of the C, N, O, P, and Cu elements were observed obviously without other impurities. The element O may come from the absorbed O species in the air. The N element came from the nitrate radical of $Cu(NO_3)_2{\cdot}3H_2O$, which was not completely removed during the washing process. The C 1s spectrum in **Figure 2B** could be attributed to three peaks at 284.6, 286.3, and 289.1 eV. The major peak at approximately 284.6 eV was attributed to graphitic carbon. The other two peaks at 286.3 and 289.1 eV were fitted by carbon bonding with phosphorus and nitrogen, respectively, which can manifest the co-doping of both P and N atoms into the carbon nanosheets. The P2p spectrum in **Figure 2C** indicates the P chemical states in Cu_3P@P/N-C. The P2p spectrum could be fitted into four peaks at 129.9, 134.2, 135.1, and 135.6 eV. The peak at 129.9 eV was attributed to the P in Cu_3P. The two peaks at 135.1 and 135.6 eV were ascribed, respectively, to P–O and P=O bonds. And the peak at 134.2 eV could be ascribed to the C–P bond, corresponding to the C 1s bonding peak at 286.3 eV. The N 1s spectrum (**Figure 2D**) can be fitted into three component peaks at 399.4, 401.8, and 402.3 eV, which can be assigned to pyridinic nitrogen, pyrrolic nitrogen, and graphitic nitrogen, respectively. This could further confirm that both P and N are doped into the as-prepared carbon nanosheets.

The electrochemical performance of Cu_3P@P/N-C was measured in detail as anode materials for SIBs. First, its electrochemical reaction was studied by cyclic voltammetry (CV) measurements from 0.01 to 3 V at a scan rate of 0.1 mV s^{-1} (**Figure 3A**). In the first cathodic process of the CV curves of Cu_3P@P/N-C, there was a reduction peak at around 1.1 V, which can be associated with side reactions [the irreversible decomposition of the electrolyte and the formation of the solid electrolyte interface (SEI) layer on the electrode surface] (Zhu et al., 2019). Then, a strong reduction peak appeared between

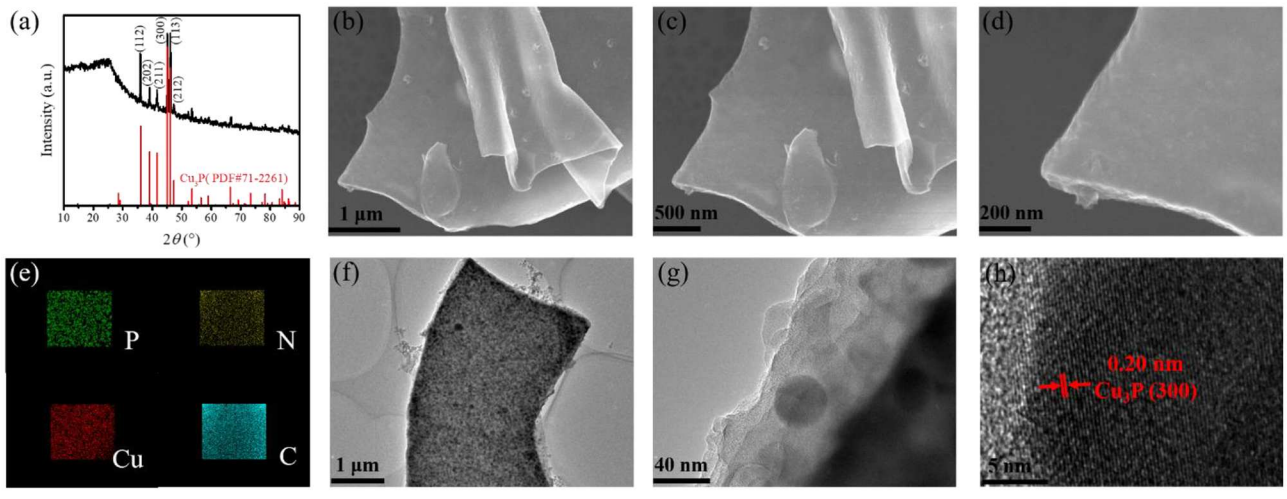

FIGURE 1 | (a) X-ray diffraction (XRD) pattern of Cu_3P@P/N-C. **(b–d)** SEM images, **(e)** energy-dispersive X-ray (EDX) mappings, **(f,g)** transmission electron microscopy (TEM) images, and **(h)** high-resolution TEM (HRTEM) image of Cu_3P@P/N-C.

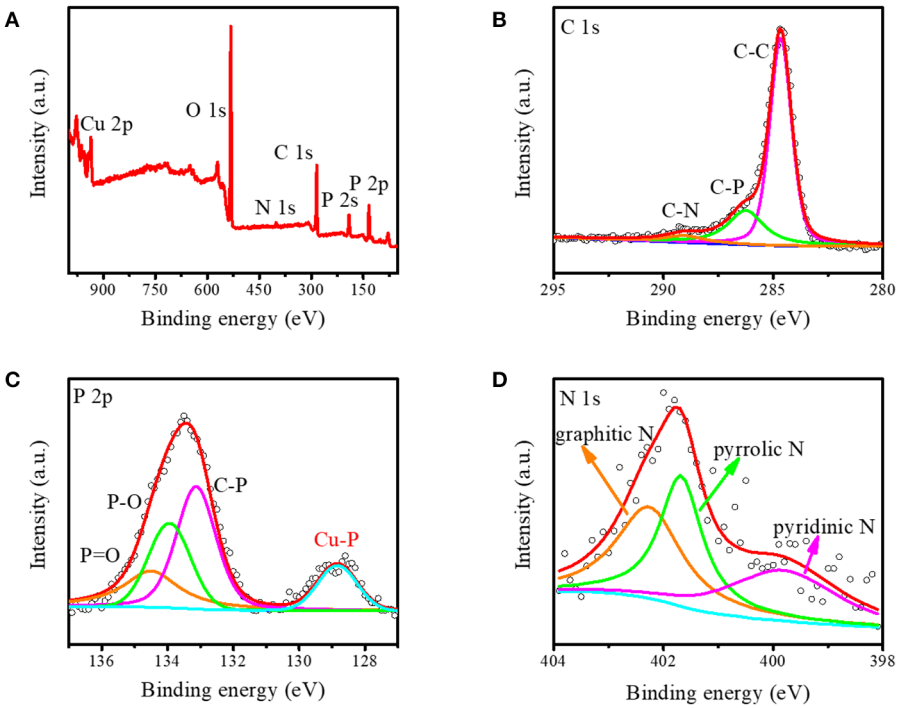

FIGURE 2 | (A) The integrated X-ray photoelectron spectroscopy (XPS) spectrum and the corresponding XPS spectrum of **(B)** carbon, **(C)** phosphorus, and **(D)** nitrogen for Cu_3P@P/N-C.

0.07 and 0.4 V, which could be ascribed to the reaction of Cu_3P with sodium. In the anodic scan process, the reverse of this reaction formed a distinct oxidation peak at around 0.9 V, as the following equation with the release of sodium ions shows:

$$Na_3P + 3Cu \rightarrow Cu_3P + 3Na^+ \quad (1)$$

The CV profiles from the second to the fifth cycles matched well, indicating the highly reversible and stable cycling performance of Cu_3P@P/N-C as SIB anode materials.

Figure 3B shows the galvanostatic cycling performance of the Cu_3P@P/N-C electrode under 1.0 A g^{-1} (0.01 and 3.0 V vs. Na^+/Na). Pure Cu_3P was also synthesized by the phosphorization of commercial Cu powder using red phosphorus as a P source for comparison (as shown in **Figures S3–S5**). Compared with pure Cu_3P, the Cu_3P@P/N-C electrode exhibited better electrochemical performance, maintaining an excellent reversible capacity of 209.3 mAh g^{-1} at 1.0 A g^{-1} after 1,000 cycles. The charge–discharge profiles of the initial three cycles of Cu_3P@P/N-C are shown in **Figure S6**. The initial discharge and charge capacities were 1,029.6 and 562.3 mAh g^{-1}; thus, the initial coulombic efficiency was 54.6%. This capacity loss was mainly caused by the irreversible formation of the SEI layer. Additionally, to estimate the sodium storage performance of the Cu_3P@P/N-C electrode at a high rate, a high current density at 5.0 A g^{-1} was chosen. An outstanding cycling performance of 118.2 mAh g^{-1} is maintained (**Figure 3E**), even after 2,000 cycles. As shown in **Table S1**, Cu_3P@P/N-C exhibited superior cycling performance and excellent rate performance. In sharp contrast to Cu_3P@P/N-C, pure Cu_3P had rapid capacity loss, resulting in only 44.0 mAh g^{-1} at 1.0 A g^{-1} after 200 cycles and 30.6 mAh g^{-1} at 5.0 A g^{-1} after 500 cycles. Thereby, the superior cycling performance of Cu_3P@P/N-C reflects their structural stability as anode materials for SIBs. The SEM images and the EDX mappings of the selected area of Cu_3P@P/N-C after 500 cycles are exhibited in **Figures S7**, **S8**. The typical nanosheet morphology of Cu_3P@P/N-C can still be observed obviously, indicating its superior stability.

Electrochemical impedance spectroscopy (EIS) was investigated to further understand the cycling performance of Cu_3P@P/N-C. As shown in **Figure 3D**, the semicircle in the high-frequency region corresponded to the charge transfer resistance of the electrode. The sloped line in the low-frequency region is attributed to the Warburg impendence. After the first cycle, the semicircle became much smaller, which could be explained by the formation of the SEI layer. The semicircles overlaid well after the second cycle, indicating the excellent cycling stability of Cu_3P@P/N-C.

Figure 3C shows the rate performance of the Cu_3P@P/N-C and pure Cu_3P electrodes. The current densities were selected from 0.2 to 10 A g^{-1}. The reversible specific capacities acquired were of 311.8, 250.3, 226.8, 207.2, 177.1, and 144.8 mAh g^{-1} at the current densities of 0.2, 0.5, 1, 2, 5, and 10 A g^{-1}, respectively. When the current density was set back to 0.2 A g^{-1}, the reversible specific capacity remained at 265.2 mAh g^{-1}, suggesting the outstanding rate performance. On the contrary,

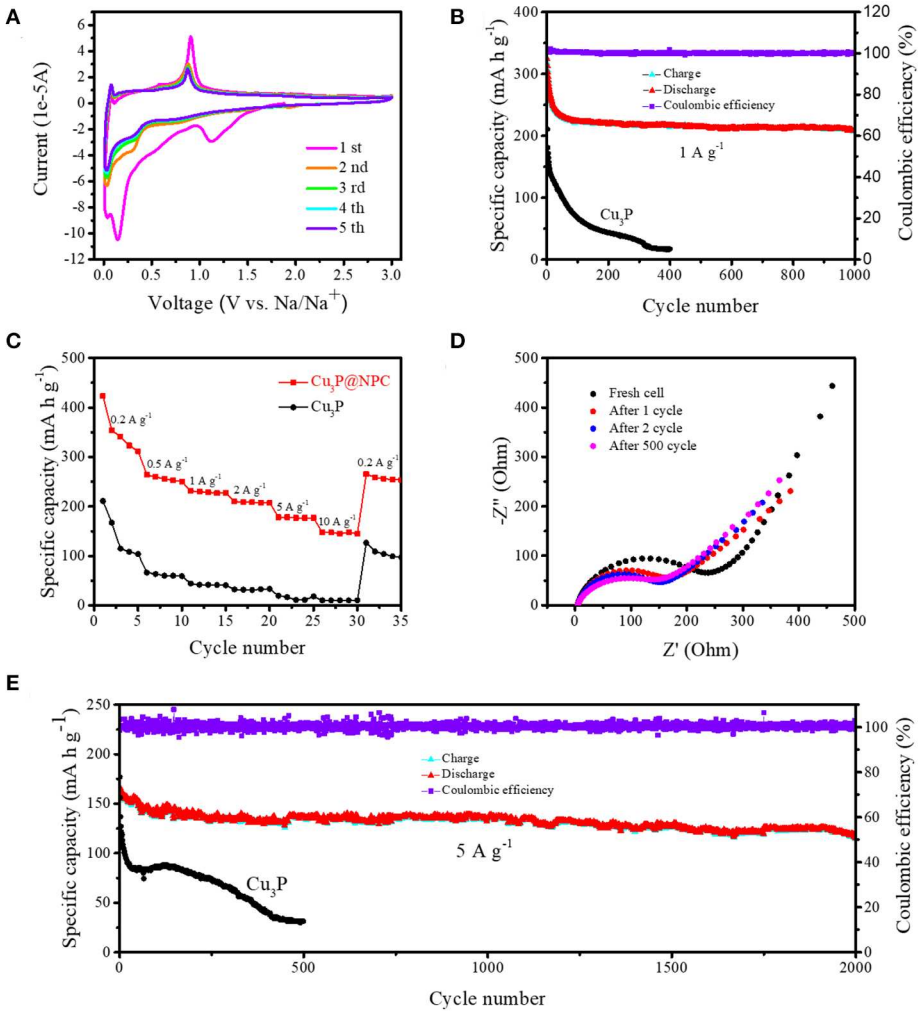

FIGURE 3 | (A) Cyclic voltammetry (CV) curves of Cu_3P@P/N-C at a scan rate of 0.1 mV s^{-1} in the initial five cycles. **(B)** Cycling performance at a current density of 1 A g^{-1} and **(C)** rate performance of Cu_3P@P/N-C and pure Cu_3P. **(D)** Electrochemical impedance spectroscopy (EIS) curves of Cu_3P@P/N-C at different cycles during the first 500 cycles. **(E)** Cycling performance at a current density of 5 A g^{-1} of Cu_3P@P/N-C and pure Cu_3P.

pure Cu_3P showed reversible specific capacities of only 104.0, 59.1, 41.0, 33.4, 18.1, and 10.2 mAh g^{-1} at the current densities of 0.2, 0.5, 1, 2, 5, and 10 A g^{-1}, respectively, which were far inferior to those of Cu_3P@P/N-C. The difference between these two materials could be ascribed to the introduction of P/N-co-doped carbon nanosheets, which could enhance the electron transfer during the discharge/charge process.

To further understand the electrochemical reaction process of the Cu_3P@P/N-C electrode, we disassembled the cells for the *ex situ* XRD measurement at different states during the charge and discharge processes. As shown in **Figure 4**, the pristine Cu_3P@P/N-C electrode only exhibited diffraction peaks of Cu_3P. During the discharge process, the primary diffraction peak of Cu_3P at around 45.1° corresponding to the (300) plane gradually receded and almost disappeared when completely discharged to 0.01 V. At the same time, a peak at about 43.5° came out, originating from the generation of Cu. In addition, a new peak came out at about 37° corresponding to the (103) plane of Na_3P. During the charging process, the above composition change reversed. Such observations can identify the reversible sodiation/desodiation process of Cu_3P conducting by conversion mechanism as in the following equation (Fan et al., 2016):

$$Cu_3P + 3Na \leftrightarrow Na_3P + 3Cu \quad (2)$$

This conversion mechanism was consistent with the CV measurements.

CONCLUSION

In summary, through a feasible aqueous reaction at room temperature followed by a phosphorization procedure, we have successfully fabricated biomass-derived P/N-co-doped

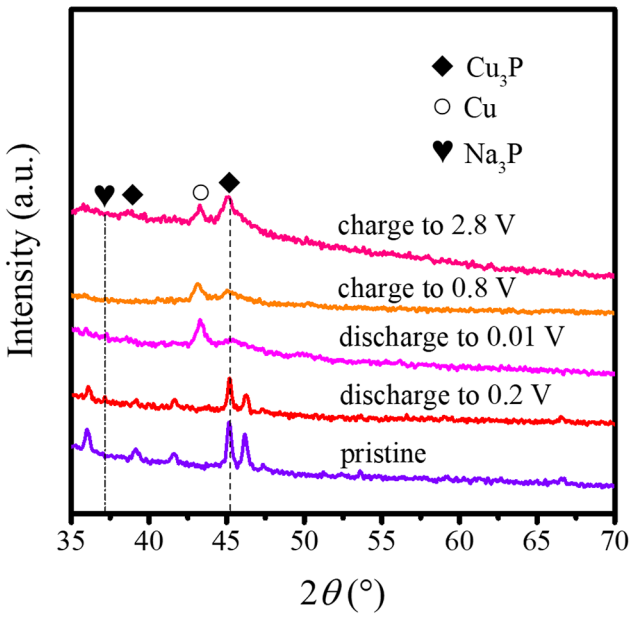

FIGURE 4 | *Ex situ* XRD patterns of Cu_3P@P/N-C at different states during charge and discharge processes.

carbon nanosheets encapsulating Cu_3P nanoparticles as high-performance anode materials for sodium-ion batteries. Given the help of the 2D P/N-co-doped carbon nanosheets, the Cu_3P nanoparticles could be well-encapsulated, thus being prevented from agglomeration. When applied as anode materials, superior cycling stability and excellent rate performance were exhibited. Prominently, Cu_3P@P/N-C exhibited an outstanding reversible capacity of 209.3 mAh g^{-1} at 1 A g^{-1} after 1,000 cycles. In particular, an excellent specific capacity of 118.2 mAh g^{-1} could be maintained after 2,000 cycles, even at an ultrahigh current density of 5 A g^{-1}. This remarkable electrochemical performance is mainly attributed to the rational design of the 2D P/N-co-doped carbon nanosheet structure, which could buffer the volume change of Cu_3P nanoparticles as well as improve the electron/ion transport kinetics during the Na^+ insertion/extraction process. Additionally, the 2D P/N-co-doped carbon nanosheets also could serve as a conductive matrix, which could enhance the electronic conductivity of the electrode. This feasible and facile preparation approach could be further developed to the synthesis of a variety of 2D P/N-co-doped carbon nanosheets encapsulating TMP electrodes for energy storage devices.

DATA AVAILABILITY STATEMENT

All datasets generated for this study are included in the article/**Supplementary Material**.

AUTHOR CONTRIBUTIONS

YY and NZ contributed to the conception and design of the study. YY organized the database. YY, YZ, and NL performed the statistical analysis. YY wrote the manuscript. BS and NZ helped perform the analysis with constructive discussions. All authors contributed to manuscript revision, read, and approved the submitted version.

FUNDING

This work was supported by the National Natural Science Foundation of China (no. 21646012), China Postdoctoral Science Foundation (nos. 2016M600253, 2017T100246), the State Key Laboratory of Urban Water Resource and Environment, Harbin Institute of Technology (no. 2019DX13), and the Fundamental Research Funds for the Central Universities (grant no. HIT. NSRIF. 201836). BS gratefully acknowledges financial support by the Australian Research Council (ARC) through the ARC Discovery Early Career Researcher Award (DE180100036).

SUPPLEMENTARY MATERIAL

The Supplementary Material for this article can be found online at: https://www.frontiersin.org/articles/10.3389/fchem.2020.00316/full#supplementary-material

REFERENCES

Comaposada, J., Gou, P., Marcos, B., and Arnau, J. (2015). Physical properties of sodium alginate solutions and edible wet calcium alginate coatings. *LWT Food Sci. Technol.* 64, 212–219. doi: 10.1016/j.lwt.2015.05.043

Fan, M., Chen, Y., Xie, Y., Yang, T., Shen, X., Xu, N., et al. (2016). Half-cell and full-cell applications of highly stable and binder-free sodium ion batteries based on Cu_3P nanowire anodes. *Adv. Funct. Mater.* 26, 5019–5027. doi: 10.1002/adfm.201601323

Fullenwarth, J., Darwiche, A., Soares, A., Donnadieu, B., and Monconduit, L. (2014). NiP_3: a promising negative electrode for Li- and Na-ion batteries. *Mater. J. Chem. A.* 2, 2050–2059. doi: 10.1039/C3TA13976J

Ge, X., Li, Z., and Yin, L. (2017). Metal-organic frameworks derived porous core/shell CoP@C polyhedrons anchored on 3D reduced graphene oxide networks as anode for sodium-ion battery. *Nano Energy* 32, 117–124. doi: 10.1016/j.nanoen.2016.11.055

Hu, Y., Li, B., Jiao, X., Zhang, C., Dai, X., and Song, J. (2018). Stable cycling of phosphorus anode for sodium-ion batteries through chemical bonding with sulfurized polyacrylonitrile. *Adv. Funct. Mater.* 28:1801010. doi: 10.1002/adfm.201801010

Kim, Y., Park, Y., Choi, A., Choi, N.-S., Kim, J., Lee, J., et al. (2013). An amorphous red phosphorus/carbon composite as a promising anode material for sodium ion batteries. *Adv. Mater.* 25, 3045–3049. doi: 10.1002/adma.201204877

Kong, M., Song, H., and Zhou, J. (2018). Metal–organophosphine framework-derived N,P-codoped carbon-confined Cu_3P nanopaticles for superb na-ion storage. *Adv. Energy Mater.* 8:1801489. doi: 10.1002/aenm.201801489

Kundu, D., Talaie, E., Duffort, V., and Nazar, F. L. (2015). The emerging chemistry of sodium ion batteries for electrochemical energy storage. *Angew. Chem. Int. Ed.* 54, 3431–3448. doi: 10.1002/anie.201410376

Larcher, D., and Tarascon, M. J. (2015). Towards greener and more sustainable batteries for electrical energy storage. *Nat. Chem.* 7, 19–29. doi: 10.1038/nchem.2085

Li, F., and Zhou, Z. (2018). Micro/nanostructured materials for sodium ion batteries and capacitors. *Small* 14:1702961. doi: 10.1002/smll.201702961

Li, Z., Zhang, L., Ge, X., Li, C., Dong, S., Wang, C., et al. (2017). Core-shell structured CoP/FeP porous microcubes interconnected by reduced graphene oxide as high performance anodes for sodium ion batteries. *Nano Energy* 32, 494–502. doi: 10.1016/j.nanoen.2017.01.009

Liu, S., He, X., Zhu, J., Xu, L., and Tong, J. (2016). Cu_3P/RGO nanocomposite as a new anode for lithium-ion batteries. *Sci. Rep*. 6:35189. doi: 10.1038/srep35189

Liu, Z., Yang, S., Sun, B., Chang, X., Zheng, J., and Li, X. (2018). Peapod-like CoP@C nanostructure from phosphorization in low-temperature molten salt for high-performance lithium ion batteries. *Angew. Chem. Int. Ed*. 57, 10187–10191. doi: 10.1002/anie.201805468

Lotfabad, M. E., Ding, J., Cui, K., Kohandehghan, A., Kalisvaart, P. W., and Hazelton, M. (2014). High-density sodium and lithium ion battery anodes from banana peels. *ACS Nano* 8, 7115–7129. doi: 10.1021/nn502045y

Ma, Y., Ma, Y., Bresser, D., Ji, Y., Geiger, D., Kaiser, U., et al. (2018). Cobalt disulfide nanoparticles embedded in porous carbonaceous micro-polyhedrons interlinked by carbon nanotubes for superior lithium and sodium storage. *ACS Nano*. 12, 7220–7231. doi: 10.1021/acsnano.8b03188

Marcos, B., Gou, P., Arnau, J., and Comaposada, J. (2016). Influence of processing conditions on the properties of alginate solutions and wet edible calcium alginate coatings. *LWT Food Sci Technol*. 74, 271–279. doi: 10.1016/j.lwt.2016.07.054

Miao, X., Yin, R., Ge, X., Li, Z., and Yin, L. (2017). Ni_2P@Carbon core–shell nanoparticle-arched 3D interconnected graphene aerogel architectures as anodes for high-performance sodium-ion batteries. *Small* 13:1702138. doi: 10.1002/smll.201702138

Moreno, N., Caballero, A., Hernán, L., and Morales, J. (2014). Lithium–sulfur batteries with activated carbons derived from olive stones. *Carbon* 70, 241–248. doi: 10.1016/j.carbon.2014.01.002

Pramanik, M., Tsujimoto, Y., Malgras, V., Dou, S. X., Kim, J. H., Yamauchi, Y., et al. (2015). Mesoporous iron phosphonate electrodes with crystalline frameworks for lithium-ion batteries. *Chem. Mater*. 27, 1082–1089. doi: 10.1021/cm5044045

Qian, J., Wu, X., Cao, Y., Ai, X., and Yang, H. (2013). High capacity and rate capability of amorphous phosphorus for sodium ion batteries. *Angew. Chem. Int. Ed*. 52, 4633–4636. doi: 10.1002/anie.201209689

Qian, J., Xiong, Y., Cao, Y., Ai, X., and Yang, H. (2014). Synergistic Na-storage reactions in Sn_4P_3 as a high-capacity, cyclestable anode of na-ion batteries. *Nano Lett*. 14, 1865–1869. doi: 10.1021/nl404637q

Qiu, L., Xiang, W., Tian, W., Xu, C.-L., Li, Y.-C., Wu, Z.-G., et al. (2019). Polyanion and cation co-doping stabilized Ni-rich Ni–Co–Al material as cathode with enhanced electrochemical performance for Li-ion battery. *Nano Energy*. 63:103818. doi: 10.1016/j.nanoen.2019.06.014

Song, J., Xiao, B., Lin, Y., Xu, K., and Li, X. (2018). Interphases in sodium-ion batteries. *Adv. Energy Mater*. 8:1703082. doi: 10.1002/aenm.201703082

Sun, J., Zheng, G., Lee, H.-W., Liu, N., Wang, H., Yao, H., et al. (2014). Formation of stable phosphorus-carbon bond for enhanced performance in black phosphorus nanoparticle-graphite composite battery anodes. *Nano Lett*. 14, 4573–4580. doi: 10.1021/nl501617j

Wang, J., Liu, Z., Zheng, Y., Cui, L., Yang, W., and Liu, J. (2017). Recent advances in cobalt phosphide based materials for energy-related applications. *J. Mater. Chem. A* 5, 22913–22932. doi: 10.1039/C7TA08386F

Wang, R., Dong, X. Y., Du, J., Zhao, J. Y., and Zang, Q, S. (2018). MOF-derived bifunctional Cu_3P nanoparticles coated by a N,P-codoped carbon shell for hydrogen evolution and oxygen reduction. *Adv. Mater*. 30:1703711. doi: 10.1002/adma.201703711

Wang, X., Chen, K., Wang, G., Liu, X., and Wang, H. (2017). Rational design of three-dimensional graphene encapsulated with hollow FeP@carbon nanocomposite as outstanding anode material for lithium ion and sodium ion batteries. *ACS Nano* 11, 11602–11616. doi: 10.1021/acsnano.7b06625

Wang, Y., Fu, Q., Li, C., Li, H., and Tang, H. (2018b). Nitrogen and phosphorus dual-doped graphene aerogel confined monodisperse iron phosphide nanodots as an ultrafast and long-term cycling anode material for sodium-ion batteries. *ACS Sustain. Chem. Eng*. 6, 15083–15091. doi: 10.1021/acssuschemeng.8b03561

Wang, Y., Wu, C., Wu, Z., Cui, G., Xie, F., Guo, X., et al. (2018a). FeP Nanorod arrays on carbon cloth: a high-performance anode for sodium-ion batteries. *Chem. Commun*. 54, 9341–9344. doi: 10.1039/C8CC03827A

Wessells, D. C., Peddada, V. S. A., Huggins, R., and Cui, Y. (2011). Nickel hexacyanoferrate nanoparticle electrodes for aqueous sodium and potassium ion batteries. *Nano Lett*. 11, 5421–5425. doi: 10.1021/nl203193q

Wu, C., Hua, W., Zhang, Z., Zhong, B., Yang, Z., Feng, G., et al. (2018). Design and synthesis of layered $Na_2Ti_3O_7$ and tunnel $Na_2Ti_6O_{13}$ hybrid structures with enhanced electrochemical behavior for sodium-ion batteries. *Adv. Sci*. 5:1800519. doi: 10.1002/advs.201800519

Wu, X., Fan, L., Wang, M., Cheng, J., Wu, H., Guan, B., et al. (2017). A long-life lithium-sulfur battery derived from nori based nitrogen and oxygen dual-doped 3D hierarchical biochar. *ACS Appl. Mater. Interfaces* 9, 18889–18896. doi: 10.1021/acsami.7b04583

Wu, Y., Liu, Z., Zhong, X., Cheng, X., Fan, Z., and Yu, Y. (2018). Amorphous red phosphorus embedded in sandwiched porous carbon enabling superior sodium storage performances. *Small* 14:1703472. doi: 10.1002/smll.201703472

Xiao, Y., Wang, P.-F., Yin, Y.-X., Zhu, Y.-F., Niu, Y.-B., Zhang, X.-D., et al. (2018). Exposing {010} active facets by multiple-layer oriented stacking nanosheets for high-performance capacitive sodium-ion oxide cathode. *Adv. Mater*. 30:1803765. doi: 10.1002/adma.201803765

Xiao, Y., Zhu, Y., Xiang, W., Wu, Z., Li, Y., Lai, J., et al. (2020). Deciphering abnormal layered-tunnel heterostructure induced via chemical substitution for sodium oxide cathode. *Angew. Chem. Int. Ed*. 59, 1491–1495. doi: 10.1002/anie.201912101

Xu, X., Cao, R., Jeong, S., and Cho, J. (2012). Spindle-like mesoporous α-Fe_2O_3 anode material prepared from MOF template for high-rate lithium batteries. *Nano Lett*. 12, 4988–4991. doi: 10.1021/nl302618s

Zhang, B., Dugas, R., Rousse, G., Rozier, P. M., Abakumov, A., and Tarascon, J. N. (2016). Insertion compounds and composites made by ball milling for advanced sodium-ion batteries. *Nat. Commun*. 7:10308. doi: 10.1038/ncomms10308

Zhang, H., Hasa, I., and Passerini, S. (2018). Beyond insertion for Na-Ion batteries: nanostructured alloying and conversion anode materials. *Adv. Energy Mater*. 8:1702582. doi: 10.1002/aenm.201702582

Zhang, K., Park, M., Zhang, J., Lee, G.-H., Shin, J., and Kang, Y.-M. (2017). Cobalt phosphide nanoparticles embedded in nitrogendoped carbon nanosheets: promising anode material with high rate capability and long cycle life for sodiumion batteries. *Nano Res*. 10, 4337–4350. doi: 10.1007/s12274-017-1649-5

Zhang, Y., Wang, G., Wang, L., Tang, L., Zhu, M., Wu, C., et al. (2019). Graphene-encapsulated CuP_2: a promising anode material with high reversible capacity and superior rate-performance for sodium-ion batteries. *Nano Lett*. 19, 2575–2582. doi: 10.1021/acs.nanolett.9b00342

Zhou, J., Liu, X., Cai, W., Zhu, Y., Liang, J., Zhang, K., et al. (2017). Wet-chemical synthesis of hollow red-phosphorus nanospheres with porous shells as anodes for high-performance lithium-ion and sodium-ion batteries. *Adv. Mater*. 29:1700214. doi: 10.1002/adma.201700214

Zhu, J., He, Q., Liu, Y., Key, J., Nie, S., Wu, M., et al. (2019). Three-dimensional, hetero-structured, Cu_3P@C nanosheets with excellent cycling stability as Naion battery anode material. *J. Mater. Chem. A*. 7, 16999–17007. doi: 10.1039/C9TA04035H

Zou, Y., Chang, G., Chen, S., Liu, T., Xia, Y., Chen, C., et al. (2018). Alginate/r-GO assisted synthesis of ultrathin $LiFePO_4$ nanosheets with oriented (0 1 0) facet and ultralow antisite defect. *Chem. Eng. J*. 351, 340–347. doi: 10.1016/j.cej.2018.06.104

Zou, Y., Yang, X., Lv, C., Liu, T., Xia, Y., Shang, L., et al. (2017). Multishelled Ni-Rich $Li(Ni_xCo_yMn_z)O_2$ hollow fibers with low cation mixing as high-performance cathode materials for li-ion batteries. *Adv. Sci*. 4:1600262. doi: 10.1002/advs.201600262

Zou, Y., Zhang, W., Chen, N., Chen, S., Xu, W., Cai, R., et al. (2019). Generating oxygen vacancies in MnO hexagonal sheets for ultralong life lithium storage with high capacity. *ACS Nano* 13, 2062–2071. doi: 10.1021/acsnano.8b08608

Conflict of Interest: The authors declare that the research was conducted in the absence of any commercial or financial relationships that could be construed as a potential conflict of interest.

frontiers in Chemistry

ORIGINAL RESEARCH
published: 04 June 2020
doi: 10.3389/fchem.2020.00428

Nitrogen-Doped Graphene via *In-situ* Alternating Voltage Electrochemical Exfoliation for Supercapacitor Application

Mingjun Jing[1,2], *Tianjing Wu*[1,2]*, *Yazheng Zhou*[2], *Xilong Li*[2] *and Yong Liu*[1]*

[1] State Key Laboratory of Powder Metallurgy, Central South University, Changsha, China, [2] Department of Chemistry, Xiangtan University, Xiangtan, China

OPEN ACCESS

Edited by:
Weihua Chen,
Zhengzhou University, China

Reviewed by:
Liwei Mi,
Zhongyuan University of Technology, China
Xifei Li,
Xi'an University of Technology, China
Yufeng Zhao,
Shanghai University, China

***Correspondence:**
Tianjing Wu
twu@xtu.edu.cn
Yong Liu
yonliu@csu.edu.cn

Specialty section:
This article was submitted to Electrochemistry, a section of the journal Frontiers in Chemistry

Received: 07 February 2020
Accepted: 23 April 2020
Published: 04 June 2020

Citation:
Jing M, Wu T, Zhou Y, Li X and Liu Y (2020) Nitrogen-Doped Graphene via In-situ Alternating Voltage Electrochemical Exfoliation for Supercapacitor Application. Front. Chem. 8:428. doi: 10.3389/fchem.2020.00428

Doping heteroatom, an effective way to enhance the electrochemical performances of graphene, has received wide attention, especially related to nitrogen. Alternating voltage electrochemical exfoliation, as a low cost and green electrochemical approach, has been developed to construct *in-situ* N-doped graphene (N-Gh) material. The N-Gh presents a much higher capacity than that of pure graphene prepared via the same method, which might be attributed to the introduction of nitrogen, which has much more effects and a disordered structure. As-prepared N-Gh exhibits a low O/C ratio that is helpful in maintaining high electrical conductivity. And the effects and disorder structure are also conductive to reduce the overlaps of graphene layers. A symmetric supercapacitor assembled with N-Gh electrodes displays a satisfactory rate behavior and long cycling stability (92.3% retention after 5,000 cycles).

Keywords: N-doped graphene, alternating voltage, electrochemical exfoliation, electrochemical performances, supercapacitors

INTRODUCTION

Graphene exhibits exceptional electronic conductive ability and carrier mobility due to its unique quantum Hall effect on a honeycomb sp^2 carbon lattice. Because of this, it became one of the most significant candidate materials for next-generation electronic and energy storage devices (Novoselov et al., 2004; Low et al., 2013; Gong et al., 2016). It is important to note that heteroatom-doped graphene might be better applied to supercapacitors through creating defects or embedding impurities. Among the various kinds of heteroatom-doped graphene materials, N atom is a general nominee because of its atomic size similarity to the carbon atom and unique valence electrons that generate a stable covalent bonds structure with adjacent C atoms (Low et al., 2013; Chaban and Prezhdo, 2015; Xu et al., 2018). Meanwhile, nitrogen atoms in N-doped graphene materials could become a redox active center, which might induce pseudocapacitance to increase the specific capacitance of materials (Luo et al., 2013; Yang et al., 2016). Hence, N-doped graphene or N-doped graphene-based composite materials are getting more and more attention.

In situ doping can be favorable for the formation of homogeneous doping (Qu et al., 2010; Yang et al., 2016). Some approaches have been developed to construct N-doped graphene. For example,

N-graphene has been obtained via the chemical vapor deposition (CVD) method using a nitrogen-containing mixed gas (Bulusheva et al., 2017; Bu et al., 2018). Additionally, N-graphene also can be formed through the segregation growth approach (Zhang et al., 2011). However, most of these methods usually require expensive devices, multistep transfer processes, or result in a low yield. At present, developing a green and low cost method to prepare mass production of N-doped graphene is still a major challenge.

There are several methods for graphene preparation, such as chemical vapor deposition (Suk et al., 2011), epitaxial growth (Yang W. et al., 2013), mechanical exfoliation (Yi and Shen, 2015), chemical exfoliation (Liu and Wang, 2011), electrochemical exfoliation (Yang et al., 2015; Bakunin et al., 2019), and so on. It is worth noting that electrochemical exfoliation has been deemed a useful technique in producing high-quality graphene on a large scale owing to it being environmentally friendly, low cost, and requiring only simple operations (Low et al., 2013; Ejigu et al., 2019). Two electrochemical types, cathodic and anodic methods, have been mainly performed in electrochemical exfoliation with graphite as a working electrode. On the one hand, cathodic exfoliation with the graphite material as a cathode usually takes place in organic solvents (Yang Y. et al., 2013; Taheri Najafabadi and Gyenge, 2015). This process typically needs some intercalates cations from the electrolyte, such as alkylammonium salts, ionic liquids, molten salts, and so on. On the other hand, anodic exfoliation is typically carried out in aqueous electrolytes with graphite as an anode (Parvez et al., 2014). The main issue of this method is the requirement of a high positive voltage (about a few tens of volts) in the electrochemical process, which might induce structural degradation and oxidation of the carbon lattice. Recently, a novel alternating voltage electrochemical exfoliation approach has been applied to prepare few-layer graphene flakes in aqueous electrolytes (Jing et al., 2015). Compared with the direct voltage exfoliation, the degree of oxidation of the carbon lattice can be reduced in the alternative redox process. And the two graphite electrodes are used as working electrodes during the alternating voltage process, which is conducive to improving the exfoliation efficiency.

Electrolyte solution is one of the key factors in all types of electrochemical exfoliation methods. Li salts as cathodic exfoliation electrolyte organic solution can release Li^+ ions that are reversibly intercalated into the inner spacing of graphite (Low et al., 2013). Aqueous H_2SO_4 solution as anodic exfoliation electrolyte system can produce oxygen radicals (O·) and hydroxyl (OH·) to open boundaries, which is helpful in facilitating SO_4^{2-} intercalation, and then releasing SO_2 to expand the interlayer distance of graphite (Yang et al., 2015). Inorganic salts aqueous solutions (such as $(NH_4)_2SO_4$) as anodic exfoliation electrolyte system shows a similar electrochemical mechanism in H_2SO_4 solution, except for the existence of OH^- ions at the edge sites and grain boundaries (Zabihi et al., 2019). Aqueous $NaOH/H_2O_2$ solution has also been utilized during anodic electrochemical exfoliation, which could generate OH^- and O_2^{2-} intercalation ions and appears to result in NaOH-induced electrochemical reduction of the oxygen functional groups of graphene (Rao et al., 2014). In addition, a range of reductive agents [such as sodium borohydride, (2,2,6,6-tetramethylpiperidin-1-yl]oxyl, ascorbic acid, and so on) as additives in electrolyte solution can improve the atomic ratio of C/O and control the exfoliation process (Rao et al., 2014). All these previous studies further indicate that the composition of electrolyte solution could mainly influence the functional groups, defects, atomic ratio of C/O, and yield of graphene. Based on the above analysis, *in-situ* nitrogen doping approaches might be achieved via adding nitrogen compounds into electrolyte solution during the electrochemical exfoliation of graphite. At present, few nitrogen compounds as additives (protic ionic liquid ethylammonium nitrate, ammonia, and natural biocompatible glycine) have been discussed to produce N-doped graphene in an anodic electrochemical exfoliation process (Usachov et al., 2011; Wang et al., 2012). But the related research is still poor, especially utilizing an alternating voltage electrochemical technique.

In this study, the alternating voltage electrochemical technique has been successfully applied to *in-situ* construct N-doped graphene (N-Gh) on a large scale by adding ammonium chloride salt to NaOH aqueous solution. Compared with as-prepared pure graphene (Gh) utilizing the same process, the N-Gh sample presents a larger size and much more effects. And the electrochemical properties of N-Gh have been investigated in three-electrode and two-electrode systems. The N-Gh sample reveals a satisfactory rate behavior and long cycling stability.

EXPERIMENTAL SECTION

Synthesis of N-Doped Graphene Electrode Material

Alternating voltage electrochemical exfoliation was fabricated with a two-electrode system utilizing two graphite rods as working electrodes. N-doped graphene (N-Gh) was prepared in 3 M NaOH and 3 M NH_4Cl mixed aqueous solution. Both graphite rods were exfoliated via 5.0 V alternating voltage (50 Hz, YK-BP81005 regulator transformer) for 5 h. Then the as-exfoliated substrate was separated, and further washed using distilled water until the pH value was close to 7. At last, the N-Gh sample was obtained via the freeze-dried method. Pure graphene (Gh) was also put in 3 M NaOH aqueous solution under the same preparation conditions.

Materials Characterization

The phase character of materials was studied via the X-ray diffractometer (XRD, Rigaku D/max 2550 VB^+) from 10 to 80^o at 5° min^{-1} with Cu Kα radiation. The raman spectra of the as-prepared products were collected using a Raman spectrometer (HORIBA Labram HR Evolution). The morphology of the as-obtained materials were explored through scanning electron microscopy (SEM, JSM-6510LV) and transmission electron microscopy (TEM, JEM-2100F). Furthermore, the atomic arrangement was studied utilizing high-resolution transmission electron microscopy (HRTEM, JEM-2100F). Then, FT–IR spectrophotometer (AVTATAR, 370) was applied to test the surface functional groups

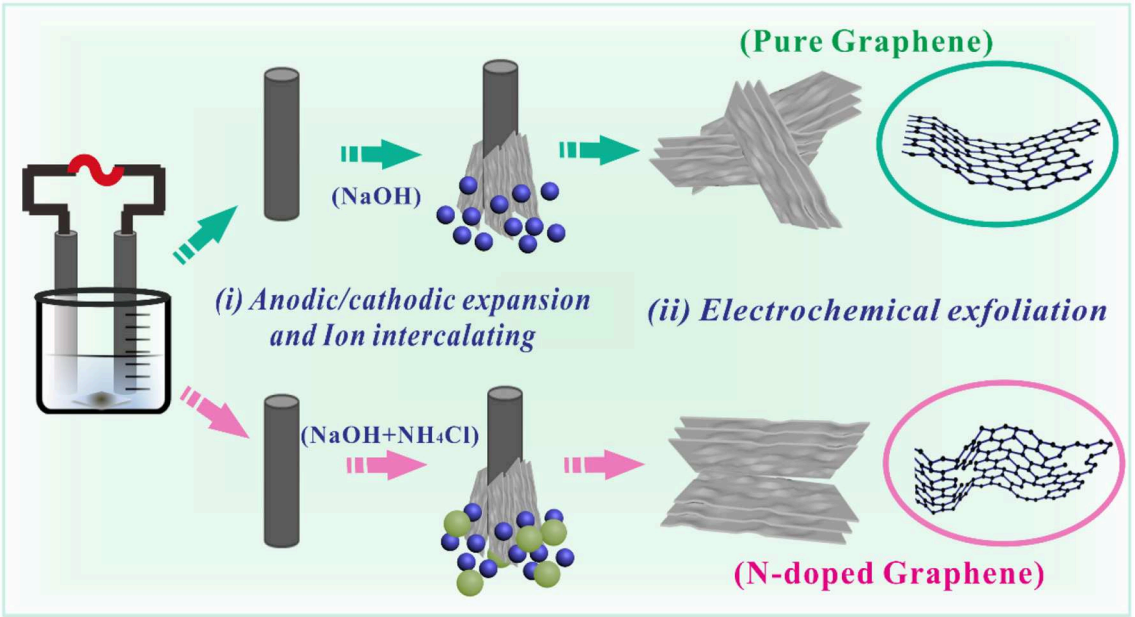

SCHEME 1 | The electrochemical formation of pure Gh and N-Gh samples.

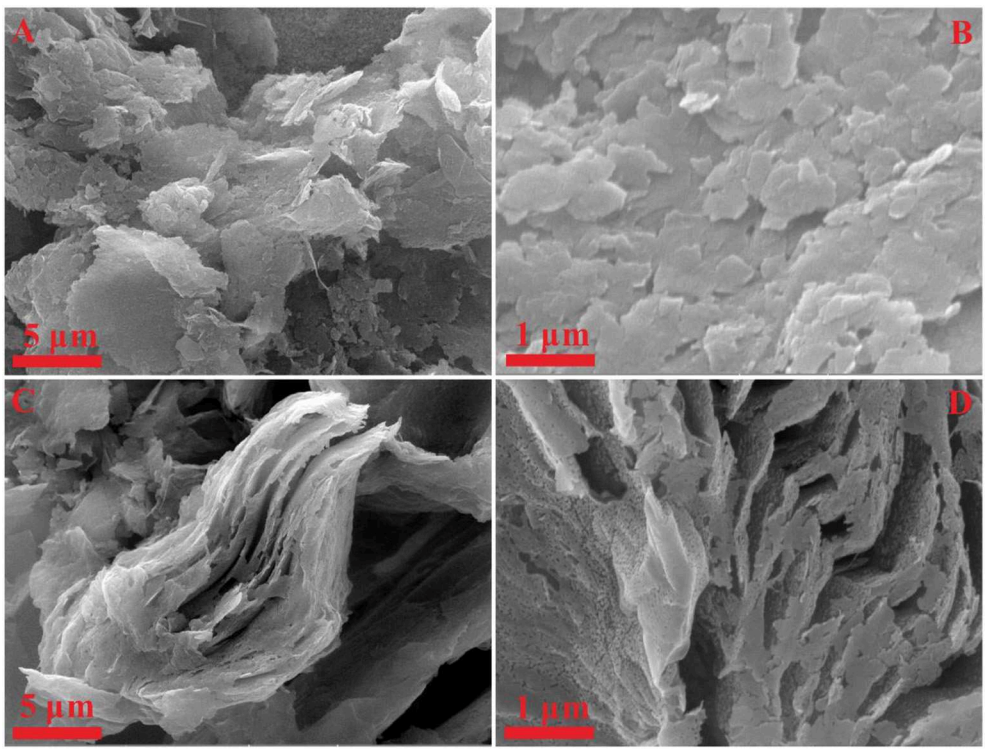

FIGURE 1 | (A,B) SEM images of pure Gh. **(C,D)** SEM images of N-Gh sample.

of materials using KBr as a reference. Thermogravimetric analysis (TGA, NETZSCH STA449F3) from 25 to 900°C was utilized to measure the thermostability of materials with a heating rate of 5°C min^{-1} in air. Moreover, X-ray photoelectron Spectroscopy (XPS, ESCALab250) was tested to analyze the surface chemical composition of the as-obtained samples with C1s photoelectron peak at 284.6 eV as the reference.

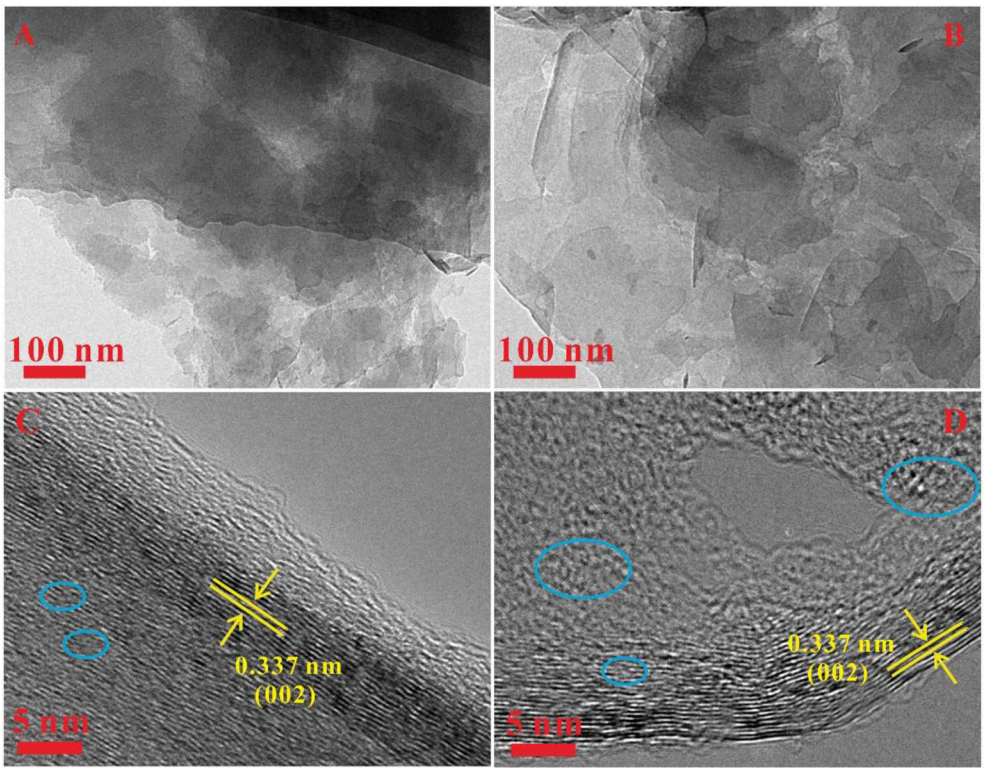

FIGURE 2 | (A,B) TEM images of the pure Gh and N-Gh samples. **(C,D)** HRTEM images of pure Gh and N-Gh samples.

Electrochemical Measurement

Active materials, super P, and polyvinylidene fluoride (PVDF) were mixed in N-methyl-2-pyrrolidone (NMP) with a mass ratio of 80:10:10 to form a coating slurry. Then, the as-obtained slurry was pressed onto a round nickel foam current collector. Finally, the electrodes with a loading mass of about 1.5 mg cm^{-2} were formed through drying at 50°C in a vacuum overnight and pressing under a 10 MPa pressure. A classic three-electrode electrochemical test system was utilized to investigate the electrochemical characteristics of the as-prepared materials. This test system was composed of a working electrode, platinum foil counter electrode, and Hg/HgO reference electrode. It is worth noting that the working electrodes should be soaked in 2 M KOH aqueous solution for 12 h before the electrochemical test. Moreover, the symmetric supercapacitor was equipped with two as-prepared working electrodes using 2 M KOH as an electrolyte solution and a glassy fibrous material as a separator. And the related calculation for the symmetric supercapacitor is based on the total mass of active material. Cyclic voltammetry (CV) curves were measured on MULTI AUTOLAB M204 (MAC90086) at various scanning rates. Electrochemical impedance measurements (EIS) were tested on a CHI 660B electrochemical working station with the frequency range between 100 and 0.01 Hz. Galvanostatic discharge/charge files were investigated at room temperature on Land CT2001A battery cycler.

RESULTS AND DISCUSSION

The Electrochemical Exfoliation via Alternating Voltage

The electrochemical processes of the as-prepared Gh and N-Gh materials via alternating voltage electrochemical exfoliation have been displayed in **Scheme 1**. On the basis of previous reports (Wang et al., 2014; Jing et al., 2015), the surface of graphite electrodes were alternately oxidized and reduced during the electrochemical process of alternating voltage. Meanwhile, some cations and anions in the electrolyte solution can intercalate the layers of graphite to accelerate stripping speed. In detail, some defects and oxygen-containing functional groups on the surface of the graphite electrode have been induced during the anodic process. Then, some oxidized graphite was reduced via a cathodic reaction. In NaOH solution, the Na^+ and OH^- can intercalate into the graphite layers. Certain amounts of hydrogen gas can be produced during the electrochemical process, which would promote the exfoliation rate of graphite. For the N-Gh sample, the addition of NH_4^+ and Cl^- ions might be conducive to exfoliate the graphite electrode through much more intercalation. Moreover, the Cl^- ions might be transformed into ClO^- or Cl_2 during the electrochemical anodic process (Munuera et al., 2017). The related oxidation-reduction of NH_4^+ also took place during alternate anodic and cathodic reactions, which could generate C-NH_2, -C-NH-C, and C-N-C_2 functional groups. With the introduction of NH_4Cl in the NaOH solution, the exfoliation

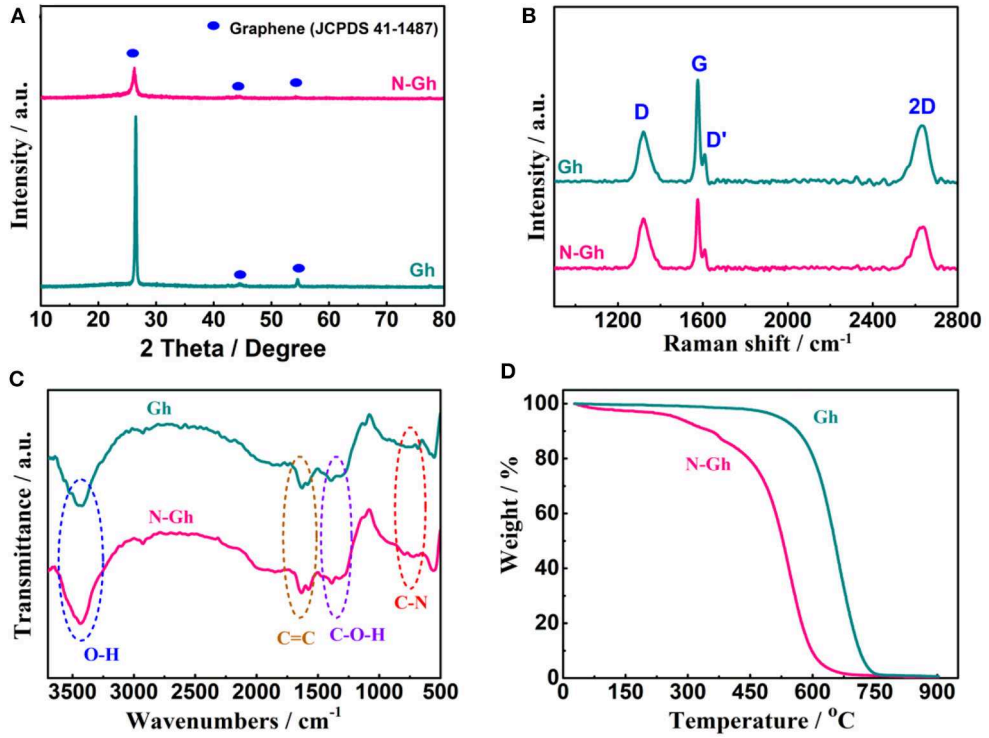

FIGURE 3 | (A) XRD patterns of pure Gh and N-Gh samples. **(B)** Raman spectra of pure Gh and N-Gh samples. **(C)** FT-IR spectra of pure Gh and N-Gh samples. **(D)** TG curves of pure Gh and N-Gh samples.

rate can be effectively enhanced via alternating the voltage electrochemical process.

The Microstructure, Morphology, and Composition of Samples

The SEM has been utilized to analyze the morphologies of the as-prepared Gh and N-Gh, which is shown in **Figure 1**. As displayed in **Figures 1A,B**, the pure Gh sample presents thin flakes with various sizes (0.5–5 μm^2). In **Figures 1C,D**, the N-Gh displays porous thin sheets. It can also be seen that the size of N-Gh is much larger than that of pure Gh. Further, the characterization of the morphology has been measured using TEM, as shown in **Figures 2A,C**. These results reveal that the exfoliated Gh and N-Gh flakes typically feature some overlapping regions. Additionally, the HRTEM image of Gh (in **Figure 2B**) presents lattice spacing of 0.337 nm, corresponding to (002) plane of graphene (Yang et al., 2014). In **Figure 2C**, a few defect-free and disorder domains can also be found in the as-obtained pure Gh. While the N-Gh sample exhibits a much more disordered structure and obvious pore structure in **Figure 2D**. The N-Gh prepared by alternating voltage exfoliation presents with a larger size and more defects than those of pure graphene, which might be due to the fast stripping and N doping processes.

Figure 3A presents the XRD powder pattern of pure Gh and N-Gh. The sharp peak of pure Gh at 26.4° is indexed as (002) crystal plane of graphene (JCPDS Card no.41-1487). This sharp peak illustrates that the Gh maintains a high degree of crystallization and electrical conductivity (Xu et al., 2015). According to the results of contrasting the curves of pure Gh and N-Gh, the peak intensity of the N-Gh sample is obviously weaker, which is consistent with the HRTEM conclusion. The order/disorder structures and defects characterization of the as-obtained materials have been further analyzed through Raman measurement, which is displayed in **Figure 3B**. The presence of G band at 1,577 cm^{-1} is related to E_{2g} symmetry phonon mode, corresponding to ordered in-plane sp^2 carbon atoms (Wang et al., 2017). The D band and D' shoulder band are at about 1,321 and 1,621 cm^{-1}, respectively, which belong to the disorder in the carbon hexagons and edge carbons (Deng et al., 2011). Moreover, the I_{2D}/I_G and I_D/I_G values of samples can typically reflect the number of layers and the degree of disorder structure, respectively (Soin et al., 2017). The I_{2D}/I_G values of pure Gh and N-Gh are 61.9 and 62.7%, respectively, which could illustrate that the flakes of both samples have only a few layers. The I_D/I_G value of N-Gh is 0.71, which is higher than that of pure Gh (0.57). This result again reveals that much more defects and disorder structure appear during the exfoliation process for N-Gh samples.

Furthermore, the surface functional groups of the as-obtained pure Gh and N-Gh have been detected via FT-IR spectrum analysis, as is displayed in **Figure 3C**. The large peaks at 3,432 cm^{-1} are related to O-H bending from H_2O (Wang X. et al., 2018). The weak peaks from 1,639 to 1,579 cm^{-1} can be indexed to sp^2-hybridized C=C stretching in plane vibrations, which

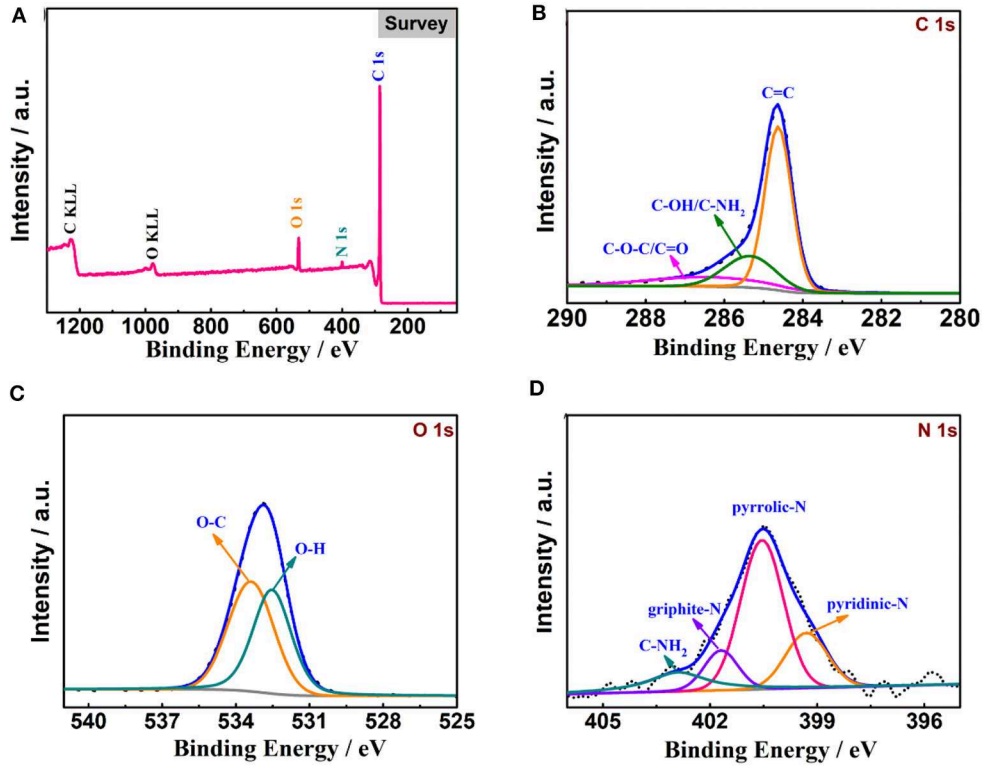

FIGURE 4 | XPS analysis of N-Gh material: **(A)** Full spectrum, **(B)** C 1 s spectrum, **(C)** O 1 s spectrum, **(D)** N 1 s spectrum.

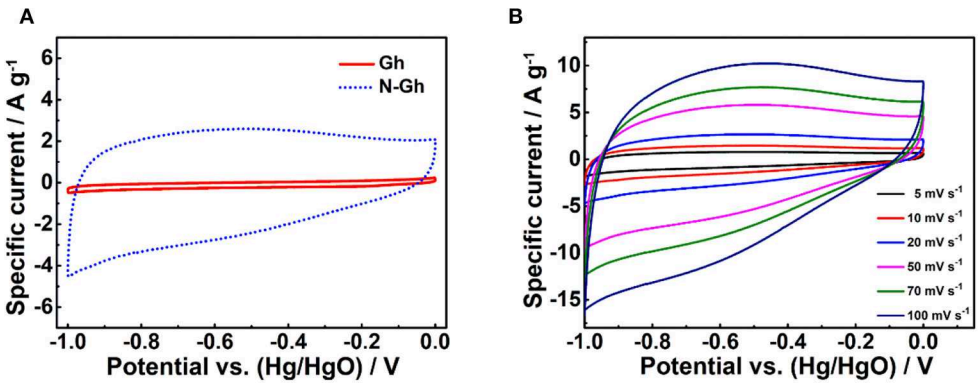

FIGURE 5 | (A) The CV files of pure Gh and N-Gh samples at a 10 mV s^{-1} based on a three-electrode system. **(B)** The CV curves of the as-prepared N-Gh under various scan rates from 5 to 100 mV s^{-1} based on a three-electrode system.

reveals the presence of the π-conjugation structure (Wang X. et al., 2018; Lee et al., 2019). The weak peaks from 1,383 to 1,308 cm^{-1} correspond to oxygen-containing functional groups (C-O, C-OH, C-O-C) which illustrate the existence of a few hydroxyl/phenolic/alkoxy groups on the surface of the exfoliated Gh and N-Gh samples (Lee et al., 2019). A small peak at 728 cm^{-1} might correspond to C-N stretching (Islam et al., 2016), which indicates that N can be successfully doped *in-situ* during alternating voltage electrochemical exfoliation. In **Figure 3D,** the mass loss from 25 to 300°C of N-Gh might be mainly resulted from adsorbed water and coordinated water (Chen et al., 2020). Compared to the pure Gh, the TGA curve of N-Gh with the temperature from 300 to 700°C displays a quick downward trend, which illustrates the existence of much more defects and disorder structure in the as-obtained N-Gh sample (Xu et al., 2015).

The XPS spectra of N-Gh are displayed in **Figure 4**. As shown in **Figure 4A**, the C, O, and N elements all lie in the as-prepared N-Gh sample. The N atom content is 4.5% and the O/C

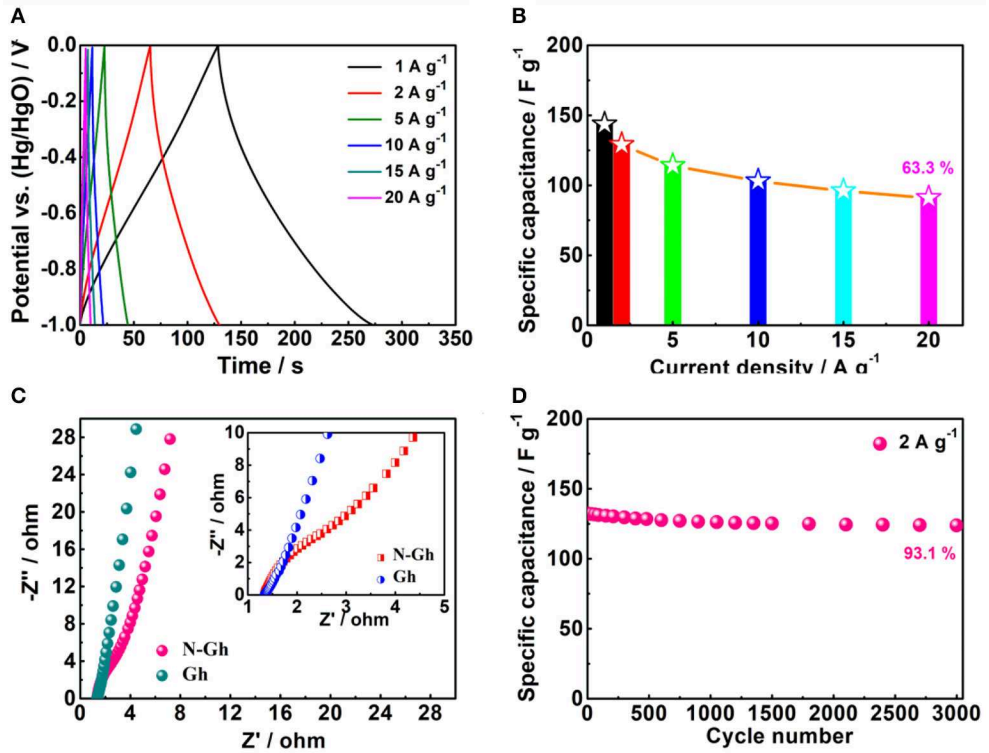

FIGURE 6 | (A) Galvanostatic charge-discharge files and **(B)** Specific capacities of the as-prepared N-Gh at various current densities from 1 to 20 A g^{-1} based on a three-electrode system. **(C)** Impedance spectroscopy plots of Gh and N-Gh in a three-electrode system (The inset is a larger version of the impedance spectroscopy plots). **(D)** Cycling stability of N-Gh at 2 A g^{-1} based on a three-electrode system.

atom ratio in this sample is 0.09. Further, a dominant peak at 284.6 eV is shown in the high-resolution XPS spectrum of C 1s (**Figure 4B**), which is assigned to graphitic C=C species, and the other two weak peaks at 285.5 eV and 286.4 eV correspond to sp^3 carbons (C-OH/C-NH_2) and oxygen carbons (C-O-C/C=O), respectively (Wang et al., 2014). The O 1s spectrum presents two peaks at 532.1 and 533.7 eV in **Figure 4C**, which are related to O=C and O-C, respectively (Hou et al., 2015; Bulusheva et al., 2017). A few oxygen-containing functional groups in the N-Gh sample could be helpful to relieve overlapping. The N 1s spectrum (in **Figure 4D**) has been fitted into four peaks at 399.3 eV, 400.5 eV, 401.7 eV, and 402.9 eV, which are assigned to pyridinic nitrogen (19.8%), pyrrolic nitrogen (54.2%), graphite nitrogen (11.9%), and C-NH_2 (14.1%), respectively (Lee et al., 2014; Hong et al., 2019). These results again confirm that N has been successfully doped in N-Gh, which might contribute to the improvement of electrochemical performances.

The Electrochemical Properties of Samples Based on a Three-Electrode System

The electrochemical performances of pure Gh and N-Gh samples have been firstly explored using CV tests in 2 M KOH electrolyte solution with the voltage range from −1.0 to 0 V based on a three-electrode system, which is shown in **Figure 5A**. It can be clearly seen that pure Gh and N-Gh samples display rectangular CV curves, suggesting obvious electric double-layer storage behaviors (Munuera et al., 2017). The curve area of N-Gh is much larger than that of the pure Gh sample, which indicates the doping of N can obviously improve the specific capacity. Furthermore, the CV measurements of N-Gh based on increased scan rates from 5 to 100 mV s^{-1} have been studied, as is revealed in **Figure 5B**. The intensities of CV files increased with the increased scan rates, yet the shapes of curves remained broadly stable (Zhu et al., 2018; Tang et al., 2019). This result reveals that N-Gh might present good electrochemical reversibility.

Then, the charge-discharge files of the as-prepared N-Gh electrode in 2 M KOH electrolyte solution at various current densities are displayed in **Figure 6A**. Based on the specific capacitance formula ($C_s = It/m\Delta V$, F g^{-1}) (Wang Y. et al., 2018; Wei et al., 2019), the specific capacitances of N-Gh electrode at the current densities of 1, 2, 5, 10, 15, and 20 A g^{-1} are 143.6, 129.1, 114.2, 103.2, 96.5, and 91.5 F g^{-1}, respectively, with high coulombic efficiency around 100%, which is displayed in **Figure 6B**. Compared with the specific capacitance at 1 A g^{-1}, the capacity retention rate is up to 63.7% even at 20 A g^{-1}. This high rate behavior might be related to the existence defects and doping N in the N-Gh sample. Moreover, the EIS curves of pure Gh and N-Gh electrodes in 2 M KOH aqueous solution at their open voltages are shown in **Figure 6C**. Both samples present very small semicircles in the high frequency and high slope in

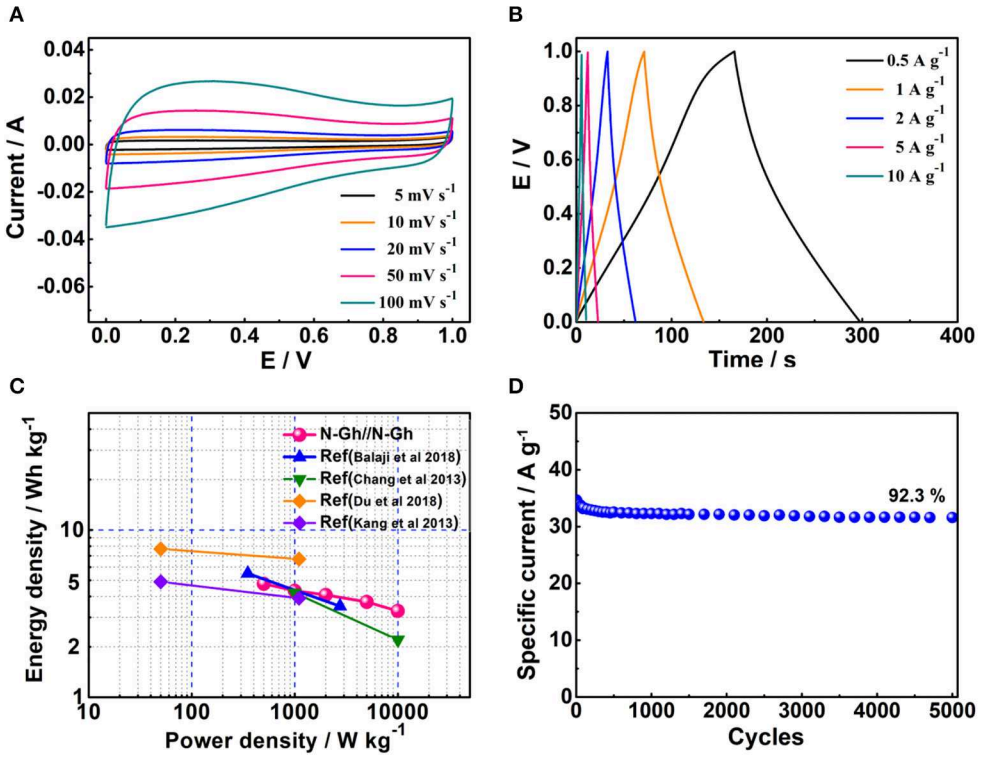

FIGURE 7 | (A) The CV files of N-Gh at various scan rates from 5 to 100 mV s^{-1} based on a two-electrode system. **(B)** Galvanostatic charge-discharge files of N-Gh//N-Gh with the current densities range from 1 to 20 A g^{-1}. **(C)** Ragone plots of N-Gh//N-Gh. **(D)** Cycling stability of N-Gh//N-Gh at 0.5 A g^{-1}.

the low frequency region, suggesting the pure Gh and N-Gh electrodes display high electrical conductivity and ion diffusion. The cycling stability of N-Gh electrodes have been investigated, which is displayed in **Figure 6D**. After 3,000 charge/discharge cycles in KOH aqueous solution, the specific capacity retention of N-Gh is up to 93.1% at a current density of 2 A g^{-1}. All these improved electrochemical performances could be derived from the structure of N-Gh sample with N doping, which has few effects and a disordered structure.

The Electrochemical Performances of N-Gh Based on a Two-Electrode System

To better study the electrochemical capacity performances of the as-obtained N-Gh, the symmetric supercapacitor has been fabricated with two N-Gh electrodes. **Figure 7A** displays the CV curves of N-Gh//N-Gh symmetric supercapacitor under the potential voltage from 0 to 1 V at different scan rates. It can be clearly seen that the shape of files stays the same as the scan rate increases (from 5 to 100 mV s^{-1}), indicating the N-Gh//N-Gh symmetric supercapacitor might display good electrochemical reversibility. The charge/discharge files of N-Gh//N-Gh symmetric supercapacitor at the current densities between 0.5 and 10 A g^{-1} are revealed in **Figure 7B**. The charge curves and discharge curves are almost symmetrical, revealing high columbic efficiency. Additionally, the specific capacities of the N-Gh//N-Gh symmetric supercapacitor have been calculated on the discharge files on the basis of the total mass of negative and positive electrode slices, as shown in **Figure 7C**. The specific capacities of the symmetric supercapacitor are 34.2, 31.2, 29.4, 26.7, and 24.2 F g^{-1} at current densities of 0.5, 1, 2, 5, and 10 A g^{-1}, respectively. The energy density of this symmetric supercapacitor is 4.76 Wh kg^{-1} at a power density of 500 W kg^{-1}, and the retention ratio is up to 68.7% at the power density of 10,000 W kg^{-1}. Compared with some other N doped carbon-based materials (in Figure 7C) (Chang et al., 2013; Kang et al., 2013; Balaji et al., 2018; Du et al., 2018), the energy density and rate behavior of N-Gh//N-Gh is satisfactory. The cycling stability has been also investigated in **Figure 7D**, presenting with 92.3% retention of N-Gh//N-Gh initial specific capacity after 5000 cycles. The perfect rate behavior and cycling stability of the N-Gh//N-Gh symmetric supercapacitor further illustrates the as-prepared N-Gh might be a promising material for various kinds of composites in supercapacitors.

CONCLUSION

In summary, the N-Gh sample has been prepared through an *in-situ* alternating voltage electrochemical exfoliation technique with the introduction of NH_4Cl in to NaOH aqueous solution. The N chemical states in the N-Gh sample mainly present pyrrolic nitrogen. Compared with the as-obtained pure Gh sample, the N-Gh shows a larger size, much more effects, and

a disordered structure. Additionally, the related electrochemical behaviors have been investigated in a three-electrode aqueous solution system, indicating that N-Gh displays a much higher specific capacity than that of pure Gh. Moreover, it also displays a good cycling stability and high rate behavior with 63.7% of the capacity retention rate even at a current density of 20 A g^{-1}. All these good electrochemical characteristics of N-Gh could be ascribed to the doping N, the existence of effects, and disorder structure, which is conducive to producing faradaic pseudocapacitance and reducing overlapping layers of graphene. The results of the symmetric supercapacitor fabricated with two N-Gh electrodes further illustrate the satisfactory cycling stability with 92.3% retention of N-Gh//N-Gh initial specific capacity after 5,000 cycles. These insights illustrate that the N-Gh sample prepared via an *in-situ* alternating voltage approach could have promising applications to construct composites for enhanced supercapacitors.

DATA AVAILABILITY STATEMENT

All datasets generated for this study are included in the article/supplementary material.

AUTHOR CONTRIBUTIONS

MJ and TW designed and engineered the samples, performed the experiments, and wrote the paper. All authors contributed to performing the data analysis and general discussion.

FUNDING

This work was supported by the National Natural Science Foundation of China (No. 21701044, 51625404), Postdoctoral Science Foundation Natural Science of China (No. 2019M662800), and Research Foundation of Education Bureau of Hunan Province, China (Grant no. 17A086).

ACKNOWLEDGMENTS

The authors also acknowledge the assistance on XPS measurements received from the Instrumental Analysis Center of Central South University.

REFERENCES

Bakunin, E. S., Obraztsova, E. Y., and Rukhov, A. V. (2019). modern methods for synthesis of few-layer graphene structures by electrochemical exfoliation of graphite. *Inorganic Mater.* 10, 249–255. doi: 10.1134/S2075113319020047

Balaji, S. S., Karnan, M., and Sathish, M. (2018). Symmetric electrochemical supercapacitor performance evaluation of N-doped graphene prepared via supercritical fluid processing. *J. Solid State Electrochem.* 22, 3821–3832. doi: 10.1007/s10008-018-4086-9

Bu, F., Chen, W., Gu, J., Agboola, P. O., Al-Khalli, N. F., Shakir, I., et al. (2018). Microwave-assisted CVD-like synthesis of dispersed monolayer/few-layer N-doped graphene encapsulated metal nanocrystals for efficient electrocatalytic oxygen evolution. *Chem. Sci.* 9, 7009–7016. doi: 10.1039/C8SC02444H

Bulusheva, L. G., Kanygin, M. A., Arkhipov, V. E., Popov, K. M., Fedoseeva, Y. V., Smirnov, D. A., et al. (2017). *In situ* X-ray photoelectron spectroscopy study of lithium interaction with graphene and nitrogen-doped graphene films produced by chemical vapor deposition. *J. Phys. Chem. C* 121, 5108–5114. doi: 10.1021/acs.jpcc.6b12687

Chaban, V. V., and Prezhdo, O. V. (2015). Nitrogen-nitrogen bonds undermine stability of N-Doped graphene. *J. Am. Chem. Soc.* 137, 11688–11694. doi: 10.1021/jacs.5b05890

Chang, Y., Han, G., Yuan, J., Fu, D., Liu, F., and Li, S. (2013). Using hydroxylamine as a reducer to prepare N-doped graphene hydrogels used in high-performance energy storage. *J. Power Sources* 238, 492–500. doi: 10.1016/j.jpowsour.2013.04.074

Chen, K., Li, G., Wang, Y., Chen, W., and Mi, L. (2020). High loading FeS2 nanoparticles anchored on biomass-derived carbon tube as low cost and long cycle anode for sodium-ion batteries. *Green Energy Environ.* 5, 50–58. doi: 10.1016/j.gee.2019.11.001

Deng, D., Pan, X., Yu, L., Cui, Y., Jiang, Y., Qi, J., et al. (2011). Toward N-Doped graphene via solvothermal synthesis. *Chem. Mater.* 23, 1188–1193. doi: 10.1021/cm102666r

Du, Y., Liu, L., Xiang, Y., and Zhang, Q. (2018). Enhanced electrochemical capacitance and oil-absorbability of N-doped graphene aerogel by using amino-functionalized silica as template and doping agent. *J. Power Sources* 379, 240–248. doi: 10.1016/j.jpowsour.2018.01.047

Ejigu, A., Le Fevre, L. W., Fujisawa, K., Terrones, M., Forsyth, A. J., and Dryfe, R. A. W. (2019). Electrochemically exfoliated graphene electrode for high-performance rechargeable chloroaluminate and dual-ion batteries. *ACS Appl. Mater. Interfaces* 11, 23261–23270. doi: 10.1021/acsami.9b06528

Gong, X., Liu, G., Li, Y., Yu, D. Y. W., and Teoh, W. Y. (2016). Functionalized-graphene composites: fabrication and applications in sustainable energy and environment. *Chem. Mater.* 28, 8082–8118. doi: 10.1021/acs.chemmater.6b01447

Hong, W., Zhang, Y., Yang, L., Tian, Y., Ge, P., Hu, J., et al. (2019). Carbon quantum dot micelles tailored hollow carbon anode for fast potassium and sodium storage. *Nano Energy* 65:104038. doi: 10.1016/j.nanoen.2019.104038

Hou, H., Banks, C. E., Jing, M., Zhang, Y., and Ji, X. (2015). Carbon quantum dots and their derivative 3D porous carbon frameworks for sodium-ion batteries with ultralong cycle life. *Adv. Mater.* 27, 7861–7866. doi: 10.1002/adma.201503816

Islam, M. S., Mandal, B. H., Biswas, T. K., Rahman, M. L., Rashid, S. S., Tan, S.-H., et al. (2016). Poly(hydroxamic acid) functionalized copper catalyzed C–N bond formation reactions. *RSC Adv.* 6, 56450–56457. doi: 10.1039/C6RA08155J

Jing, M., Wang, C., Hou, H., Wu, Z., Zhu, Y., Yang, Y., et al. (2015). Ultrafine nickel oxide quantum dots enbedded with few-layer exfoliative graphene for an asymmetric supercapacitor: enhanced capacitances by alternating voltage. *J. Power Sources* 298, 241–248. doi: 10.1016/j.jpowsour.2015.08.039

Kang, E., Jeon, G., and Kim, J. K. (2013). Free-standing, well-aligned ordered mesoporous carbon nanofibers on current collectors for high-power micro-supercapacitors. *Chem. Commun.* 49, 6406–6408. doi: 10.1039/c3cc42436g

Lee, J., Noh, S., Pham, N. D., and Shim, J. H. (2019). Top-down synthesis of S-doped graphene nanosheets by electrochemical exfoliation of graphite: metal-free bifunctional catalysts for oxygen reduction and evolution reactions. *Electrochim. Acta* 313, 1–9. doi: 10.1016/j.electacta.2019.05.015

Lee, K. H., Oh, J., Son, J. G., Kim, H., and Lee, S.-S. (2014). Nitrogen-Doped graphene nanosheets from bulk graphite using microwave irradiation. *ACS Appl. Mater. Interfaces* 6, 6361–6368. doi: 10.1021/am405735c

Liu, W. W., and Wang, J. N. (2011). Direct exfoliation of graphene in organic solvents with addition of NaOH. *Chem. Commun.* 47, 6888–6890. doi: 10.1039/c1cc11933h

Low, C. T. J., Walsh, F. C., Chakrabarti, M. H., Hashim, M. A., and Hussain, M. A. (2013). Electrochemical approaches to the production of

graphene flakes and their potential applications. *Carbon N. Y.* 54, 1–21. doi: 10.1016/j.carbon.2012.11.030

Luo, G., Liu, L., Zhang, J., Li, G., Wang, B., and Zhao, J. (2013). Hole defects and nitrogen doping in graphene: implication for supercapacitor applications. *ACS Appl. Mater. Interfaces* 5, 11184–11193. doi: 10.1021/am403427h

Munuera, J. M., Paredes, J. I., Enterría, M., Pagán, A., Villar-Rodil, S., Pereira, M. F. R., et al. (2017). Electrochemical exfoliation of graphite in aqueous sodium halide electrolytes toward low oxygen content graphene for energy and environmental applications. *ACS Appl. Mater. Interfaces* 9, 24085–24099. doi: 10.1021/acsami.7b04802

Novoselov, K. S., Geim, A. K., Morozov, S. V., Jiang, D., Zhang, Y., Dubonos, S. V., et al. (2004). Electric field effect in atomically thin carbon films. *Science* 306, 666. doi: 10.1126/science.1102896

Parvez, K., Wu, Z.-S., Li, R., Liu, X., Graf, R., Feng, X., et al. (2014). Exfoliation of graphite into graphene in aqueous solutions of inorganic salts. *J. Am. Chem. Soc.* 136, 6083–6091. doi: 10.1021/ja5017156

Qu, L., Liu, Y., Baek, J.-B., and Dai, L. (2010). Nitrogen-doped graphene as efficient metal-free electrocatalyst for oxygen reduction in fuel cells. *ACS Nano* 4, 1321–1326. doi: 10.1021/nn901850u

Rao, K. S., Senthilnathan, J., Liu, Y.-F., and Yoshimura, M. (2014). Role of peroxide ions in formation of graphene nanosheets by electrochemical exfoliation of graphite. *Sci. Rep.* 4, 4237. doi: 10.1038/srep04237

Soin, N., Ray, S. C., Sarma, S., Mazumder, D., Sharma, S., Wang, Y.-F., et al. (2017). Tuning the Electronic and magnetic properties of nitrogen-functionalized few-layered graphene nanoflakes. *J. Phys. Chem. C* 121, 14073–14082. doi: 10.1021/acs.jpcc.7b01645

Suk, J. W., Kitt, A., Magnuson, C. W., Hao, Y., Ahmed, S., An, J., et al. (2011). Transfer of CVD-grown monolayer graphene onto arbitrary substrates. *ACS Nano* 5, 6916–6924. doi: 10.1021/nn201207c

Taheri Najafabadi, A., and Gyenge, E. (2015). Synergistic production of graphene microsheets by simultaneous anodic and cathodic electro-exfoliation of graphitic electrodes in aprotic ionic liquids. *Carbon N. Y.* 84, 449–459. doi: 10.1016/j.carbon.2014.12.041

Tang, T., Cui, S., Chen, W., Hou, H., and Mi, L. (2019). Bio-inspired nano-engineering of an ultrahigh loading 3D hierarchical Ni@$NiCo_2S_4$/Ni_3S_2 electrode for high energy density supercapacitors. *Nanoscale* 11, 1728–1736. doi: 10.1039/C8NR09754B

Usachov, D., Vilkov, O., Gruneis, A., Haberer, D., Fedorov, A., Adamchuk, V. K., et al. (2011). Nitrogen-doped graphene: efficient growth, structure, and electronic properties. *Nano Lett.* 11, 5401–5407. doi: 10.1021/nl2031037

Wang, H., Maiyalagan, T., and Wang, X. (2012). Review on recent progress in nitrogen-doped graphene: synthesis, characterization, and its potential applications. *ACS Catal.* 2, 781–794. doi: 10.1021/cs200652y

Wang, H., Wei, C., Zhu, K., Zhang, Y., Gong, C., Guo, J., et al. (2017). Preparation of graphene sheets by electrochemical exfoliation of graphite in confined space and their application in transparent conductive films. *ACS Appl. Mater. Interfaces* 9, 34456–34466. doi: 10.1021/acsami.7b09891

Wang, P., Xiao, J., Guo, M., Xia, Y., Li, Z., and Huang, W. (2014). Preparation of graphite nanoflakes and supported noble metal/alloy nanoparticles by paired electrolysis with graphite electrodes. *J. Electrochem. Soc.* 161, H606–H611. doi: 10.1149/2.1211409jes

Wang, X., Ding, Y., Chen, F., Lu, H., Zhang, N., and Ma, M. (2018). Hierarchical porous N-doped graphene monoliths for flexible solid-state supercapacitors with excellent cycle stability. *ACS Appl. Energy Mater.* 1, 5024–5032. doi: 10.1021/acsaem.8b01011

Wang, Y., Lu, Y., Chen, K., Cui, S., Chen, W., and Mi, L. (2018). Synergistic effect of Co3O4@C@MnO2 nanowire heterostructures for high-performance asymmetry supercapacitor with long cycle life. *Electrochim. Acta* 283, 1087–1094. doi: 10.1016/j.electacta.2018.06.163

Wei, W., Ye, W., Wang, J., Huang, C., Xiong, J.-B., Qiao, H., et al. (2019). Hydrangea-like α-Ni1/3Co2/3(OH)2 reinforced by Ethyl Carbamate "Rivet" for all-solid-state supercapacitors with outstanding comprehensive performance. *ACS Appl. Mater. Interfaces* 11, 32269–32281. doi: 10.1021/acsami.9b09555

Xu, J., Lin, Y., Connell, J. W., and Dai, L. (2015). Nitrogen-doped holey graphene as an anode for lithium-ion batteries with high volumetric energy density and long cycle life. *Small* 11, 6179–6185. doi: 10.1002/smll.201501848

Xu, Y., Zhang, C., Zhou, M., Fu, Q., Zhao, C., Wu, M., et al. (2018). Highly nitrogen doped carbon nanofibers with superior rate capability and cyclability for potassium ion batteries. *Nat. Commun.* 9:1720. doi: 10.1038/s41467-018-04190-z

Yang, S., Brüller, S., Wu, Z.-S., Liu, Z., Parvez, K., Dong, R., et al. (2015). Organic radical-assisted electrochemical exfoliation for the scalable production of high-quality graphene. *J. Am. Chem. Soc.* 137, 13927–13932. doi: 10.1021/jacs.5b09000

Yang, W., Chen, G., Shi, Z., Liu, C.-C., Zhang, L., Xie, G., et al. (2013). Epitaxial growth of single-domain graphene on hexagonal boron nitride. *Nat. Mater.* 12, 792–797. doi: 10.1038/nmat3695

Yang, Y., Lu, F., Zhou, Z., Song, W., Chen, Q., and Ji, X. (2013). Electrochemically cathodic exfoliation of graphene sheets in room temperature ionic liquids N-butyl, methylpyrrolidinium bis(trifluoromethylsulfonyl)imide and their electrochemical properties. *Electrochim. Acta* 113, 9–16. doi: 10.1016/j.electacta.2013.09.031

Yang, Y., Qiao, B., Yang, X., Fang, L., Pan, C., Song, W., et al. (2014). Lithium titanate tailored by cathodically induced graphene for an ultrafast lithium ion battery. *Adv. Funct. Mater.* 24, 4349–4356. doi: 10.1002/adfm.201304263

Yang, Y., Shi, W., Zhang, R., Luan, C., Zeng, Q., Wang, C., et al. (2016). Electrochemical exfoliation of graphite into nitrogen-doped graphene in glycine solution and its energy storage properties. *Electrochim. Acta* 204, 100–107. doi: 10.1016/j.electacta.2016.04.063

Yi, M., and Shen, Z. (2015). A review on mechanical exfoliation for the scalable production of graphene. *J. Mater. Chem. A* 3, 11700–11715. doi: 10.1039/C5TA00252D

Zabihi, O., Ahmadi, M., Li, Q., Fakhrhoseini, S.M., Komeily Nia, Z., Arjmand, M., et al. (2019). Simultaneous electrochemical-assisted exfoliation and *in situ* surface functionalization towards large-scale production of few-layer graphene. *FlatChem* 18:100132. doi: 10.1016/j.flatc.2019.100132

Zhang, C., Fu, L., Liu, N., Liu, M., Wang, Y., and Liu, Z. (2011). Synthesis of nitrogen-doped graphene using embedded carbon and nitrogen sources. *Adv. Mater.* 23, 1020–1024. doi: 10.1002/adma.201004110

Zhu, Y., Huang, Z., Hu, Z., Xi, L., Ji, X., and Liu, Y. (2018). 3D interconnected ultrathin cobalt selenide nanosheets as cathode materials for hybrid supercapacitors. *Electrochim. Acta* 269, 30–37. doi: 10.1016/j.electacta.2018.02.146

Conflict of Interest: The authors declare that the research was conducted in the absence of any commercial or financial relationships that could be construed as a potential conflict of interest.

Advantages of publishing in Frontiers

OPEN ACCESS
Articles are free to read for greatest visibility and readership

FAST PUBLICATION
Around 90 days from submission to decision

HIGH QUALITY PEER-REVIEW
Rigorous, collaborative, and constructive peer-review

TRANSPARENT PEER-REVIEW
Editors and reviewers acknowledged by name on published articles

Frontiers
Avenue du Tribunal-Fédéral 34
1005 Lausanne | Switzerland

Visit us: www.frontiersin.org
Contact us: info@frontiersin.org | +41 21 510 17 00

REPRODUCIBILITY OF RESEARCH
Support open data and methods to enhance research reproducibility

DIGITAL PUBLISHING
Articles designed for optimal readership across devices

FOLLOW US
@frontiersin

IMPACT METRICS
Advanced article metrics track visibility across digital media

EXTENSIVE PROMOTION
Marketing and promotion of impactful research

LOOP RESEARCH NETWORK
Our network increases your article's readership